High-energy Collision-induced Dissociation of Macromolecules using Tandem Double-focusing/ Time-of-Flight Mass Spectrometry.

Andrew R. Bottrill

Submitted for the qualification of Doctor of Philosophy.

University of Warwick.
Chemistry Department

September 2000

Contents

List of Figures

Chapter 1 - Introduction

Chapter 2 - Instrumentation

Chapter 3 - Development of the MALDI Ion Source of the MAG-TOF Instrument

Page Number

Chapter Four - Collision-induced Dissociation of Fullerenes.

Page Number

Chapter Five: Collision-induced Dissociation of Alkali-metal Cationised Polyglycols

Page Number

Chapter Six –Collision-Induced Dissociation of Protonated Polyglycols.

Page Number

Acknowledgements.

Throughout the course of my Ph.D., many people have given me invaluable support and assistance. In particular I would like to thank:

Professor Peter Derrick for giving me the chance to be involved in such a stimulating project, and for the guidance and encouragement that he has provided.

Dr. Anastasios Giannakopulos for his invaluable help in solving numerous experimental problems during this study, as well as for his support and friendship.

Dr. Ulla Andersen for her patient tuition on the mass spectrometer used in this work and for answering an endless number of questions.

Dr. Ken Lee for all his ideas and discussion throughout this work, and for providing me with the oportunity to visit his laboratory.

Dr. Thomas Drewello for the introduction to mass spectrometry of fullerenes and whose enthusiasm for this area of research has provided strong motivation.

Mr. Benjamin Thomas, Mr. David Morsley and Mr. Sajid Bashir for being dear friends and colleagues during the course of this study.

All the members of Professor Derrick's research group, both past and present, whom I have had the pleasure of knowing and working alongside during my Ph.D. Especially I would like to thank Mr Alex Colburn, Mr Mark Barrow, Mr. Philip Green, Dr. Anne-Mette Hoberg, Dr. Daniel Lafitte, Mr Yi-Bing Zhang, Dr. Julie Varney and Dr. Helen Cooper.

Unilever Research Port Sunlight for providing financial support.

My parents, Adrian and Hilary Bottrill, and my sisters, Jennie and Hannah Bottrill, for their encouragement and support throughout my education, and especially during the last four years.

My partner Ms. Grania Towle for her unconditional love and understanding that have inspired me and helped me complete this work

Declaration

I hereby declare that this thesis is my own work and that, to the best of my knowledge and belief, it contains no material previously published or written by another person, nor material which to a substantial extent has been accepted for the award of any other degree or diploma of a university or institute of higher education, except where due acknowledgement is made in the text.

Andrew Robert Bottrill

Abstract

The first part of this study involves the adaptation of a matrix-assisted laser desorption/ionisation (MALDI) ion source for a tandem double-focusing/time-of-flight instrument (MAG-TOF). Ion trajectory modelling was carried out for defining the optimum ion optical configuration for a new extraction region and associated ion optics that were designed and constructed. Installation of the new ion source resulted in increased sensitivity and no loss of resolution.

The second part of this study involves the analysis of fullerenes and fullerene derivatives by high-energy collision-induced dissociation (CID). The structure of fullerenes formed by coalescence under the conditions of laser desorption were shown to be that of a single fullerene closed-cage structure. The dissociation of exohedral fullerene hydride derivatives was investigated.

The third part of this study investigates the high-energy collision-induced dissociation of polyglycol polymer ions generated by MALDI. Mechanisms have been proposed for the dissociation of poly(ethylene glycol) and poly(propylene glycol). High-energy CID has been shown to be particularly useful for the determination of polymer end-group structure.

Chapter One: *Introduction*

1.1 Mass Spectrometry - A Historical Background

The dawn of mass spectrometry occurred over one hundred years ago. In 1886 luminous rays were found to emanate from a perforated cathode plate inside a discharge tube.[1] Those rays, named "Kanal Strahlen", were observed to be deflected by a magnetic field, but in a direction opposite to that observed for cathode rays (electron beams). They later proved to be the first ion beams ever observed.

A positive ray analyser was built in 1907 by Thomson.[2] A narrow pipe through the cathode allowed a portion of the rays from a discharge tube to pass through superimposed parallel magnetic and electric fields. Ion detection was performed by observing the glow on the walls of the glass tube.

The combination of magnetic and electric fields caused the ions to strike the glass tube along lines with parabolic shapes. The intersection point of the parabolas corresponded to the non-deflected beam position. Using the same laws of motion that had been found for the electron,[3,4,5] Thomson found that each of the parabolas corresponded to a specific mass-to-charge ratio, with the arc length dependent on the spread of initial velocities of the particles.

Thomson established that the positively charged particles were formed by the removal of electrons from the neutral gas molecules in the discharge tube,[6] and further experiments revealed the presence of isotopes.

Thomson had unlocked the door to mass spectrometry. With improved instrumentation, mass spectrometry has become a powerful analytical tool in a variety of research fields, including biochemistry and, increasingly, polymer science.

1.2 Mass Analysers

1.2.1 Sector Mass Analysers

Perhaps one of the most obvious methods for the analysis of a beam of charged particles is deflection in different directions according to their masses. This can be achieved by the application of either magnetic or electric fields.

1.2.1.1 Magnetic Sector Deflection

A simple magnetic sector instrument consists of an ion source, a homogeneous magnetic field region and a detector. Ions are generated in the source and accelerated by an electric field through a potential difference V_0. Upon exiting the source the ions have a kinetic energy E_k, given by the equation:

$$E_k = qeV_0 = \frac{mv^2}{2} \qquad \textit{Eq. 1.1}$$

q = number of charges

e = electronic charge

V_0 = accelerating potential

m = mass of the particle

v = velocity

An ion entering a homogeneous magnetic field (B) experiences a force perpendicular to both the magnetic field and to the ion velocity (v). The ion follows a circular path

of radius r. The force on the ion due to the magnetic field must balance the centripetal force:

$$Bqev = \frac{mv^2}{r} \qquad \textit{Eq. 1.2}$$

Combining Equations 1.1 and 1.2 gives:

$$\frac{m}{qe} = \frac{B^2 r^2}{2V_0} \qquad \textit{Eq. 1.3}$$

Equation 1.3 can be written as:

$$r = \frac{1}{B}\left(\frac{2V_0 m}{qe}\right)^{\frac{1}{2}} \qquad \textit{Eq. 1.4}$$

With B and V_0 constant, the radius r is directly proportional to the square root of the mass-to-charge ratio m/qe. Thus an ion beam consisting of species of different masses will separate within the magnetic field into a number of different ion beams following circular trajectories with differing well-defined radii. The different species will each arrive at a characteristic point on the detector, and can be assigned a particular mass-to-charge ratio. The principle of operation of a single-focusing magnetic sector instrument is illustrated in figure 1.1.

1.2.1.2 Electric Sector Deflection

An electric field can be applied as an alternative to a homogeneous magnetic field. An electric field is applied across two parallel cylindrical plates of mean radius r'. The radial electrostatic field (E) produced by these plates will affect the ion beam such that the ions follow a circular path of radius r'. The equation of motion of an ion under the influence of a radial electric field E of radius r' is given by equation 1.5:

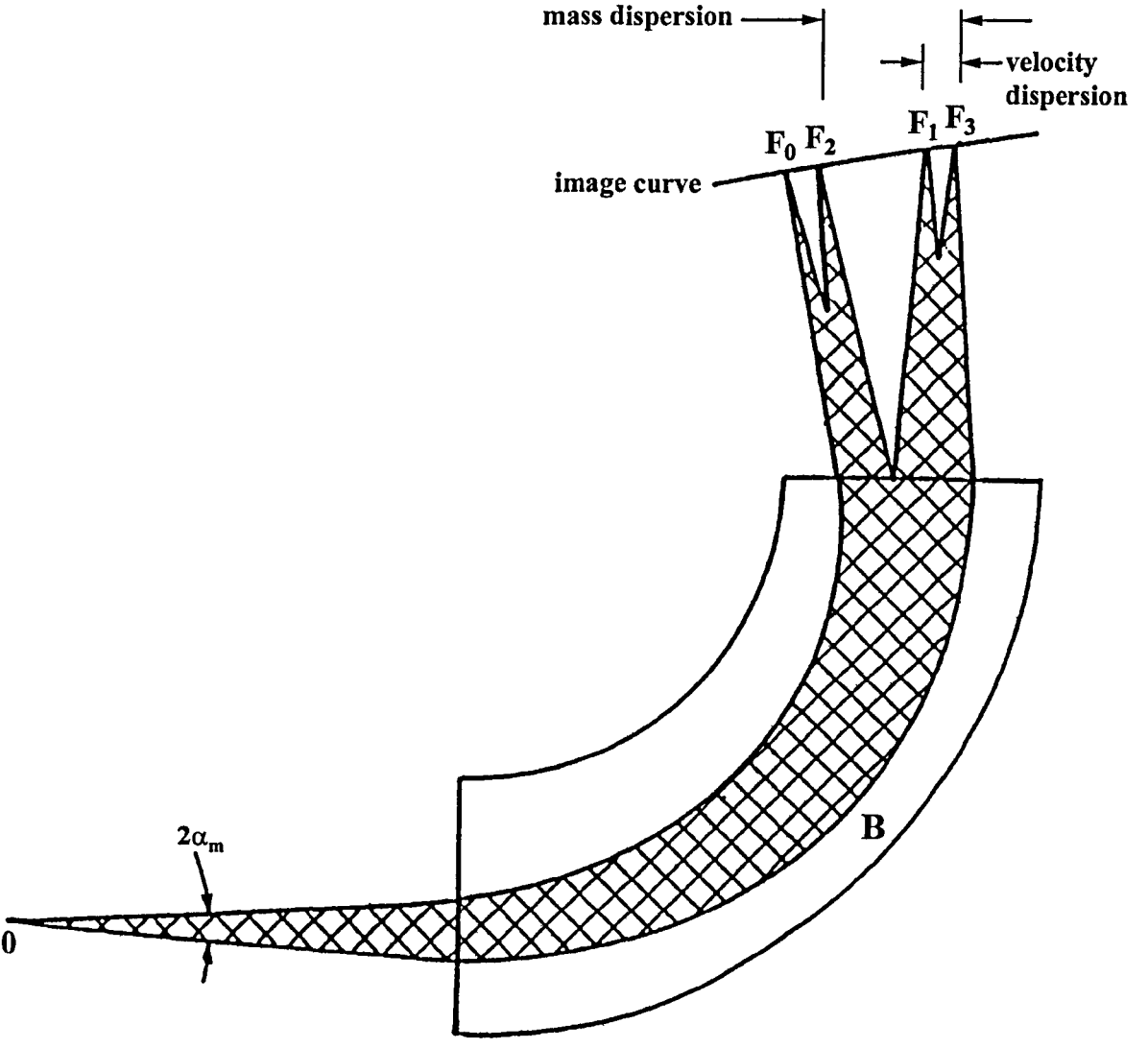

0	Point source for ions of mass M_0 and M_1 and velocity v_0 and v_1, with angular divergence of $2\alpha_m$ (where $M_1 > M_0$, $v_1 > v_0$ and $M_1v_0 > M_0v_1$).
F_0	Direction focus point for ions of mass M_0 and velocity v_0
F_2	Direction focus point for ions of mass M_0 and velocity v_1
F_1	Direction focus point for ions of mass M_1 and velocity v_0
F_3	Direction focus point for ions of mass M_1 and velocity v_1

Figure 1.1 – Principle of operation of magnetic sector (momentum) analyser.

$$r = \frac{1}{E}\left(\frac{mv}{qe}\right) \qquad \textit{Eq. 1.5}$$

Ions are spatially focused according to their kinetic energy-to-charge ratio. The principle of operation of an electrostatic sector instrument is illustrated in figure 1.2.

1.2.1.3 Combinations of Electrostatic and Magnetic Sectors

In practice, an ion source always gives the ions an energy spread, so that the ideal situation where all ions are accelerated to the same precise energy qeV_0 does not exist. The mass resolution of a single magnetic sector is limited by the mean energy spread of an ion ($qe\Delta V_0$).

In 1919 Aston developed an instrument employing separated electrostatic and magnetic fields, in order to address the problem of energy spread caused by the ion source.[7] Aston succeeded in obtaining velocity focusing of the ion beam. Ions of higher velocity would undergo a smaller amount of deflection in the electrostatic field and would thus pass through a smaller part of the magnetic field. The detector (a photographic plate) was placed along the axis where trajectories of higher and lower velocities crossed. Using this method ions of the same mass but differing velocities created a sharp image at the detector. Species of a certain mass-to-charge ratio could thus be detected as an electron current at a focal point. A spectrum could be obtained by varying the accelerating potential V_0. The principle of operation of Aston's instrument is illustrated in figure 1.3.

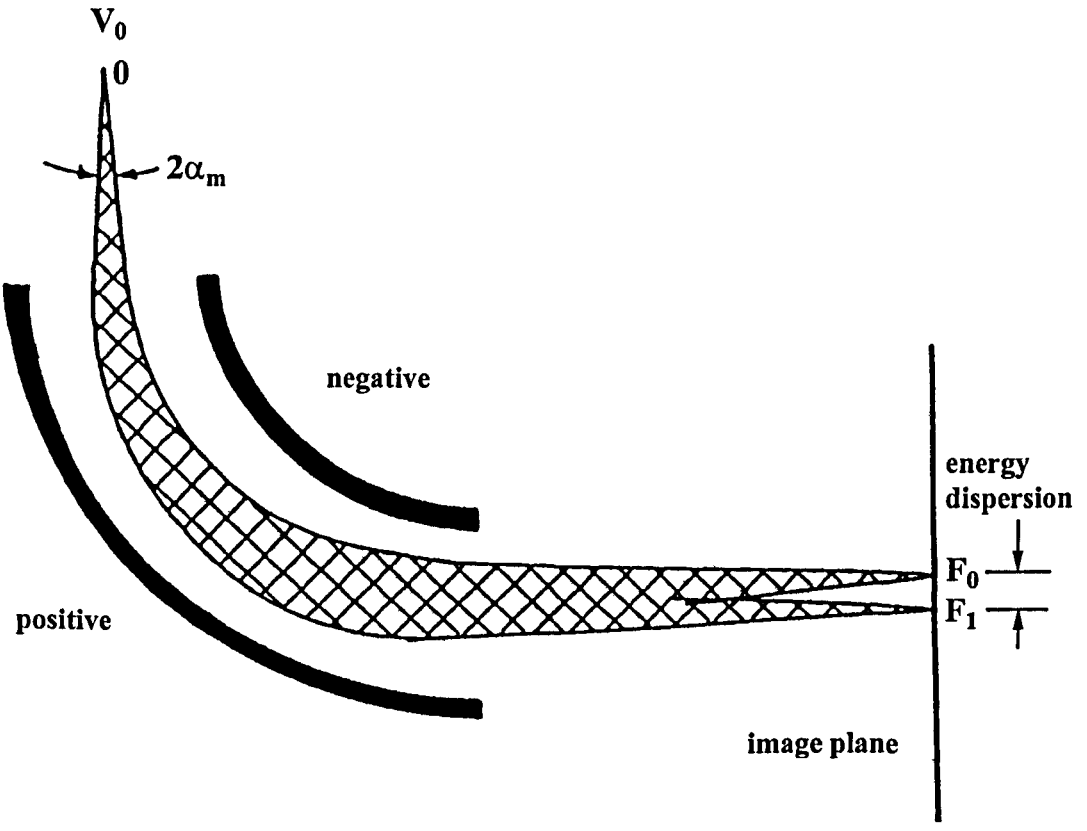

0 Point source for ions of mass M_0 and M_1, and energies E_0 and E_1, with angular divergence of $2\alpha_e$ (where $E_1 > E_0$).

F_0 Focus point for ions with energy E_0, mass M_0 and M_1, and with angular divergence of $2\alpha_e$.

F_0 Focus point for ions with energy E_1, mass M_0 and M_1, and with angular divergence of $2\alpha_e$.

Figure 1.2 – Principle of operation of an electric sector (kinetic energy) analyser.

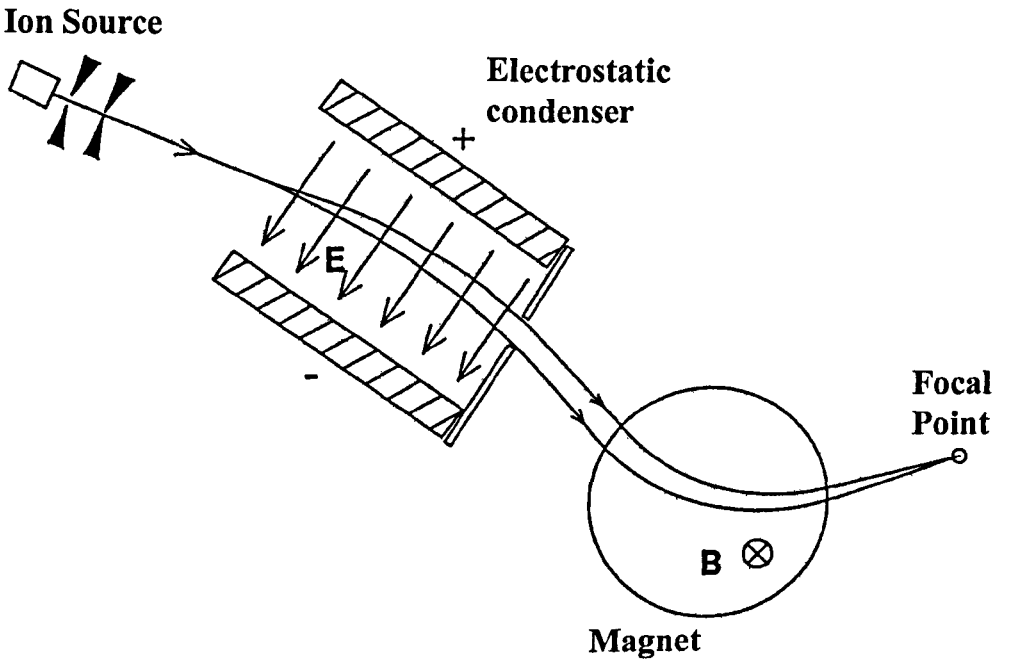

Figure 1.3 – The operating principle of a 'velocity focusing' mass spectrograph, similar to the one designed by Aston.

1.2.1.4 Double-Focusing Mass Spectrometers

Electrostatic sectors focus ions spatially and disperse ions according to their energies. Magnetic sectors also focus ions spatially and disperse them according to their momenta. It is possible to achieve an arrangement such that the velocity dispersion of the electrostatic sector is contradictory to that of the magnetic sector and that when combined the velocity dispersion of each sector cancels the other out. The two counts of focusing, the velocity focusing and spatial focusing, give rise to the term 'double-focusing' for a combination of electric and magnetic sectors. The double-focusing principle is illustrated in figure 1.4.

A general solution for the paths of charged particles in magnetic and electric sectors was solved by Herzog.[8] Based on those calculations Mattauch and Herzog matched complementary sectors in order to focus a diverging and non-monoenergetic ion beam.[9]

Johnson and Nier improved on previous designs by discovering an arrangement that in theory eliminated second-order spatial aberrations.[10] A Nier-Johnson geometry instrument, as the first stage (MS-1) of a tandem mass spectrometer, will be examined further in this work.

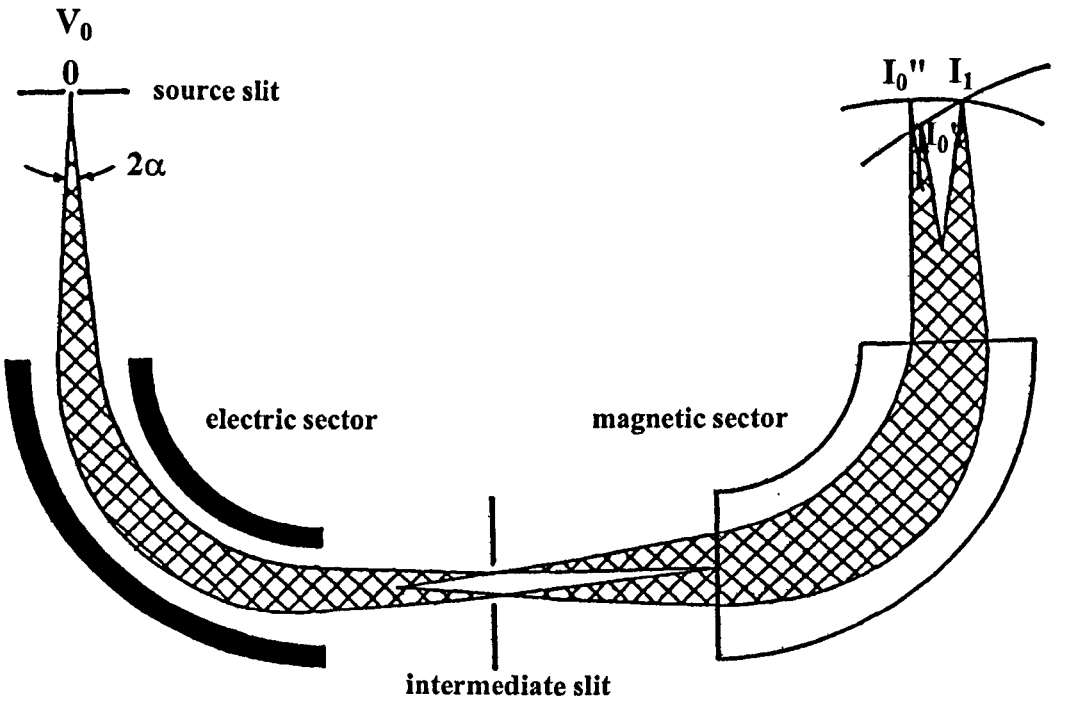

I_0' Velocity focus point for ion of mass M_0 and angular divergence $\alpha=0$.
I_0'' Direction focus point for monoenergetic ions of mass M_0 and angular divergence of 2 α.
I_1 Double-focusing point for ions of mass M_1.

Figure 1.4 – The double-focusing principle.

1.2.2 Time-of-Flight Mass Analysers

1.2.2.1 Linear Time-of-Flight Mass Spectrometers

Time-of-flight mass spectrometers are based on a simple mass separation principle. Consider ionised species starting from the same position at the same time, being accelerated by means of a constant homogeneous electrostatic field. Their velocities are unambiguously related to their mass-to-charge ratio and times of arrival at a detector directly indicate their masses:

$$t = \left(\frac{2md}{eE}\right)^{\frac{1}{2}} + L\left(\frac{m}{2eV_0}\right)^{\frac{1}{2}} \qquad \textit{Eq. 1.6}$$

m = *mass of particle*

e = *electronic charge*

E = *electrostatic field applied in source*

d = *length of accelerating region*

L = *length of field-free region*

V_0 = *accelerating potential*

The principle of time-of-flight has been known since Thomson carried out his experiments on ionised particles. The first proposal, however, for a mass spectrometer based on the time-of-flight principle was made by Stephens.[11]

The time-of-flight instrument possesses a number of extraordinary advantages over most other types of mass analyser:

- Theoretically unlimited mass range.
- Ideal where ionisation is pulsed or spatially confined.
- Complete mass spectrum for each ionisation event.
- High transmission
- No need for scanning the ion beam (the Fellgett advantage[12]).
- Spectra can be obtained for extremely small sample amounts ($<10^{-18}$ mole in the most modern instruments).
- Relatively low cost.

Table 1.1 - Advantages of Time-of-Flight Mass Spectrometry

Wiley and McLaren observed that ions of a particular mass-to-charge ratio would reach the detector with a spread in arrival times, due to the effects of uncertainty in the time of ion formation, location in the extraction field and initial kinetic energy, resulting in reduced resolution. Wiley and McLaren devised an instrument, incorporating a pulsed two-grid ion source, to compensate for temporal, spatial and initial kinetic energy distributions.[13] The basic geometry of the Wiley-McLaren design is shown in figure 1.5.

Temporal Distribution.

Two ions of the same mass that are formed at different times with the same kinetic energy will traverse the field-free region maintaining a constant difference in time and space.

$$\frac{\Delta m}{m} = \frac{2\Delta t}{t} \qquad \textit{Eq. 1.7}$$

As the time interval (Δt) is constant , the mass resolution ($\Delta m/m$) in a linear time-of-flight instrument can be improved by increasing the flight time (t) by using either a low accelerating potential or a long field-free region.

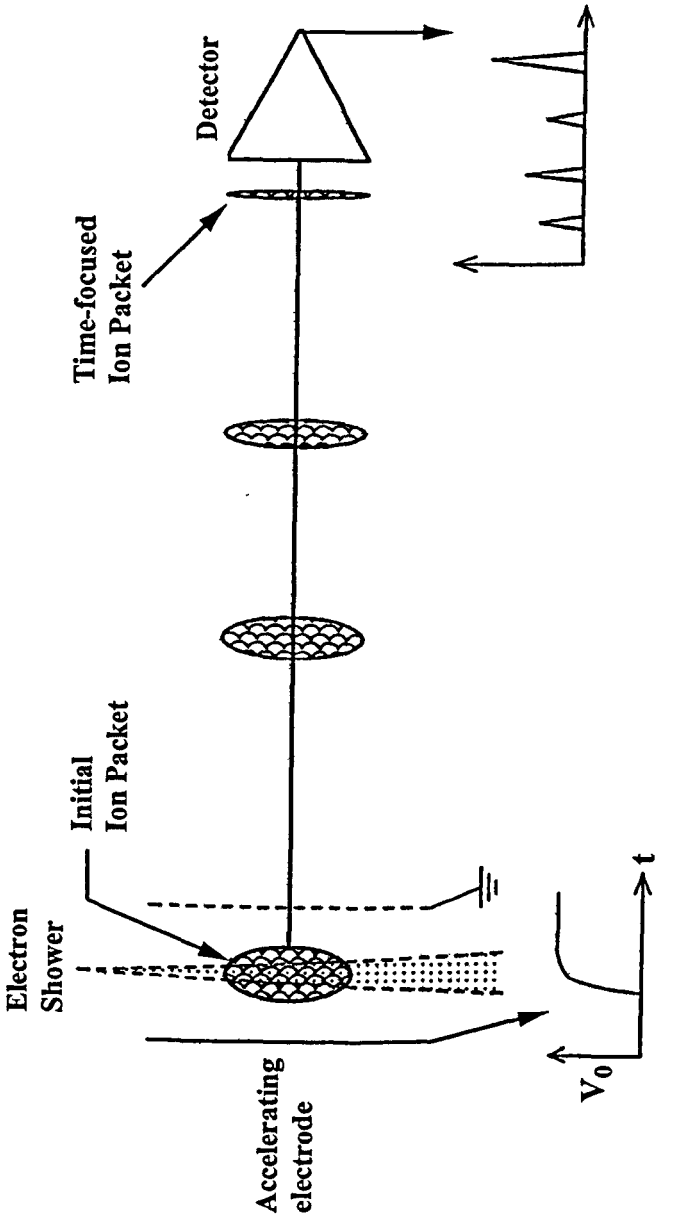

Figure 1.5 – Schematic diagram of the Wiley-MacLaren time-of-flight mass spectrometer.

In the Wiley and McLaren instrument the electron beam pulses used for ionisation were of the order of 0.5 to 5.0 microseconds, necessitating a reduction in the effective value of Δt. This was achieved by using pulsed extraction. Whilst the ions are being formed, they do not experience a potential gradient as the backing plate is held at the same voltage as the first grid. After a certain time, which is longer than the time for ion formation to occur, a positive pulse is applied to the backing plate such that a potential gradient is formed, accelerating the ions toward the detector. This reduces the effective value of Δt as all the ions experience the potential gradient at approximately the same time.

Spatial Distribution

When ions of the same mass are formed at the same time with the same initial kinetic energy, but are formed at different locations in the extraction field, the ions near the back of the source will experience a larger potential gradient and be accelerated to higher kinetic energy, than those formed close to the extraction grid. The ions formed at the back of the source will enter the field-free region later, but will eventually pass the ions formed closer to the extraction grid due to having larger velocities.

By adjusting the extraction field it is possible to achieve a space focus plane, where ions of any given mass arrive at the space focus plane at the same time. The location of the space focus plane is independent of mass, but ions of different masses will arrive at the space focus plane at different times.

Kinetic Energy Distribution

Ions formed with different initial kinetic energies will have different final velocities after acceleration and arrive at the detector at different times. The initial kinetic energy distribution also includes ions with the same kinetic energy, but velocities in

different directions. Ions of the same kinetic energy but with velocities in different directions will arrive at the detector at different times corresponding to their turn around time in the source. This effect can be minimised by utilising longer field-free regions:

$$t = t_s + t_D + t_0 \qquad \textit{Eq. 1.8}$$

(t_s = time in the source and t_D = time in the drift region)

$$t = \frac{(2m)^{\frac{1}{2}}}{eE}\left[(U_0 + eEs_0)^{\frac{1}{2}} \mu U_0^{\frac{1}{2}}\right] + \frac{(2m)^{\frac{1}{2}} D}{2(U_0 + eEs_0)^{\frac{1}{2}}} + t_0 \qquad \textit{Eq. 1.9}$$

The quantity (U_0+eEs_0) is the final kinetic energy of an ion having initial kinetic energy (U_0) and accelerated from position s_0.

Thus the longer the drift length (D), the greater the magnitude of t_D. This reduces the effect of turn-around time on resolution, as well as uncertainties in the time of ion formation (t_D).

The first commercial time-of-flight instrument was produced in the late 1950's by the Bendix Corporation. This was a linear instrument, with mass resolution of around 200-300 for organic species, and with a very high recording speed (20 kHz), giving the potential to monitor very fast reactions.

1.2.2.2 The Ion Reflectron in Time-of-Flight Mass Spectrometry

In 1966 Mamyrin and co-workers[15] proposed a way to correct for the temporal spread due to the initial velocity of the ions. This technique utilises a device called a '*reflectron*' consisting of a decelerating and reflecting field. For ions of the same m/z

entering such a field, those with higher kinetic energy (and velocity) will penetrate the decelerating field further than ions with lower kinetic energy. Therefore the faster ions will spend more time within the reflecting field, and 'catch up' with lower energy ions further down the flight path. By adjusting the reflectron voltages it is possible to achieve a time-focusing plane. In this ideal case, the resolution of the peaks in the mass spectrum will only be dependent on the time-width of ion formation.

In practical cases, there are a number of time-widening parameters that can degrade resolution. These include, spatial and initial-energy distributions, and metastable ion formation.

1.2.2.2.1 Single-Stage Reflectrons.

The single-stage reflectron is the simplest type of ion reflectron. A homogeneous reflecting electrostatic field is created between two parallel flat grids. The first grid constitutes the entrance of the ion mirror, and the second the end. A detector is usually placed behind the reflectron for linear time-of-flight experiments when the reflectron is grounded. In order to improve the homogeneity of the field in the reflectron a number of equally spaced ring electrodes are usually placed between the end electrodes, connected by a chain of equal value resistors.

Mass measurement in a single-stage ion reflectron is obtained by applying the following equation:

$$m = q(at + b)^2 \qquad \textit{Eq. 1.10}$$

where t is the time-of-flight, m and q are the mass and charge of an ion respectively, and a and b are calibration constants that depend on instrument dimensions. In

practice a and b are determined experimentally, calculated from the flight times and masses of known peaks in a particular mass spectrum.

The mass resolution that can be obtained using this type of mass spectrometer is limited by the temporal width of the initial ion pulse from the ion source, and the initial kinetic energy distribution of the ions, as it only corrects to the first order of approximation for the initial velocity spread:

$$t = \frac{L}{v_0}\left[2 + \left(\frac{\delta}{v_0}\right)^2 - \left(\frac{\delta}{v_0}\right)^3 + \ldots\right] \qquad \textit{Eq. 1.11}$$

where t is the time-of-flight, v_0 is the initial velocity of the ions and δ is a deviation in the initial velocity.

1.2.2.2.2 Double-Stage Reflectrons

In a double-stage reflectron, two separate homogeneous field regions, of different potential gradient, are utilised. A schematic diagram demonstrating the use of double-stage ion reflectron is shown in figure 1.6. Mamyrin has shown that, by choosing mirror voltages and dimensions to match the lengths of the field-free region, that it is possible to solve Eq. 1.11 to the second order of approximation.[14, 15, 16] The result is a large enhancement in resolution, in particular for ion beams with broad kinetic energy distributions.

1.2.2.2.3 Quadratic Field Reflectrons

By introducing a second finite region of different potential gradient it is possible to make the second-order term in Eq. 1.11 vanish. Extending this reasoning, if a field with an infinite number of changes in field gradient were introduced, all terms of

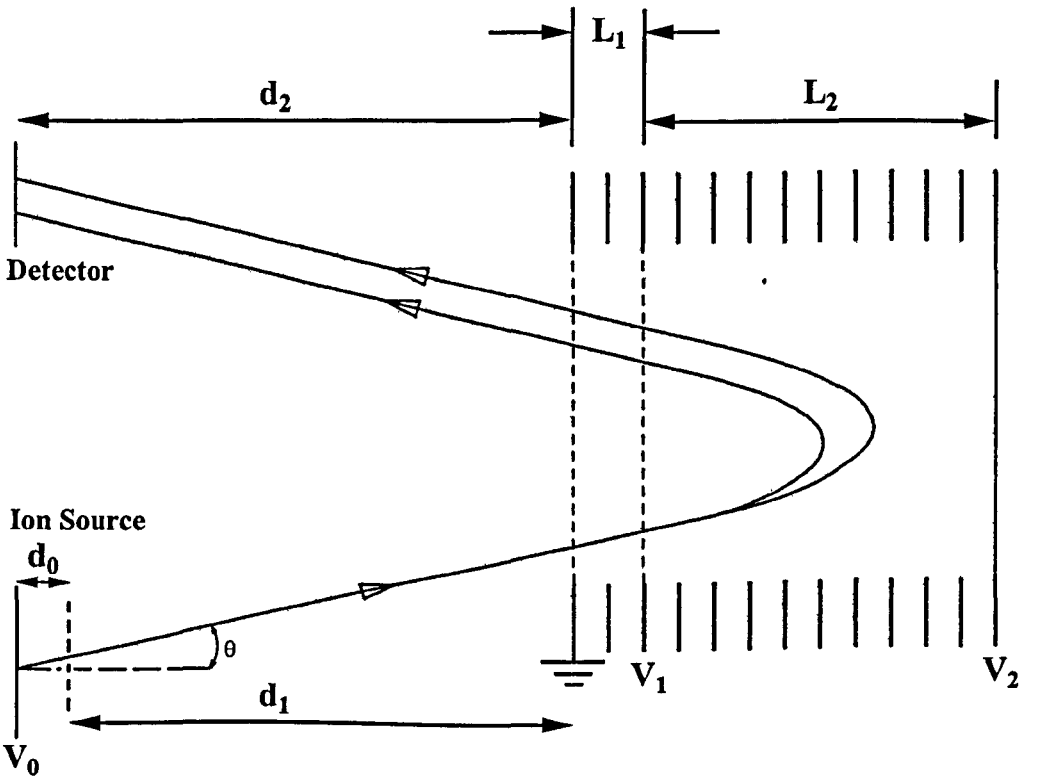

V_0 The accelerating potential
V_1 Applied potential to create first homogeneous field region.
V_2 Applied potential to create second homogeneous field region ($V_2 \neq V_1$).
d_0 Length of accelerating potential gradient.
d_1 Length of first field-free region.
d_2 Length of second field-free region
L_1 Length of first potential gradient of ion mirror.
L_2 Length of second potential gradient of ion mirror.

Figure 1.6 – Schematic diagram of a time-of-flight mass spectrometer with a double-stage reflectron.

time-aberration could be made to vanish. This would mean that the time-of-flight in an ion reflectron would be independent of the initial velocity of the ion, and depend only upon the specific charge *qe/m* (ideal time-focusing).[17] An ion mirror with this characteristic can be thought of in the same way as a pendulum, where the frequency of the body is dependent only on its mass and the length of the pendulum.

There are a variety of fields that can be utilised to provide ideal time-focusing. It has been shown that when demands of high transmission and simplicity of construction are taken into account, that only a few fields can be practicably useful:[18]

1) axially-symmetrical hyperbolic potential

$$U(r,z)=\frac{k}{2}(z-a)^2-\frac{k}{4}r^2+C \qquad \textit{Eq. 1.12}$$

r, z are cylindrical co-ordinates. k, a and C are constants.

2) axially symmetrical hyper-logarithmic potential

$$U(r,z)=\frac{k}{2}(z-a)^2-\frac{k}{4}r^2+b\ln\left(\frac{r}{d}\right)+C \qquad \textit{Eq. 1.13}$$

$d>0$ and $b>0$ are constants.

3) planar hyperbolic potential[19]

$$U(x,y,z)=\frac{k}{2}(x-a)^2-\frac{k}{2}(y-b)^2+dz+C \qquad \textit{Eq. 1.14}$$

a, b and d are constants.

A tandem mass spectrometer, utilising a quadratic field reflectron with a planar hyperbolic field as the second mass spectrometer (MS-2), will be examined in greater detail in this work.

1.3 Ionisation Techniques

Progress in mass spectrometry has been as dependent on discovery of new ionisation techniques, as it has on development of novel instrumentation. Discovery of new ionisation techniques has allowed compounds, previously inaccessible to analysis by mass spectrometry, to be studied.

Acceptance of mass spectrometry as an analytical technique was generally given when electron impact ionisation (EI) was shown to ionise gaseous atoms and small molecules. The next important steps were chemical ionisation (CI),[20, 21] field ionisation (FI)[22] and, with the advent of lasers, photo-ionisation.[23, 24]

The main limitation of all the techniques listed above, was that they could only be used to ionise relatively volatile, and therefore small, compounds that could easily be transferred to the gas-phase. Perhaps the most important discovery in the history of mass spectrometry, after the development of electron impact ionisation, was the introduction of ionisation/desorption techniques that have allowed large non-volatile molecules to be transferred to the gas-phase

The most important of these ionisation/desorption techniques are thermospray ionisation (TI), secondary ion mass spectrometry (SIMS), field desorption (FD), fast atom bombardment (FAB), electrospray ionisation (ESI) and matrix-assisted laser desorption/ionisation (MALDI).

The desorption/ionisation techniques that have been utilised in this work are reviewed below.

1.3.1 Field Ionisation and Field Desorption

The foundations for field ionisation and field desorption were laid by Muller during the 1930's.[25] His experiments were concerned with the emission of electrons from a sharp metal tips. A large negative potential sufficient to form fields of between 10^8 - 10^{10} Vm^{-1} was applied to the metal tip. Eventually these experiments were repeated using a positive applied potential, and Müller detected charged species hitting the screen of his apparatus. In this experiment, Müller demonstrated that the electric field had ionised background molecules in the vacuum apparatus.[26] Müller's apparatus became known as a 'field ion microscope'. The use of a field ion microscope as the ionisation source for a mass spectrometer was reported by Inghram and Gomer.[27]

Electron impact remained the most common ionisation technique during the 1950's, although the inability of electron impact to ionise fragile molecules without complete fragmentation, stimulated interest in other ionisation techniques. Field ionisation was able to ionise unstable molecules since the interaction between the electric field and the gaseous molecule imparted little vibrational energy, resulting predominantly in molecular ions with little fragmentation.

A number of laboratories investigated field ionisation of adsorbed species during the 1960's, including Robertson's in London[28] and Beckey's in Bonn.[29] In 1969, conditions were reported for field ionisation with an emitter loaded with a solid sample, allowing formation of molecule ions from the sample.[30] This technique of direct loading of a solid sample onto an emitter became known as 'field desorption'. The field desorption technique extended the range of samples for analysis by mass spectrometry to many solid organic and inorganic compounds, previously inaccessible.

1.3.2 Electrospray Ionisation

The possibility of generating gas-phase ions by spraying a solution from the tip of an electrically charged capillary was reported by Dole and co-workers.[31] This early work was hampered by the use of an ion-drift spectrometer for ion analysis. Building upon the ideas of Dole, Fenn and co-workers developed electrospray as an ionisation technique for mass spectrometry.[32, 33]

The development of electrospray ionisation (ESI) has had a major impact on the mass spectrometric analyses of a broad range of analytes, and in particular for the analysis of macromolecules. Recent emphasis has been on the analysis of compounds of biological significance.

In electrospray ionisation, an analyte solution is passed, at atmospheric pressure, through a capillary into a small-diameter tip held at high potential (a few kV). The effect of the electric field as the solution emerges from the tip is to generate a spray of highly charged droplets that pass down a potential (and pressure) gradient towards the analyser. In order to establish a stable spray, it is important to have full control over parameters such as:

- the conductivity of the capillary and the needle tip
- the surface tension of the analyte solution
- the flow rate of the analyte solution
- the composition of the analyte solution
- the potential applied to the capillary tip

In most commercial instruments the facility to use a sheath flow of nebulizer gas is incorporated. Its use is determined by the flow rate employed, the composition of the solvent and the potential applied to the capillary tip. In addition, some electrospray

source designs allow a part of the capillary to be heated to facilitate droplet evaporation. Ultimately, fully desolvated ions result from evaporation of the solvent or field desorption of the droplets (see below). The desolvated ions are passed through one or two (usually conical) skimmer electrodes into increasingly higher-vacuum regions.

1.3.2.1 Theory of Electrospray Ionisation

The solution at the tip of the electrospray needle experiences the electric field associated with the maintenance of the tip at high potential. Assuming a positive potential, positive ions in the solution will accumulate at the surface, and are drawn out to form a 'Taylor cone'. If the surface tension at the tip of the Taylor cone is exceeded by the applied electrostatic force, a droplet is formed.

There is still no consensus on the mechanism by which solute ions are formed from charged droplets. Dole and co-workers proposed that ions originate from small droplets containing one molecule of the analyte, the 'charge residue model' (CRM).[34] Evaporation of the solvent from the initially formed droplet as it traverses a pressure gradient toward the analyser leads to a reduction in diameter, and an increase in surface field, until the Rayleigh limit is reached. A coulomb explosion occurs, as the magnitude of the charge is sufficient to overcome the surface tension holding the droplet together. The resulting instability disperses the droplet into a collection of smaller droplets, that continue to evaporate until they too reach the Rayleigh limit and disintegrate. A continuation of this process may be envisaged to result in the formation of an ion containing a single analyte molecule. The molecule retains some of its droplet's charge to become a free ion as the last of the solvent vaporises.

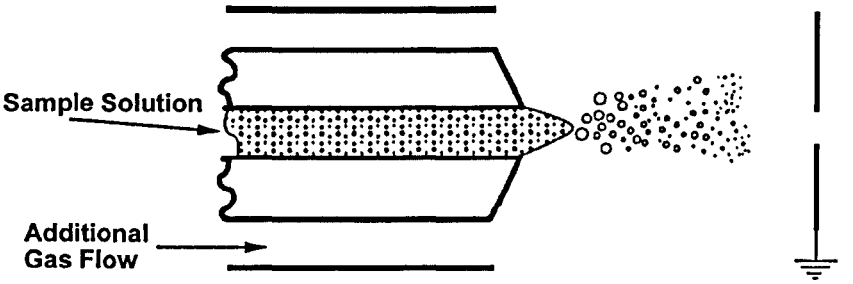

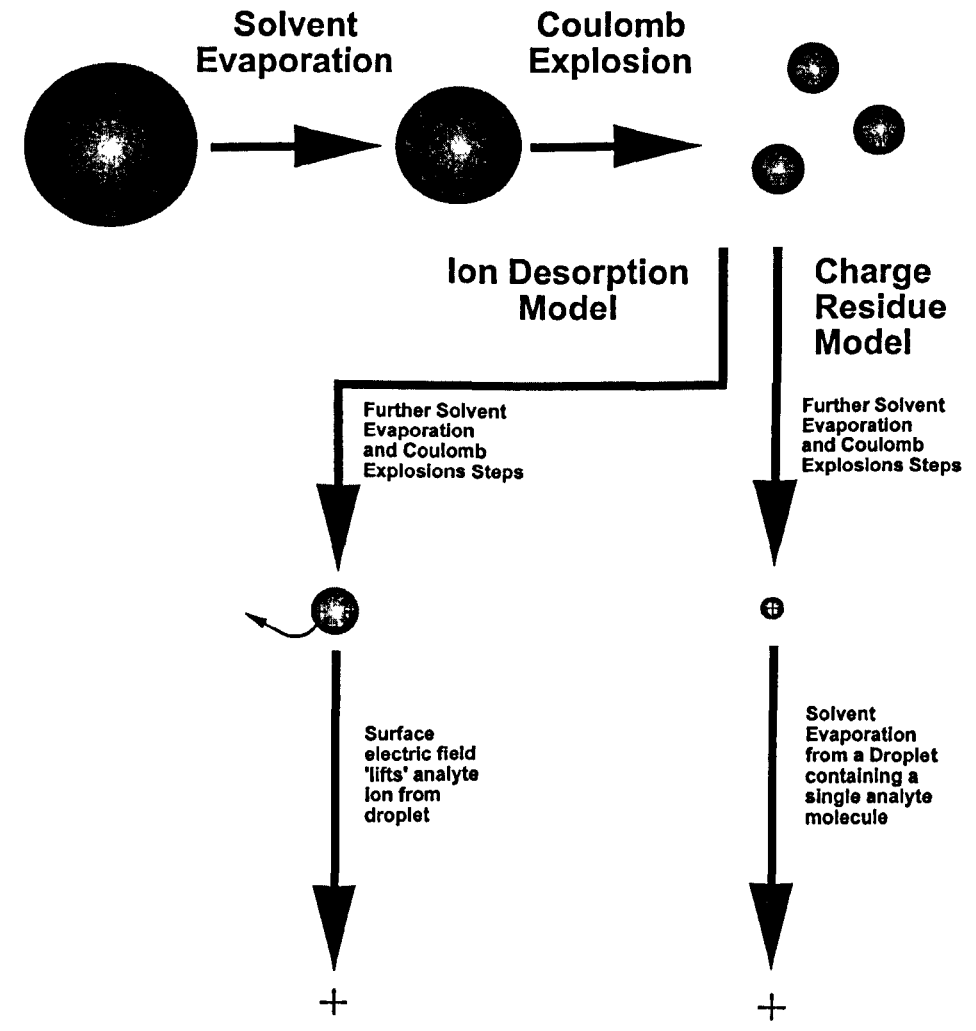

Figure 1.7 - Diagram illustrating the charge-residue, and ion-desorption models of electrospray ionisation.

A second mechanism of ion formation, the ion desorption model (IDM) is based on the work of Iribarne and Thomson.[35, 36] The ion desorption model assumes that before a droplet reaches the ultimate stage its surface electric field becomes sufficiently large to lift an analyte ion at the surface of the droplet over the energy barrier that prevents its escape. A diagram illustrating the CRM and IDM models of ion formation in electrospray is shown in Figure 1.7.

1.3.3 Matrix-assisted Laser Desorption/ionisation

Lasers were first utilised in ion sources during the late 1960's and early 1970's. It was quickly found that laser light, incident on a pure solid or liquid sample deposited on a sample slide, could be used to create small inorganic and organic gas-phase ions.[37] It was possible to avoid thermal decomposition of fragile analyte molecules by carefully controlling the power density of the laser beam.

The upper mass for laser desorption of biological molecules appears to be about 1000 Da, and for synthetic polymers can be up to a few thousand. Higher-mass ions, however, require higher laser fluences and are destroyed by the laser light. The use of a matrix, together with the analyte, was introduced by Tanaka and co-workers to facilitate desorption/ionisation of high-mass molecules without inducing fragmentation.[38] The breakthrough came from the novel sample preparation that was used. The analyte was dissolved in glycerol, and this glycerol solution was mixed with a fine cobalt powder. The glycerol is virtually transparent at 337 nm, the wavelength of the laser beam utilised, but the cobalt particles would have absorbed the light with high efficiency. The cobalt particles heated up severely, and heat was transferred to the surrounding glycerol/analyte solution. Energy was transferred to the analyte molecules desorbing them into the gas-phase,

where they were detected as ions. Experiments using lysozyme as the analyte yielded singly and doubly charged ions.

In 1985 Hillenkamp and co-workers promoted the hypothesis that mixing an analyte with an organic matrix, chosen to absorb at the wavelength of the laser, could ionise large molecules.[39, 40] It was expected that the ablated matrix would absorb sufficient light to result in its ablation, carrying some of the analyte material with it into the gas phase. In the dense cloud above the sample surface, chemical reactions would occur giving a charge to the analyte molecules, and allowing their detection by time-of-flight mass spectrometry.

The first experimental demonstration utilised nicotinic acid as the matrix material for the analysis of large polypeptides.[41] An aqueous solution of the analyte biomolecule was mixed with an aqueous solution of the nicotinic acid, deposited onto a stainless steel substrate, and dried. The ratio of matrix-to-analyte molecules was approximately 1000:1. A Nd:YAG laser was used to irradiate the crystallised mixture at 266 nm, the wavelength at which the nicotinic acid was strongly absorbing. Adjustment of the laser power and matrix-to-analyte ratio for each of the analytes studied gave high signal-to-noise mass spectra.

The advantage of the Hillenkamp method of preparation over the one introduced by Tanaka is the sensitivity, which is especially important for the analysis of precious biological materials. The Hillenkamp method routinely gives high quality results using femtomoles of analyte, while the Tanaka method required nanomoles. The Hillenkamp method, known as matrix-assisted laser desorption/ionisation has been demonstrated to be extraordinarily efficient for the desorption and ionisation of

many different types of large molecule, including proteins,[42, 43, 44, 45] carbohydrates [46, 47] and synthetic polymers.[48, 49, 50]

The mechanism of ion formation in MALDI is not well understood, and is currently a matter of active research. An understanding of ionisation pathways should help to maximise ion yields, control fragmentation and give access to new classes of analyte.

It is clear that only a few types of ion are commonly observed in MALDI. These are radical cations, protonated molecules and cationised molecules in the form of metal-ion adducts. Many and varied chemical and physical pathways have been suggested for MALDI ion formation, including gas-phase photoionisation, ion-molecule reactions, disproportionation, excited-state proton transfer, energy pooling, thermal ionisation and desorption of pre-formed ions. An excellent review of 'ion formation in MALDI mass spectrometry' has been given by Zenobi and Knochenmuss.[51]

1.3.3.1 Matrices in Matrix-assisted Laser Desorption/ Ionisation

The selection of a compound for use as a MALDI matrix can be particularly difficult. A suitable MALDI matrix must, firstly, be soluble in solution with the analyte. If this is not possible the matrix and analyte must be deposited separately onto the sample stage in layers.

A second necessary characteristic is to have a strong absorption coefficient at the wavelength of the laser. Research has concentrated on the near-UV region, limiting the choice of matrices to aromatic compounds with electron-withdrawing groups.

A further requirement for a matrix is to be chemically inert in terms of reactivity with the analyte.

Potential matrix compounds must also have low sublimation rates, as the sample must be introduced into vacuum for mass spectrometric analysis. High sublimation rates would result in significant changes in the matrix-to-analyte ratio during an experiment, affecting the results.

Even when these criteria are met, most potential matrices do not yield ions when experimentally tested. Nicotinic acid and 2,5-dihydroxybenzoic acid were introduced as matrix materials by Karas and Hillenkamp.[42, 52] Beavis and Chait introduced several derivatives of cinnamic acid, such as 3-methoxy-4-hydroxycinnamic acid and 3,5-dimethoxy-4-hydroxycinnamic acid,[53] and α-cyano-4-hydroxycinnamic acid.[54] The structures of some commonly used MALDI matrices are illustrated in figure 1.8.

1.4 Collision-induced Dissociation

Fragmentation of an ion, whether as the result of a collision or not, can occur at any point in a mass spectrometer. Ions which fragment directly after being formed are described as unstable ions. Stable ions will survive the full duration of their flight to the detector. Ions that decompose before reaching the detector, as a result of unimolecular dissociation due to high internal energy, are thought of as metastable ions. In practice it is difficult to distinguish spontaneous dissociation as a result of excitation in the ion formation process from dissociation as a result of collision with the background gas.

Introduction of a precursor gas atom or molecule can result in ion decomposition through collision between the ion and the gas atom. This process is called collision-

a-cyano-4-hydroxycinnamic acid

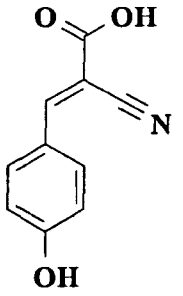

3-methoxy-4-hydroxycinnamic acid

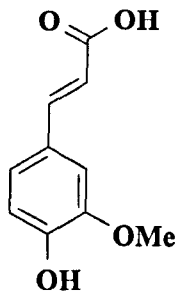

3,5-dimethoxy-4-hydroxycinnamic acid

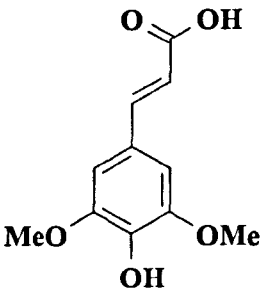

2,5-dihydroxybenzoic acid

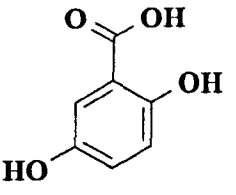

9-nitroanthracene

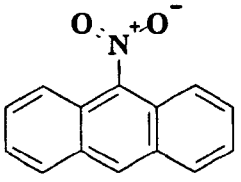

Nicotinic Acid

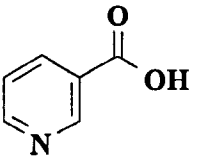

Figure 1.8 – Commonly used matrices for matrix-assisted laser desorption/ionisation.

induced dissociation (CID).[55] Ions that decompose as a direct result of collision do so in two distinct phases. The first, collisional activation (CA) gives rise to an excited intermediate:

$$m_1^+ + A \longrightarrow m_1^{+*} + A' \qquad \textit{Eq. 1.15}$$

The second stage of collision-induced dissociation is the unimolecular decomposition of the excited intermediate:

$$m_1^{+*} \longrightarrow m_2^+ + m_n \qquad \textit{Eq. 1.16}$$

An overall equation can be written for the CID process:

$$m_1^+ + A + q \longrightarrow m_2^+ + m_n + A' + T \qquad \textit{Eq. 1.17}$$

where:

m_1^+ is the parent ion m_1^{+*} is the excited parent ion

m_2^+ is the fragment ion A is the pre-collision state of the target gas

A' is the post-collision state of the target gas

q is the amount of translational energy of the colliding species converted into internal energy

T is the internal energy liberated as translation in unimolecular dissociation.

1.4.1 Centre-of-Mass Frame and Laboratory Frame Co-ordinates

It is essential when dealing with conversions of translational energy to internal energy for the fragmentation of ions to distinguish the different frames of reference. If the collision gas is assumed to be stationary, the laboratory frame collision energy for a singly-charged projectile ion, travelling with energy equivalent to the accelerating potential, V_0, entering a grounded collision cell, is given by:

$$E_{Lab} = V_0 e \qquad \textit{Eq. 1.18}$$

When a projectile ion collides with a stationary neutral gas atom, of mass m_{gas}, the maximum amount of translational energy transferable to internal energy is equal to the centre-of-mass frame collision energy;

$$E_{com} = V_0 e\left(\frac{m_{gas}}{m_{ion}+m_{gas}}\right) = E_{Lab}\left(\frac{m_{gas}}{m_{ion}+m_{gas}}\right) \qquad \textit{Eq. 1.19}$$

m_{ion} is the mass of the ion.

It can be seen that, for a fixed ion energy and a particular collision gas, E_{com} is proportional to the mass of the collision gas. The centre-of-mass collision energy can hence be increased in one of two ways: (i) increase the mass of the gas, and (ii) increase the laboratory frame collision energy (i.e. increase V_0).

1.4.2 Collisional Activation

It has been common to distinguish two types of collisional activation, on the basis of the laboratory frame collision energy of the parent ions: low-energy collisions, where the energy of the parent ion is below 100 eV, appropriate for low-energy instrumentation such as quadrupole analysers,[56] and high laboratory frame collision energy, where the energy of the parent ion is a few keV, utilised in sector and time-of-flight tandem mass spectrometers.[57]

The collision cross-section for a multiatomic ion is generally between 10 to 200 Å, depending upon the mass of the ion, and indicates the probability of reaction. The collision gas pressure is one of several parameters critical to the efficiency of the collision. Other characteristics of collisional activation to be considered are the amount of energy deposited into the ion (as discussed above), how this energy is

distributed and how it can be varied.

Beer's law can be applied to these collision experiments:

$$I=I_0e^{-n\sigma l} \qquad Eq.\ 1.20$$

where I_0 is the parent ion intensity before collision and I is the attenuated parent ion beam, n is the number density of the target gas, l is the length of the collision cell and σ is the cross-section of all processes that bring about the loss of intensity of the parent ion. Such processes include decomposition of the collisionally activated species, charge exchange with the target gas or charge stripping and scattering of ions.

1.4.3 Mechanisms of Energy Transfer

Classification of mechanisms of collisional energy transfer was discussed by Durup in 1970.[58] Four possibilities were suggested:

1) electronic excitation

2) direct vibrational excitation

3) vibration involving a long-lived intermediate

4) perturbation of a highly excited species, and subsequent dissociation

For small organic ions (<100 Da) with keV translational energies the interaction time is of the order of 10^{-15} s, and electronic excitation is believed to be the dominant pathway. For larger multiatomic ions the interaction times become of the order of the molecular vibrations (~10^{-14} s), and these ions are considered to be excited by direct momentum transfer of translational energy of the ion to its vibrational modes.[59]

Two mechanisms for direct momentum transfer have been proposed as a means of estimating the internal energy uptake by an ion from a collision. The quasi-diatomic approximation [60, 61] considers a multiatomic ion, treated as an entity, and a

monoatomic gas. The internal energy uptake (Q) of an ion from a single collision is related to translational energy loss by:

$$Q = \left(\frac{m_{ion} + m_{gas}}{m_{gas}}\right)\Delta E - \frac{2m_{ion}E}{m_{gas}}\left[1 - \left(\frac{E - \Delta E}{E}\right)^{\frac{1}{2}}\cos\Phi\right] \qquad \textit{Eq. 1.21}$$

m_{ion} is the mass of the ion, m_{gas} is the mass of the gas, E is the translational energy of the ion, ΔE is the translational energy loss of the ion, and Φ is the scattering angle of the ion.

The impulsive collision transfer theory (ICT), proposed by Uggerud and Derrick,[62] does not consider the ion as a single entity. The target gas is considered to collide impulsively with a single atom of the ion, and the two colliding atoms are treated as hard spheres. The internal energy uptake is give by:

$$Q = \left(\frac{\mu}{2\varepsilon}\right)\Delta E \qquad \textit{Eq. 1.22}$$

where:

$$\mu = \frac{m_{ion}\left(m_{atom} + m_{gas}\right)}{m_{ion}\left(m_{atom} + m_{gas}\right) - m_{atom}m_{gas}} \qquad \textit{Eq. 1.23}$$

$$\varepsilon = \frac{m_{ion}\left(m_{atom} + m_{gas}\right)}{2m_{gas}\left(m_{ion} - m_{atom}\right)} \qquad \textit{Eq. 1.24}$$

The impulsive collision transfer theory predicts that:

1) both the average translational energy loss and the average internal energy uptake of the ion increase with increasing translational energy of the ion, *i.e.* internal energy uptake is directly proportional to the translational energy loss, and is independent of the scattering angle
2) the greatest transfer efficiency of translational energy to internal energy is obtained when the mass of the gas equals the mass of the colliding atom of the ion
3) internal energy increases as the mass of the gas increases, as the centre-of-mass collision energy increases with the mass of the gas.
4) scattering increases with the mass of the gas, but decreases as the mass of the ion increases.

The impulsive collision theory gives good agreement with many, but not all, experimental results.[63, 64, 65]

1.5 Objectives of this study.

The main focus of this project was to utilise the tandem double-focusing/time-of-flight instrument (MAG-TOF) (described in Chapter 2) to investigate the effect of high-energy collisions on the fragmentation of synthetic polymer ions.

In order to achieve that goal, it was immediately evident from the outset that a significant amount of instrument development was necessary. Primarily, this would involve achieving increased sensitivity of the MAG-TOF instrument, whilst avoiding any reduction in resolution. It was envisaged that redesign of the MALDI ion source would be a significant step in resolving this issue.

A further instrumental problem that needed to be resolved was the calibration of the fragment-ion spectra, in order to provide meaningful results. It was decided that this could most easily be achieved by comparison against compounds with well-known fragmentation spectra. Fullerenes were ideal candidates, due to their distinctive fragmentation patterns.

Polyglycol polymers were chosen as 'model systems' for investigating the fragmentation of synthetic polymers under the conditions of high-energy collision-induced dissociation. It was hoped that collision-induced dissociation would allow the unambiguous assignment of features such as the polymer end-groups, and in the case of polyglycol copolymers reveal the polymer structure (sequence). Obtaining mechanistic information about the dissociation process was also an objective.

Chapter Two: Instrumentation

2.1 Introduction

Sensitivity is becoming an overriding concern for the application of mass spectrometry, and in particular tandem mass spectrometry. Even though mass spectrometry is often superior to other techniques in terms of sensitivity, samples can often be scarce or valuable, and much information must be drawn from the minute amounts of sample available.

Scanning mass spectrometers have an inherent disadvantage in obtaining high sensitivity. Mass spectra are acquired by filtering a continuous ion beam, throwing away all but one single m/z species during any given moment of the acquisition cycle. In a scanning double-focusing mass spectrometer, if a 10 second acquisition cycle is assumed for an m/z range of 1000, with a one-mass resolving power, each m/z species is being detected for approximately 10 ms. Thus 99.9 % of the ions produced are not detected. This situation becomes worse when wider mass ranges or higher resolutions are necessary.

In tandem mass spectrometry, where activation methods such as collision-induced dissociation (CID) are utilised, the situation is particularly demanding due to the relatively low efficiency of the activation method. It has been recognised that, if a time-of-flight analyser was used as the second stage (MS-2) of a tandem mass spectrometer, there would be an immediate gain in sensitivity, as there is no requirement to scan a time-of-flight analyser. A number of instruments have been constructed employing a time-of-flight analyser as the second stage of a tandem mass

spectrometer, utilising a double-focusing mass spectrometer[66,67] or another time-of-flight analyser[68,69,70,71] for parent ion selection (MS-1).

A further practical concern arises with the use of continuous ion sources such as LSIMS or electron impact. Such ion sources produce approximately the same throughput of ions during tuning, acquisition and breaks between acquisitions. It can be estimated that utilising such an ion source, data acquisition time may be limited to approximately 10 % of the total running time of the mass spectrometer. A pulsed ion source, such as matrix-assisted laser desorption/ionisation (MALDI) ion source, would significantly increase the acquisition time.

2.2 A Tandem Double-focusing Time-of-flight Mass Spectrometer.

The tandem double-focusing time-of-flight instrument (MAG-TOF) comprised a Kratos Concept H double–focusing magnetic–sector, of Nier-Johnson type geometry, and associated ion-buncher as the first mass spectrometer (MS–1) and a planar hyperbolic (so called quadratic field) ion–mirror as the second mass spectrometer (MS–2). The ion mirror was in–line with the optical axis of the magnetic–sector instrument and the ion-buncher. The collision energies employed spanned the range 8 to 12 keV. The method of ionisation employed was MALDI. Full details of the design have been published.[72] A schematic diagram of the MAG-TOF instrument is shown in figure 2.1. Photographs demonstrating the layout of the MAG-TOF instrument are shown in figure 2.2

The MAG-TOF instrument was designed and built in order to be able to perform collision-induced dissociation on large ions at high laboratory-frame collision energy E_{LAB} and with high sensitivity for the tandem mass spectra. High sensitivity has been

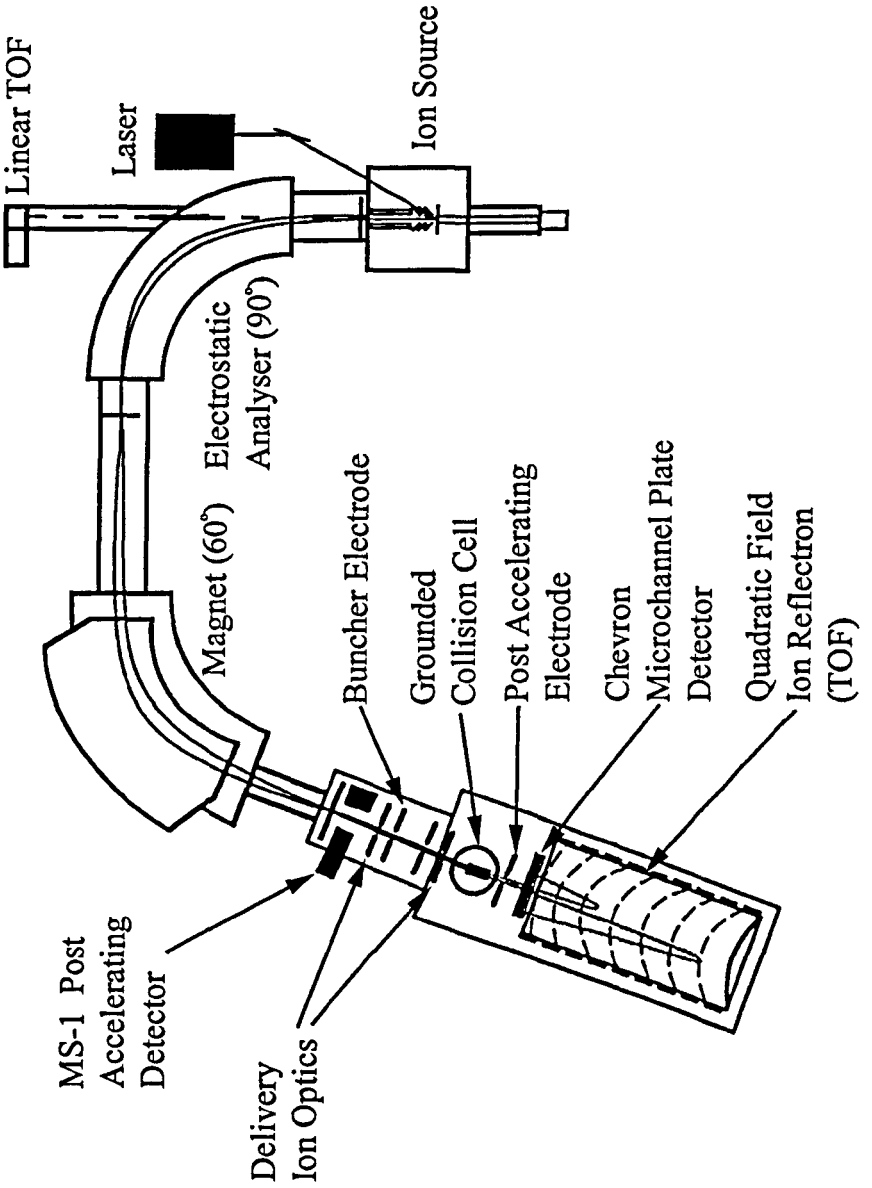

Figure 2.1 - A schematic diagram of the tandem double-focusing time-of-flight instrument (MAG-TOF).

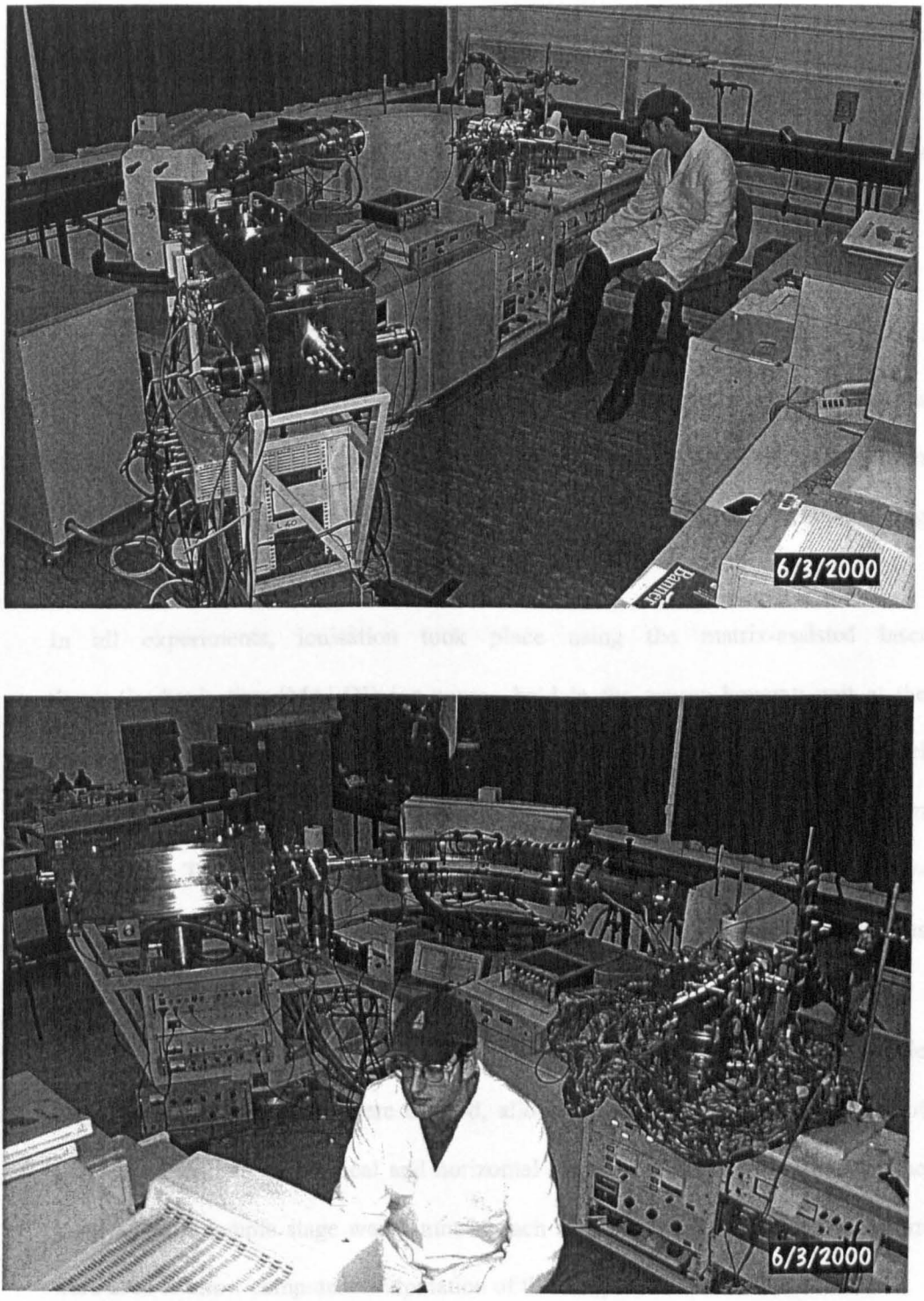

Figure 2.2 - Photographs illustrating the layout of the MAG-TOF instrument.

achieved through the use of time-of-flight (TOF) to measure the tandem mass spectra. The MAG-TOF instrument used in this study made possible full control over the laboratory-frame collision energy. The expectation was that the high laboratory-frame collision (10^3-10^4 eV) accessible in MAG-TOF would be advantageous as regards fragmentation of large ions.

2.2.1 The Ion Source

The source housing of the Kratos Concept H double-focusing mass spectrometer was designed to house a number of interchangeable ion sources. A matrix-assisted laser desorption/ionisation (MALDI) ion source was designed to fit around the existing source housing.[78]

In all experiments, ionisation took place using the matrix-assisted laser desorption/ionisation (MALDI) ion source held in the source housing unit at the front of the instrument. A nitrogen laser (Laser Science Inc., Newton USA. Model VSL337ND) was used for desorption/ionisation. The laser produced light of 337 nm wavelength. The time length of the light pulse was 3 ns and the maximum energy-per-pulse was 250 μJ. A variable density wheel attenuator (Ealing Scientific) was used to control the laser power reaching the sample surface.

The utilisation of solid matrices in MALDI made it necessary to raster the sample stage. Two push-activators were utilised, allowing movement of the inner part of probe shaft in both the vertical and horizontal directions. The overall travel of the stainless steel sample stage was 1 mm in each direction. A pair of stepper motors were used to allow computer manipulation of the sample surface.

The accelerating electrode was held at a potential of 8 kV. This meant that singly

charged ions exiting the source slit, that was earthed, would be travelling with a laboratory-frame collision energy of 8 keV.

2.2.2 The Electrostatic Analyser

The electrostatic analyser was comprised of two curved plates that had a sector angle of 90 degrees and a mean radius of 381 mm. A potential difference between the two plates focused the ions onto an image plane, according to ion energies, situated between the electric and magnetic sector.

The large-radius electrode of the electric sector contained a hole, positioned at a point coaxial with the ion optical axis of the ion source, to allow entrance to the parallel linear time-of-flight mass analyser (see section 2.1.4). The hole was small enough so that the electrostatic field created by the plates of the electric sector would not be disturbed during normal operation.

2.2.3 The Magnet

The magnetic field was generated by an electromagnet that had a sector angle of 60 degrees and a central radius of 686 mm. The strength of the electromagnet was controlled by magnetic field measurements from a Hall probe. The shape of the electromagnet caused the ion beam to converge at a focal point close to the exit slit of the magnet. Current shims on the magnet permitted the magnetic field to be finely tuned to improve peak shape and resolution if necessary.

2.2.4 Intermediate Detection Systems

2.2.4.1 The Parallel Time-of-Flight Detector

For the purpose of optimising the ion source parameters, such as laser power, a linear time-of-flight analyser (TOF-1) was utilised. As stated above, a hole contained in the vacuum chamber and the electric sector along the ion optical axis of the ion source allowed access to TOF-1 when the electric sector was grounded. Ion detection was made using an ETP electron multiplier.

The resolution achieved in TOF-1 was related to the energy spread of the MALDI ion beam produced in the source. By maximising the resolution achieved in TOF-1 it was possible to limit the size of the ion packet after the double-focusing mass spectrometer.

2.2.4.2 MS-1 Post-Accelerating Detector

For the purpose of optimising the transmission through the double-focusing mass analyser, a second intermediate detection system was located after the exit-slit of the double-focusing mass spectrometer. The signal from the preamplifier of the post-accelerating detector was monitored for each laser shot using a LeCroy 7200A oscilloscope.

The MS-1 post-accelerating detector was necessary to achieve high transmission through the double-focusing mass spectrometer, as the ion source conditions that gave optimum transmissions through the double-focusing mass spectrometer were different to those that gave optimum conditions for TOF-1. Various other tuning parameters of the double-focusing mass spectrometer were optimised using this mode of operation (hexapoles, deflectors, magnet shims and the width of the source

and detector slits). The magnetic field was fine-tuned in order to select the pure ^{12}C isotope.

2.2.5 The Ion Buncher and associated Ion Optics

The passage of ions through the electric and magnetic sectors of MS-1 results in spatial and temporal aberrations. The Nier-Johnson combination of sectors utilised in the MAG-TOF instrument can in principle eliminate spatial aberrations to the second order. The same is not true for temporal aberrations, with the result that ions of the same mass but different initial conditions may have different time-of-flights through the sectors. The initial conditions that contribute to temporal aberrations are the angle of the ion velocity from the optical axis, the distance of the ion from the central axis, the relative energy spread of the ions and the absolute time that the ion passes through the source slit.

In the MAG-TOF instrument, the contribution of the time deviation to the final spread is low due to the short time length of the laser pulse (~3 ns). The initial angle and distance from the central axis are confined by the acceptance parameters of the double-focusing mass spectrometer. The main contribution to the temporal spread of ions after MS-1 is the initial energy spread of the ions produced in the ion source.

The first ion optical component located after the exit-slit of the double-focusing mass spectrometer was the ion buncher. The ion buncher was used to time-compress the ion packet before entering the time-of-flight analyser (MS-2).

The ion buncher consisted of two electrodes, made of 1mm thick stainless steel plates with rectangular slits, separated by a distance of 30 mm, allowing complete containment of an ion packet with an energy spread of 25 eV. The first electrode was connected to a high-voltage feedthrough. A high-voltage pulse was applied by means

of a BEHLKE (Frankfurt, Germany) fast high-voltage switch. The timing of the high voltage-pulse was computer controlled. The computer received a zero-time signal from a photodiode placed in the path of a small reflection of the laser beam. Control software calculated the delay of the trigger pulse given the mass of the parent ion and the path length of the double-focusing mass spectrometer. The second electrode was kept grounded during all experiments. The time-focus of the ion buncher was the collision cell. Figure 2.3 shows an illustration of the time-focusing action of the ion buncher.

At the exit slit of the double-focusing mass spectrometer, the precursor ion packet was effectively an identical image of the ion packet at the source slit. The ion packet was approximately parallel in both the z-plane (vertical direction) and in the y-plane (horizontal direction) (see chapter 3). A number of ion optical elements were used to match the beam to the acceptance parameters of the quadratic-field reflectron. Due to the large energy spread introduced by the ion buncher, electrostatic lenses were necessarily weak and were used to provide steering rather than sharp focusing. Three planar split-electrodes situated at different distances from the exit slit of MS-1 were used for focusing and deflection of the ion beam in the y-plane. Figure 2.4 shows a schematic of the MS-2 region of the MAG-TOF instrument and illustrates the positions of these lens/deflectors. The first lens was situated 45 mm after the exit slit of MS-1, before the entrance to the ion buncher. The second y-lens was positioned after the ion buncher, 200 mm after the exit slit, and was mounted on the entrance aperture to the vacuum chamber containing the quadratic mirror. The third y-lens was mounted on the entrance to the differentially pumped collision cell.

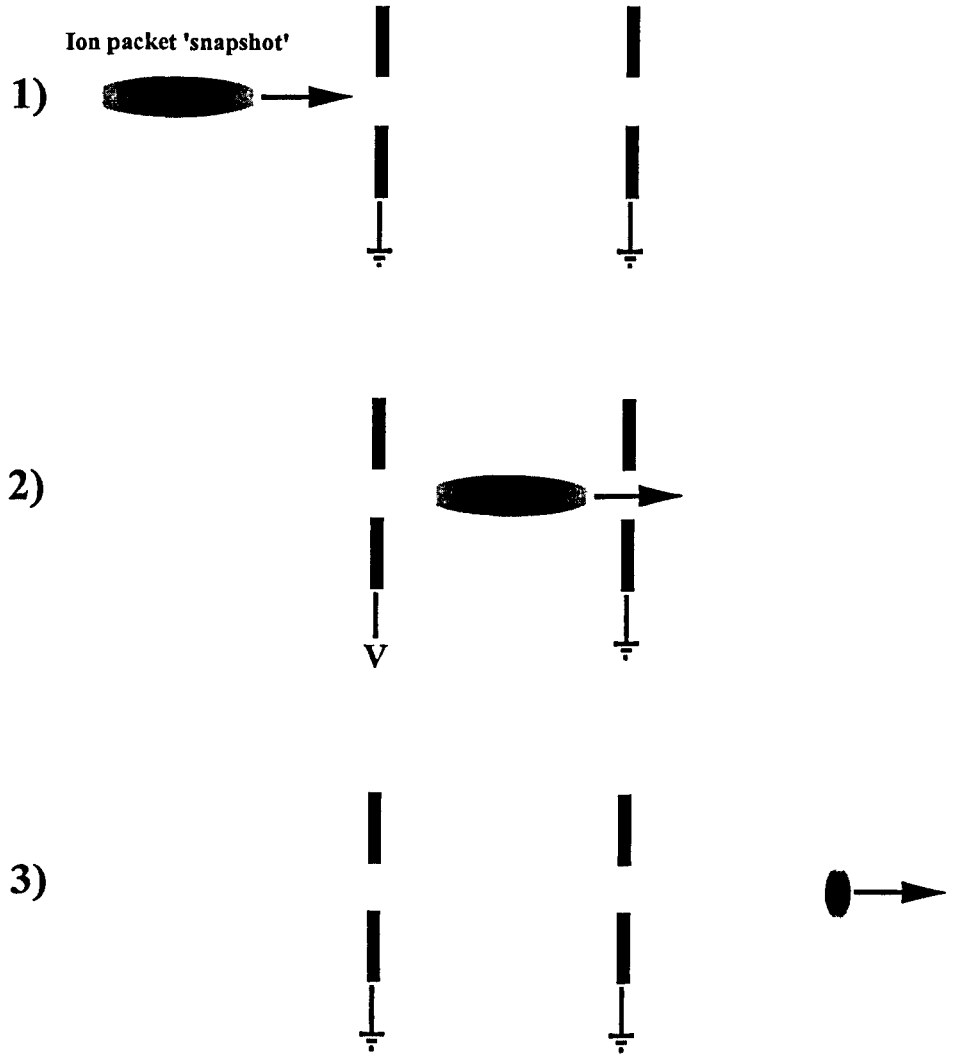

Figure 2.3 - An illustration of the time-focusing action of the ion buncher.

1) Shows a broad ion packet snapshot after the exit slit of MS-, representing a large temporal spread due to the initial energy spread from the ion source.
2) When the ion packet is contained within the electrodes of the ion buncher a high voltage pulse is applied to the first electrode. The ions closest to the first electrode experience a greater potential, and thus a greater acceleration than those further from the first electrode.
3) The ions with greater velocity 'catch up' with the slower ions, decreasing the temporal spread. The time-focus of the ion buncher was the collision cell.

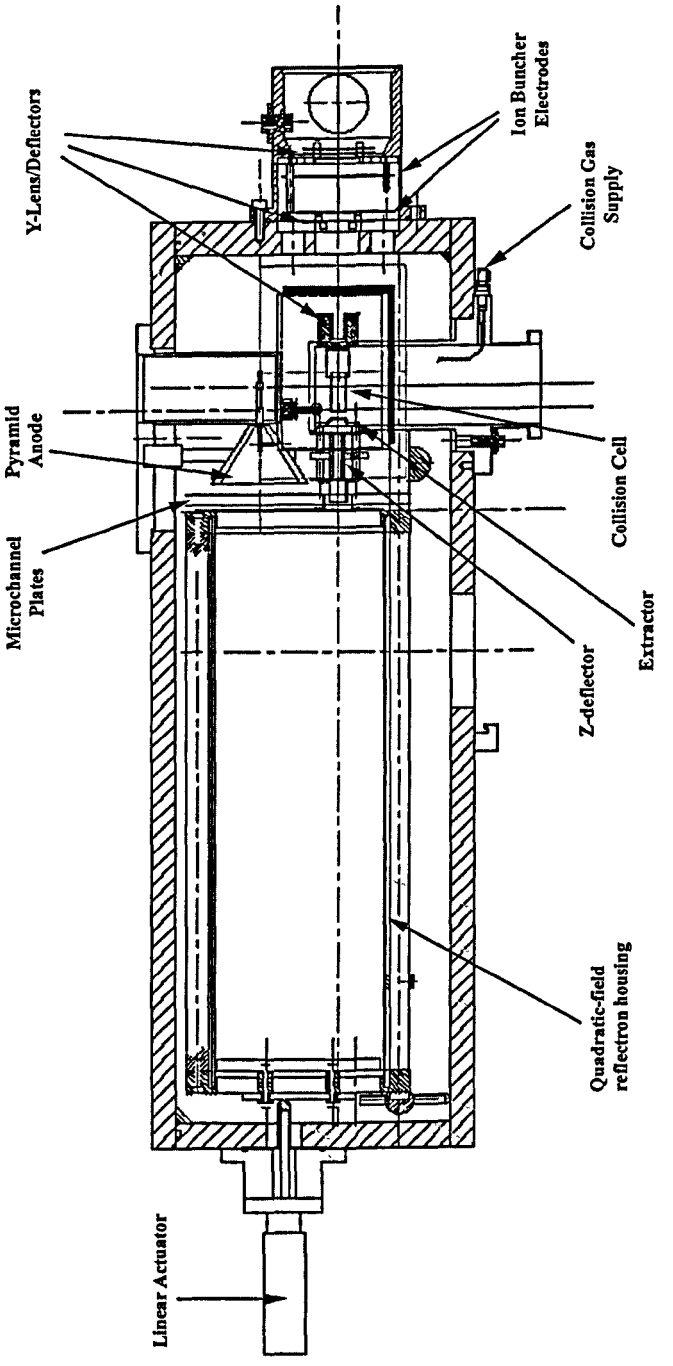

Figure 2.4 - Schematic diagram of the MS-2 region of the MAG-TOF instrument.

2.2.6 The Collision Cell and Post-accelerating Region

The location of the differentially pumped collision cell is displayed in figure 2.4. The collision cell was designed to sustain collision gas density at a level of 10^{16} molecules/m^3. The pressure inside the collision cell was of the order of magnitude of 10^{-4} torr, while the pressure of the differentially pumped region was in the region of 10^{-5} torr. The length of the collision cell was 10 mm and the slits of the collision cell were 7 mm high and 1 mm wide, allowing the use of any collision gas (including xenon) without loss of resolution in the quadratic-field reflectron. The collision cell was mounted from the top of the differentially pumped chamber and the flow of gas controlled by means of a Negretti leak valve. During collision-induced dissociation experiments, the collision gas pressure was adjusted to provide approximately 30-40 % attenuation (60-70 % transmission) of the parent ion beam.

As the ions exited the collision cell, they entered a post-accelerating region. An extraction electrode, located at a distance of 5 mm from the differentially pumped chamber, was floated at -2.15 kV. The extraction electrode was shaped to provide a low divergence of low m/z fragment ions. All of the ion optical elements following the post-accelerating region, including the front end of the quadratic-field mirror, were floated at the same potential as the extraction electrode.

A z-deflector was necessary to direct the ion beam towards the microchannel plate detector. The length of the deflector was 40 mm and the separation between the plates was 10 mm. The upper plate was floated at the same potential as the extraction potential (-2150 V). The lower plate was floated at a potential of -2050V, resulting in a 100 V bias. The combination of this deflection potential together with a mirror tilt of 1.2 degrees ensured maximum transmission through the quadratic-field mirror.

2.2.7 The Quadratic-field Ion Mirror and Detection System

The three-dimensional potential distribution describing the field of the quadratic-field reflectron was given by:

$$U(x,y,z)=\frac{k}{2}(x-a)^2-\frac{k}{2}y^2+C \qquad \textit{Eq. 2.1}$$

a and C are constants, and k is a coefficient reflecting the field-strength. The electrostatic field of the ion mirror was approximated by a multi-electrode system. The potential distribution was created in the region contained between four flat fibreglass plates, of dimension 520 x 150 mm, internally coated with a copper layer. The quadratic field was sustained by means of 38 electrodes, the shapes of which were determined by the quadratic equation. The shape of the electrodes at the top and bottom surfaces followed the quadratic equation $U(x,y)$. The electrodes in the side surfaces were parallel, corresponding to the field-free z-direction Insulating 2 mm wide gaps were etched onto the internal surface of the boards with 5 μm accuracy in order to separate the different potential regions. The widths of the electrodes varied from 25 mm to 5 mm, in order to reduce the variety of resistors required for the resistor chain. The density of electrodes was greater toward the back of the mirror. The four fibreglass boards were clamped between two aluminium end-plates and held together by three stainless steel rods. The rear end of the assembly was supported against the surface of the vacuum chamber by means of two long screws, that allowed adjustment of the tilt-angle of the ion-mirror.

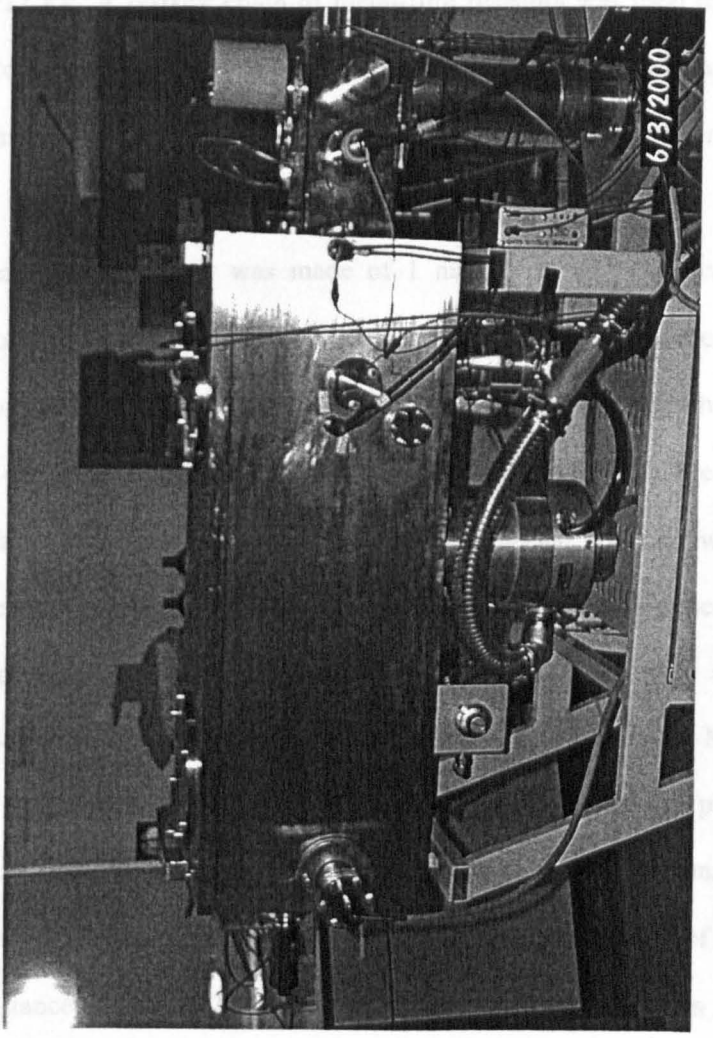

Figure 2.5 - Photograph of the vacuum chamber containing MS-2.

The high-voltages for the front and rear of the mirror were supplied by means of a purpose-made power supply (HD Technologies, Manchester, UK). The mirror front was maintained at a potential of -2.15 kV and the mirror end was maintained at a potential of +12 kV. A resistor chain of metal-film resistors was used to distribute the potential to each of the different electrodes of the mirror. Two external resistors were used to supply the two electrodes closest to the mirror front for optimisation of resolution.

The front flange of the mirror was made of 1 mm thick stainless steel directly mounted onto the aluminium frame. Above the slit entrance to the mirror a rectangular area of the front flange was cut away to allow ions to reach the detector. The hole was covered with high transmission mesh. The gap between the mesh and the front surface of the first microchannel plate was biased with a low potential gradient to prevent secondary electrodes being accelerated back toward the mirror.

The channel plate assembly of the detector was mounted on the front of the ion mirror. The assembly consisted of two 100 x 80 mm Galileo (Sturbridge, MA, USA) microchannel plates clamped between two rectangular stainless steel plates. The potential difference across the channel plates was typically 2 kV. Electrons from the rear of the channel plate assembly were accelerated toward the surface of the anode located at a distance of 10 mm. The large surface anode was pyramidal in shape and capacitively coupled to a feedthrough that carried the signal to a preamplifier.

A photograph of the vacuum chamber containing MS-2 is shown in figure 2.5.

2.2.8 The Vacuum System

The high vacuum required for the MAG-TOF mass spectrometer was achieved through use of a series of pumps. Three two-stage rotary pumps and five turbomolecular pumps were utilised. Thermocouple gauges were used to monitor the pressure given by the rotary pumps and ion gauges were used to monitor the pressure in the various housing units of the mass spectrometer. The flow of gas through these pumps and housing units was controlled by a selection of valves: diaphragm ball, isolation and solenoid operated valves. Typical pressures for MS-2 and the sector parts of the instrument were of the order of 10^{-7} torr. Typical pressure for the ion source was of the order of 10^{-6} torr.

Chapter Three - Development of the MALDI Ion Source of the MAG-TOF Instrument

3.1 Introduction

The design of an ion-source for any mass spectrometer imposes a number of considerations. The main purpose is to achieve the highest possible sensitivity, without compromising the resolution. Therefore, for time-of-flight instruments, the ions created in the ion source should be collimated towards the detector with minimum loss, while the time-aberrations in the source region should be kept low. Additionally, for the tandem double-focusing / time-of-flight mass spectrometer (MAG-TOF), time-aberrations from the source must be kept low so that the ion-packet can be contained within the ion-buncher (see chapter 2). Furthermore, the ion-packet must match the acceptance parameters of the double-focusing mass spectrometer.

The MAG-TOF instrument was equipped with a matrix-assisted laser desorption/ionisation (MALDI) ion source (see chapter 2.1.1). While sensitivity may be compromised by highly diverging ion beams and scattering on optical components, resolution is affected by three main factors:

1) the finite time of ion formation
2) the finite volume of ion formation
3) the initial velocity of the ions

For MALDI ion beams, the first parameter is caused by the duration of the laser pulse, which may vary from several picoseconds to several nanoseconds. Ions can

also be created in the gas-phase above the sample surface, even after the laser is switched off. This gives rise to both spatial and temporal aberrations.

It is known that MALDI ions possess mean velocity of ~ 500-1000 ms^{-1}, with a large velocity distribution.[73] The initial velocity distribution causes flight-time broadening, that can be separated into a spatial and temporal effect.[74] Spatial effects can be corrected by means of energy compensation (e.g. reflectron). Temporal focusing needs other means of correction, such as time-lag focusing, post-source pulse focusing (both unavailable in the MAG-TOF instrument) or high extraction fields. The use of high extraction fields can lower the Zavoiskii-Fanchenko aberration,[75] but will result in higher energy spread due to the finite volume of ion formation.

3.2 Ion Trajectory Simulations.

It was clear from experimental results that the performance of the MAG-TOF instrument was insufficient for the study of compounds such as fullerenes and synthetic polymers. Figure 3.1 shows the helium collision-induced dissociation spectrum of C_{60}^+ using the existing MALDI ion source (cf. chapter 4.3). Figure 3.2 shows the argon CID spectrum of the poly(ethylene glycol) $[M+Na]^+$ adduct ion m/z 1097.6 (n=24) using the existing ion source (cf. chapter 6.3). Both of these spectra were acquired over a 60 minute period.

Sensitivity (rather than resolution) was the overriding concern, particularly considering the value and scarcity of many samples. In particular it was necessary to achieve high sensitivity for ions in the m/z range 1000-3000, as the majority of samples to be analysed by this instrument were intended to be within this m/z range. For synthetic polymers there was an additional need for high sensitivity, as the ion

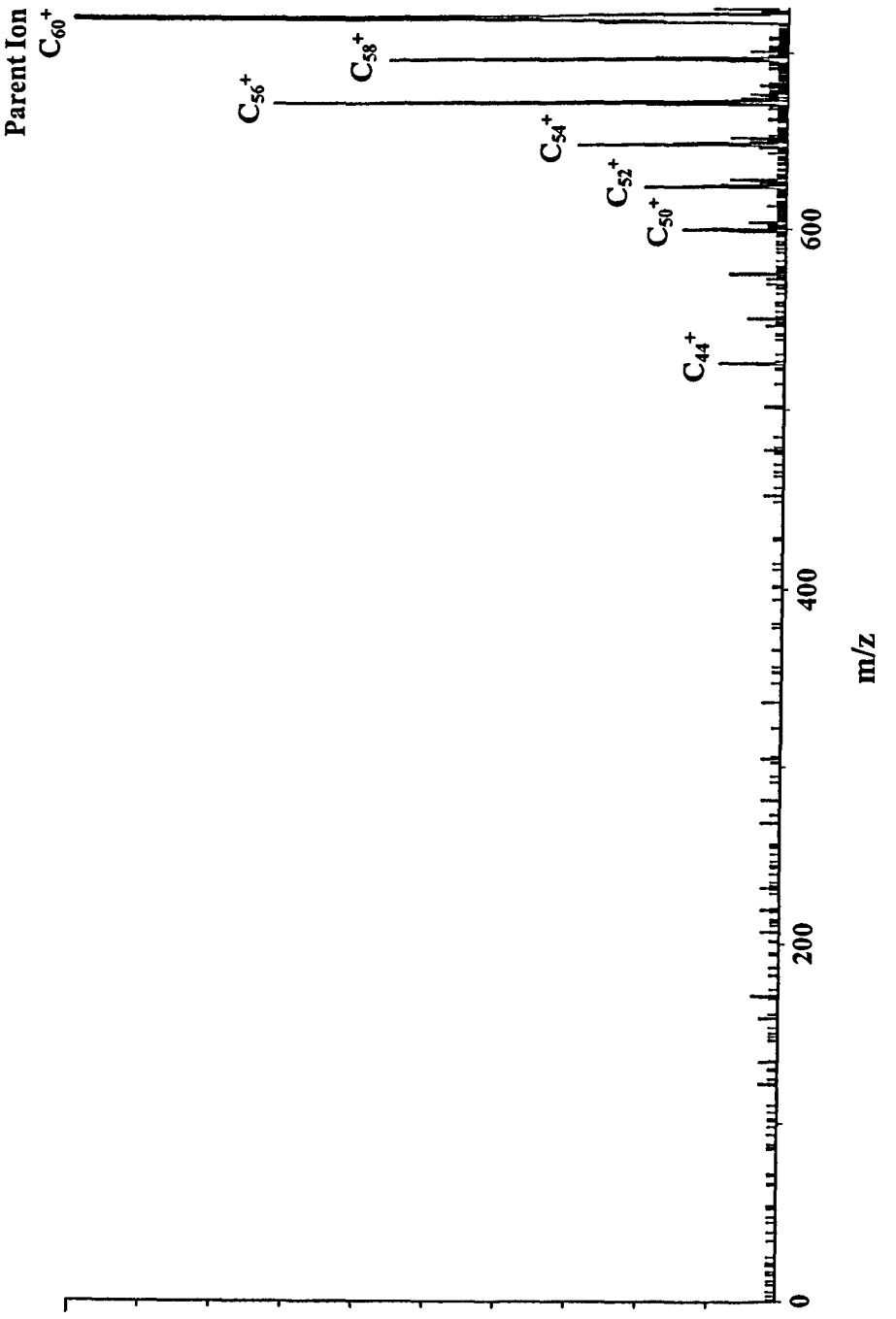

Figure 3.1 - High-energy collision-induced dissociation spectrum of C_{60}^+, generated by direct laser desorption, and using helium as the collision gas.

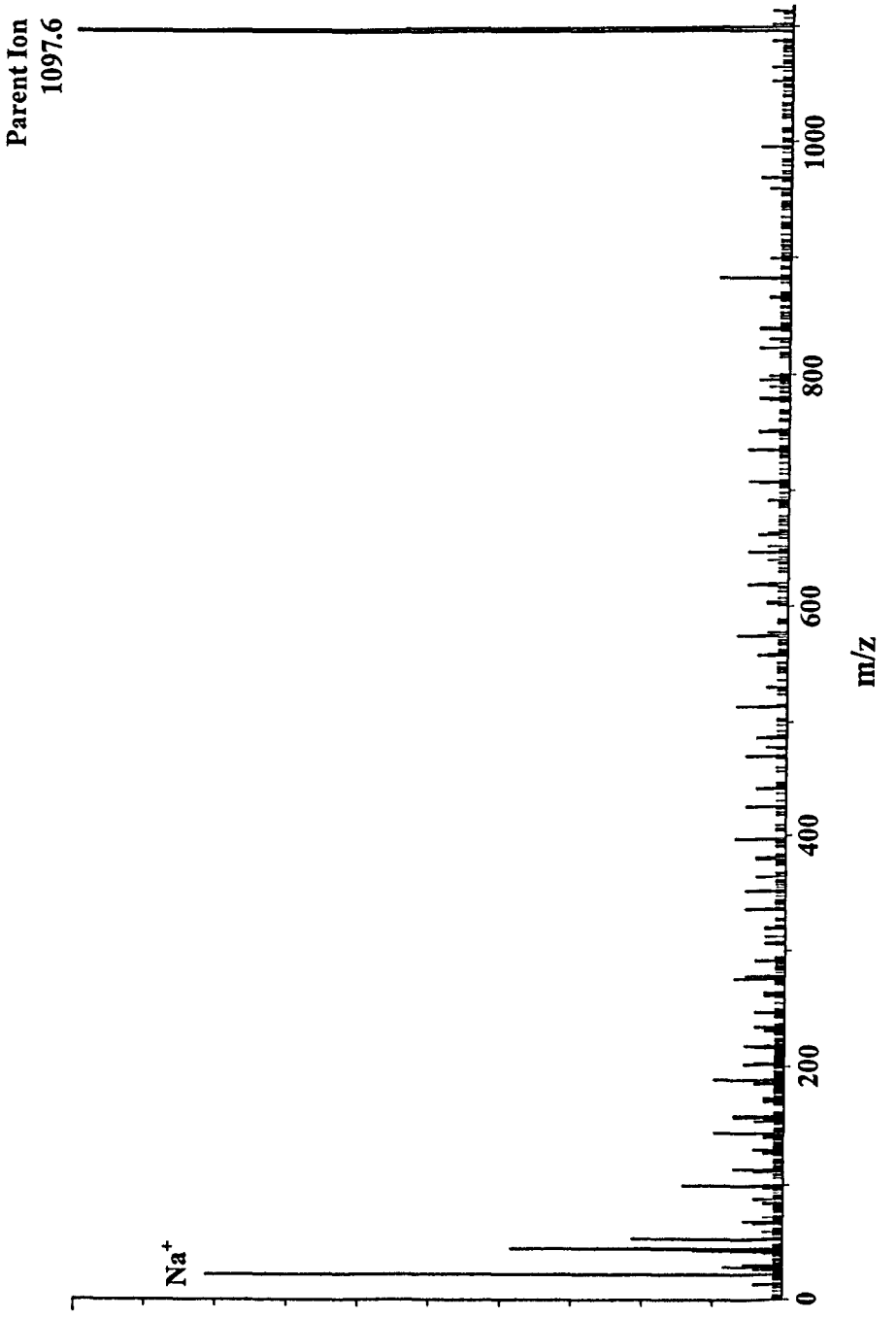

Figure 3.2 - High-energy collision-induced dissociation spectrum the poly(ethylene glycol) $[M+Na]^+$ adduct ion m/z 1097.6 (n=24), generated by MALDI, and using argon as the collision gas.

selected by the double-focusing mass spectrometer would be one of a large number of oligomers, and the majority of ions produced at the ions source would be 'wasted'.

Computer simulations of ion trajectories were performed as part of this study, in order to optimise the ion source of the MAG-TOF mass spectrometer. The SIMION software (Idaho National Engineering Laboratory, Idaho Falls, USA) was utilised to calculate the potential distribution created by combinations of different electrode geometries at different potentials. Typical initial conditions of MALDI ions were defined in order to calculate ion trajectories and flight-times in the source region.

The existing ion-source consisted of a homogeneous extraction region, in order to minimise sensitivity to minor misalignments, followed by a series of electrostatic lenses that provided deflection and focusing (see figure 3.3). The extraction electrode was constructed from a thin stainless steel plate (1 mm thickness) with a small slit size (2 mm by 1 mm). The extraction electrode was grounded and mounted onto the accelerating electrode by means of three purpose-made PEEK screws and 6mm long insulating spacers. The extraction electrode was followed by a short field-free region up to the ion source cradle, located at a distance of 25 mm from the accelerating electrode. The first deflecting electrode was located at a distance of 40 mm from the accelerating electrode, and the first focusing electrode was located at a distance of 53 mm from the accelerating electrode.

SIMION simulations were performed to establish the ion-trajectories through the ion-source, and in particular the effect of the extraction region. Figures 3.4-3.5 show these simulated ion trajectories, separated for the xy (horizontal) and xz (vertical) planes, and tables 3.1 and 3.2 list the specified initial (and the resulting final)

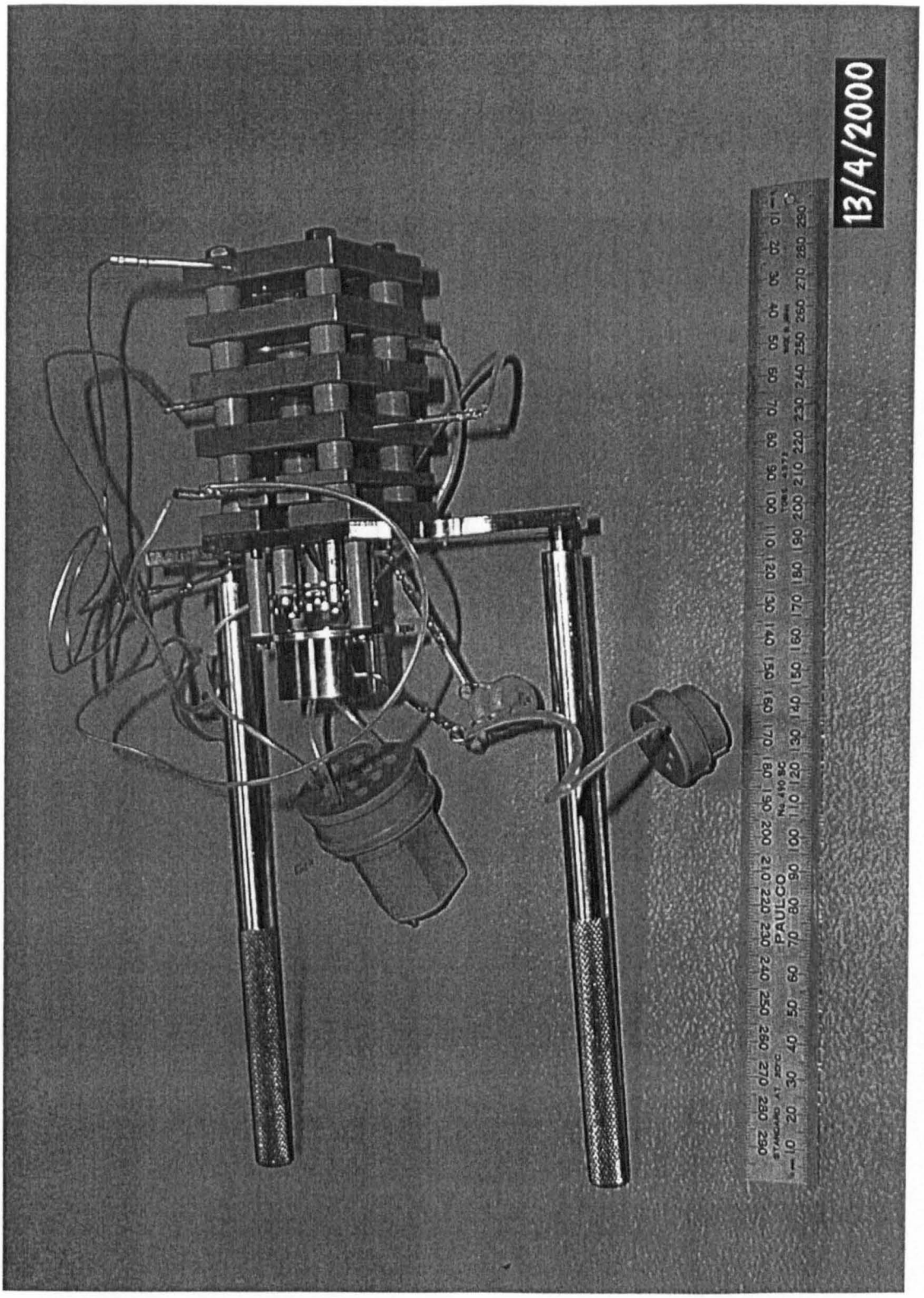

Figure 3.3 – Photograph of the planar-symmetry focusing and collimating ion optics of the MAG-TOF ion source.

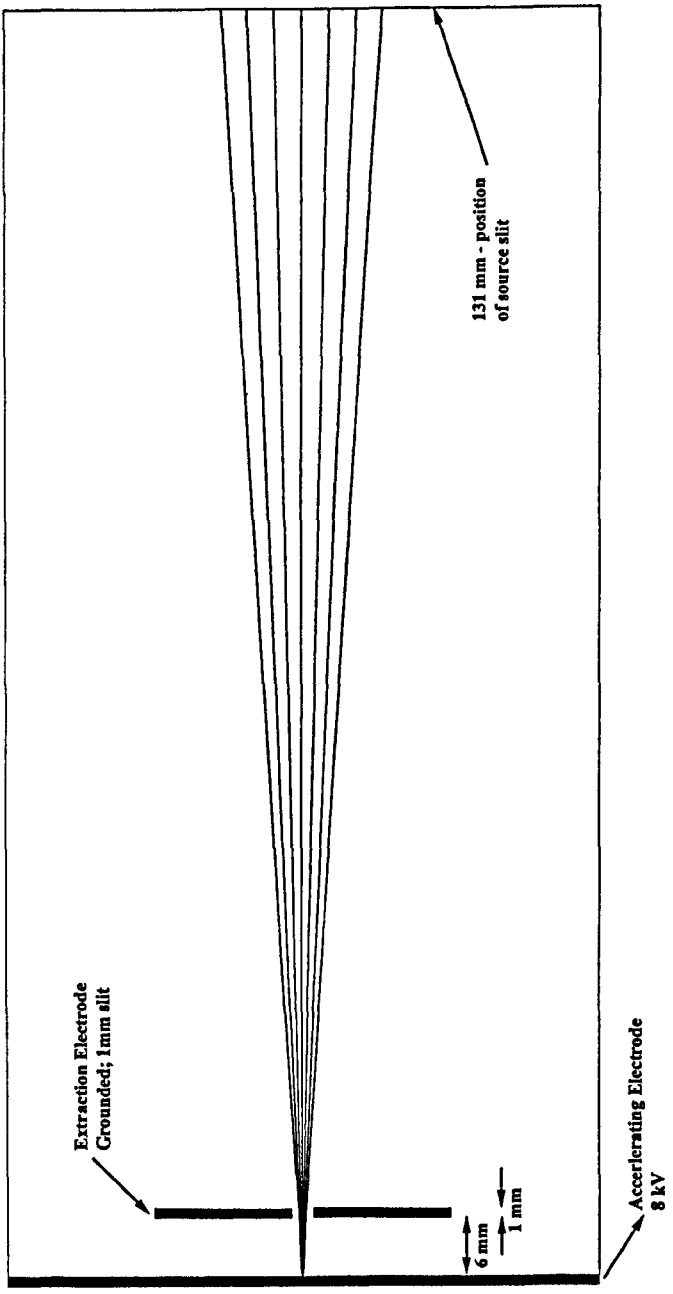

Figure 3.4 – Ion trajectory simulation of the extraction region of the MALDI ion source in the yx-plane. Ion m/z=1000, initial kinetic energy=30eV, initial position=0.0mm from axis.

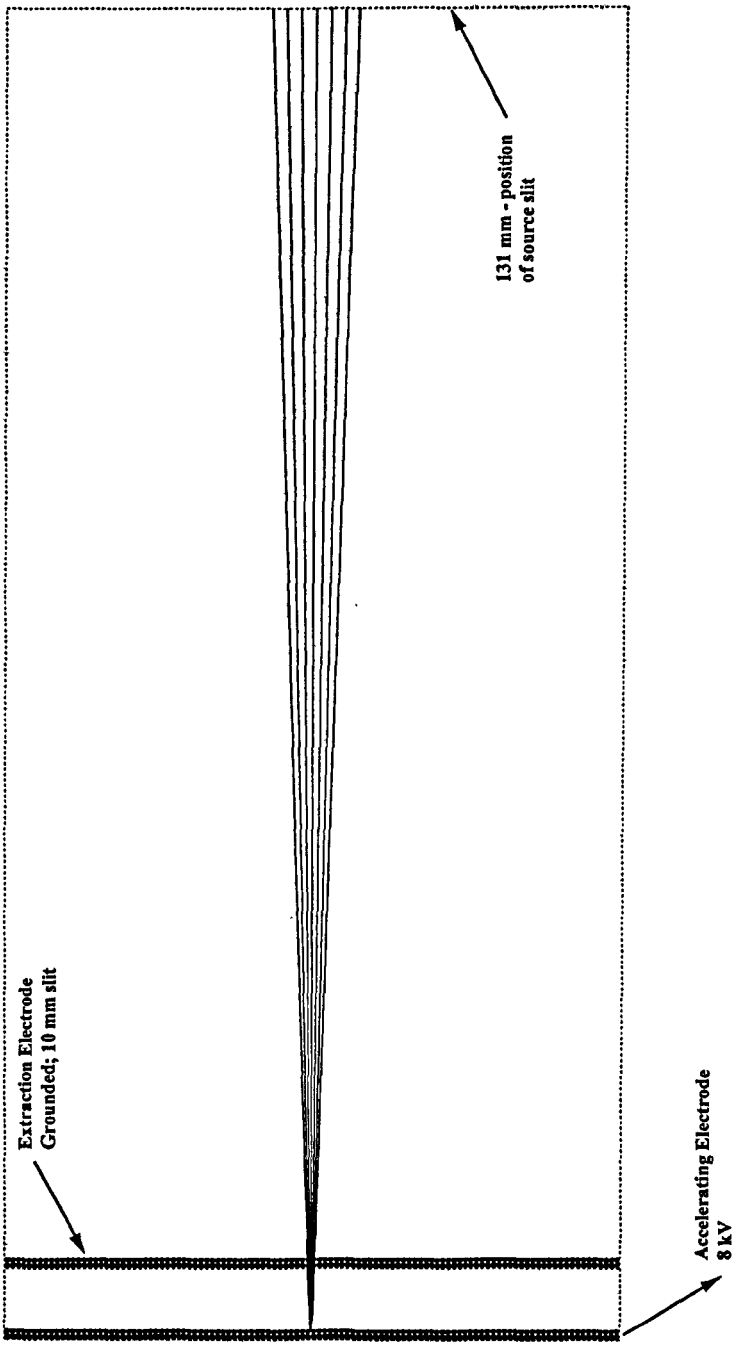

Figure 3.5 – Ion trajectory simulation of the extraction region of the MALDI ion source in the xz-plane. Ion m/z=1000, initial kinetic energy=30eV, initial position=0.0mm from axis.

Table 3.1 – Initial and final conditions utilised for SIMION ion trajectory calculations of the existing MALDI ion-source, in the xy (horizontal) plane.

Initial y /mm	Initial Angle / degrees	Final y /mm	Final x / mm	Final Angle / degrees	Time-of-flight / μsec
0	30	-8.12451	131	-3.58729	3.46119
0	20	-5.545	131	-2.45033	3.45712
0	10	-2.81215	131	-1.24335	3.45457
0	0	0.00E+00	131	0	3.45362
0	-10	2.81215	131	1.24335	3.45457
0	-20	5.545	131	2.45033	3.45712
0	-30	8.12451	131	3.58729	3.46119
0.1	30	-6.88177	131	-3.0614	3.45994
0.1	20	-4.29863	131	-1.92173	3.45631
0.1	10	-1.56317	131	-0.712921	3.45418
0.1	0	1.24878	131	0.530487	3.45374
0.1	-10	4.05746	131	1.77188	3.45509
0.1	-20	6.78617	131	2.97611	3.45808
0.1	-30	9.35935	131	4.10895	3.46258
0.2	30	-5.63402	131	-2.53266	3.45883
0.2	20	-3.04966	131	-1.3916	3.45564
0.2	10	-0.314499	131	-0.1825	3.45392
0.2	0	2.4949	131	1.05967	3.45398
0.2	-10	5.297	131	2.29744	3.45574
0.2	-20	8.01956	131	3.49781	3.45919
0.2	-30	10.582	131	4.62475	3.46412
		TOFmax - TOFmin =9.6 ns			

Initial y = the initial distance of an ion from the ion optical axis (mm)
Initial Angle = the initial angle of an ion from the ion optical axis (degrees)
Final y = the distance of an ion from the ion optical axis at the source slit (mm)
Final x = the distance an ion travels along the ion optical axis. The simulation ends at

a distance of 131 mm, the location of the source slit.

Final Angle = the final angle of an ion from the ion optical axis (degrees)
Time-of-flight = length of time taken for an ion to reach the source slit (μsec).

Table 3.2 – Initial and final conditions utilised for SIMION ion trajectory calculations of the existing MALDI ion-source, in the xz (vertical) plane.

Initial z /mm	Initial Angle / degrees	Final z /mm	Final x / mm	Final Angle / degrees	Time-of-flight / μsec
0	30	4.15952	131	-1.7583	3.45754
0	20	2.84354	131	-1.20265	3.45542
0	10	1.44314	131	-0.61056	3.45407
0	0	0.00E+00	131	0	3.45362
0	-10	-1.44314	131	0.61056	3.45407
0	-20	-2.84354	131	1.20265	3.45542
0	-30	-4.15952	131	1.7583	3.45754
0.1	30	4.05952	131	-1.7583	3.45754
0.1	20	2.74354	131	-1.20265	3.45542
0.1	10	1.34314	131	-0.61056	3.45407
0.1	0	-0.1	131	0	3.45362
0.1	-10	-1.54314	131	0.61056	3.45407
0.1	-20	-2.94354	131	1.20265	3.45542
0.1	-30	-4.25952	131	1.7583	3.45754
0.2	30	3.95952	131	-1.7583	3.45754
0.2	20	2.64354	131	-1.20265	3.45542
0.2	10	1.24314	131	-0.61056	3.45407
0.2	0	-0.2	131	0	3.45362
0.2	-10	-1.64314	131	0.61056	3.45407
0.2	-20	-3.04354	131	1.20265	3.45542
0.2	-30	-4.35952	131	1.7583	3.45754
		TOFmax - TOFmin =3.9 ns			

Initial z = the initial distance of an ion from the ion optical axis (mm)
Initial Angle = the initial angle of an ion from the ion optical axis (degrees)
Final z = the distance of an ion from the ion optical axis at the source slit (mm)
Final x = the distance an ion travels along the ion optical axis. The simulation ends at a distance of 131 mm, the location of the source slit.

Final Angle = the final angle of an ion from the ion optical axis (degrees)
Time-of-flight = length of time taken for an ion to reach the source slit (μsec).

conditions.

It is clear from figure 3.4 and 3.5 that the extraction region did not offer any collimation of an ion beam with typical parameters (sample spot size 200 μm, angular spread 30 degrees, energy spread 30 eV). By the time the ion-beam reached the source slit of the double-focusing mass spectrometer (131 mm), it was highly divergent. The application of high potentials would allow the ion-beam to be focused into the source slit in the y-plane. Collimation of the ion-beam in the z-plane, however, would not maintain an appropriate vertical height for transmission through the sectors of the double-focusing mass spectrometer, using the electrostatic einzel lenses available.

It was evident that better design of the extraction region of the ion-source would provide superior collimation of the ion-beam, in particular in the z-direction, enabling higher transmission through the double-focusing mass spectrometer.

Various methods have been used to focus or collimate diverging beams of ions using electrostatic fields. One of the most common is the "Einzel" lens, which is usually created by a combination of three rotationally or planar symmetric electrodes with appropriate applied voltages. The curved electrostatic field created in the region between the electrodes can be utilised to focus ions. Einzel lenses can be of two types: accelerating, where for positive ions the middle electrode has a more negative potential than the two end-electrodes, or a decelerating lens, where for positive ions the middle electrode is more positive than the two end-electrodes. In the accelerating lens ions are weakly focused, while in the decelerating lens they are focused strongly. The advantage of using an accelerating lens for the MAG-TOF instrument is that the accelerating lens introduces lower time-aberrations, and is thus advantageous for use with an the ion buncher. The disadvantage is that higher

voltages are required to achieve the same focusing effect as a similar decelerating lens.

SIMION ion trajectory simulations were made for a variety of accelerating einzel lenses of different geometries placed in front of the ion-source cradle. Due to the limitation of available space in front of the ion-source cradle only one lens could be placed here. From the simulations it quickly became evident that an accelerating einzel lens placed before the ion-source cradle could be used to collimate the ion beam tightly enough that it would pass through the source slit of the double-focusing mass spectrometer. This meant that an accelerating einzel lens of rotational symmetry could be used to provide all the necessary ion-beam focusing, and that the orginal electrostatic lenses situated after the cradle would be unnecessary, except for fine-tuning.

SIMION ion trajectories for an accelerating einzel lens of rotational symmetry and capable of meeting the requirements imposed by the acceptance characteristics of the double-focusing mass spectrometer are shown in figures 3.6-3.8. Table 3.3 lists the initial and final conditions of the ion beam. The time aberrations imposed by such a lens on an ion-beam with typical initial parameters (sample spot size 200 μm, angular spread 30 degrees, energy spread 30 eV) were about 3 ns.

It was necessary for the first (and last) of the einzel lens plates to be grounded in order to provide a suitable extraction potential gradient. The rear einzel lens electrode (nearest the cradle) was made of stainless steel and mounted by means of three 11 mm stainless steel studs screwed onto the cradle. The front electrode was attached to the rear electrode by means of three 5 mm stainless steel spacers. The centre electrode was mounted by three specially designed PEEK studs screwed to the

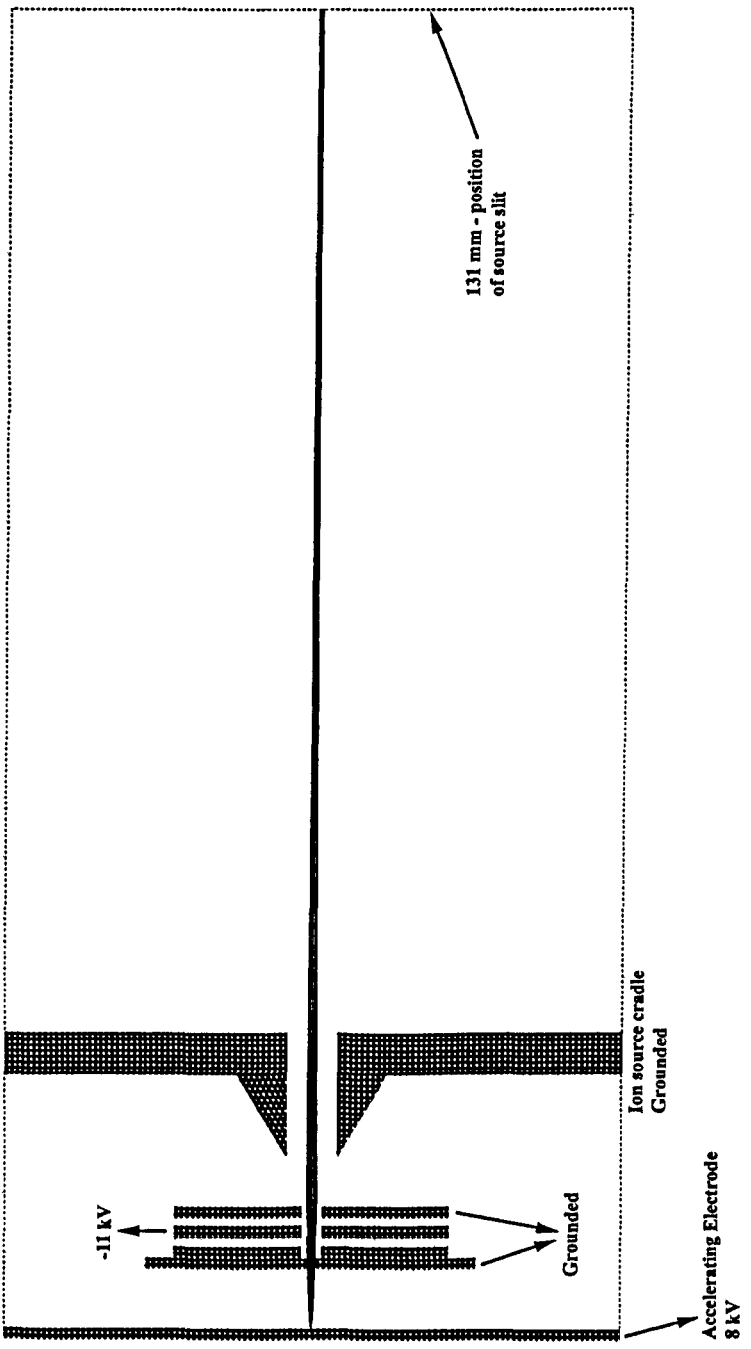

Figure 3.6 – Ion trajectory simulations of the ion-source of the MAG-TOF mass spectrometer, utilising an accelerating einzel lens to provide focusing and collimation. Ion m/z=1000, initial kinetic energy=30eV, initial position=0.0mm from axis.

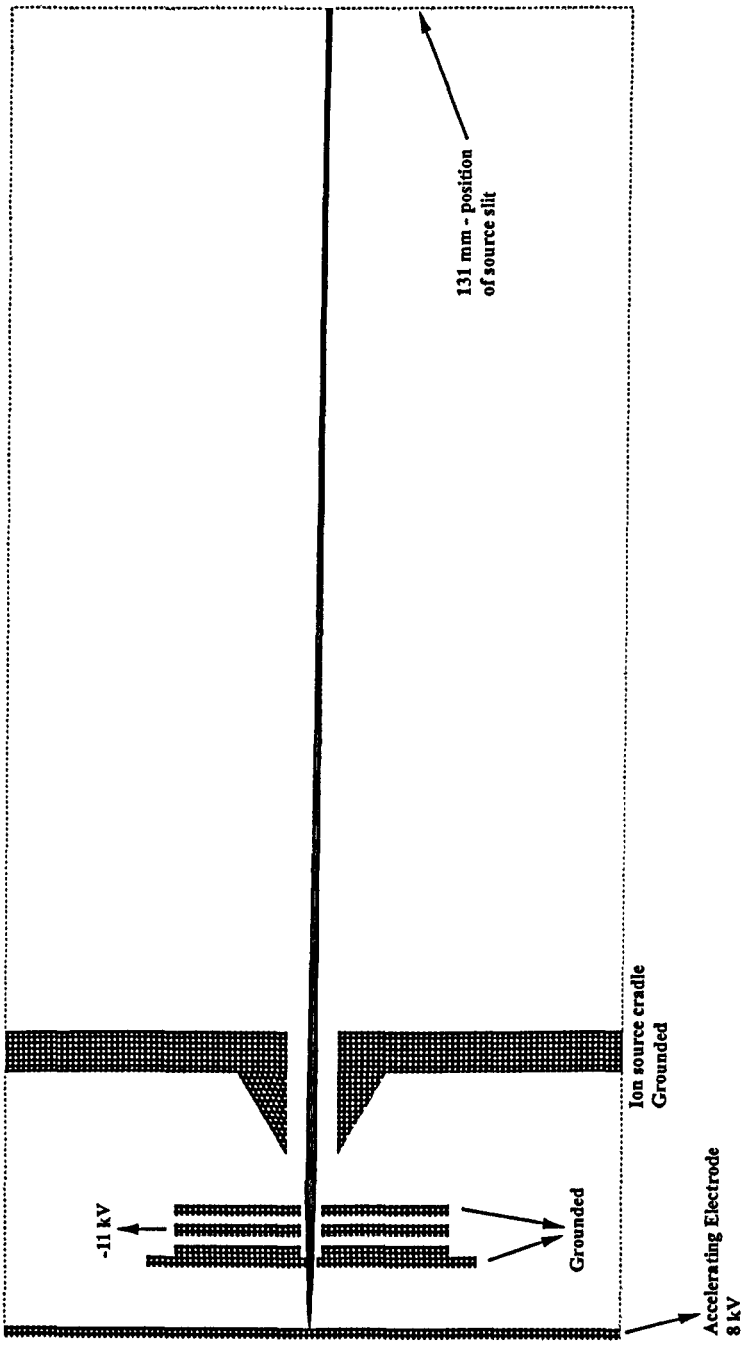

Figure 3.7 – Ion trajectory simulations of the ion-source of the MAG-TOF mass spectrometer, utilising an accelerating einzel lens to provide focusing and collimation. Ion m/z=1000, initial kinetic energy=30eV, initial position=0.1mm from axis.

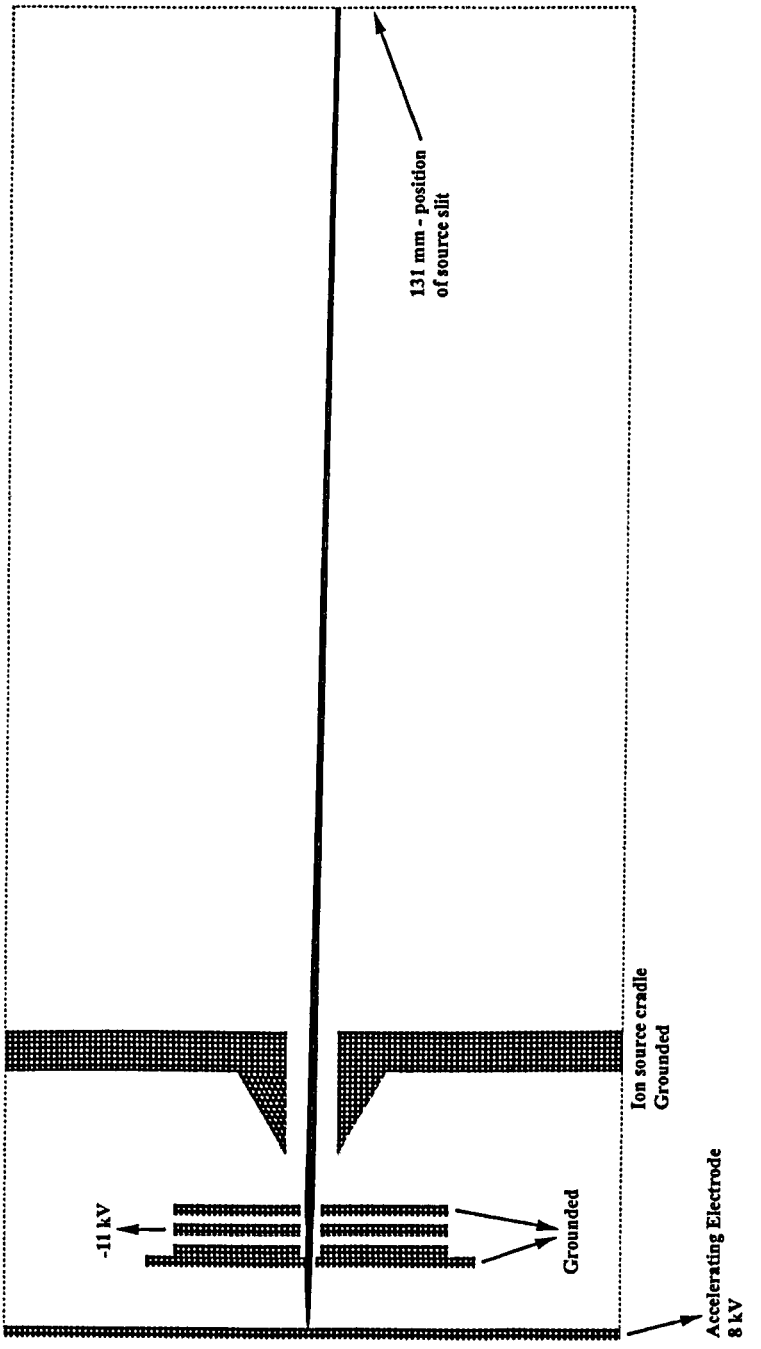

Figure 3.8 – Ion trajectory simulations of the ion-source of the MAG-TOF mass spectrometer, utilising an accelerating einzel lens to provide focusing and collimation. Ion m/z=1000, initial kinetic energy=30eV, initial position=0.2mm from axis.

Table 3.3 - Initial and final conditions utilised for SIMION ion trajectory calculations of the MAG-TOF ion-source utilising an accelerating einzel lens to provide focusing and collimation.

Initial y /mm	Initial Angle/ degrees	Final y /mm	Final x / mm	Final Angle / degrees	Time-of-flight / μsec
0	30	0.0620015	131	0.275669	3.42031
0	20	-0.202104	131	0.0715544	3.41641
0	10	-0.1747	131	0.00183557	3.41602
0	0	0.00E+00	131	0	3.41513
0	-10	0.1747	131	-0.00183557	3.41602
0	-20	0.202104	131	-0.0715544	3.41641
0	-30	-0.0620015	131	-0.275669	3.42031
0.1	30	-0.85885	131	-0.217473	3.41911
0.1	20	-0.920007	131	-0.325001	3.41529
0.1	10	-0.785366	131	-0.343706	3.41619
0.1	0	-0.591775	131	-0.336508	3.41651
0.1	-10	-0.486783	131	-0.371522	3.4168
0.1	-20	-0.649213	131	-0.53151	3.41557
0.1	-30	-1.02756	131	-0.793065	3.42101
0.2	30	-1.62862	131	-0.638729	3.4196
0.2	20	-1.55848	131	-0.683763	3.4164
0.2	10	-1.37499	131	-0.679154	3.41622
0.2	0	-1.22446	131	-0.692424	3.4165
0.2	-10	-1.2553	131	-0.792007	3.41686
0.2	-20	-1.58691	131	-1.03407	3.4154
0.2	-30	-	-	-	-
		TOFmax - TOFmin =5.8 ns			

Initial y = the initial distance of an ion from the ion optical axis (mm)
Initial Angle = the initial angle of an ion from the ion optical axis (degrees)
Final y = the distance of an ion from the ion optical axis at the source slit (mm)
Final x = the distance an ion travels along the ion optical axis. The simulation ends at

a distance of 131 mm, the location of the source slit.

Final Angle = the final angle of an ion from the ion optical axis (degrees)
Time-of-flight = length of time taken for an ion to reach the source slit (μsec).

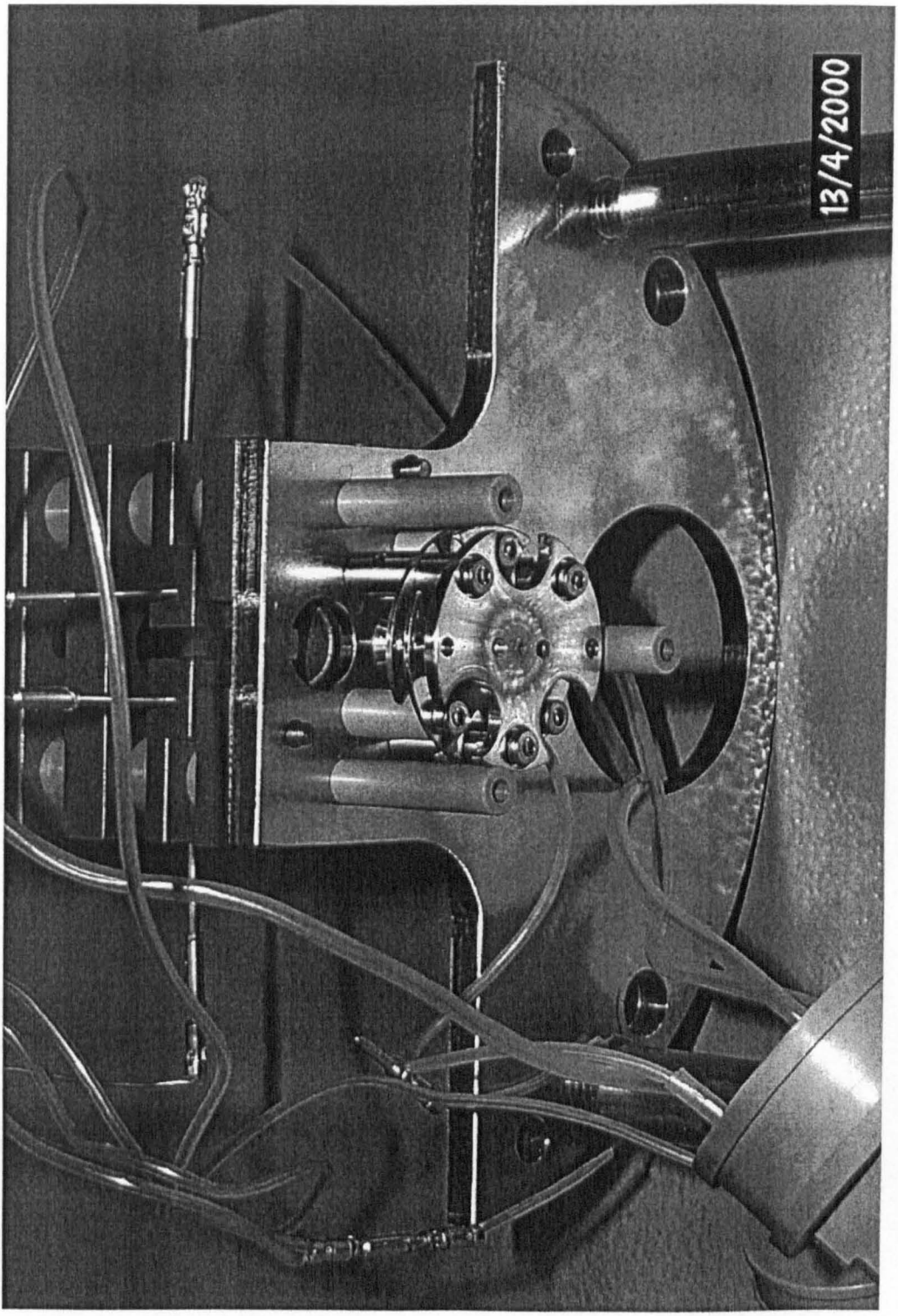

Figure 3.9 – Photograph of the MAG-TOF ion source. The foreground shows the newly designed einzel lens and its mountings. The accelerating electrode was detached to allow this photograph.

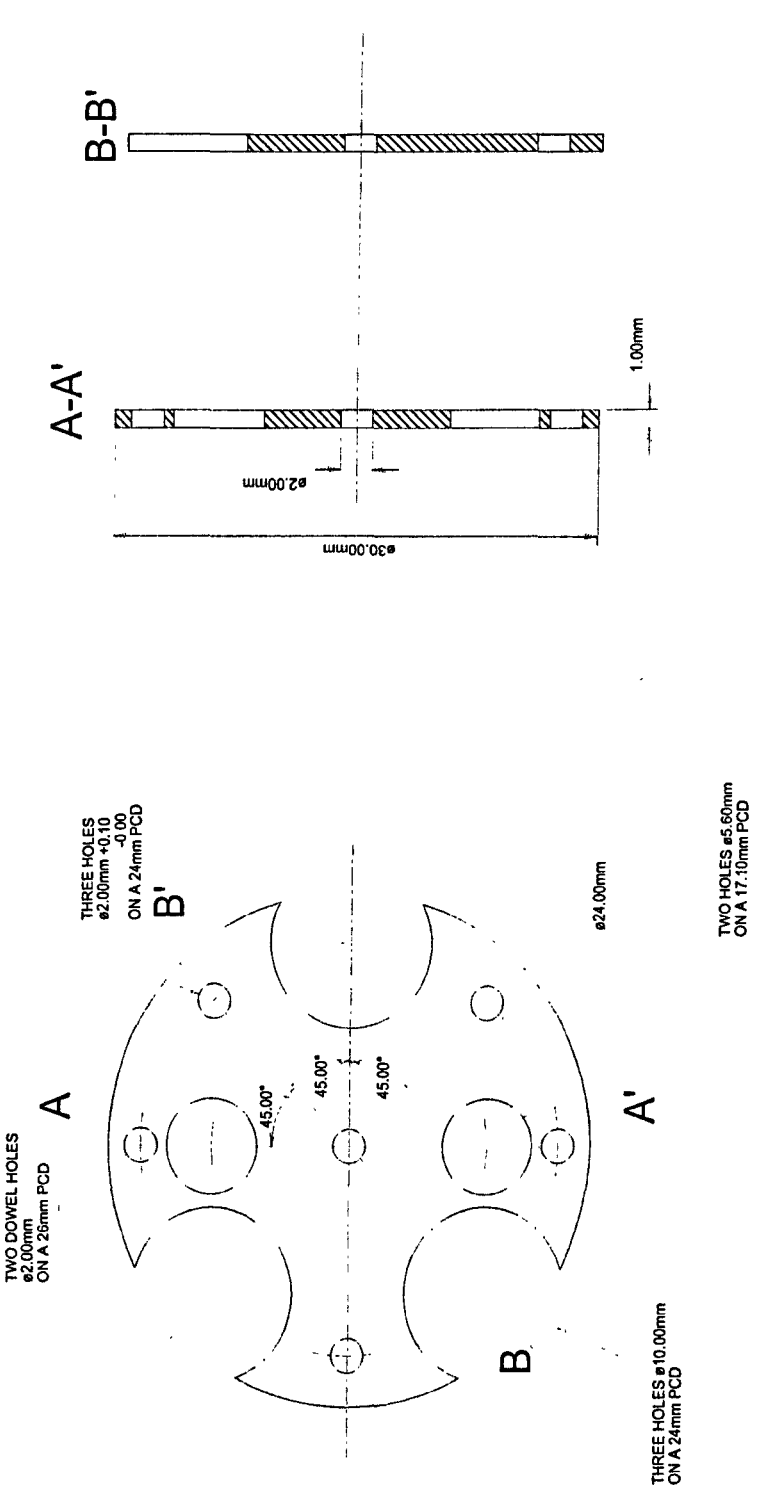

Figure 3.10 – Mechanical drawing of the first electrode of the accelerating einzel lens.

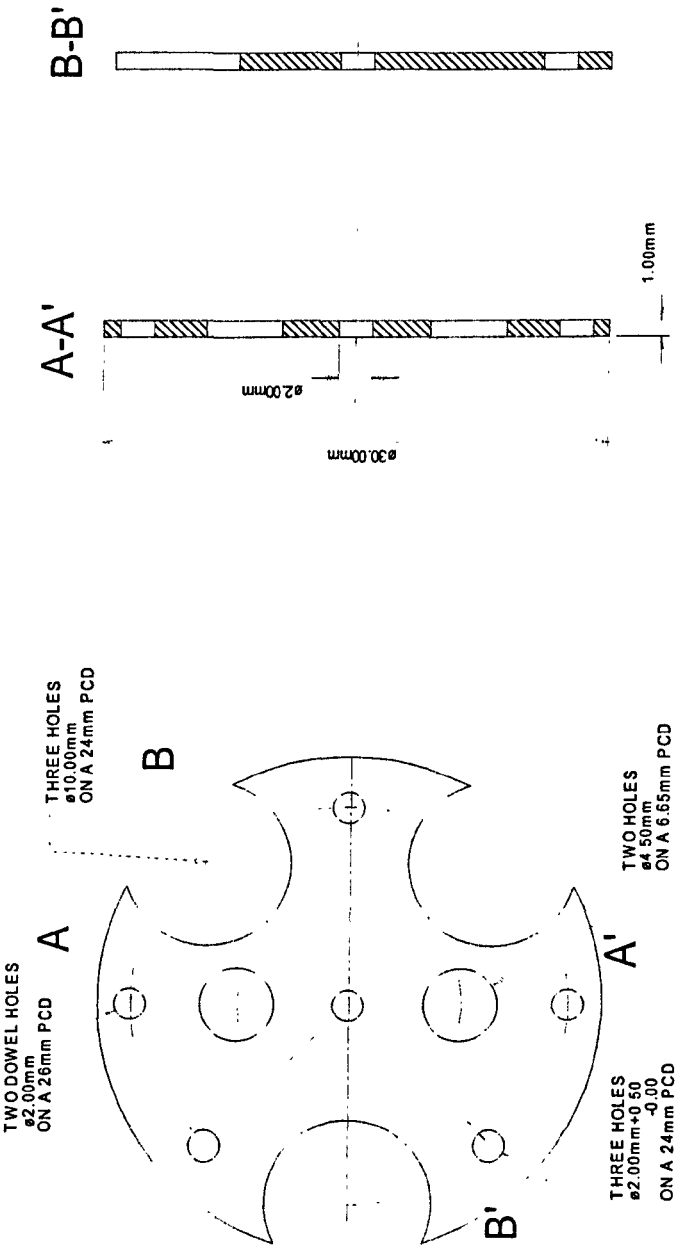

Figure 3.11 – Mechanical drawing of the second electrode of the accelerating einzel lens.

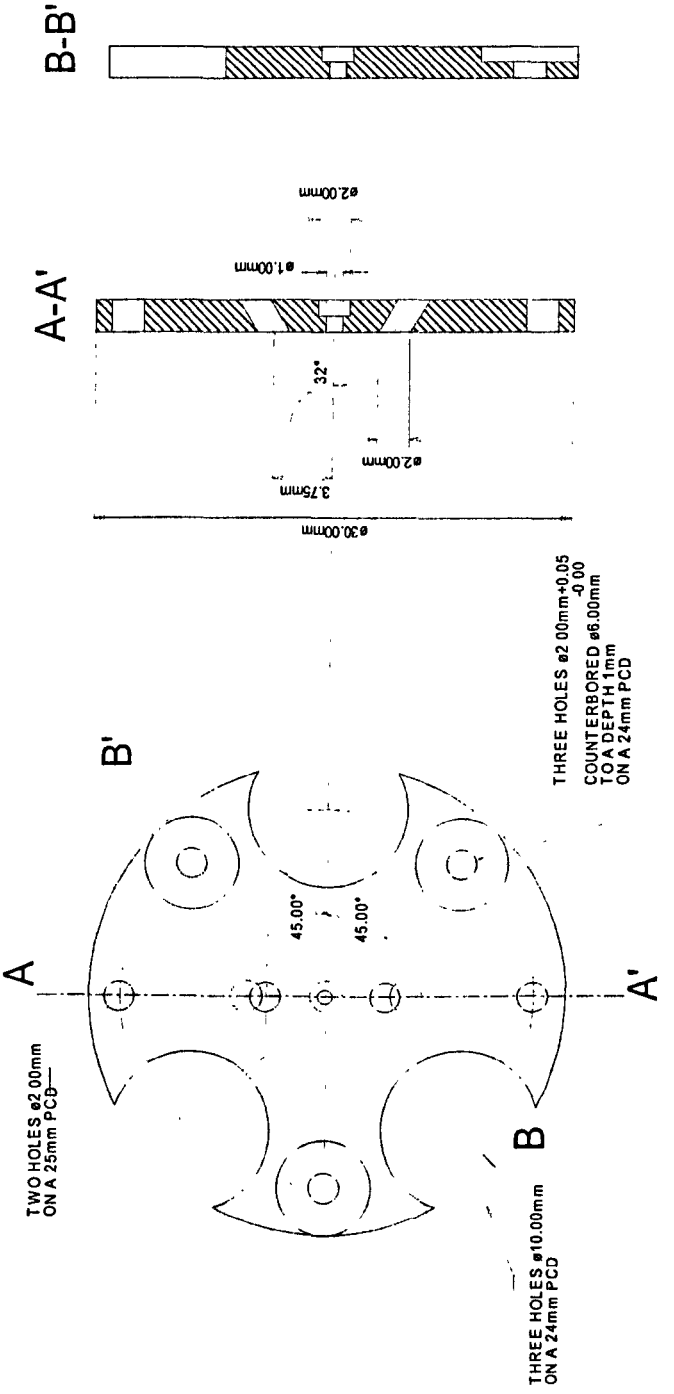

Figure 3.12 – Mechanical drawing of the third electrode of the accelerating einzel lens.

cradle, that allowed for electrical isolation of this lens. A photograph illustrating the accelerating einzel lens and its mountings is shown in figure 3.9. Mechanical drawings of the accelerating einzel lens electrodes are shown in figures 3.10-3.12.

Experimentally, the highest sensitivity and resolution were achieved if the potential applied to the accelerating einzel lens was approximately -10.5 kV for an ion with an m/z of 1000. The applied potential could easily be altered by a few hundred volts to provide fine-tuning of the ion-beam.

With the source and exit slits of the double-focusing mass spectrometer fully open, it was routine to achieve a resolution of ~ 2500 (full width at half the maximum height (FWHM)) after the quadratic-field time-of-flight reflectron (TOF-2), for a parent ion with an m/z of ~ 1000. By decreasing the width of the source and exit slits of the double-focusing mass spectrometer it was possible to achieve a resolution of 3500-4000 (FWHM) for a parent ion of m/z ~ 1000 after TOF-2. Fragment ion resolution was typically in the range 1000-1200 (FWHM) for a fragment ion of m/z ~ 1000 after TOF-2.

Figures 3.13 and 3.14 show high-energy collision-induced dissociation spectra of the poly(propylene glycol) $[M+Na]^+$ adduct ion m/z=969.5 (n=16), generated using the new MALDI ion-source, and using argon as the collision gas. The source and exit slits of the double-focusing mass spectrometer were closed to ½ of their fully open values. A resolution of 3343 (FWHM) was obtained for the parent ion, m/z=969.5 (figure 3.13), and a resolution of 1299 (FWHM) was obtained for the fragment ion m/z=909.6 (figure 3.14). Closure of the source and exit slits to these values did not result in a *significant* decrease in sensitivity (cf. chapter 5.4).

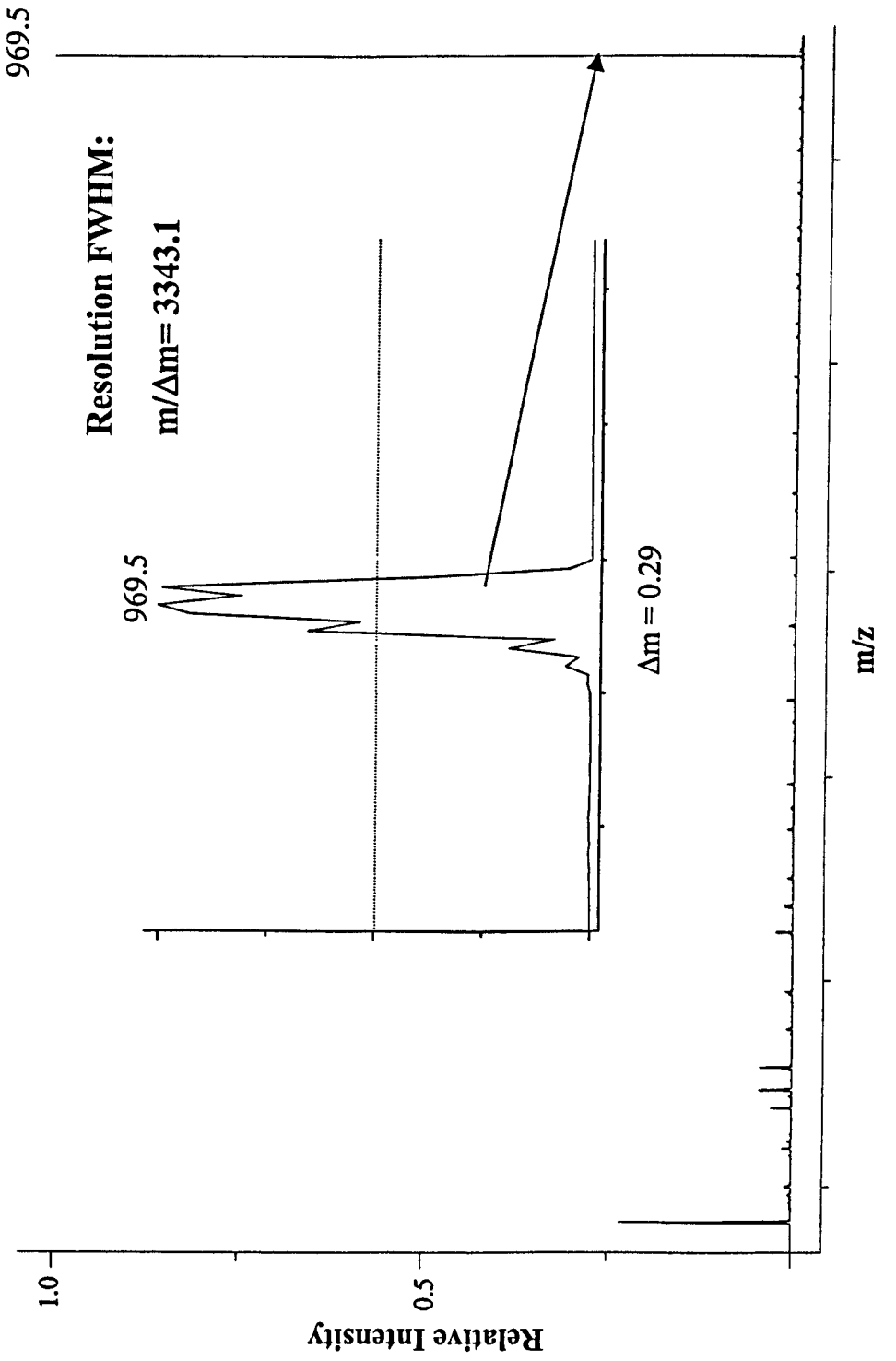

Figure 3.13 – high-energy collision-induced dissociation spectrum of the poly(propylene glycol) $[M+Na]^+$ adduct ion m/z=969.5 (n=16), generated using the new MALDI ion-source, and using argon as the collision gas. Inset shows enlargement of the parent ion.

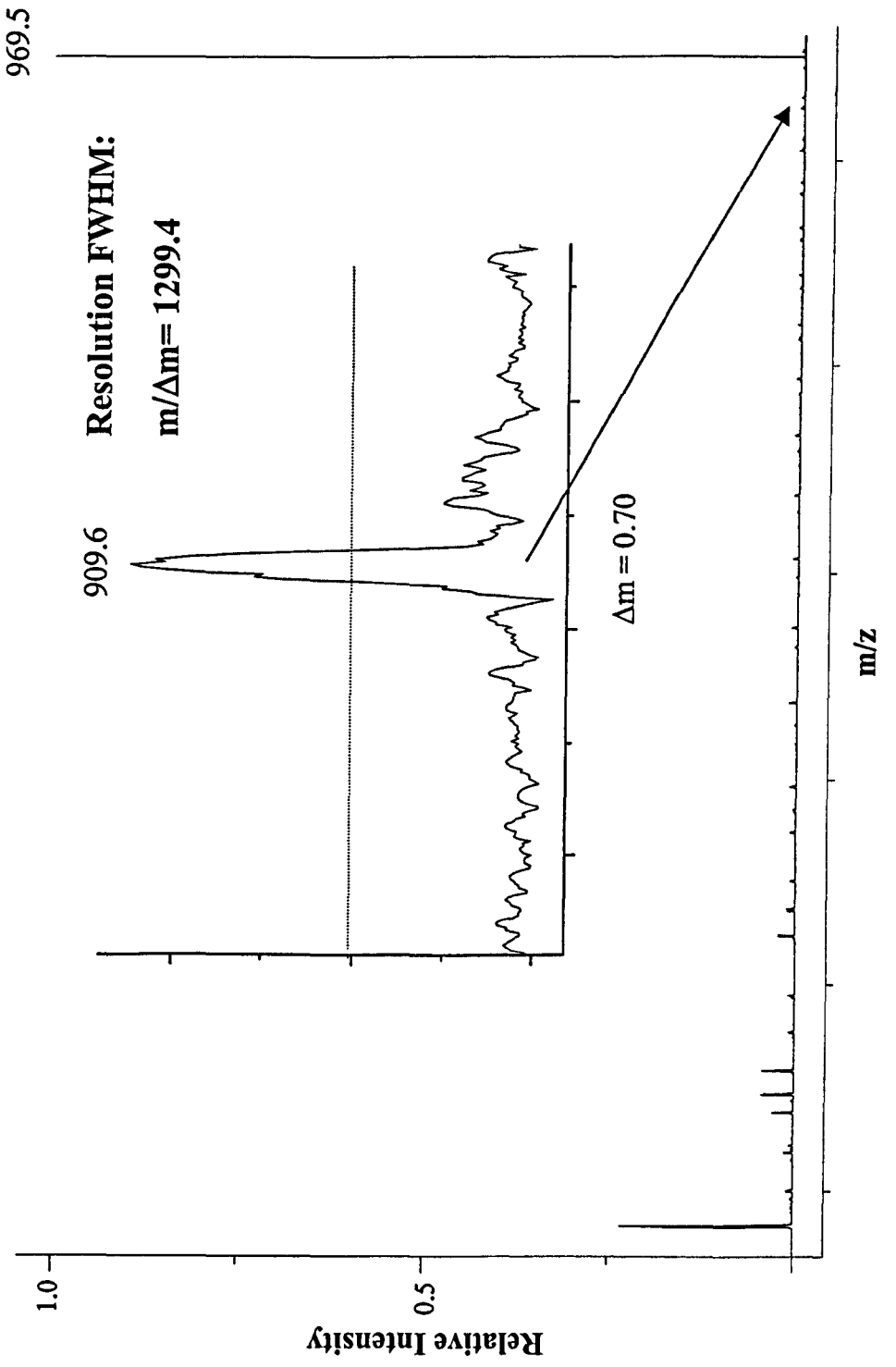

Figure 3.14 – high-energy collision-induced dissociation spectrum of the poly(propylene glycol) $[M+Na]^+$ adduct ion m/z=969.5 (n=16), generated using the new MALDI ion-source, and using argon as the collision gas. Inset shows enlargement of the fragment ion m/z=909.6.

All of the experimental results obtained using the MAG-TOF instrument, and presented in chapters four and five of this study, were obtained using this ion source design.

Chapter Four – High-energy Collision-induced Dissociation of Fullerenes

4.1 Introduction

In 1985, Kroto et al were carrying out laser mass spectrometric experiments in order to study long-chain carbon molecules.[76] One laser was used to vapourise the carbon species from the surface of a solid graphite disk, a second laser was used for photoionisation of the carbon species and a time-of-flight mass spectrometer was used for analysis. Using this experimental arrangement, Kroto et al detected a number of carbon clusters.[76] Certain 'magic number' peaks were observed, one of which corresponded to a sixty carbon atom cluster. This species appeared to be particularly stable, a factor attributed to its structure, that was proposed to be a truncated icosahedron.[76] Constructions by architect R. Buckminster Fuller with the same geodesic structure led to the naming of C_{60} as buckminsterfullerene.[77] The structure of C_{60} was confirmed by x-ray crystallography,[78] and was shown to resemble the soccer ball structure initially proposed by Kroto et al.[76]

Other closed-cage carbon clusters became known as fullerenes. The next most common fullerene, after C_{60}, was C_{70}. The structure of C_{70} was comprised of twenty-five hexagon rings of carbon atoms, twelve pentagonal carbon atom rings, and resembles a rugby ball in shape. The growth of fullerenes arises in the gas phase from ion-molecule reactions. The presence of atomic carbon is thought to be necessary. Linear chains of carbon link together to form graphite sheets, which curl around and anneal, forming a fullerene. Several years after the discovery of C_{60} by Kroto et al, a synthetic method was devised for the preparation of fullerenes.[79]

The hollow-caged structures allow fullerenes to be derivatised in any one of three ways. Exohedral derivatives are formed from the addition of one or more atoms or molecules to the *outer* surface of the fullerene cage. Species that have been attached onto the outer surface of fullerenes include halogens,[80] oxygen,[81, 82] metals,[83, 84] and small organic molecules.[85, 86]

Endohedral derivatives are formed from the encapsulation of one or more atoms by the fullerene cage. Metals,[87] alkali earth metals [88] and noble gases [89, 90] have been encapsulated by fullerenes. Smalley et al introduced a method of nomenclature in order to prevent confusion between exohedral and endohedral fullerene derivatives.[91] The term $M@C_n$ denoted atom M inside the C_n cage. Exohedral derivatives were denoted MC_n, where atom or molecule M was bound to the outer surface of the fullerene, C_n cage.

Doped derivatives are products formed by the substitution of one of the atoms of the fullerene cage by a heteroatom. The nomenclature for these derivatives is $C_{n-1}M$, where one of the carbon atoms in a fullerene C_n has been replaced by heteroatom M. Boron-doped fullerenes have been formed by laser vapourisation of boron nitride doped graphite.[92, 93] Nitrogen has been shown to replace a carbon atom in C_{60} and C_{70} producing $C_{59}N$ and $C_{69}N$ species.[94]

This chapter describes the investigation of fullerenes and derivatised fullerenes by high-energy collision-induced dissociation, for the purpose of testing the new ion source of the tandem double-focusing/time-of-flight instrument (MAG-TOF).

4.2 Experimental

C_{60} or C_{70} (Southern Chemicals, USA) was deposited upon the stainless steel probe tip from saturated solutions in toluene. C_{60}^+ or C_{70}^+ ions were generated by laser desorption, and accelerated to 8 keV at the ion source. The particular ion to be investigated was selecting by adjusting the magnetic-field strength of the double-focusing mass spectrometer (MS-1), and the width of the exit slit. The resolution of the double-focusing mass spectrometer ensured that only the desired monoisotopic peak was selected. An additional translational energy spread of up to 4 keV was imposed upon the ion packet before collision by the ion buncher. The pressure of the collision gas, usually helium, argon or xenon, was set to give 30% attenuation (i.e. 70% transmission) of the selected ion.

4.3 High-Energy Collision-induced Dissociation of C_{60}^+ and C_{70}^+ Ions generated by Laser Desorption.

Collision-induced dissociation of C_{60}^+ and C_{70}^+ has been reported previously.[95, 96] The CID of these compounds result in a large number of evenly spaced fragment ions over a wide m/z range. This makes them particularly suited as test materials for the MAG-TOF instrument, particularly for the calibration of the instrument (see Appendix I).

C_{60}^+ and C_{70}^+ ions were selected by adjusting the magnetic-field strength in MS-1. The resolution of the double-focusing mass spectrometer was sufficient to ensure that only the monoisotopic (^{12}C only) isotope passed through the exit-slit of MS-1. Collision-induced dissociation was performed on the selected ion by introducing an inert gas into the collision chamber.

The high-energy collision-induced dissociation spectra of C_{60}^+ using xenon as the collision gas are shown in figures 4.1 and 4.2. The laboratory frame collision energy was of the range 8-12 keV, due to the energy spread imposed by the ion buncher, corresponding to a centre-of-mass collision energy range of 1234-1851 eV for C_{60}^+.

High-energy collision-induced dissociation was found to result in the loss of an even number of carbon atoms from C_{60}^+, observed as C_n^+ fragments (for n>30), in the high m/z region of the spectra (C_{36}^+ through C_{58}^+ were observed). It has been proposed that the dissociation leading to these fullerene fragments is by the loss of C_{2n} rather than consecutive loss of nC_2 from the cage.[97] In the low m/z region of the CID spectra, peaks were observed that corresponded to the loss of odd and even numbers

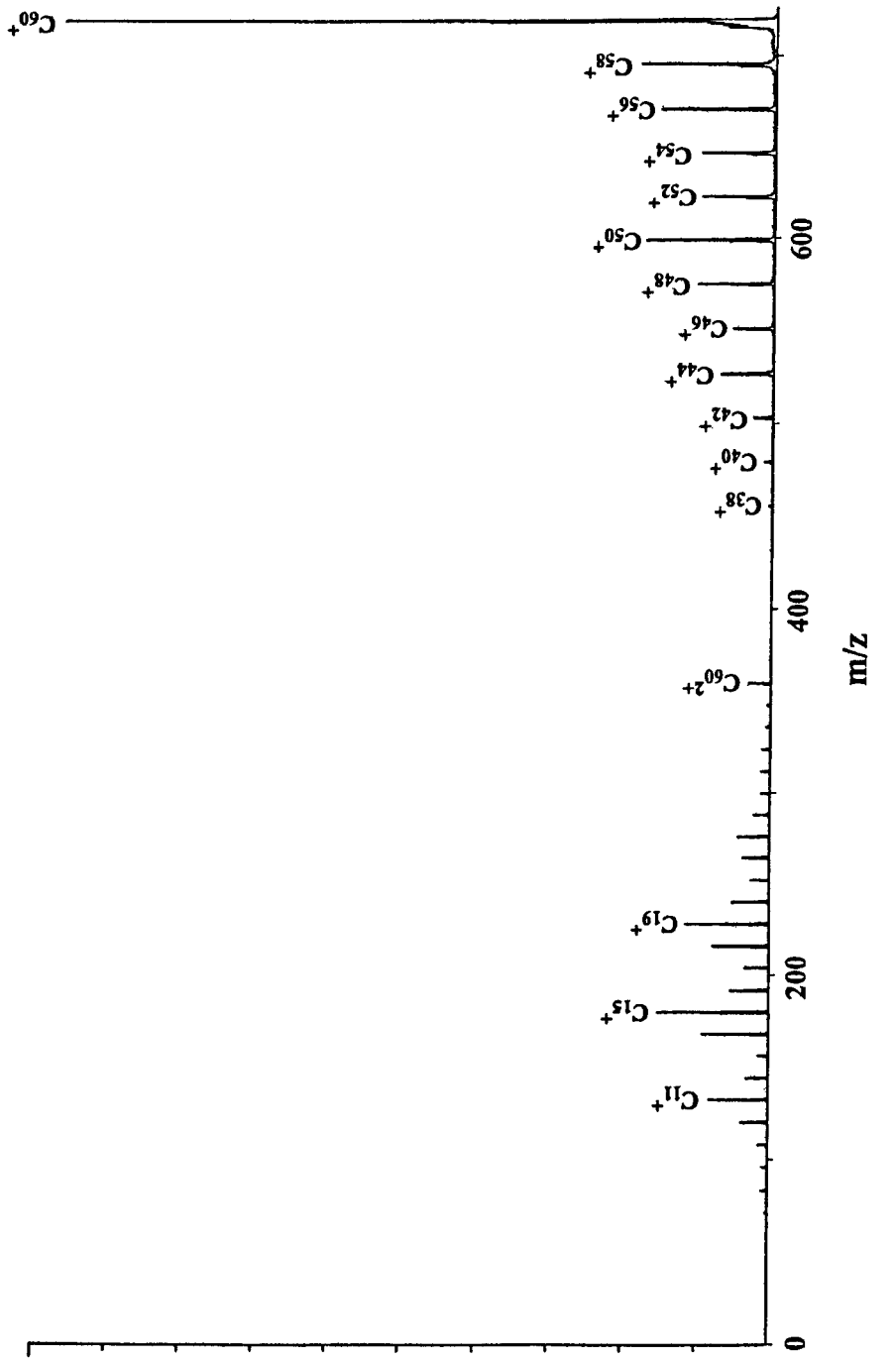

Figure 4.1 - High-energy collision-induced dissociation spectrum of C_{60}^+, generated by laser desorption and using xenon as the collision gas. Scaled to show 100 % of parent ion intensity.

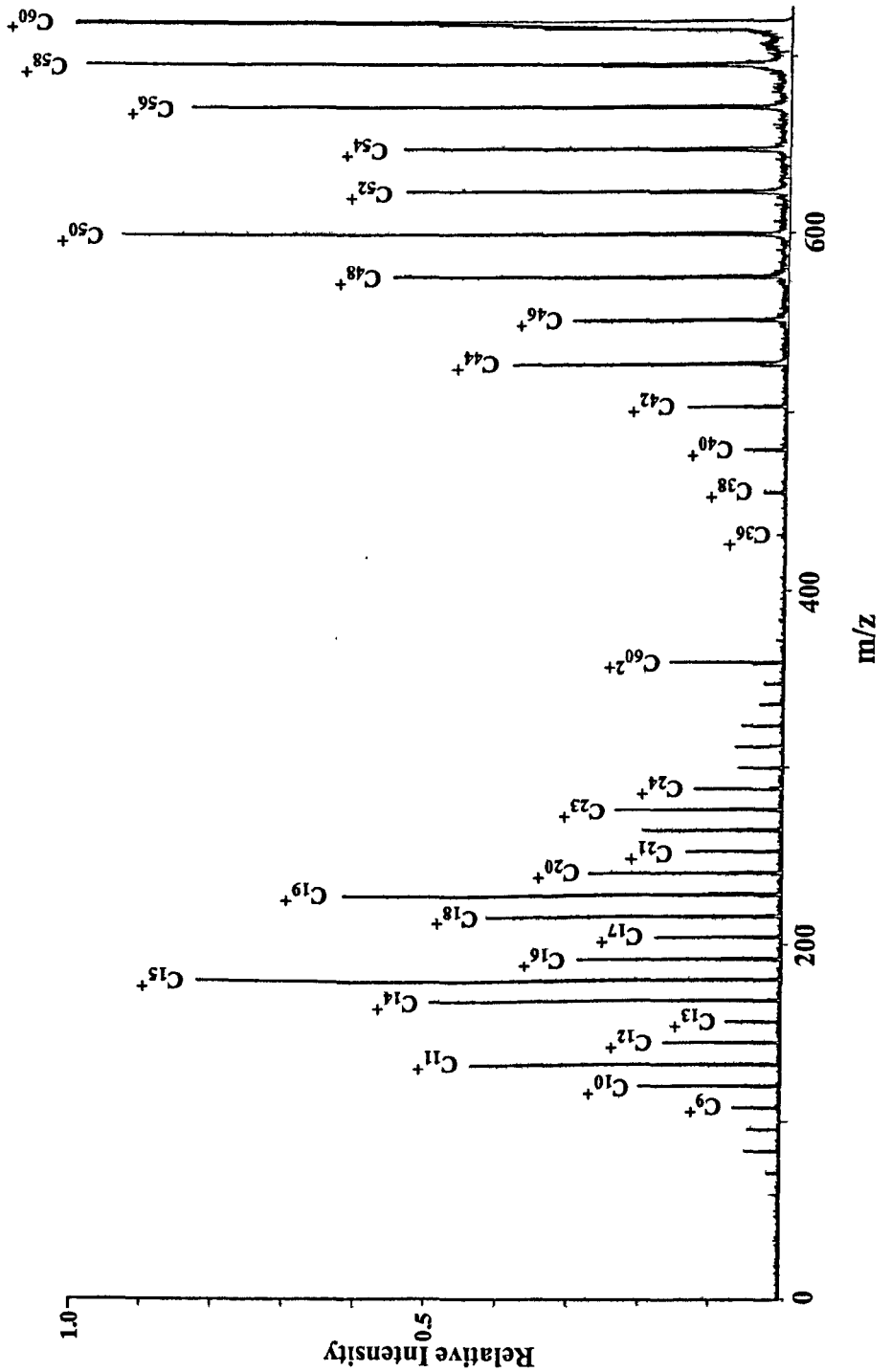

Figure 4.2 - High-energy collision-induced dissociation spectrum of C_{60}^+, generated by laser desorption and using xenon as the collision gas. Scaled to show 22 % of parent ion intensity.

of carbon atoms, presumably as larger fragments were ejected from the fullerene.[98, 99, 100] C_5^+ through C_{29}^+ were observed.

The peak at m/z 360 was observed to be intense, compared with its neighbours. It was not clear whether this was due to the particular stability of C_{30}^+, or whether there was a significant contribution from C_{60}^{2+}.

The CID spectra of C_{60}^+ shown in figures 4.1 and 4.2 represented a significant improvement in fragment ion intensity, as compared with the spectrum illustrated in figure 3.1. The sensitivity was due to the redesign of the ion source discussed in chapter 3.

The high-energy collision-induced dissociation spectra of C_{70}^+ using xenon as the collision gas are shown in figures 4.3. The laboratory frame collision energy was of the range 8-12 keV, due to the energy spread imposed by the ion buncher, corresponding to a centre-of-mass collision energy range of 1081-1622 eV for C_{70}^+. As for C_{60}^+, fragments with even numbers of carbon atoms were observed in the high m/z region of the spectrum (C_{38}^+ through C_{68}^+). Below m/z 420 fragments with odd and even numbers of carbon atoms were observed (C_3^+ through C_{34}^+).

The peak at m/z 420 was observed to be intense, compared with its immediate neighbours. It was not clear whether this was due to the stability of C_{35}^+, or whether there was a significant contribution from C_{70}^{2+}.

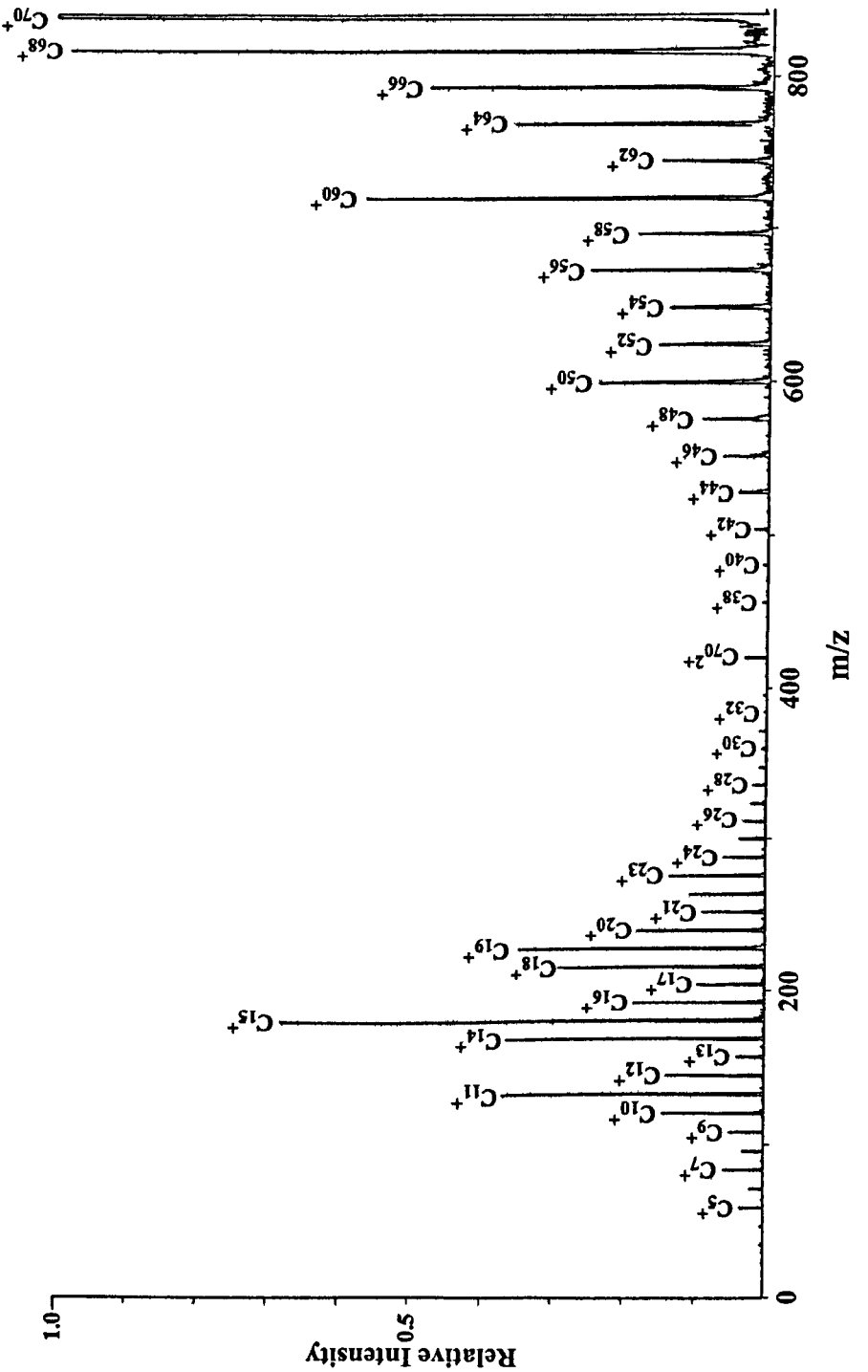

Figure 4.3 - High-energy collision-induced dissociation spectrum of C_{70}^+, generated by laser desorption and using xenon as the collision gas. Scaled to show 20% of parent ion intensity.

4.4 High-Energy Collision-induced Dissociation of $^{12}C_{59}{}^{13}C_1{}^+$ generated by Laser Desorption.

The $^{12}C_{59}{}^{13}C_1{}^+$ isotope of $C_{60}{}^+$ was selected by adjusting the magnetic-field strength of the double-focusing mass spectrometer (MS-1), and the width of the exit slit. The resolution of the double-focusing mass spectrometer was sufficient to ensure that only this particular isotope passed through the exit-slit of MS-1. Collision-induced dissociation was performed on the selected ion by introducing an inert gas into the collision chamber.

The high-energy collision-induced dissociation spectrum of $^{12}C_{59}{}^{13}C_1{}^+$ using helium as the collision gas is shown in figures 4.4 - 4.6. The CID spectrum showed fragments containing only even numbers of carbon atoms in the high m/z region of the spectrum, and fragments containing both odd and even numbers of carbon atoms in the low m/z region of the spectrum, as described for $C_{60}{}^+$.

In the high m/z end of the spectrum, the most intense fragment ion peaks represented $^{12}C_{n-1}{}^{13}C_1{}^+$ fragments. These decreased in intensity toward the centre of the spectrum, with $^{12}C_n{}^+$ fragments increasing in intensity. At the low m/z end of the spectrum, peaks corresponding to $^{12}C_n{}^+$ fragments were observed to be the most intense.

During the CID of $^{12}C_{59}{}^{13}C_1{}^+$, there is a possibility that the fragment ejected from the ion may contain the ^{13}C atom. Statistically, for each carbon atom ejected from the ion, there is a 1 in 60 chance that the ^{13}C atom is ejected, explaining the presence of fragments containing only ^{12}C atoms, and the relative intensities of $^{12}C_n{}^+$: $^{12}C_{n-1}{}^{13}C_1{}^+$.

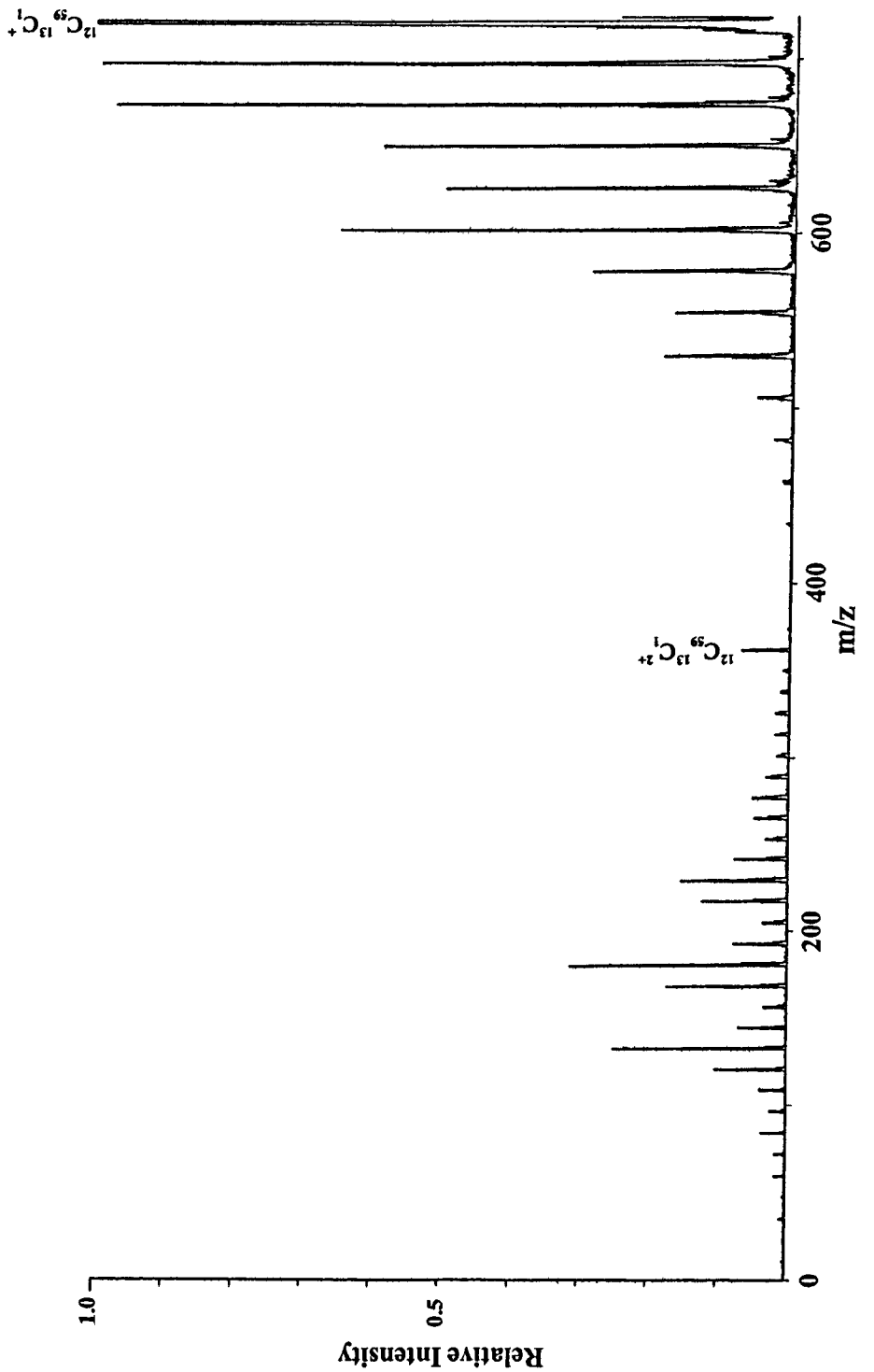

Figure 4.4 - High-energy collision-induced dissociation spectrum of $^{12}C_{59}{}^{13}C_1{}^+$, generated by laser desorption and using helium as the collision gas. Scaled to show 50 % of parent ion intensity.

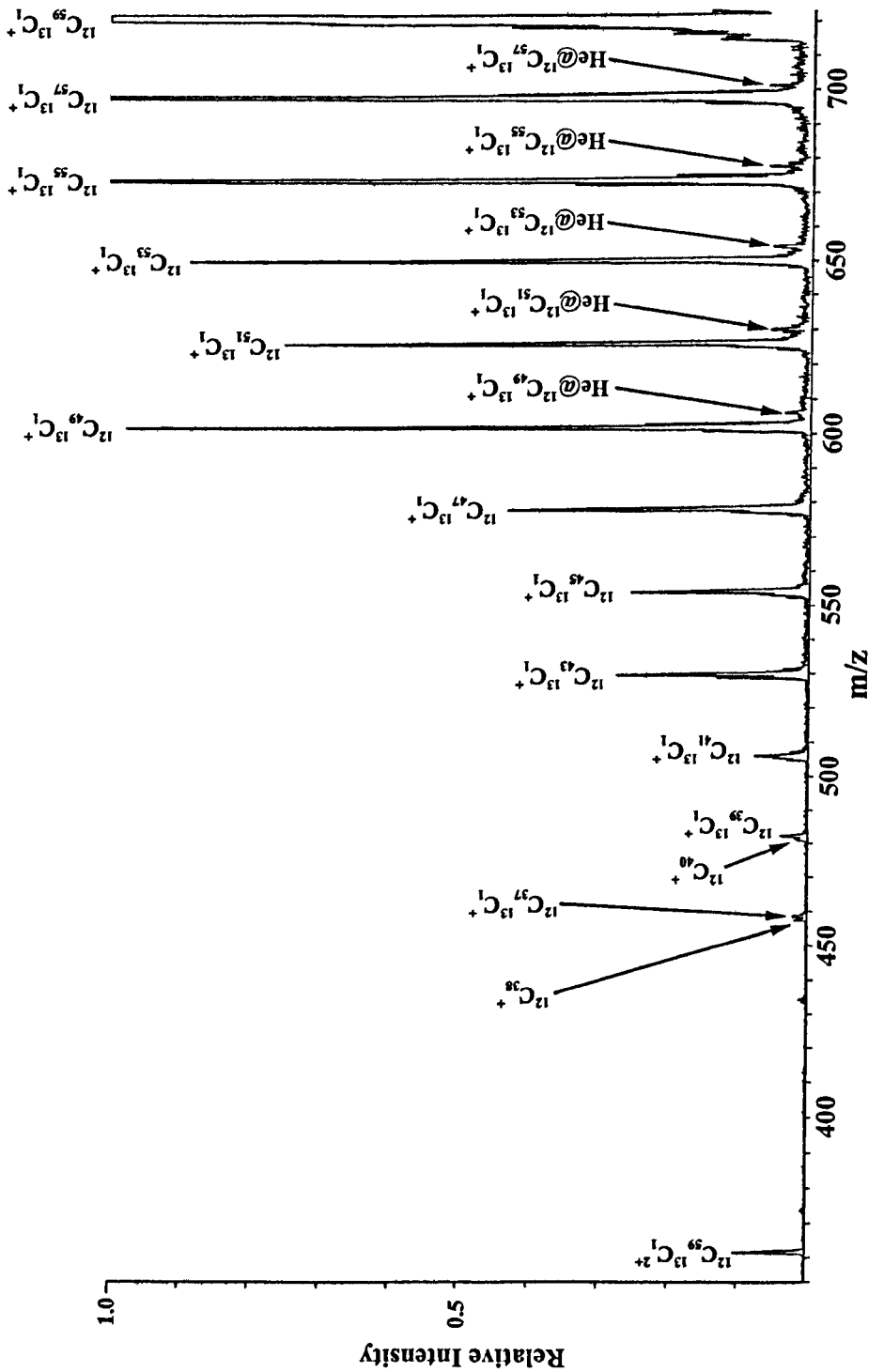

Figure 4.5 - High-energy collision-induced dissociation spectrum of $^{12}C_{59}{}^{13}C_1{}^+$, generated by laser desorption and using helium as the collision gas. Scaled to show m/z range 355-723 and 33% of parent ion intensity.

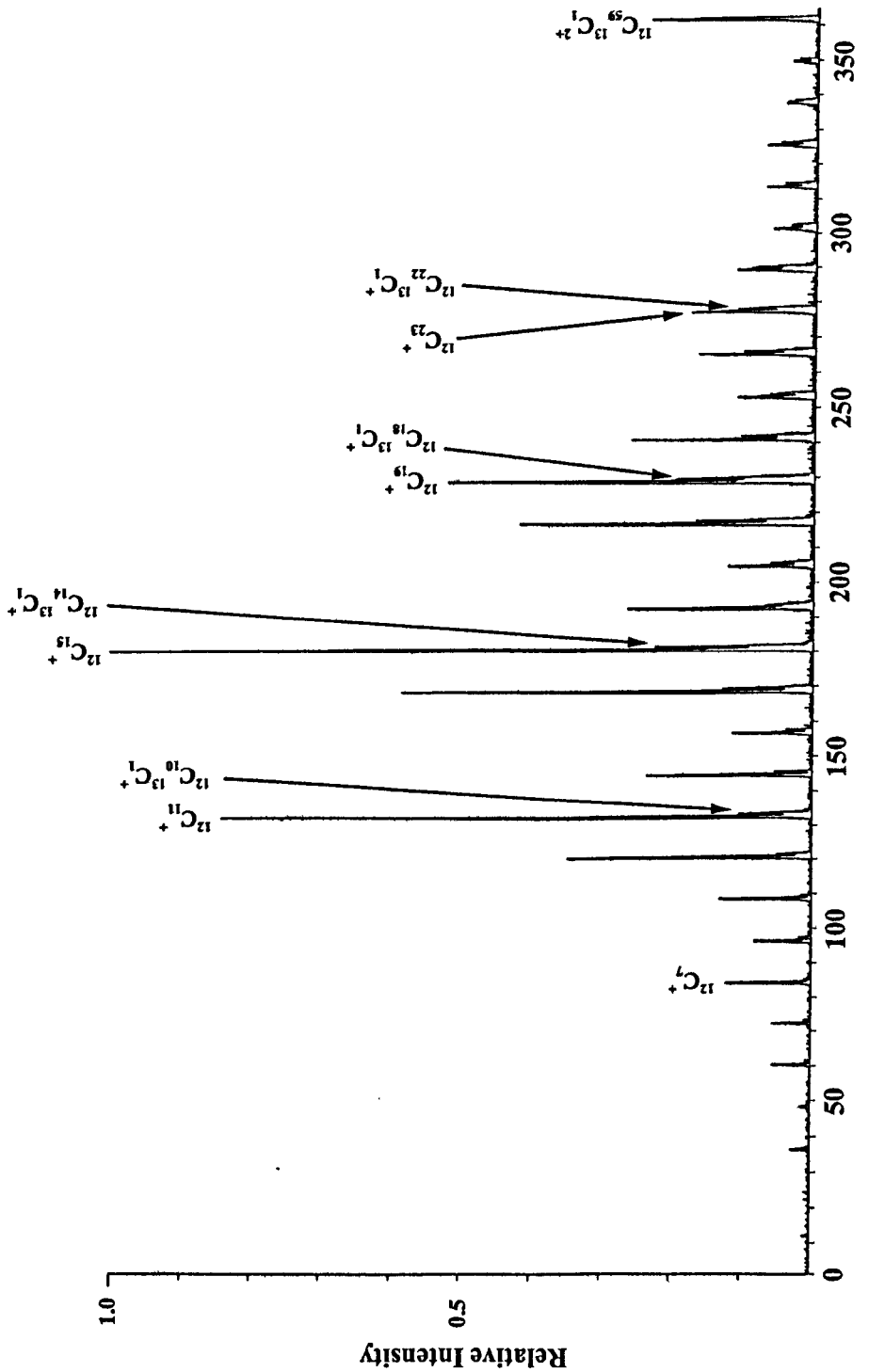

Figure 4.6 - High-energy collision-induced dissociation spectrum of $^{12}C_{59}{}^{13}C_1{}^{+}$, generated by laser desorption and using helium as the collision gas. Scaled to show m/z range 1-368 and 10% of parent ion intensity.

The peak at m/z 360.5 can be assigned as $^{12}C_{59}{}^{13}C_1{}^{2+}$. Peaks corresponding to $^{12}C_{30}{}^{+}$ and $^{12}C_{29}{}^{13}C_1{}^{+}$ were not observed

No adducts of $^{12}C_{59}{}^{13}C_1{}^{+}$ were observed due to a high noise level above the parent ion. Helium adducts were observed, however, for the loss of 2, 4, 6, 8 and 10 carbon atoms. As fullerenes are closed-cage structures, and that fragment adducts were observed for the loss of up to 10 carbon atoms, it is most likely that the adduct is endohedrally bound by the fullerene cage.[101] Assignments have been made as, He@$^{12}C_{49}{}^{13}C_1{}^{+}$, He@$^{12}C_{51}{}^{13}C_1{}^{+}$, He@$^{12}C_{53}{}^{13}C_1{}^{+}$, He@$^{12}C_{55}{}^{13}C_1{}^{+}$ and He@$^{12}C_{57}{}^{13}C_1{}^{+}$. The laboratory-frame collision energy employed for the formation of these endohedrally bound helium adducts was of the range 8-12 keV, giving a centre-of-mass collision energy of 44-66 eV. Studies by other workers have shown that the formation of He@C_{60} can be optimised at laboratory-frame collision energies of between 5 and 6 keV,[96] and is most probable for a centre-of-mass collision energy range of 31±3 eV.[97]

4.5 High-Energy Collision-induced Dissociation of C_{130}^+ generated by Laser Desorption/Ionisation.

Laser-induced coalescence reactions, in which fullerenes coalesce to form higher carbon cluster ions have been widely reported.[102, 103, 104, 105] There has not been, however, a consensus about the structures of the coalescence products. One proposal is that the coalescence products are "giant" fullerene ions. Another proposal is that the coalescence products are smaller fullerenes "stuck" together.

Collision-induced dissociation has been utilised to probe the structure of one such fullerene, C_{130}^+.

An endohedral metallo-fullerene sample consisting of a mixture of $Tb@C_{82}$ and $Tb@C_{80}$ was synthesised by the Kratschmer-Huffman method using metal oxide doped graphite rods.[106] The metallo-fullerene was deposited on a stainless steel slide from a saturated solution of the metallo-fullerene in dimethylformamide, and allowed to dry in a stream of warm air. The sample was investigated using a Kratos Kompact MALDI IV instrument. The method of ionisation was laser desorption.

Figure 4.7 shows the laser desorption/ionisation time-of-flight mass spectrum obtained for the mixture of $Tb@C_{82}$ and $Tb@C_{80}$. Coalescence products were readily generated by the laser desorption/ionisation of the sample. Large carbon clusters were observed, that either contained or did not contain the metal adduct. The most intense peaks in the mass spectrum corresponded to pure C_n^+ clusters, containing even numbers of carbon atoms. A less intense series of peaks corresponded to endohedral $Tb@C_n^+$ clusters.

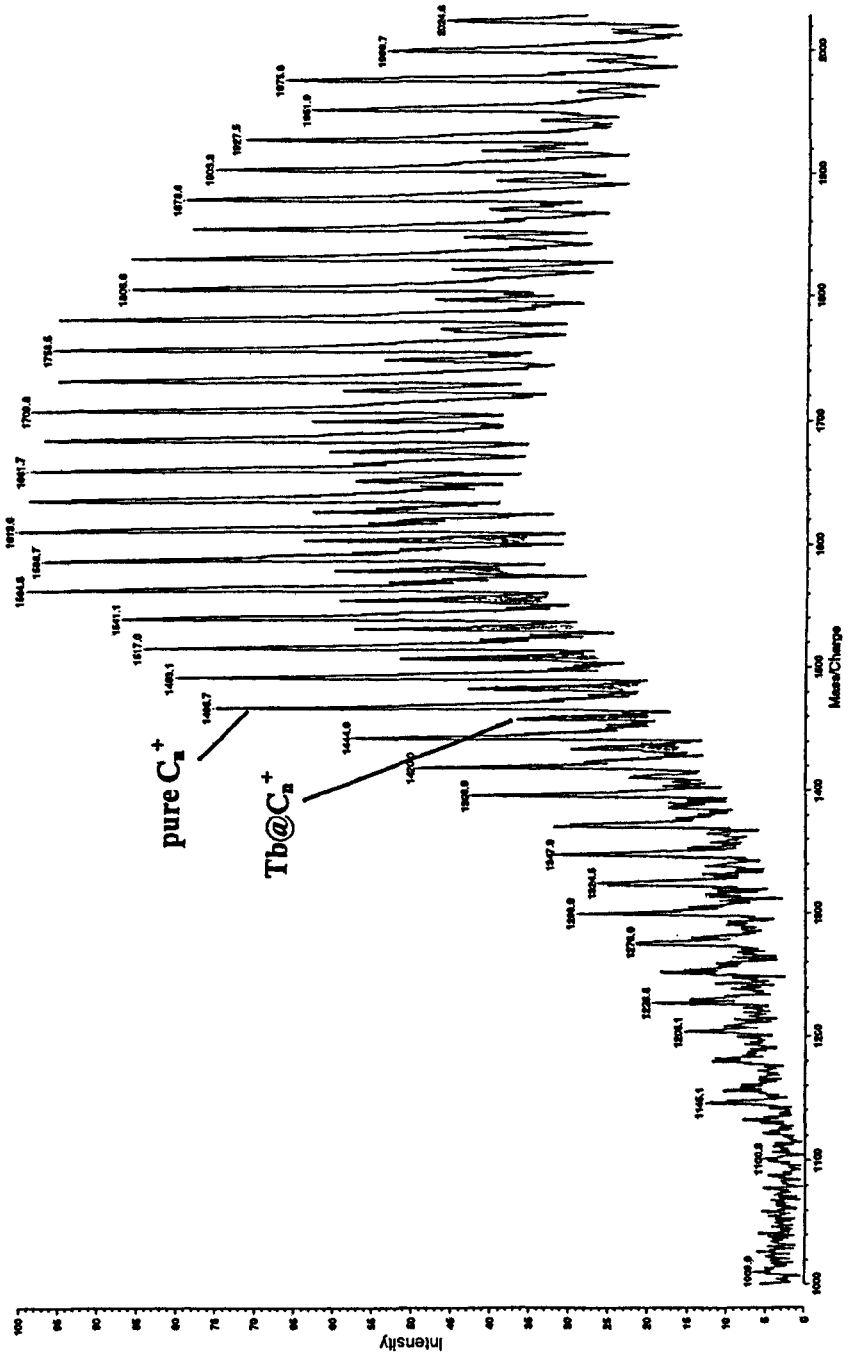

Figure 4.7 - Positive ion time-of-flight mass spectrum of a $Tb@C_{82}/Tb@C_{80}$ mixture. The ionisation technique was laser desorption. Obtained using a Kratos Kompact MALDI IV instrument in reflectron mode.

This laser desorption experiment was repeated using the MAG-TOF instrument, and the ions observed at the parallel time-of-flight detector (TOF-1). One of the pure C_n^+ clusters, C_{130}^+ (m/z 1560), was selected for collision-induced dissociation by adjusting the magnetic-field strength of the double-focusing mass spectrometer (MS-1). Collision-induced dissociation was performed on the selected ion by introducing an inert gas into the collision chamber.

The high-energy collision-induced dissociation spectrum of C_{130}^+ using helium as the collision gas is shown in figure 4.8. The centre-of-mass collision energy was in the range 20-31 eV.

Coalescence of fullerenes by laser desorption was at the limit of the laser power for the MAG-TOF instrument. This meant that the observed coalescence products were always very weak peaks.

From figure 4.8, it can be seen that the intensities of the fragment ions for the helium collision-induced dissociation of C_{130}^+ were not intense (due to the low intensity of the parent ion). As for the CID of C_{60}^+ and C_{70}^+, the high m/z region of the spectrum showed peaks corresponding to C_{2n} loss. The significance of this is that these species would be much more likely to arise from a "giant" fullerene type of structure. Futhermore, coalescence products consisting of smaller fullerenes "stuck" together would be extremely likely to show intense C_{60}^+ and C_{70}^+ peaks in the CID spectra as there is essentially a 'memory' of the precursor structures. No intense peaks were observed for C_{60}^+, C_{70}^+ or C_{84}^+ in the CID spectra.

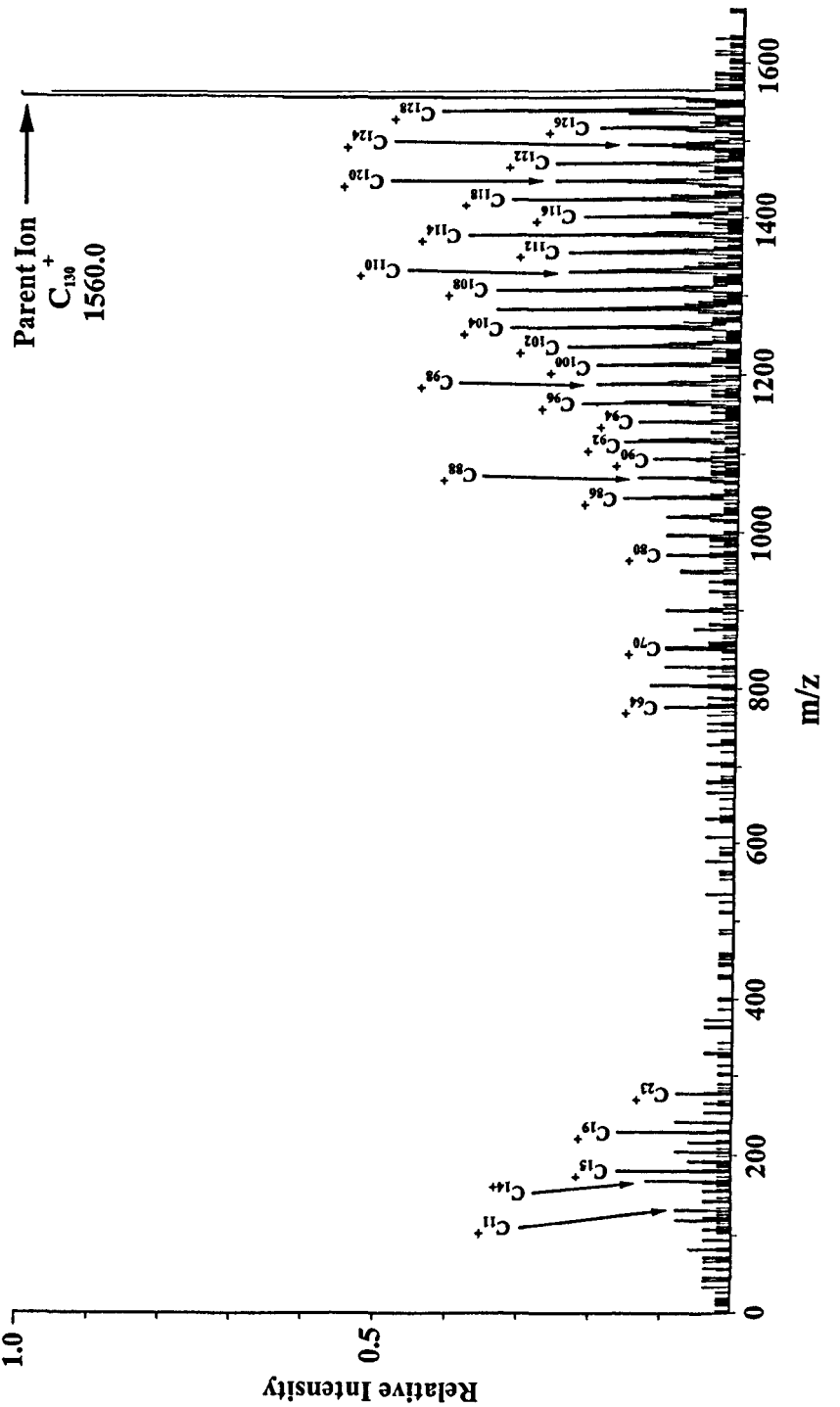

Figure 4.8 - High-energy collision-induced dissociation spectrum of C_{130}^+, generated by laser desorption from a $Tb@C_{82}/Tb@C_{80}$ precursor, and using helium as the collision gas.

4.6 High-Energy Collision-induced Dissociation of $C_{60}H_x^+$ generated by Laser Desorption/Ionisation.

A sample[107] of pure $C_{60}H_{36}$ was investigated by laser desorption, using a Kratos Kompact MALDI IV instrument.[108] The spectra obtained by laser desorption showed a series of $C_{60}H_x^+$ peaks. By using the MAG-TOF instrument, it has been possible to perform collision-induced dissociation on several of the exohedral fullerene species produced by this method.

$C_{60}H_{30}^+$ was selected by adjusting the magnetic-field strength in MS-1. The resolution of the double-focusing mass spectrometer was sufficient to ensure that only the monoisotopic (^{12}C only) isotope passed through the exit-slit of MS-1. Collision-induced dissociation was performed on the selected ion by xenon gas into the collision chamber.

The high-energy collision-induced dissociation spectra of $C_{60}H_{30}^+$ are shown in figure 4.9-4.12. The laboratory-frame collision energy was in the range 8-12 keV, due to the energy spread imposed by the ion buncher, corresponding to a centre-of-mass collision energy range of 1190-1784 eV.

The high-energy collision-induced dissociation of $C_{60}H_{30}^+$ did not show the characteristic C_{2n} loss exhibited for pure carbon fullerenes. The loss of H_m (where m=1-14) from $C_{60}H_{30}^+$ was observed. For this process there seemed to be an odd/even effect with respect to the intensities of the fragments observed. The loss of an even number of hydrogen atoms produced more intense peaks than did the loss of an odd number of hydrogen atoms (see figure 4.12).

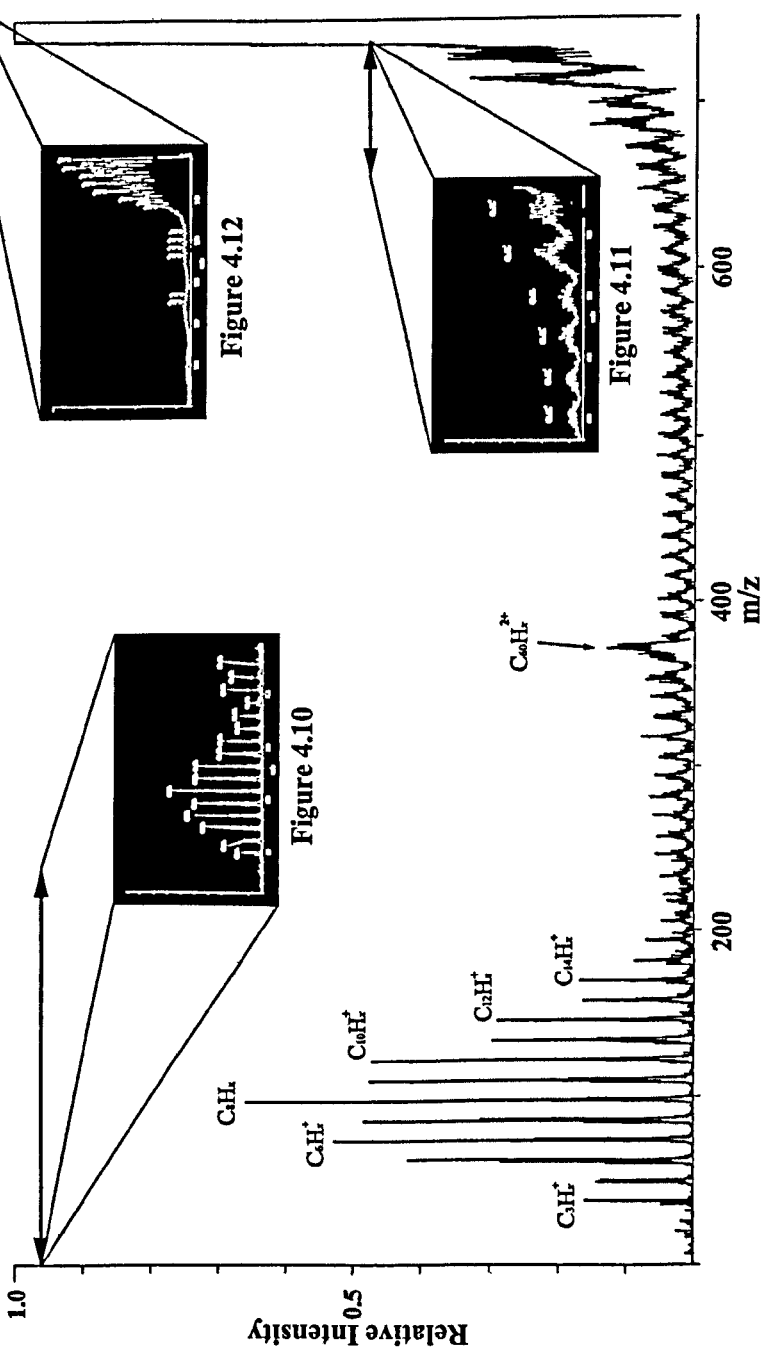

Figure 4.9 – High-energy collision-induced dissociation of $C_{60}H_{30}^+$ generated by laser desorption and using xenon collision gas. Full m/z range.

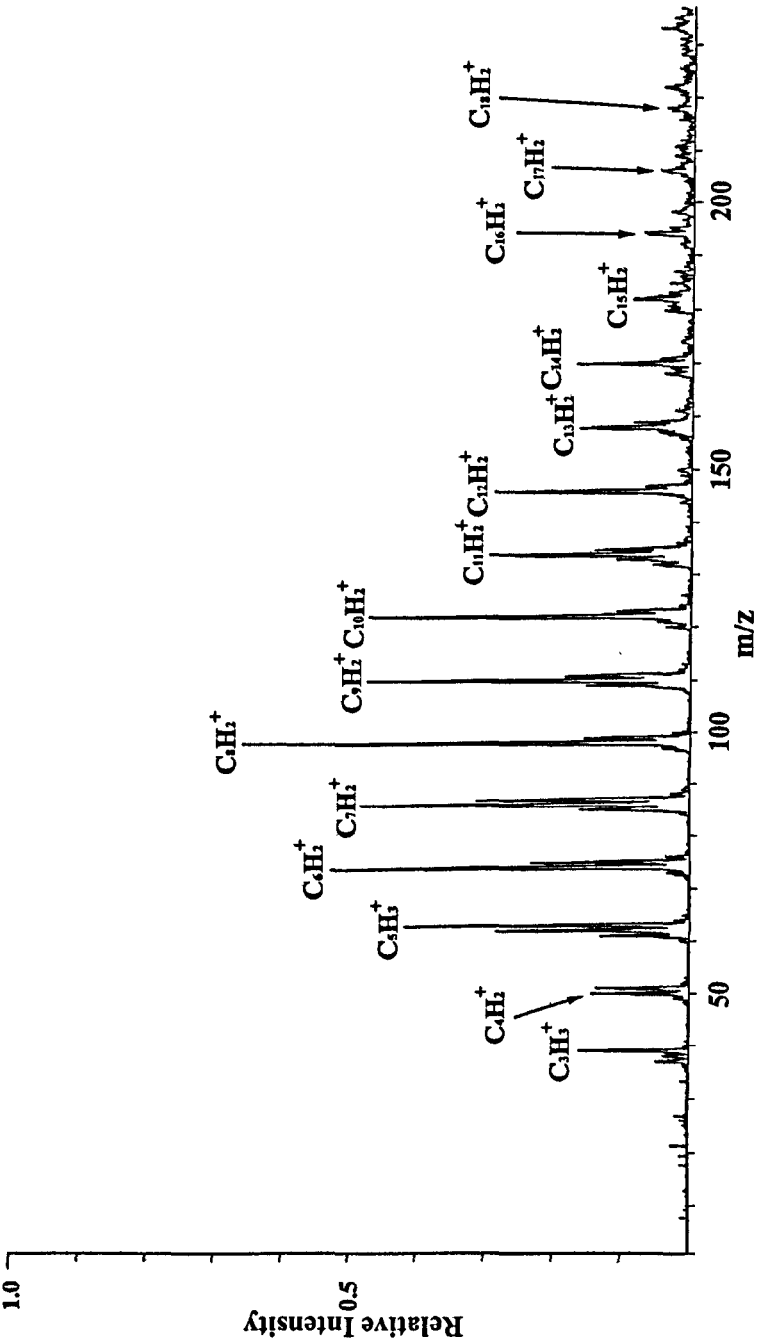

Figure 4.10 – High-energy collision-induced dissociation of $C_{60}H_{30}^+$ generated by laser desorption and using xenon collision gas. m/z range 1-250.

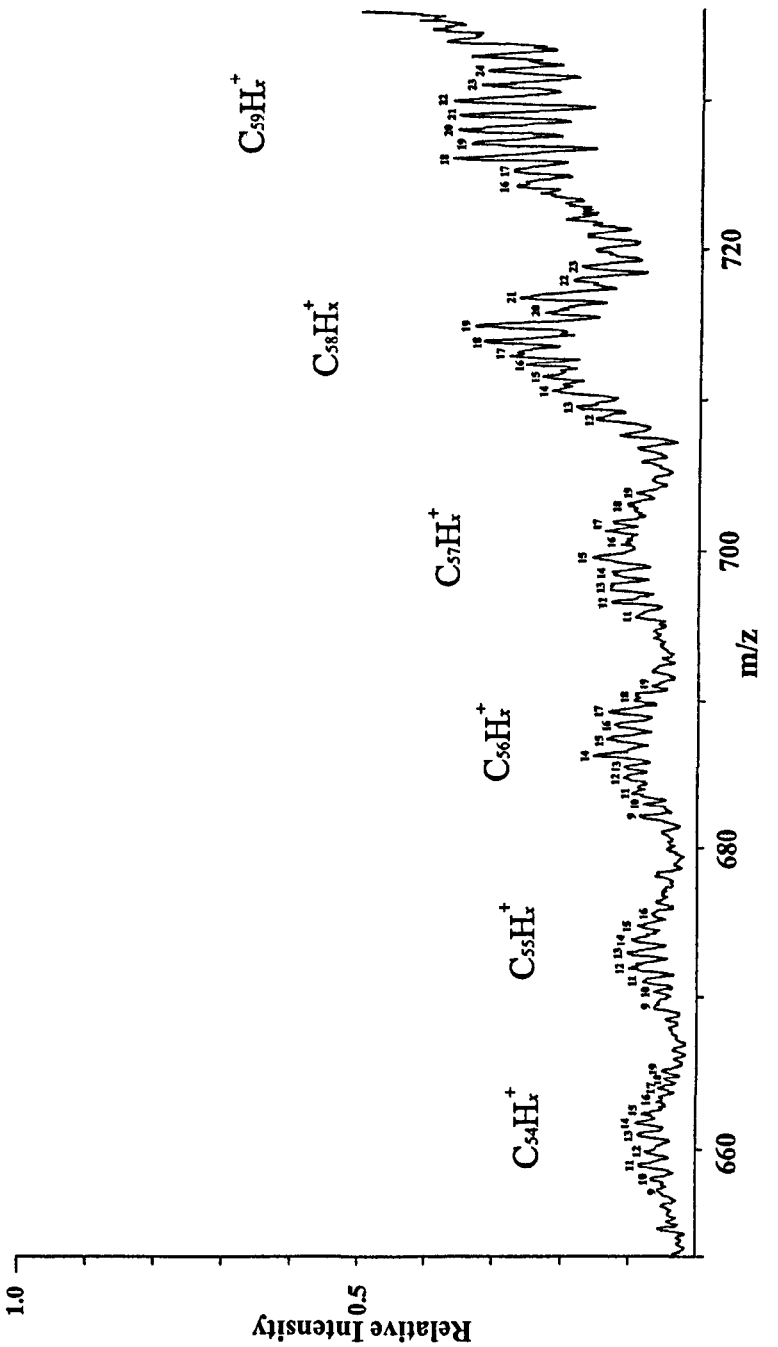

Figure 4.11 – High-energy collision-induced dissociation of $C_{60}H_{30}^+$ generated by laser desorption and using xenon collision gas. m/z range 650-730.

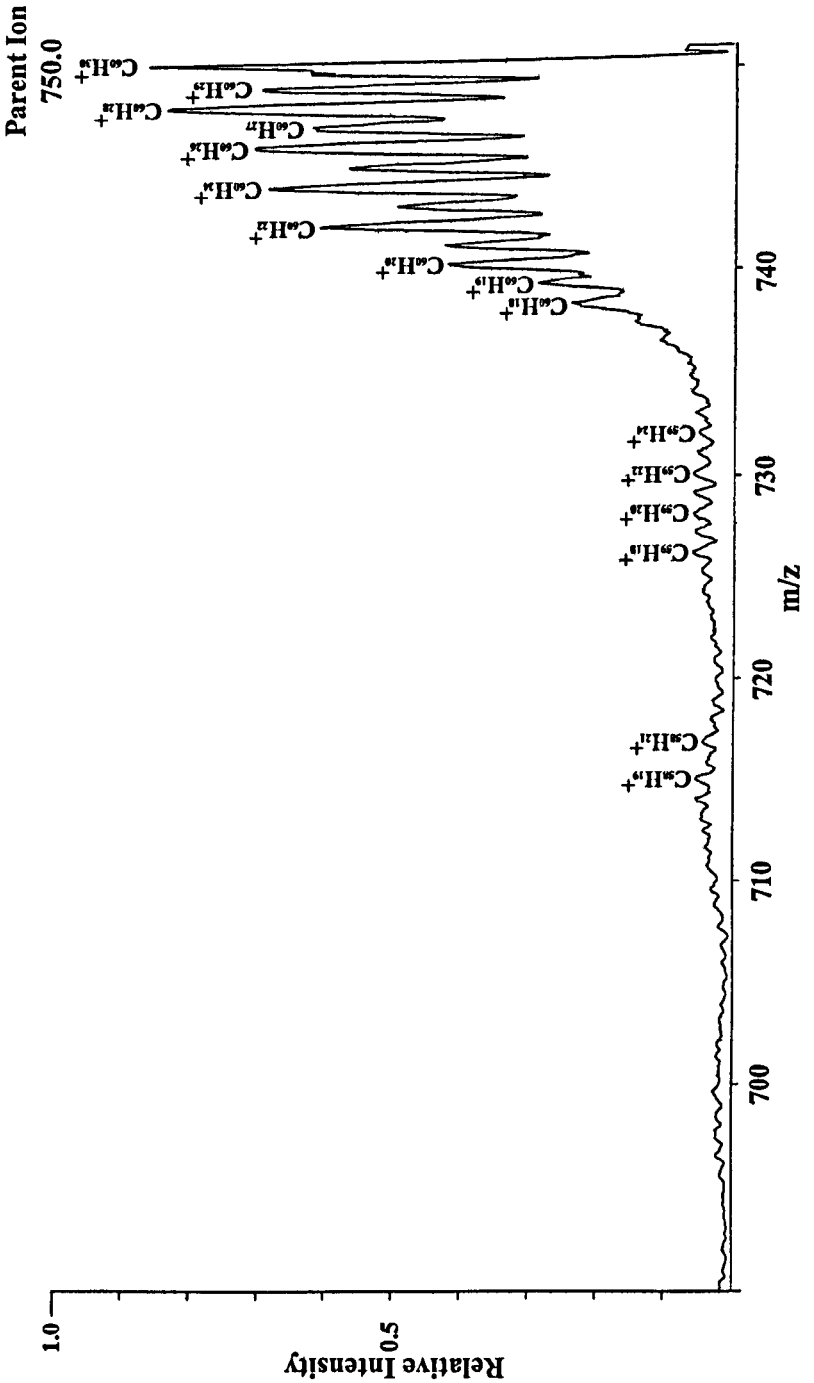

Figure 4.12 – High-energy collision-induced dissociation of $C_{60}H_{30}^+$ generated by laser desorption and using xenon collision gas. m/z range 690-750.

In addition to H_m loss from $C_{60}H_{30}^+$, the loss of C_nH_m species were observed. These were observed for both odd and even numbers of carbon atoms for n=1-57. There were no clear intensity differences for a given carbon-atom loss n, between the odd and even numbers, m, of hydrogen atoms lost.

In the low m/z region of the spectra (m/z 1-200), only fragment ions corresponding to $C_nH_1^+$, $C_nH_2^+$ and $C_nH_3^+$ were observed, of which $C_nH_2^+$ was the most common and the most intense. The intensities of these species bear no resemblance to the intensities observed for the low m/z species resulting from the CID of C_{60}^+ and C_{70}^+, suggesting that the structures are very different. It is possible the low m/z species resulting from the CID of $C_{60}H_{30}^+$ are predominantly long chains of carbon atoms with a hydrogen atom at either end.

Similar spectra were observed for the high-energy collision-induced dissociation of $C_{60}H_{25}^+$ (figure 4.13) and $C_{60}H_{35}^+$.(figure 4.14).

Figure 4.13 – High-energy collision-induced dissociation of $C_{60}H_{25}^+$ generated by laser desorption and using xenon collision gas. Full m/z range.

Figure 4.14 – High-energy collision-induced dissociation of $C_{60}H_{35}^+$ generated by laser desorption and using xenon collision gas. Full m/z range.

Chapter Five: *Collision-induced Dissociation of Alkali-metal Cationised Polyglycols*

5.1 Introduction

Mass spectrometry of synthetic polymers is providing unprecedentedly high–quality information to the synthetic polymer chemist. Matrix-assisted laser desorption/ionisation (MALDI) has been shown to be an especially useful tool for the direct analysis of synthetic polymers.[109, 110, 111, 112, 113, 114, 115, 116] The results obtained for polymers from MALDI mass spectrometry experiments typically give qualitative molecular-weight information, but normally not structural information. Nevertheless MALDI has been utilised to gain information on monomer reactivity ratios,[117] end groups [118, 119, 120, 121] and mechanisms of polymerisation.[122, 123, 124] Many attempts, with a variety of success, have also been made to use MALDI–time–of–flight (TOF) mass spectrometry to obtain values for molecular mass averages, Mn and Mw, especially in combination with size exclusion chromatography.[125, 126, 127, 128]

Techniques of polymer synthesis are becoming increasingly sophisticated with a move towards the attempt to design macromolecules for specific applications. This has usually been centred around living, or *pseudo*-living, polymerisation which allows the incorporation of different functionality at precise positions by judicious choice of reaction conditions.[129, 130, 131, 132, 133, 134, 135] For example, α and β terminally functional polymers may have very different properties in certain applications. Thus it is important for techniques to be developed which can confirm, or refute,

synthetically targeted macromolecular structures. In addition to empirical molecular-mass data, it is important to be able to determine information regarding the end-groups of and the sequence of monomers/groups within a synthetic macromolecule. Tandem mass spectrometry can in principle provide such structural information for a synthetic polymer. Tandem mass spectrometry has been widely used in the biological area, combined with ionization techniques such fast atom bombardment,[136, 137] liquid secondary ion mass spectrometry (LSIMS)[138, 139] and electrospray ionization.[140, 141] Early investigations with field desorption established how tandem mass spectrometry could be used to investigate the structures of synthetic polymers.[142, 143]

Polyglycols represent a commercially important class of synthetic polymer. Their analysis by tandem mass spectrometry has experienced a growth after desorption/ionisation techniques allowed the ionisation of these materials. The original approach was to convert the polyglycol sample to gaseous molecular adduct-ions $[M+X]^+$, where X is a proton or alkali metal ion, by utilising field desorption[144, 145] or fast-atom bombardment[144] ion sources.

Collision-induced dissociation (CID) of small polyglycol oligomers (no. of repeat units <10), generated by fast-atom bombardment, at laboratory-frame collision energies of 8 keV was reported by Lattimer and co-workers.[150] CID of poly(ethylene glycol) ions generated by matrix-assisted laser desorption/ionisation has been reported by Jackson and co-workers, utilising laboratory-frame collision energies of 800 eV.[145]

This chapter describes the study of high-energy collision-induced dissociation of polyglycol ions generated by matrix-assisted laser desorption/ionisation.

5.2 Experimental Conditions

Cationised molecules were produced using a MALDI ion source and accelerated to 8 keV at the ion source. Particular ions were selected for fragmentation by adjusting the magnetic field strength and exit slit. An additional translational energy spread of up to 4 keV was imposed upon the ion packet before collision by the ion buncher. The pressure of the collision gas, usually helium, argon or xenon, was set to give 30% attenuation (i.e. 70% transmission) of the selected ion.

α–cyano–4–hydroxycinnamic acid (Sigma–Aldrich, Poole, Dorset, U.K.) was the matrix used for all of the MALDI experiments. A matrix solution 0.1M in 30:70 water/ methanol (analytical grade Fisher Scientific, Loughborough, U.K.) was used throughout the experiments. A 0.5 μl aliquot of the matrix solution was deposited on the probe tip and was dried using a stream of air. The cation in the form of a salt solution (100μl, 0.1M) was added to 1ml of the analyte, $3x10^{-3}$ M in 30:70 water/ acetone (analytical grade Fisons Scientific, Loughborough, U.K.). A 0.5 μl aliquot of the cation–analyte solution was deposited on top of the matrix layer and dried using a stream of air.

A series of poly(ethylene glycol) standards (Polymer Laboratories, Shropshire, U.K.) were obtained for the high-energy collision-induced dissociation of poly(ethylene glycol). Poly(propylene glycol) (Sigma–Aldrich, Poole, Dorset, U.K.) and poly(ethylene glycol)-*co*-poly(propylene glycol) monobutyl ether (Sigma–Aldrich, Poole, Dorset, U.K.) were utilised for collision-induced dissociation of the respective samples.

5.3 High-Energy Collision-induced Dissociation of Poly(ethylene glycol) ions generated by Matrix-assisted Laser Desorption/ionisation

$[M+Na]^+$ adduct ions of poly(ethylene glycol) were selected by adjusting the magnetic field strength in MS-1.The resolution of the double-focusing mass spectrometer was sufficient to ensure that only the monoisotopic (^{12}C only) isotope passed through the exit-slit of MS-1. Collision-induced dissociation was performed on the selected ion by introducing an inert gas into the collision chamber. The fragments from these collisions were observed at a planar array detector located after MS-2.

The high-energy collision-induced dissociation spectra of the $[M+Na]^+$ n=24 (where n is the number of repeat units) oligomer of poly(ethylene glycol), m/z = 1097.6, using helium and xenon as the collision gases are shown in figures 5.1-5.4.

The spectra obtained using helium and xenon as the collision gases were similar to each other, although not identical. The centre-of-mass collision energy was approximately 30 times higher with xenon (figures 5.3 and 5.4) as compared to helium (figures 5.1 and 5.2); the interaction times were approximately the same for both. An increase in the intensity of the low m/z fragment ions (and a decrease in intensity of the higher m/z fragment ions) was observed in the xenon spectra compared with those obtained using helium.

It is apparent from figures 5.1-5.4 that many of the fragment ions constitute series of peaks. These peaks correspond to the same bond dissociations, but at different positions along the polymer ion. A detailed analysis of the xenon CID spectrum (figures 5.3 and 5.4) is given in table 5.1. Five fragment-ion series have been identified, corresponding to (44.03m+22.99+31.02), (44.03m+22.99+45.03),

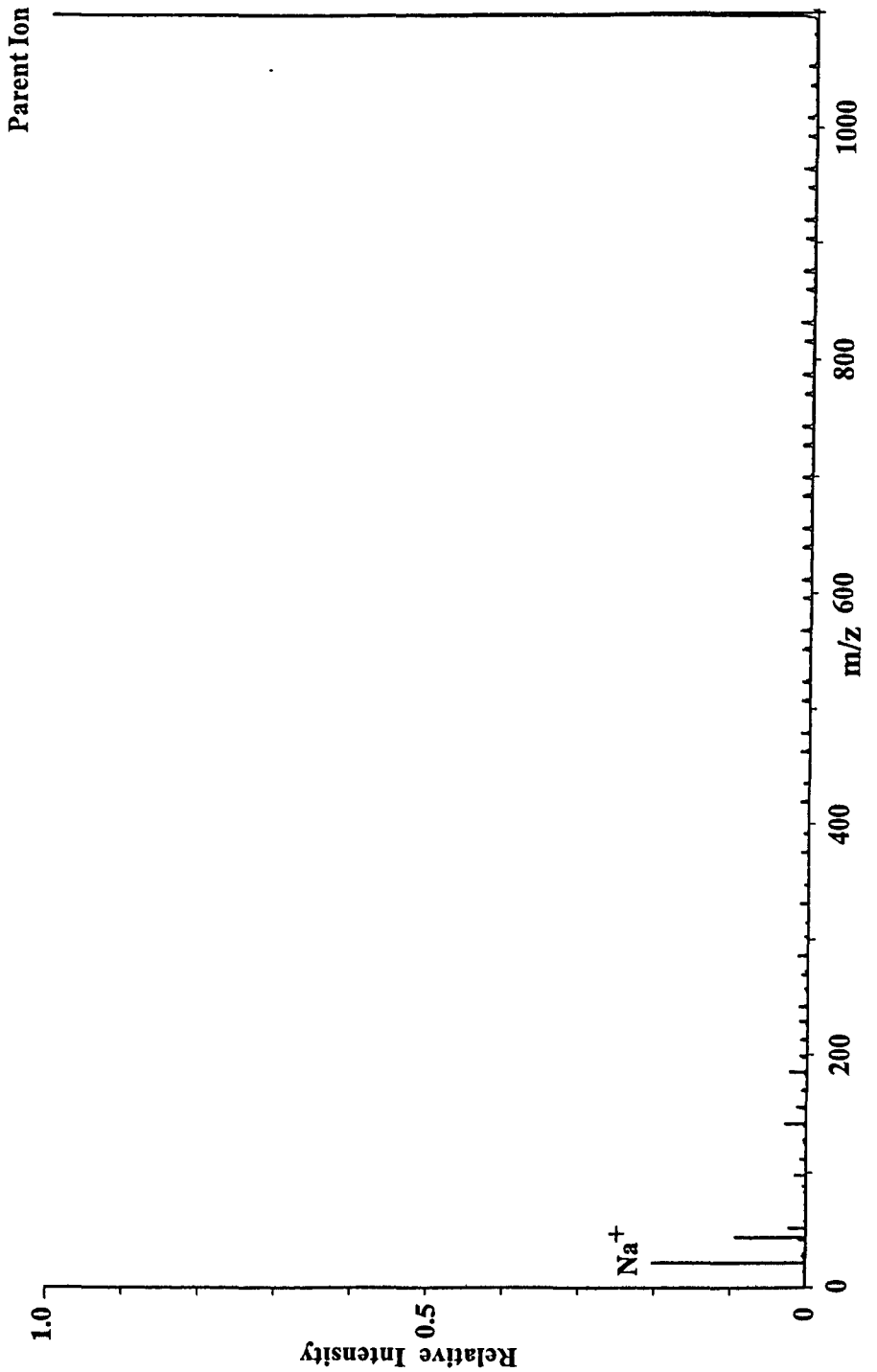

Figure 5.1 - Collision-induced dissociation spectrum of m/z 1097.6 $[M+Na]^+$ produced by MALDI. Helium collision gas. Scaled to show 100% of the parent ion.

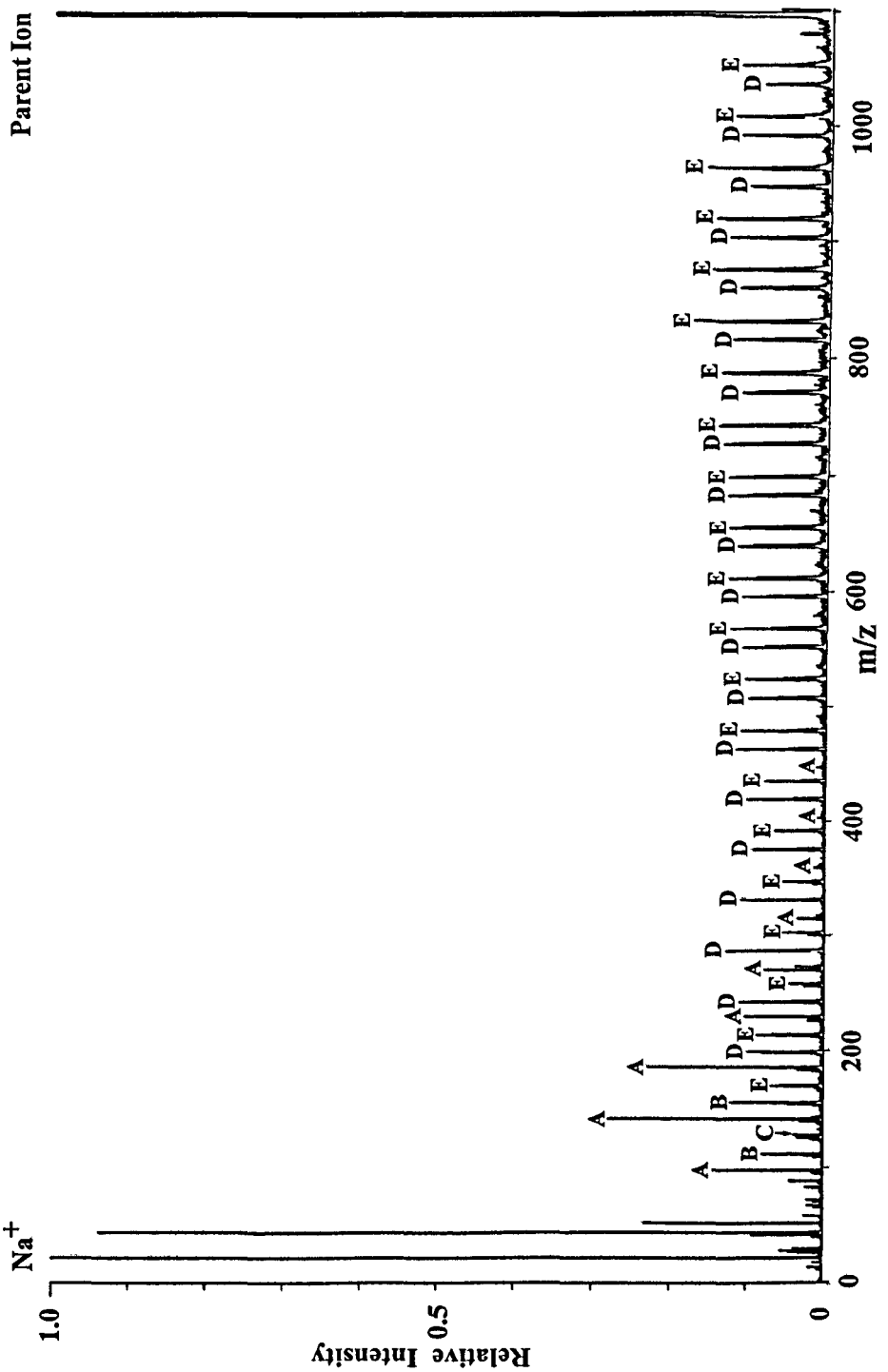

Figure 5.2 - Collision-induced dissociation spectrum of m/z 1097.6 $[M+Na]^+$ produced by MALDI. Helium collision gas. Scaled to 10% of the parent ion intensity.

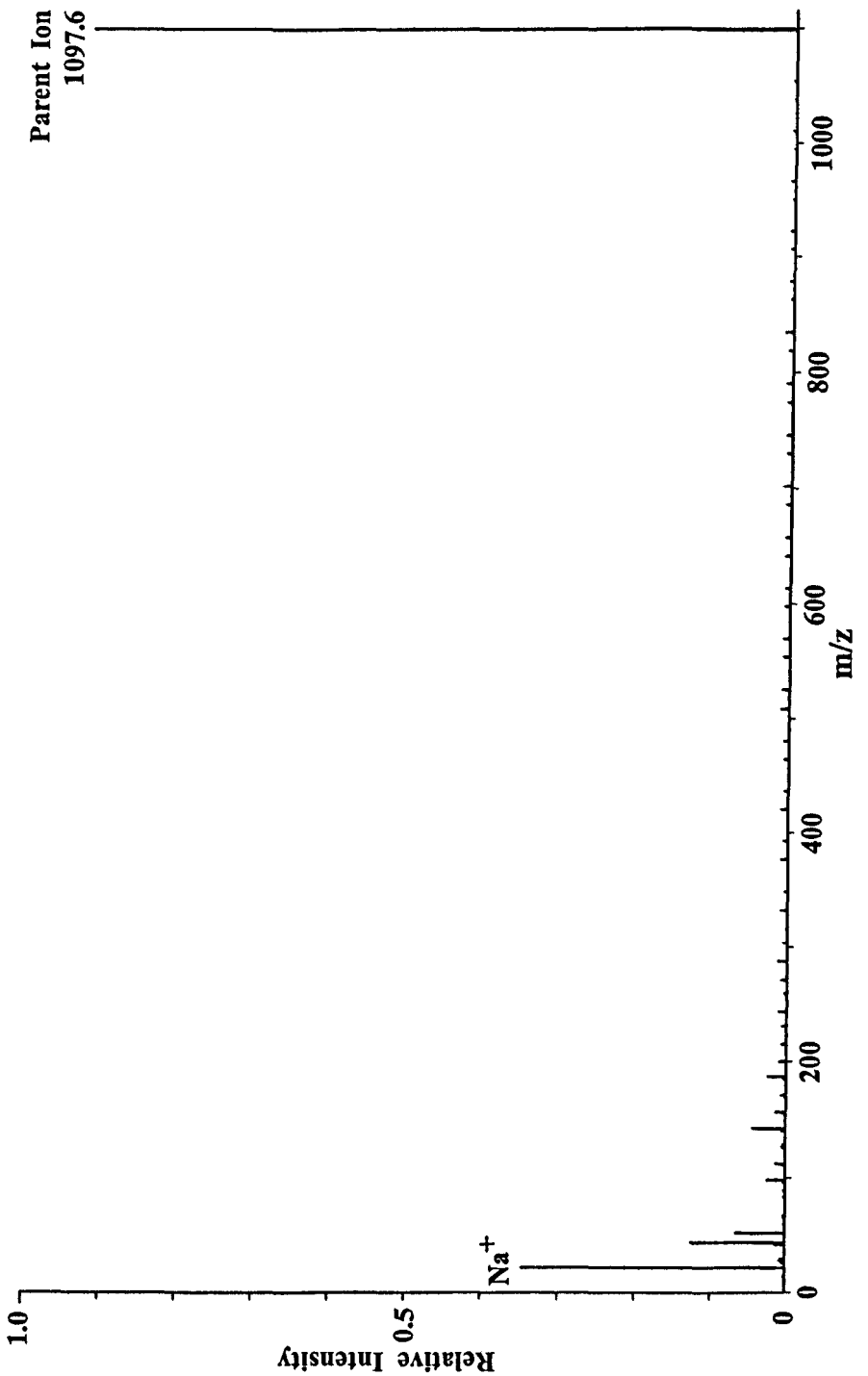

Figure 5.3 - Collision-induced dissociation spectrum of m/z 1097.6 $[M+Na]^+$ produced by MALDI. Xenon collision gas. Scaled to show 100% of the parent ion.

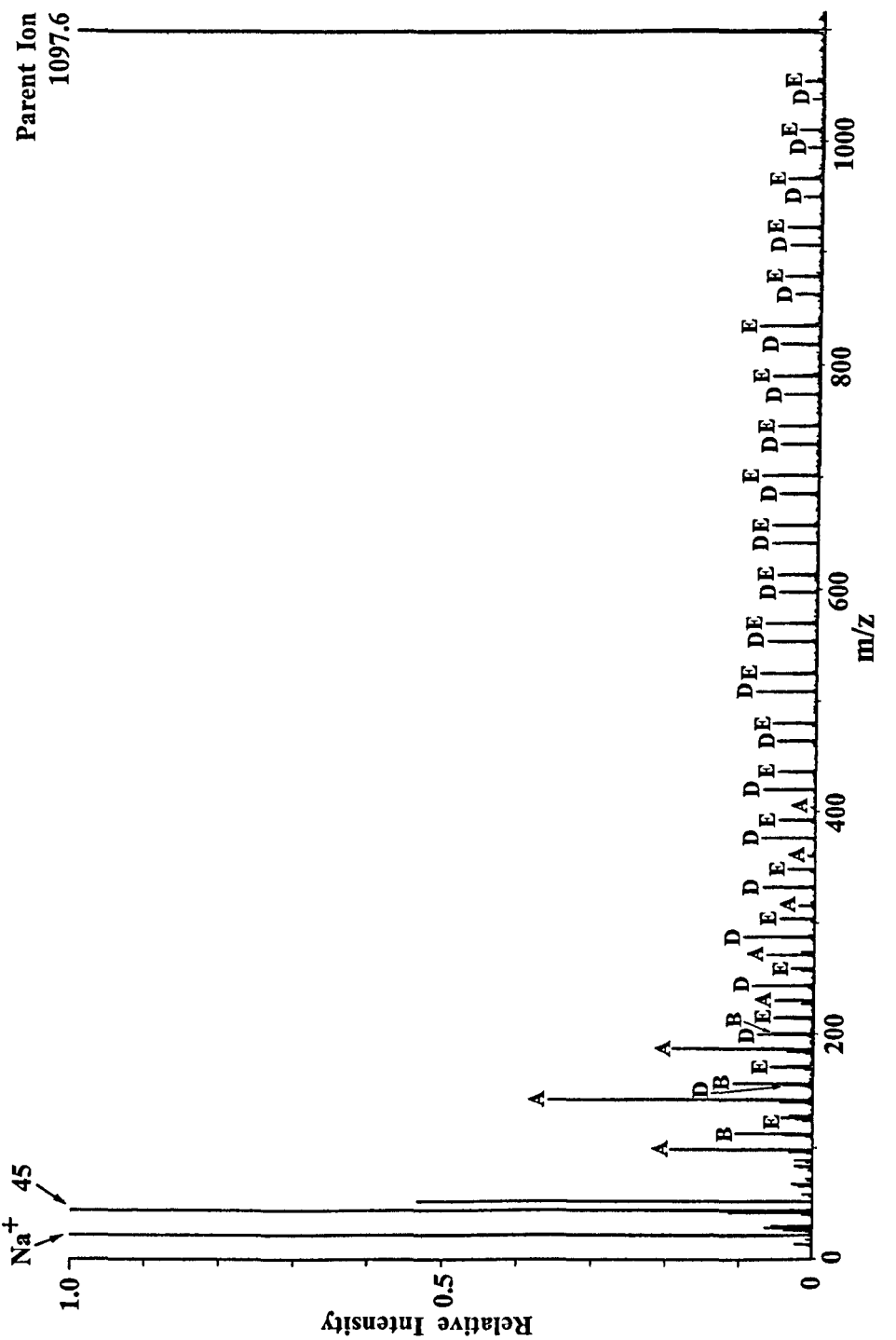

Figure 5.4 - Collision-induced dissociation spectrum of m/z 1097.6 $[M+Na]^+$ produced by MALDI. Xenon collision gas. Scaled to 12.5% of the parent ion intensity.

Table 5.1 - Analysis of the xenon CID spectrum of the poly(ethylene glycol) $[M+Na]^+$ adduct ion m/z 1097.6 (n=31).

m/z_{obs}	Intensity†	Assignment‡	m/z_{calc}	$m/z_{obs} - m/z_{calc}$
1097.6	100.00	Parent	1097.60	0.00
1051.4	0.40	E	1051.59	-0.19
1035.3	0.22	D	1035.59	-0.29
1007.5	0.47	E	1007.56	-0.06
991.5	0.32	D	991.56	-0.06
963.6	0.66	E	963.53	0.07
947.7	0.34	D	947.54	0.16
919.7	0.69	E	919.51	0.19
903.5	0.60	D	903.51	-0.01
875.5	0.71	E	875.48	0.02
859.7	0.52	D	859.48	0.22
831.8	1.17	E	831.45	0.35
815.7	0.77	D	815.46	0.24
787.6	0.89	E	787.42	0.18
771.5	0.69	D	771.43	0.07
743.6	0.78	E	743.40	0.20
727.6	0.73	D	727.41	0.19
699.6	1.05	E	699.38	0.22
683.7	0.74	D	683.38	0.32
655.6	0.87	E	655.35	0.25
639.6	0.87	D	639.36	0.24
611.4	0.78	E	611.32	0.08
595.3	0.73	D	595.33	-0.03
567.3	0.97	E	567.30	0.00
551.4	0.92	D	551.30	0.10
523.4	1.10	E	523.27	0.13
507.4	1.16	D	507.28	0.12
479.3	0.84	E	479.25	0.05
463.3	0.73	D	463.25	0.05
435.4	0.71	E	435.22	0.18
419.4	0.98	D	419.22	0.18
391.3	0.70	E	391.19	0.11
375.4	0.99	D	375.20	0.20
359.4	0.17			
347.3	0.52	E	347.17	0.13
331.3	0.96	D	331.17	0.13
315.3	0.30			
303.2	0.67	E	303.14	0.06
287.2	1.35	D	287.15	0.05
274.1	0.25	A	274.14	-0.04
271.2	0.91			
259.1	0.43	E	259.12	-0.02
258.2	0.16			
257.2	0.26			
243.2	1.17	D	243.12	0.08
230.2	0.73	A	230.11	0.09

227.1	0.25			
215.1	0.70	E	215.09	0.01
214.2	0.73			
200.2	0.76	B	200.10	0.10
199.1	1.08	D	199.09	0.01
186.1	2.59	A	186.09	0.01
184.1	0.51			
171.1	0.49	E	171.06	0.04
170.2	0.82			
156.1	1.48	B	156.08	0.02
155.1	0.55	D	155.07	0.03
142.1	4.70	A	142.06	0.04
140.1	0.63			
128.1	0.43	C	128.04	0.06
127.2	0.22	E	127.04	0.16
126.2	0.62			
125.2	0.35			
124.1	0.22			
112.2	1.49	B	112.05	0.15
111.2	0.53	D	111.04	0.16
110.2	0.16			
98.2	2.68	A	98.03	0.17
96.1	0.46			
89.2	0.35			
87.1	0.17			
84.2	0.34	C	84.01	0.19
83.2	0.26	E	83.01	0.19
73.2	0.16	$C_3H_5O_2^+$		
68.2	0.38	B	68.02	0.18
66.2	0.29	Na+43		
59.2	0.19	$C_2H_3O_2^+$		
53.2	7.25	$NaCH_2O$		
45.2	13.50	$C_2H_5O^+$		
44.2	0.24	$C_2H_4O^+$		
43.2	1.58	$C_2H_3O^+$		
41.2	0.20	C_2HO^+		
31.1	0.79	CH_3O^+		
29.1	0.80	$C_2H_5^+$ / CHO^+		
28.1	0.42	$C_2H_4^+$		
27.1	0.53	$C_2H_3^+$		
23.0	39.00	Na^+		
15.0	0.33	CH_3^+		

† Intensity of peak heights. The parent ion intensity corresponds to 100%. The fragment ion intensities are given as percentages of the parent ion intensity. Only fragment ions with intensities greater than a threshold value of 0.15% are displayed.

‡ The assignments A, B, C, D and E correspond to repeating series of fragments. These are illustrated in reactions 5.1 and 5.2

Reaction 5.1 [A] - proposed by Craig.

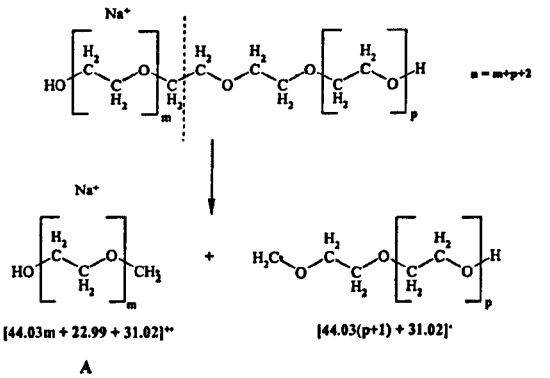

A

Reaction 5.1 [B] - proposed by Craig.

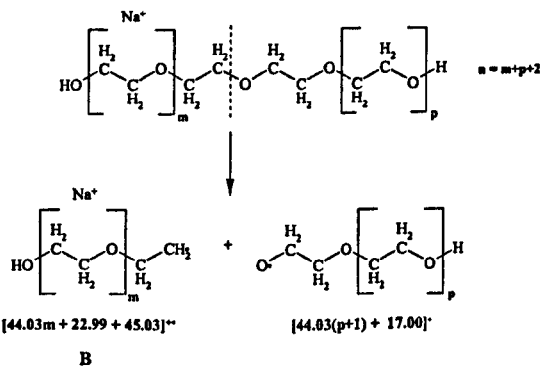

B

Reaction 5.1 [C] - proposed by Craig.

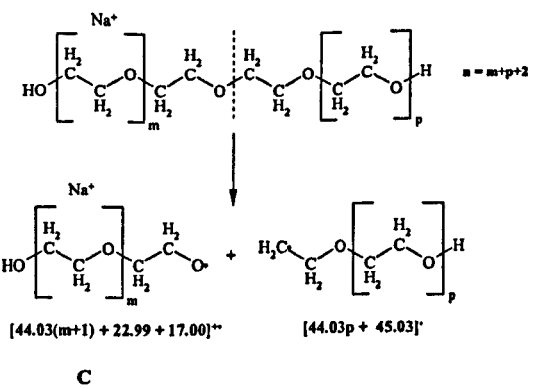

C

Reaction 5.1 [D] - proposed by Agma.

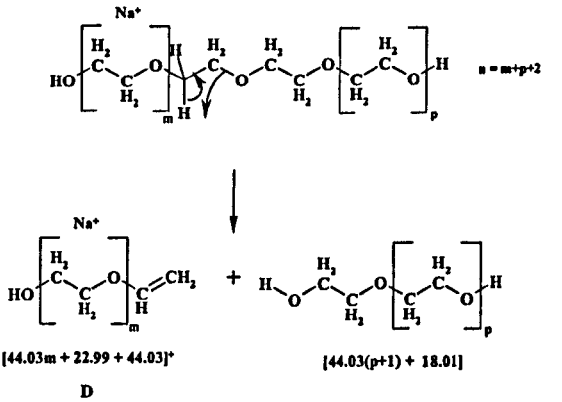

D

Reaction 5.1 [E] - proposed by Agma.

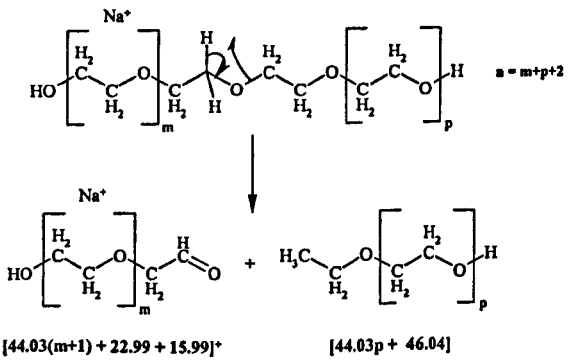

E

(44.03m+22.99+17.00), (44.03m+22.99+44.03), (44.03m+22.99+15.99), and have been labelled **A-E** respectively in table 5.1.

Several mechanisms have previously been proposed to give rise to fragment ion series **A-E**. Craig proposed that direct chain scission of a C-C or C-O bond in the polymer backbone were the major fragmentation pathways, for dissociation of cationised poly(propylene glycol) ions generated by field desorption.[146] Fragment ion series **A, B** and **C** would be satisfactorily explained by these mechanisms. The formation of fragment ion series **A-C** by direct chain scission mechanisms are shown in reactions 5.1[A]-5.1[C]. Direct chain scission of the C-C and C-O bonds in the polymer backbone cannot, however, explain fragment ion series **D** and **E**.

Rearrangement reactions were proposed by Agma in order to explain fragment ion series **D** and **E**.[147] The mechanisms proposed by Agma are shown in reactions 5.1[D] and 5.1[E]. A major concern about the validity of these mechanisms arises as only fragment ion series arising from one end of the ion were observed in the spectra generated by Agma. For example from reaction 5.1[D], a fragment ion corresponding to $[44.03m+22.99+44.03]^+$ was observed, whereas its counterpart $[44.03+22.99+18.01]^+$ (the ion analogue of the neutral shown in reaction 5.1[D]) was *not* observed in the CID spectra. The absence of these peaks has been confirmed from the results shown in figures 5.1-5.4. To overcome this problem Agma proposed that the cation (in this case Na^+) was located at the site of every rearrangement reaction, and dictated which fragment ion series would result.

A concerted mechanism was proposed by Selby and co-workers, from investigation of low molecular weight (<500) cationised polyglycol ions obtained by fast atom bombardment at slightly lower laboratory-frame collision energies,[148] presumably to account for fragment ion series **D** and **E** being observed in the CID spectra, and their

counterparts, $[44.03+22.99+18.01]^+$ and $[44.03+22.99+46.04]^+$ as described by Agma, *not* being observed. This type of concerted rearrangement mechanism would seem unlikely from the standpoint of what is nowadays accepted about concerted mechanisms in organic chemistry.[149, 150, 151, 152]

It is proposed here that homolytic cleavage was not limited to the C-C (ΔH^0=348kJ.mol^{-1}) and C-O (ΔH^0=360kJ.mol^{-1}) bonds in the polymer backbone, but that there was sufficient energy for cleavage of C-H bonds (ΔH^0=412kJ.mol^{-1}). Reactions 5.2[A] and 5.2[B] are proposed as mechanisms for the formation of fragment ion series **D** and **E**. These proposed mechanisms involve homolytic cleavage of a C-H bond and loss of a H$^{\bullet}$ radical as an initial (rate determining) step, that can occur at different positions along the alkyl chain. Subsequent rearrangement results in scission at one of two possible positions, β to the site of the radical, giving rise to either an ion and a neutral radical (from positions ***1*** and ***3*** indicated in reactions 5.2[A] and 5.2[B]) or a radical ion and a neutral (from positions ***2*** and ***4*** indicated in reactions 5.2[A] and 5.2[B]). The significant advantage of this multi-step radical mechanism is that the cation is not required to be at the site where dissociation takes place for formation of fragment ion series **D** and **E**, and may actually be remote from the site of fragmentation.

This type of multi-step radical mechanism does not only account for fragment ion series **D** and **E**, but also for fragment ion series **A**, **B** and **C** (in addition to direct homolytic cleavage of the polymer backbone). From the CID spectra fragment ion series **A**, **B** and **C** were observed to be intense only at low m/z (<250). This can be

Reaction 5.2[A]

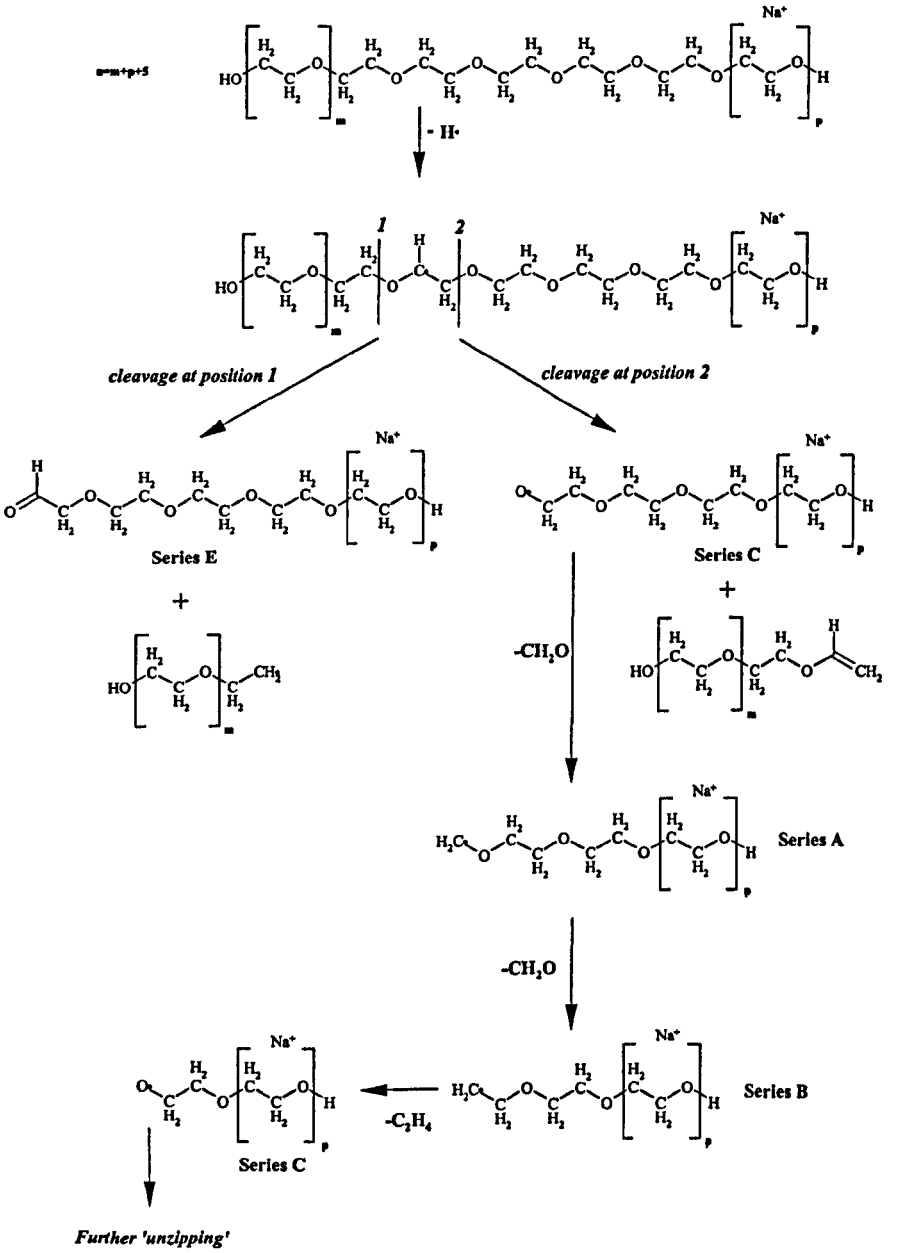

Reaction 5.2[B]

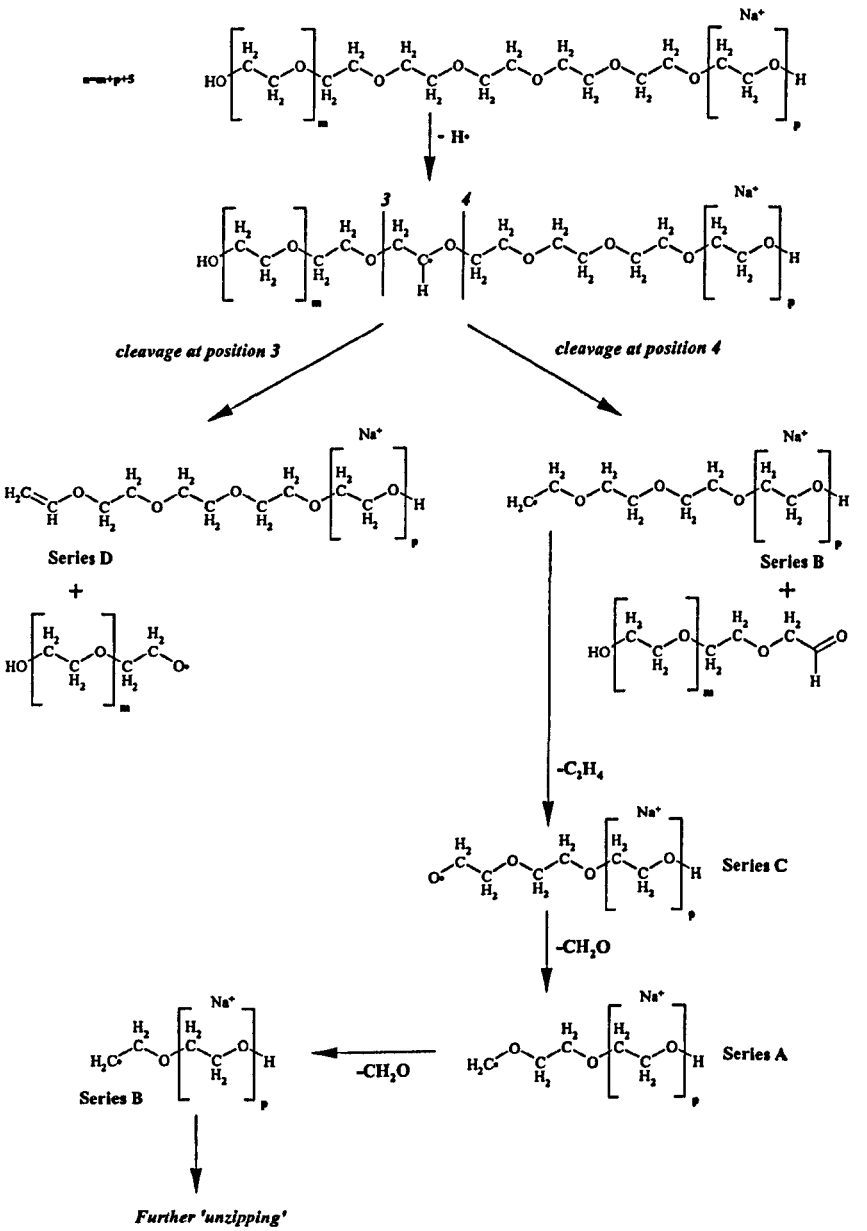

explained by *unzipping* of the larger members of these ion series by a radical backbiting mechanism, illustrated in reactions 5.2[A] and 5.2[B].

Similar multi-step have been proposed for the collision-induced dissociation of saturated and unsaturated fatty acids.[153, 154] The location of the cation is well understood for fatty-acids, and these type of fragmentation are described as being'charge-remote'. Evidence supporting the elimination of an $H^{\bullet}$ radical as a rate-determining step, for fatty acids, was indicated by the existence of a ^{2}H kinetic isotope effect for the formation of particular ions.[164]

A comparison of the collision-induced dissociation spectra of the poly(ethylene glycol) $[M+Na]^{+}$ adduct ions m/z 1009.6 (n=22), m/z 1097.6 (n=24) and 1405.8 (n=31) generated by MALDI and using helium as the collision gas is shown in figure 6.5. It can be seen that the intensity of the fragment ions decreases at higher m/z, due to the greater number of fragmentation pathways available, and hence greater number of different fragment ions observed. In all cases fragment ion series **D** and **E** were the most intense fragment ion series above m/z ~ 200.

The addition of a lithium halide salt to the analyte prior to matrix-assisted laser desorption/ionisation generated $[M+Li]^{+}$ adduct ions.[155, 156]

The $[M+Li]^{+}$ adduct of poly(ethylene glycol), m/z 1389.9 (n=31), was selected for collision-induced dissociation by adjusting the magnetic-field strength in MS-1 of the MAG-TOF instrument. Collision-induced dissociation was performed on the selected ion by introducing xenon into the collision chamber. Figure 5.6 shows the CID spectrum of the poly(ethylene glycol) $[M+Li]^{+}$ adduct ion m/z 1389.9

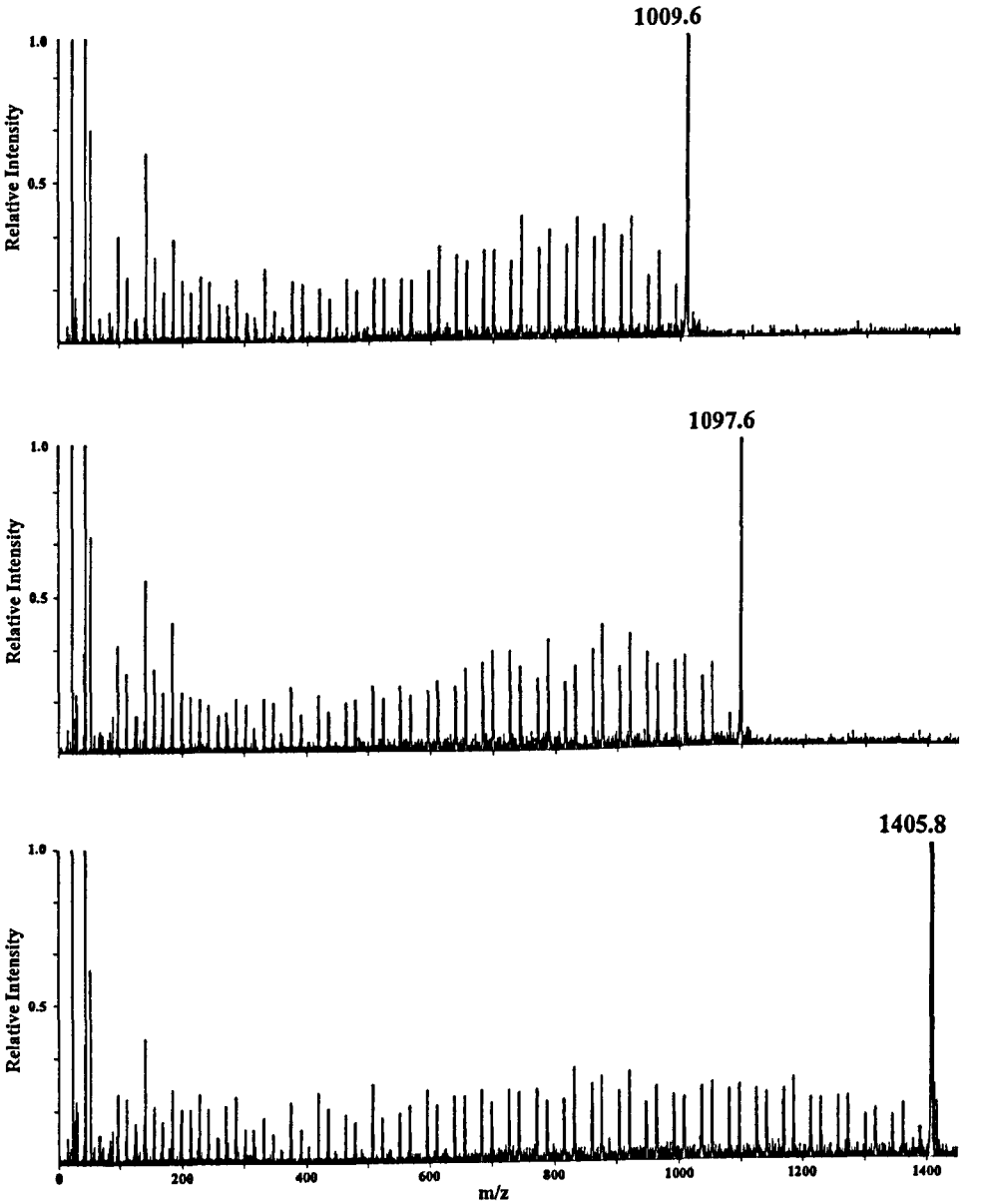

Figure 5.5 - A comparison of the collision-induced dissociation spectra of the poly(ethylene glycol) $[M+Na]^+$ adduct ions m/z 1009.6 (n=22), m/z 1097.6 (n=24) and 1405.8 (n=31) generated by MALDI. Helium collision gas.

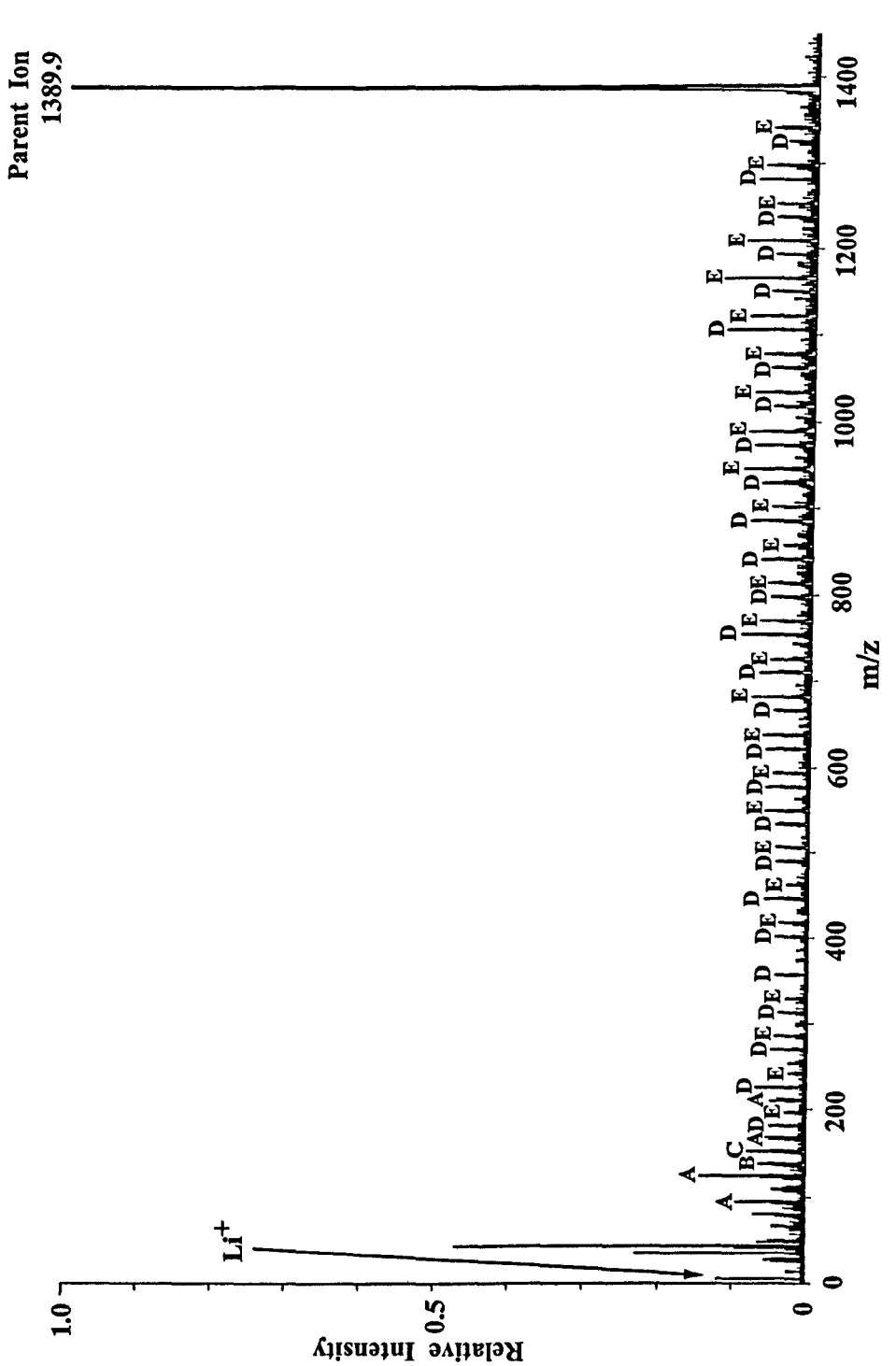

Figure 5.6 - Collision-induced dissociation spectrum of the poly(ethylene glycol) $[M+Li]^+$ adduct ion m/z 1389.9 (n=31) generated by MALDI. Helium collision gas. Scaled to show 3.3 % of the parent ion.

(n=31) using xenon as the collision gas. Fragment ion series were observed for the CID of the poly(ethylene glycol) $[M+Li]^+$ adduct ions, and correspond to the lithium analogues of fragment ions series **A-E** arising from reaction schemes 5.2[A] and 5.2[B]. The distinguishing feature of figure 5.6 was the relative weakness of low m/z ions in the $[M+Li]^+$ adduct spectrum as compared with $[M+Na]^+$ (figures 5.1-5.4), and in particular the intensity of the Li^+ peak in comparison with that of the Na^+ peak. This is thought to be due to the larger binding energy of Li^+ compared with Na^+ i.e. the lithium cation is more tightly bound, presumably to the oxygen atoms of the poly(ethylene glycol).

In addition to a reduced intensity of low m/z ions compared with the $[M+Na]^+$ adduct, a major drawback with the analysis of $[M+Li]^+$ adduct polyglycol ions was that it was difficult to generate a high proportion of lithium adduct ions due to there usually being a large amount of Na^+ contamination in the sample material, the matrix, the solvents and from the wobble-probe tip. The result was that, without elimination of all sources of Na^+ contamination in the sample preparation, the ions generated in a MALDI experiment were usually a mixture of $[M+Li]^+$ and $[M+Na]^+$ adducts, causing a decrease in sensitivity, hence the poor quality of figures 5.6.

The combination of reduced sensitivity and reduced intensity of low m/z ions (that provide vital structural information about polymer end-groups) meant that there was no practical advantage in doping with Li^+ for MS/MS analysis of polyglycols.[157]

5.4 High-Energy Collision-induced Dissociation of Poly(propylene glycol) ions generated by Matrix-assisted Laser Desorption/ionisation

Poly(propylene glycol) adduct ions were readily generated by matrix-assisted laser desorption/ionisation. A MALDI-TOF spectrum of poly(propylene glycol) Mn ~ 1300 obtained using a Kratos Kompact IV instrument in reflectron mode is shown in figure 5.7.

Using the MAG-TOF instrument, $[M+Na]^+$ adduct ions of poly(ethylene glycol) were selected by adjusting the magnetic field strength in MS-1. The resolution of the double-focusing mass spectrometer was sufficient to ensure that only the monoisotopic (^{12}C only) isotope passed through the exit-slit of MS-1. Collision-induced dissociation was performed upon the selected ion by introducing an inert gas into the collision chamber. The fragments arising from these collisions were observed at a planar array detector situated after MS-2.

High-energy collision-induced dissociation spectra of the poly(propylene glycol) $[M+Na]^+$ adduct ion m/z 969.7 (n=16) using helium and argon collision gases are shown in figures 5.8-5.11. A detailed analysis of the helium CID spectrum is given in table 5.2.

Seven fragment-ion series have been identified from the CID spectra, corresponding to **A1** (58.04m+22.99+45.03), **B** (58.04m+22.99+59.05), **C** (58.04m+22.99+17.00), **D** (58.04m+22.99+58.04), **E** (58.04m+22.99+15.99), **F1** (58.04m+22.99+44.03) and **G** (58.04+22.99+60).

Unlike poly(ethylene glycol), poly(propylene glycol) is unsymmetrical, thus it was necessary to consider from which end of the parent ion a particular fragment ion series originated.

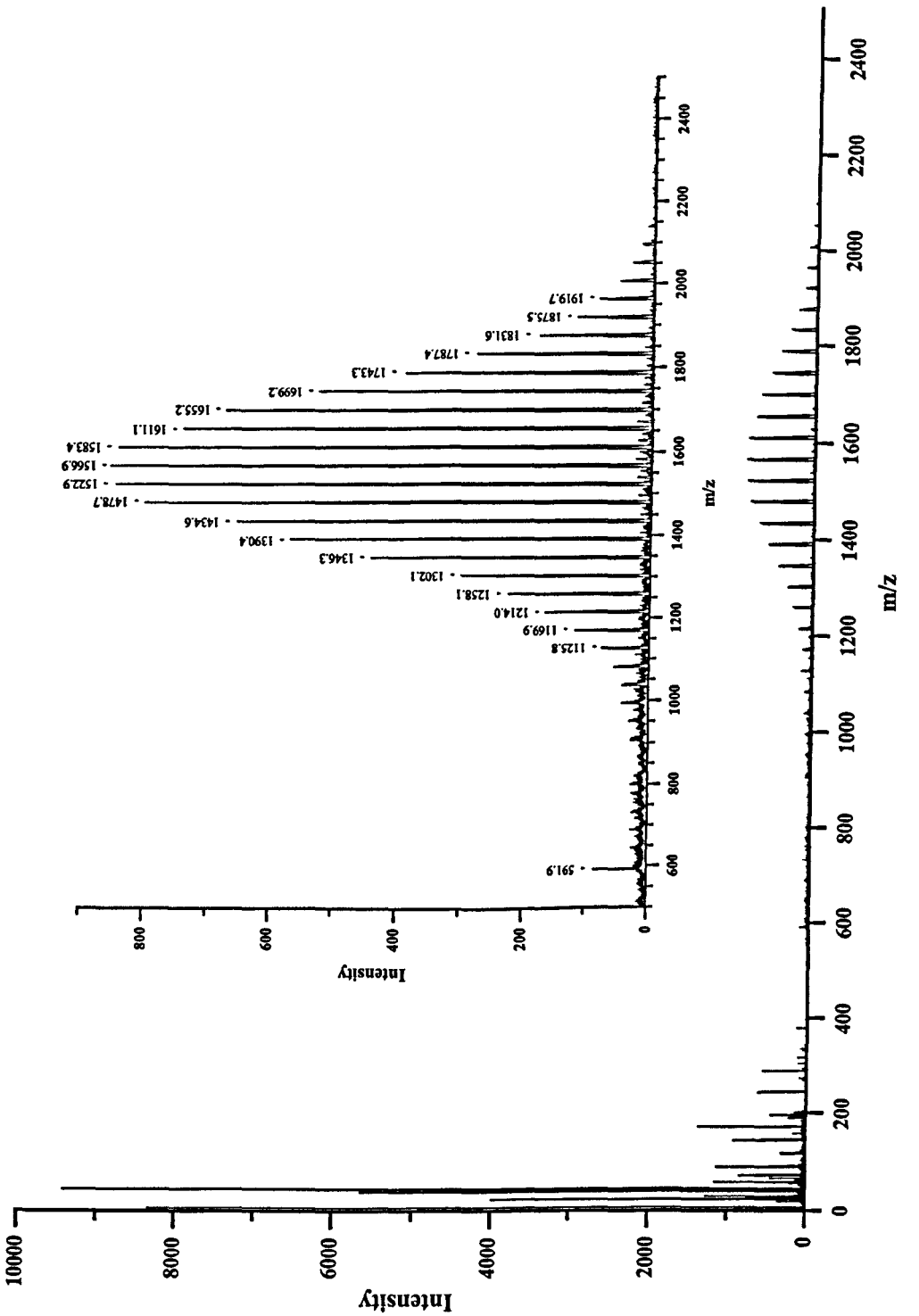

Figure 5.7 - MALDI-TOF spectrum of poly(propylene glycol) Mn~1300. Obtained using a Kratos Kompact IV instrument in reflectron mode.
INSET: enlargement of m/z 500-2500

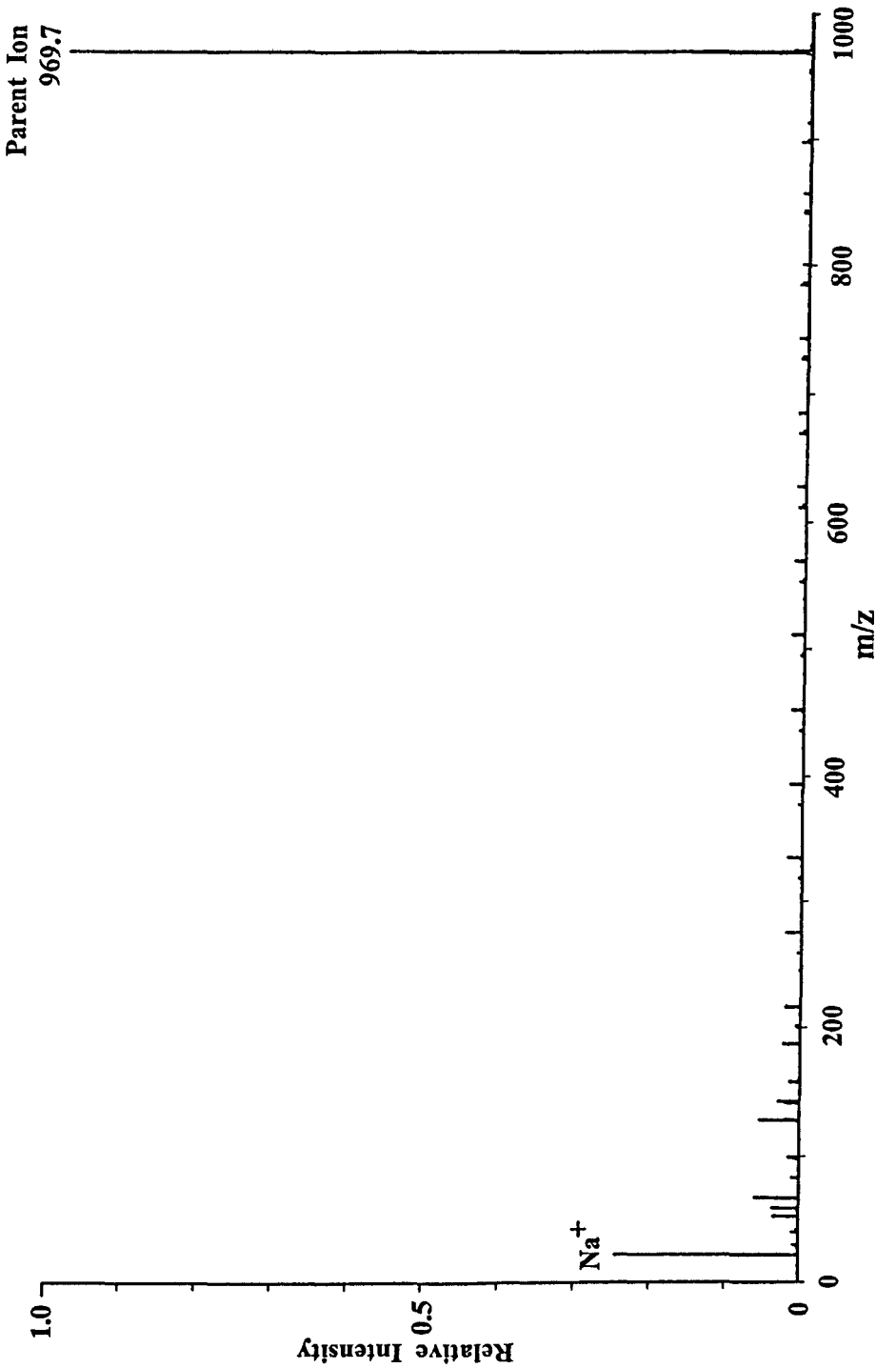

Figure 5.8 - Collision-induced dissociation spectrum of the poly(propylene glycol) $[M+Na]^+$ adduct ion m/z 969.7 (n=16) generated by MALDI. Helium collision gas. Scaled to 100 % of the parent ion.

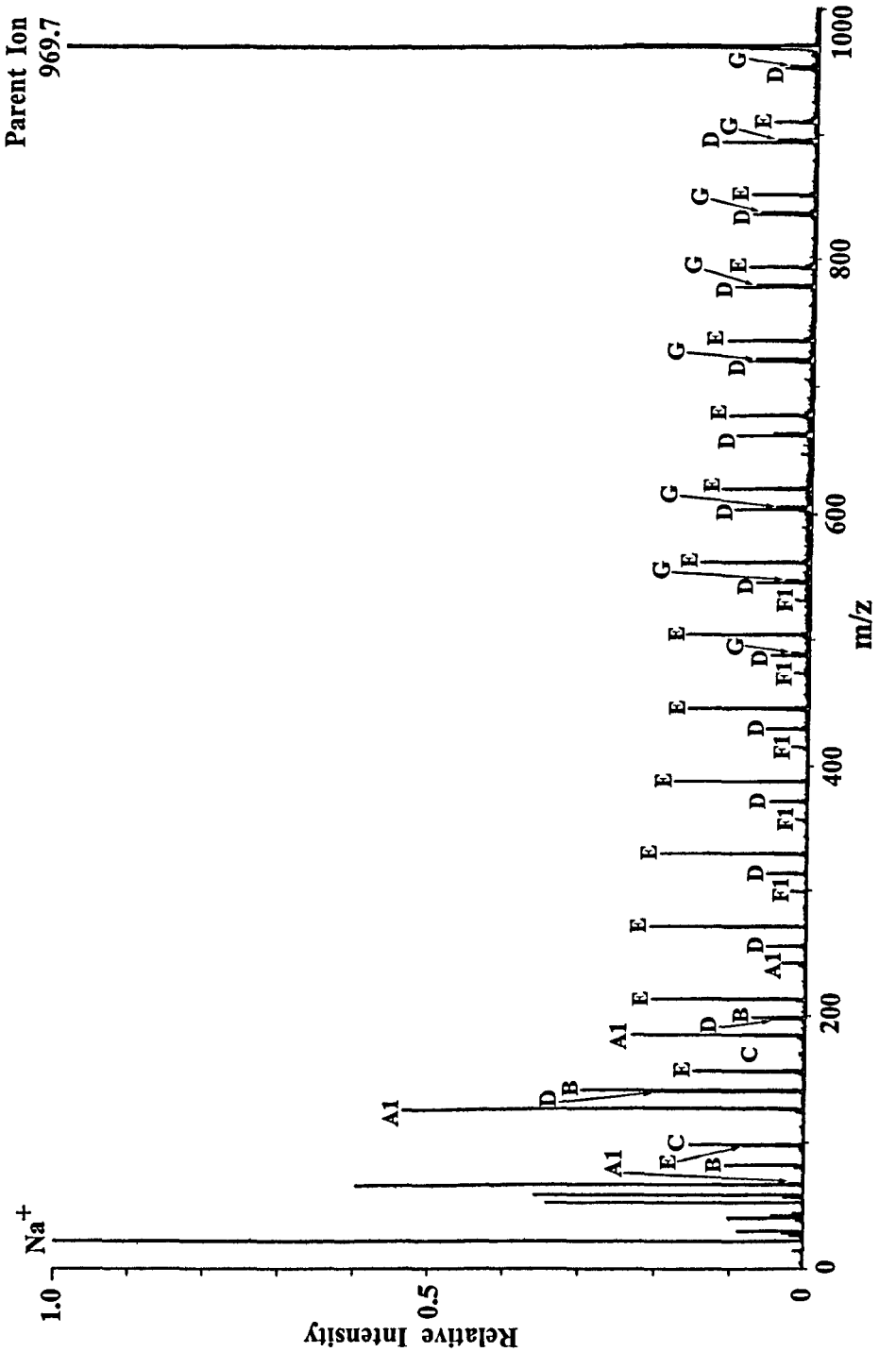

Figure 5.9 - Collision-induced dissociation spectrum of the poly(propylene glycol) $[M+Na]^+$ adduct ion m/z 969.7 (n=16) generated by MALDI. Helium collision gas. Scaled to show 10 % of the parent ion.

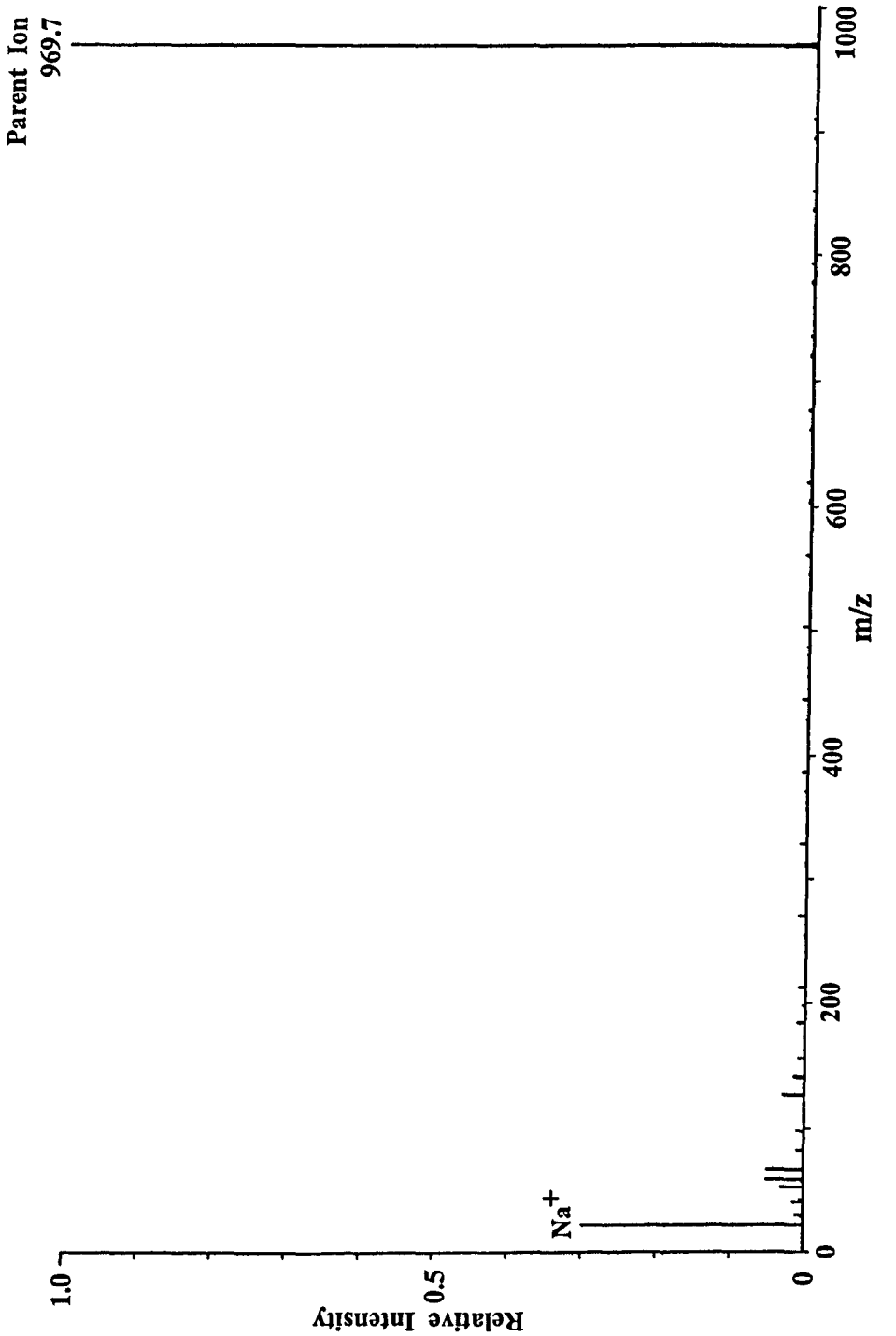

Figure 5.10 - Collision-induced dissociation spectrum of the poly(propylene glycol) $[M+Na]^+$ adduct ion m/z 969.7 (n=16) generated by MALDI. Xenon collision gas. Scaled to 100 % of the parent ion.

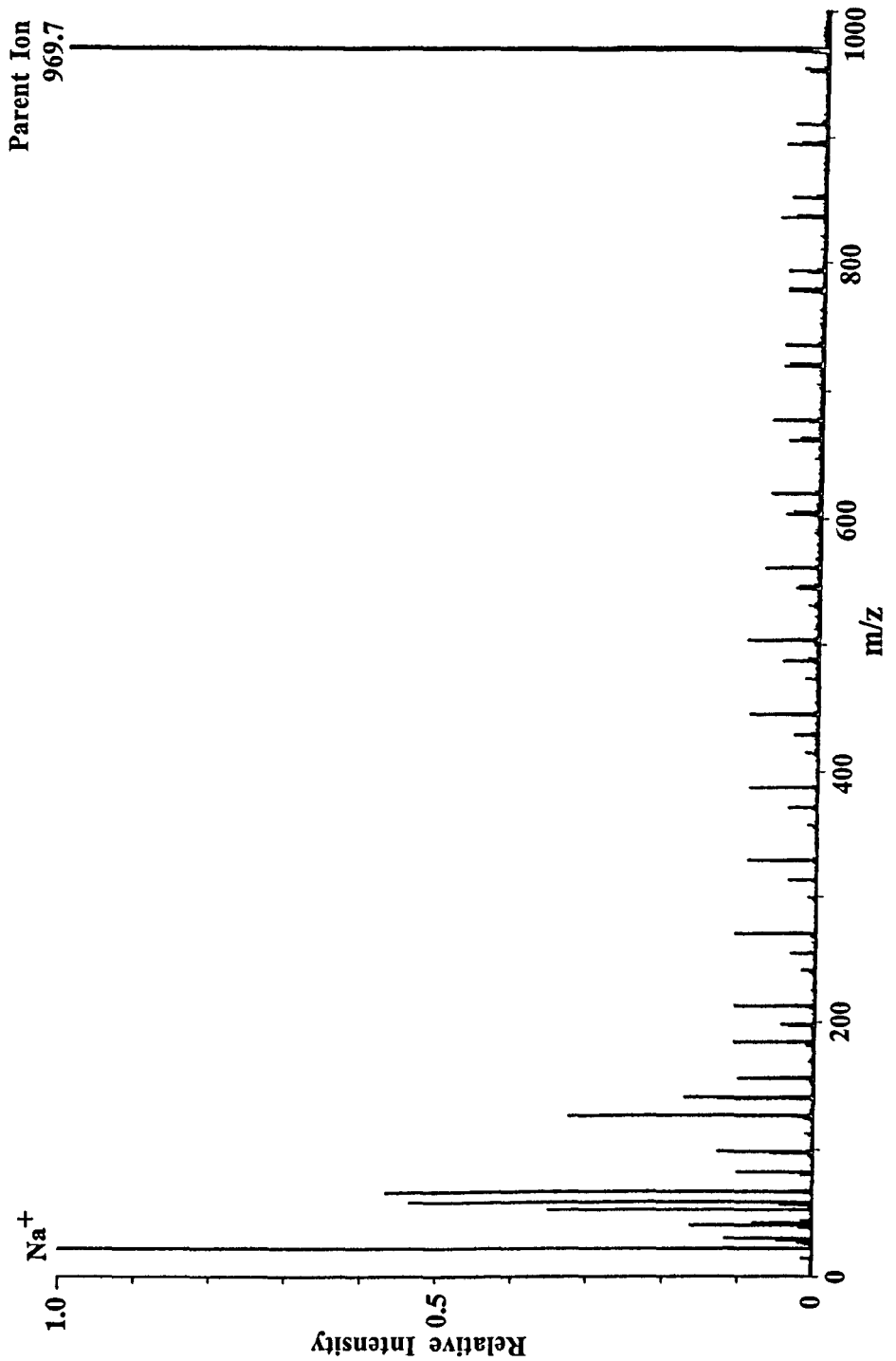

Figure 5.11 - Collision-induced dissociation spectrum of the poly(propylene glycol) $[M+Na]^+$ adduct ion m/z 969.7 (n=16) generated by MALDI. Xenon collision gas. Scaled to show 10 % of the parent ion.

Table 5.2 - Analysis of the helium CID spectrum of the poly(propylene glycol) $[M+Na]^+$ adduct ion m/z 969.7 (n=16) generated by MALDI.

m/z_{obs}	Intensity†	Assignment‡	m/z_{calc}	$m/z_{obs} - m/z_{calc}$
969.7	100.00	Parent	969.70	0.00
954.0	0.40	G		
952.0	0.46	D	951.63	0.37
909.8	0.70	E	909.58	0.22
895.7	0.55	G		
893.6	1.30	D	893.59	0.01
851.8	0.88	E	851.54	0.26
837.7	0.75	G		
835.7	0.87	D	835.55	0.15
793.6	0.90	E	793.50	0.10
779.5	0.79	G		
777.6	1.10	D	777.51	0.09
735.6	1.23	E	735.46	0.14
721.7	0.79	G		
719.7	0.90	D	719.47	0.23
677.4	1.40	E	677.42	-0.02
663.5	0.50	G		
661.4	1.08	D	661.43	-0.03
619.5	1.25	E	619.38	0.12
605.5	0.51	G		
603.4	1.08	D	603.39	0.01
561.2	1.45	E	561.34	-0.14
547.4	0.38	G		
545.3	0.76	D	545.35	-0.05
531.3	0.23	F1	531.34	-0.04
503.4	1.65	E	503.30	0.10
489.3	0.26	G		
487.3	0.53	D	487.31	-0.01
473.3	0.22	F1	473.30	0.00
445.3	1.65	E	445.26	0.04
429.3	0.60	D	429.27	0.03
415.4	0.23	F1	415.26	0.14
387.3	1.85	E	387.22	0.08
371.3	0.53	D	371.23	0.07
357.2	0.18	F1	357.22	-0.02
329.2	1.99	E	329.18	0.02
313.2	0.58	D	313.19	0.01
299.2	0.23	F1	299.18	0.02
271.2	2.10	E	271.14	0.06
255.2	0.56	D	255.15	0.05
242.2	0.34	A1	242.14	0.06
213.1	2.08	E	213.10	0.00
198.2	0.76	B	198.12	0.08
197.1	0.50	D	197.11	-0.01
184.1	2.35	A1	184.10	0.00

156.1	0.32	C	156.07	0.03
155.2	1.53	E	155.06	0.14
140.2	3.10	B	140.08	0.12
139.2	2.00	D	139.07	0.13
126.2	5.40	A1	126.06	0.14
125.3	0.35	F1	125.06	0.24
98.2	1.63	C	98.03	0.17
97.2	0.84	E	97.02	0.18
82.1	1.09	B	82.04	0.06
68.2	0.21	A1	68.02	0.18
67.1	6.25	F1	67.02	0.08
59.1	3.73	C3H9O+	59.05	0.05
57.1	0.28	C3H7O+	57.03	0.07
53.0	3.54	NaCH2O+	53.00	0.00
45.0	0.15	C2H5O+	45.03	-0.03
43.0	0.46	C2H3O+	43.02	-0.02
42.0	0.18			
41.0	1.02	C2HO+	41.00	0.00
31.0	0.91	CH3O+	31.02	-0.02
29.0	0.32	C2H5+/CHO+	29.04/29.00	
27.0	0.19	C2H3+	27.02	-0.02
23.0	26.00	Na^+	22.99	0.01
15.0	0.15	CH_3^+	15.02	-0.02

† IntensityThe parent ion intensity corresponds to 100%. The fragment ion intensities are given as percentages of the parent ion intensity. Fragment ions with intensities greater than a threshold value of 0.15% are displayed.

‡ The assignments A1, B, C, D, E, F1 and G correspond to the fragment-ion series illustrated in reactions 5.3[A]-5.3[G].

As for poly(ethylene glycol) the collision process was of sufficiently high energy to cause homolytic cleavage of either a C-C, C-O or C-H bond in the selected poly(propylene glycol) ion. Homolytic cleavage of a C-C or C-O bond in the polymer backbone has previously been described to give rise to fragment ion series A1, B and C.[146] Cleavage of these bonds cannot explain fragment ion series D, E, F1 and G.

A multi-step radical mechanism is proposed here to account for these fragment-ion series. The initial step involves the scission of a C-H bond, and loss of a $H^{\bullet}$ radical, which can occur at 3 different positions in the poly(propylene glycol) repeat unit Subsequent rearrangement of the radical ion results in scission of the polymer chain at one of two possible positions, β to the site of the initial radical position. Reactions 5.3[A]-5.3[C] show the possible mechanisms from one particular end of the parent ion, with all the fragment ion series labelled: Series *X*1. Reactions 5.3[D]-5.3[F] show the possible mechanism from the other end of the molecular ion, with the fragment ion series labelled: Series *X*2. The positions were chain cleavage can take place has been illustrated for each of reactions 5.3[A]-5.3[F]. A list of the calculated m/z's for the fragment ion series proposed in reactions 5.3[A]-5.3[F] are shown in table 5.3.

Table 5.3 - Calculated m/z's for the fragment ion series proposed from reactions 5.3[A]-5.3[F].

Fragment Ion Series	Calculated m/z
A1	58.04n+Na+45.03
A2	58.04n+Na+31.02
B1, B2	58.04n+Na+59.05
C1, C2	58.04n+Na+17.00
D1, D2	58.04n+Na+58.04
E1, E2	58.04n+Na+15.99
F1	58.04n+Na+44.03

Reaction 5.3[A]

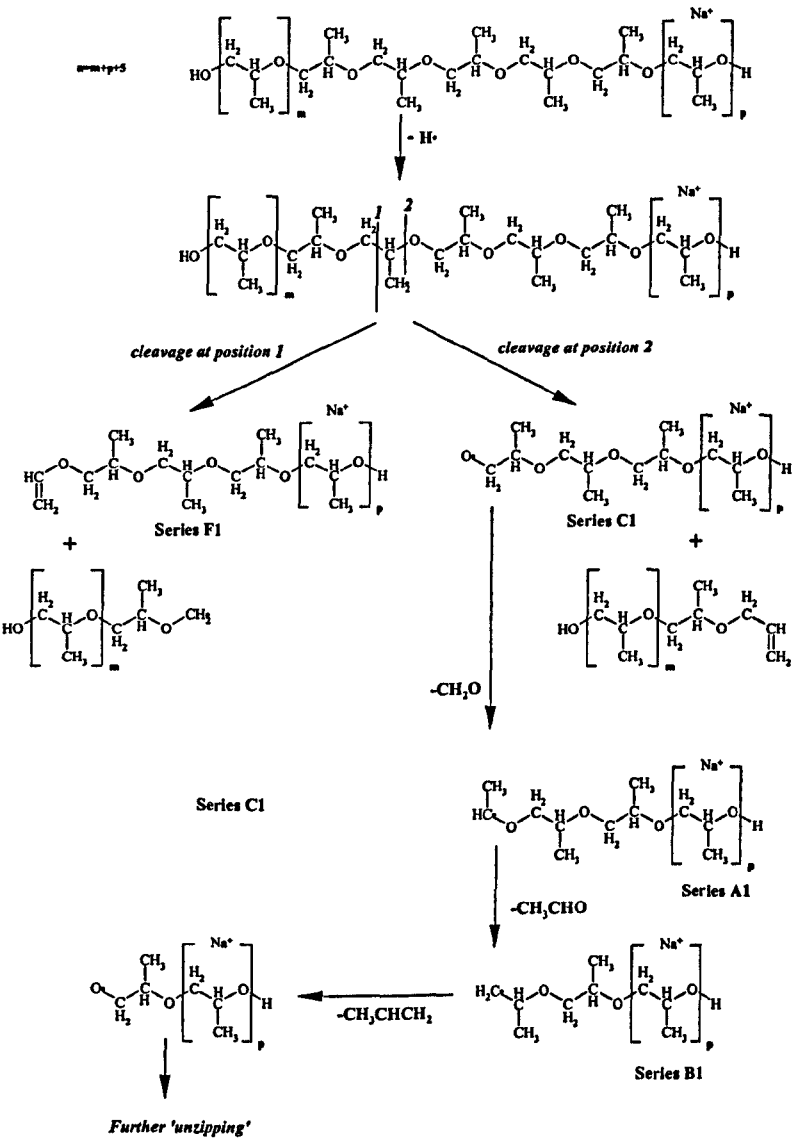

Reaction 5.3[B]

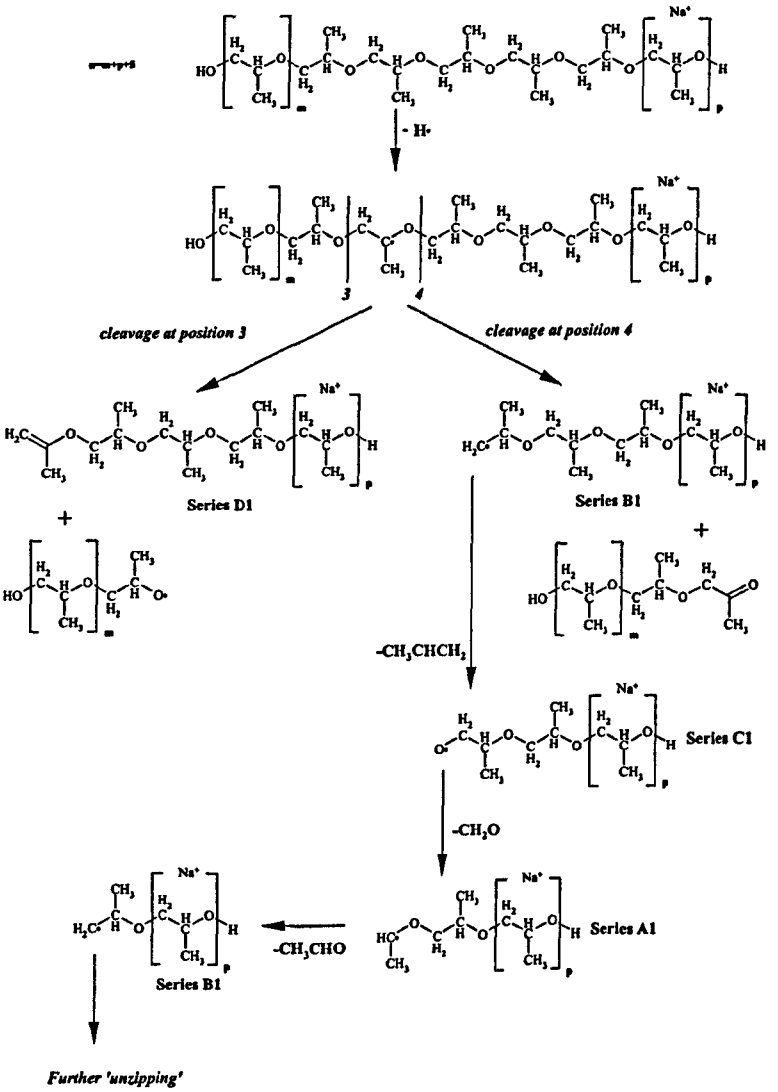

Reaction 5.3[C]

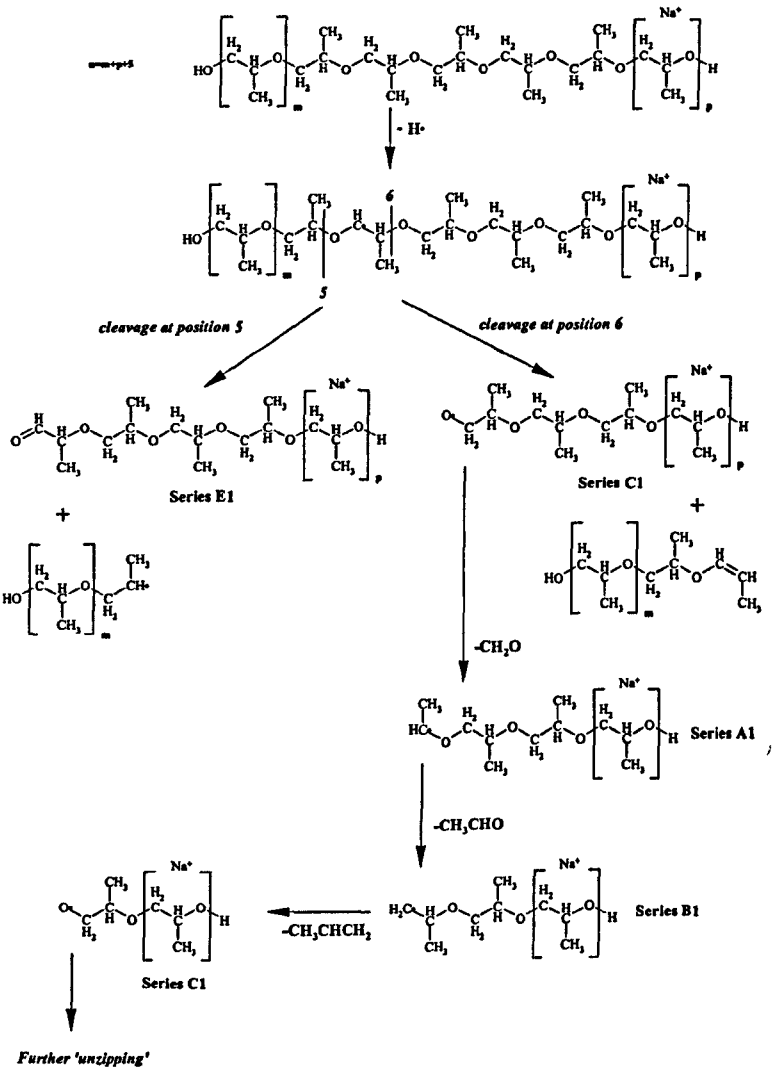

Reaction 5.3[D]

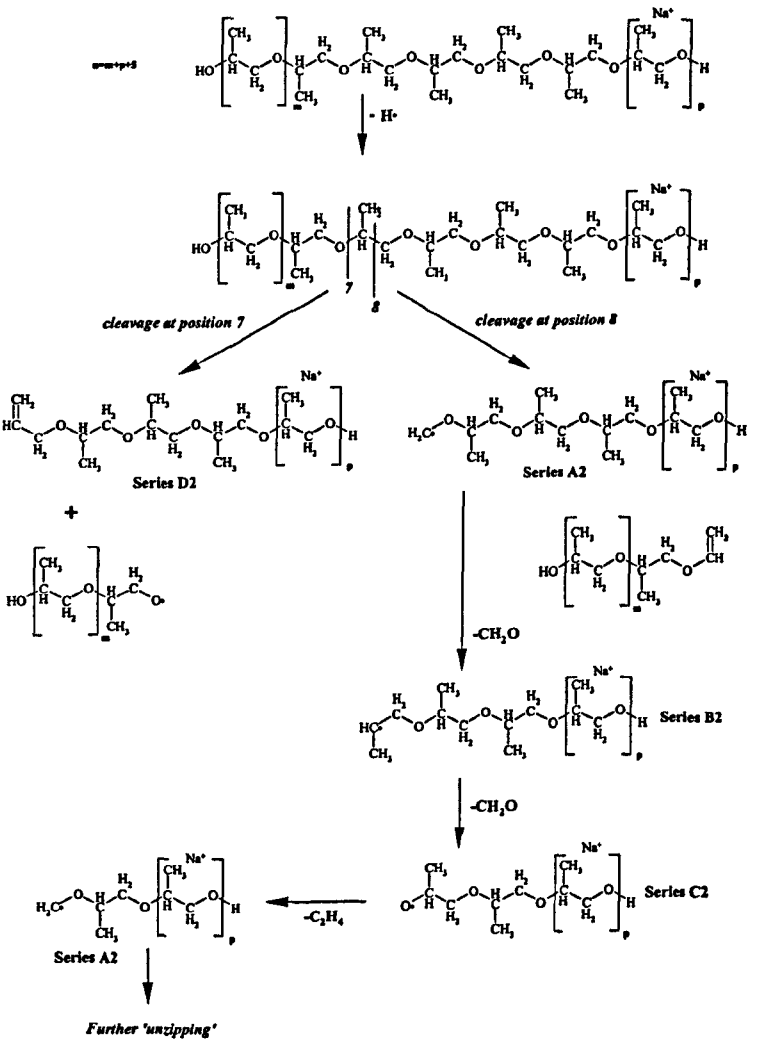

Reaction 5.3[E]

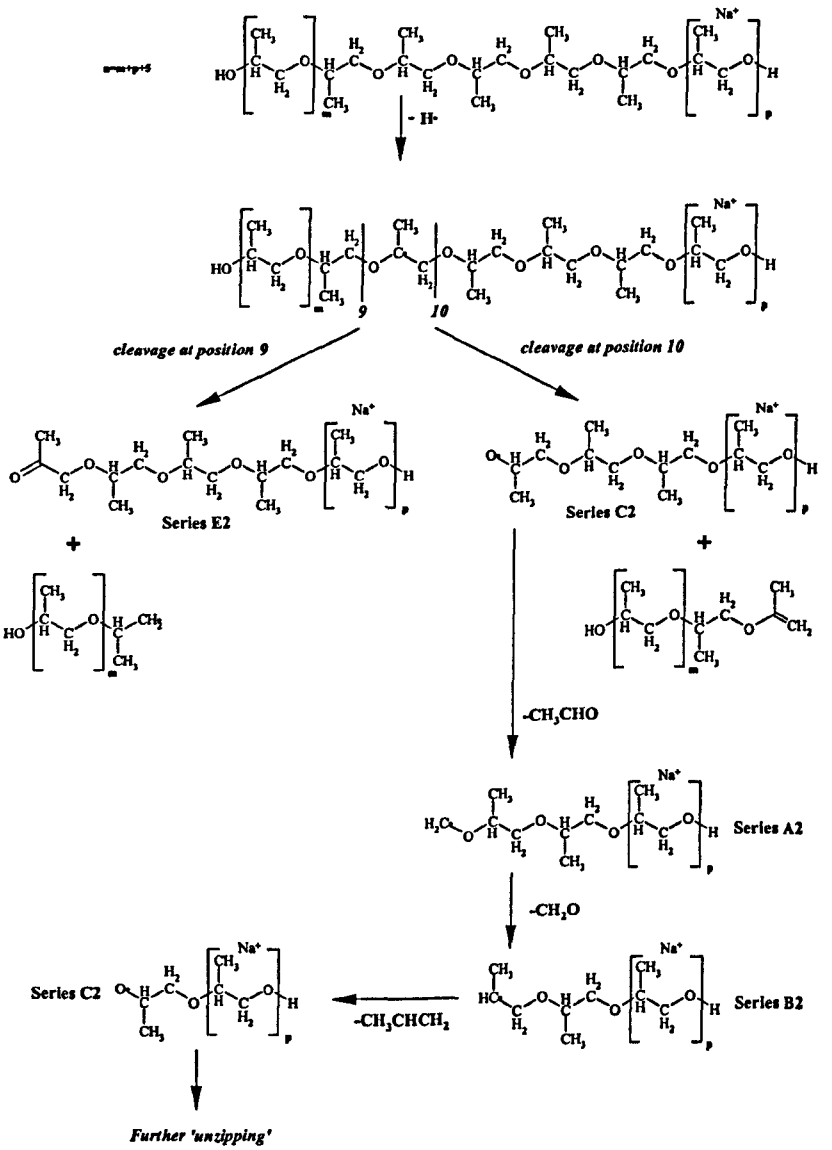

Reaction 5.3[F]

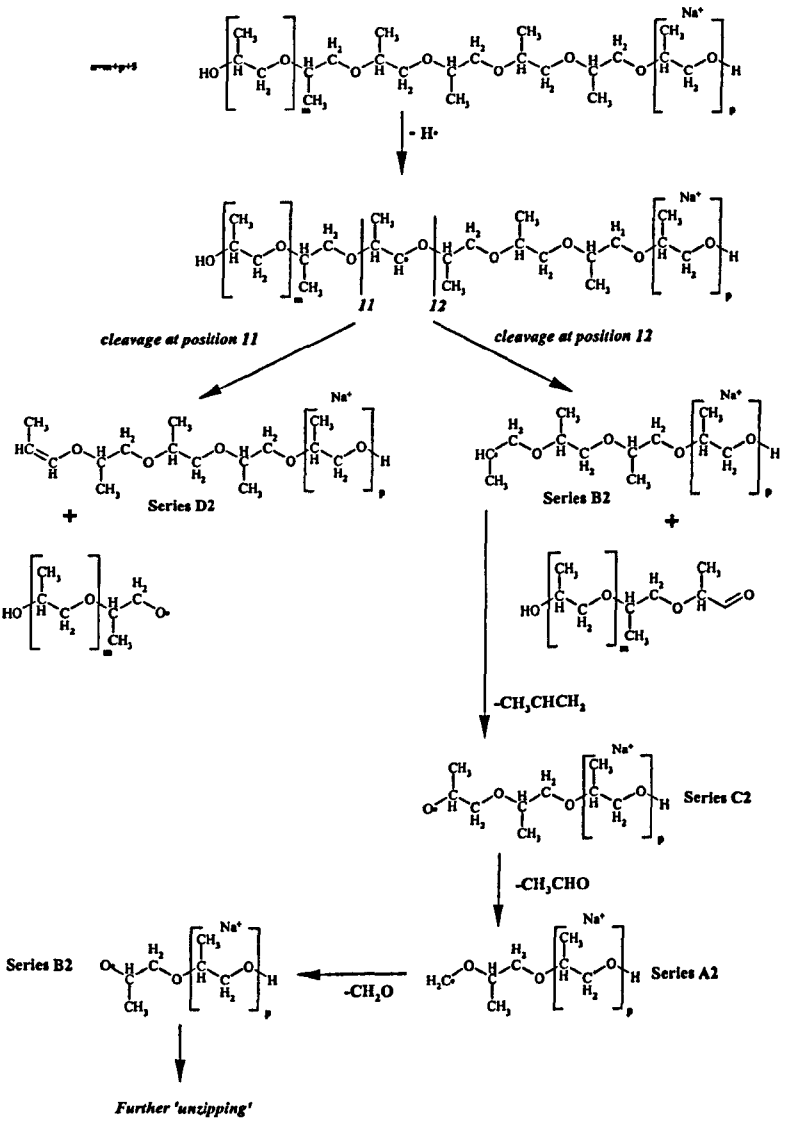

As fragment ion series B1 was a structural isomer of series B2 it was not possible to distinguish between them in the CID spectra, as they have the same m/z. The same was true for C1=C2, D1=D2 and E1=E2. These fragment-ion series have thus been labelled **B, C, D** and **E** in table 5.2.

Although it was not possible to distinguish between these isomers, the likelihood of formation can be assessed by examining which C-H bond is initially cleaved, and by the stability of the fragments produced (both the ion and the neutral). In particular, the stability of the radical containing portion must be assessed.

The formation of fragment-ion series **A1, A2, B1, B2, C1** and **C2**, although feasible from the mechanisms described in reactions 5.3[A]-5.3[F], most likely results from homolytic cleavage of C-C and C-O bonds in the polymer backbone. Fragment-ion series **A2** was not observed in any of the CID spectra.

For this reason, only the likelihood of formation of fragment-ion series **D1, D2, E2** and **F1** by these mechanisms are examined further. A summary of the type of C-H bond cleaved and type of neutral radical formed for fragment-ion series **D, E** and **F1** is given in table 5.4.

Table 5.4 - Type of C-H cleavage and type of neutral radical formed for fragment ion series **D, E** and **F1**

	Type of C-H cleavage	Type of Neutral Radical (atom radical situated upon)
D1	Tertiary	Primary (O)
D2	Primary	Primary (O)
D2	Secondary	Primary (O)
E1	Secondary	Secondary (C)
E2	Tertiary	Primary (C)
F1	Primary	Primary (C)

There are three different C-H bonds that can be cleaved in the initial step of the mechanisms outlined above; a primary, a secondary and a tertiary C-H bond. Fragment-ion series **F1**, although weak, was observed in the CID spectra. This fragment-ion series can only arise from the mechanism illustrated in reaction 5.3[A], and involves the scission of a primary C-H bond. As the primary C-H bond is the strongest, this could explain the intensity of this particular fragment ion series when compared with the intensity of fragment ion series **D** and **E**, which can arise from secondary and/or tertiary C-H cleavage.

As there was sufficient energy to result in dissociation of each of the three different types of C-H bond (as evidenced by fragment-ion series **F1**) it is necessary to consider the stability of both the ion and neutral produced by the fragmentation to determine the likelihood of formation.

For fragment-ion series **D**, **E** and **F1** the radical containing part after fragmentation is the neutral. For the formation of **D1**, **D2**, **E2** and **F1**, a primary radical is formed although for **D1** and **D2** this was located on the heteroatom. For the formation of **E1** a secondary radical was formed.

It is clear from this type of assessment that the least likely fragment-ion series is **F1**, as it involves cleavage of a primary C-H bond, and formation of a primary radical. This species was nonetheless observed in the CID spectra, and suggests that all of reaction schemes 5.3[A]-5.3[F1] are feasible mechanisms, although determining whether a particular mechanism is more (or less) feasible than another is not easily assessed.

A further fragment ion series (labelled **G** in table 5.2) was observed in the high m/z region of the CID spectra. The formation of this fragment ion series is not easy to rationalise using the multi-step radical mechanisms involving C-H scission as an

initial step.. One possible candidate is loss of a methyl radical ($CH_3^{\bullet}$) as the initial step (see reaction 5.3[G]).

Reaction 5.3 [G].

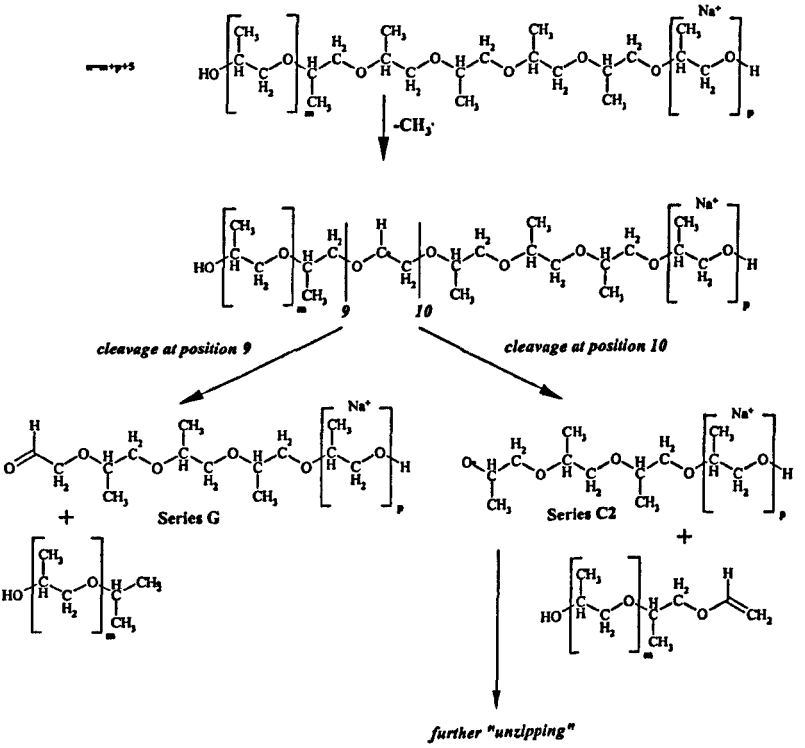

5.5 High-Energy Collision-induced Dissociation of a Random Ethylene Glycol/Propylene Glycol Copolymer

Copolymers are an important class of synthetic polymer, comprised of two or more different monomers. By using different monomers, a synthetic polymer chemist can design materials for specific applications. Furthermore, the polymer chemist can alter the performance of the material by changing the arrangement of the monomer units within a polymer molecule.

Water-soluble copolymers of poly(ethylene glycol) and poly(propylene glycol) find widespread application as non-ionic surface active agents,[158] and have been utilised as lubricants, dispersants, antistatic agents, foam control agents and solubilisers in the areas of pharmaceuticals, cleaning agents, foods and personal care products.[159,160] The diversity in application results from the structural arrangements of the monomers within the copolymer. In this context, it is necessary to obtain a complete description of the molecular composition distribution of the copolymer in order to understand how the structure affects physical, rheological and mechanical properties. It is important to have detailed knowledge about the sequence of the monomer units and the identity and structure of particular end-groups.

In principle, tandem mass spectrometry can provide such structural information. In this section, high-energy collision-induced dissociation is utilised to probe the structure of a random poly(ethylene glycol)/(propylene glycol) copolymer.

A poly(ethylene glycol)-*co*-poly(propylene glycol) monobutyl ether random copolymer, $M_n \sim 970$, was obtained (Sigma-Aldrich, Dorset, U.K.). The most intense peak observed at the parallel time-of-flight detector (TOF-1) of the MAG-TOF

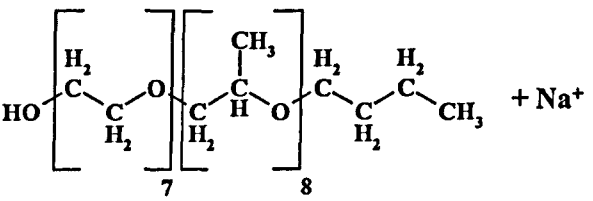

Figure 5.12 - Poly(ethylene glycol)-*co*-poly(propylene glycol) oligomer selected for investigation by high-energy collision-induced dissociation, mz = 869.6

instrument was chosen for further investigation. This particular oligomer of the copolymer corresponded to an $[M+Na]^+$ adduct ion containing 7 ethylene glycol units and 8 propylene glycol units (PEG=7, PPG=8). Using the MAG-TOF instrument, the $[M+Na]^+$ adduct ion of this particular oligomer, m/z = 869.6, was selected by adjusting the magnetic-field strength of MS-1. The resolution of the double-focusing mass spectrometer was sufficient to ensure that only the monoisotopic (^{12}C only) isotope passed through the exit-slit of MS-1. Collision-induced dissociation was performed by introducing xenon gas into the collision chamber.

The high-energy collision-induced dissociation spectrum of the $[M+Na]^+$ adduct ion m/z 869.6 (PEG=7, PPG=8) using xenon as the collision gas is shown in Figure 5.13. An m/z vs. intensity list of all observed peaks is shown in table 5.4

A challenge in analysing the spectrum arose from the very large number of peaks observed in the mass spectrum; 150 separate peaks were observed. For the purpose of analysing the spectrum, two separate regions were defined: the high m/z region (m/z 200-869.6) and the low m/z region (m/z 0-200). The high m/z region will be examined first.

A feature of the high-energy collision-induced dissociation spectra of both poly(ethylene glycol) (chapter 5.3) and poly(propylene glycol) (chapter 5.4) was that

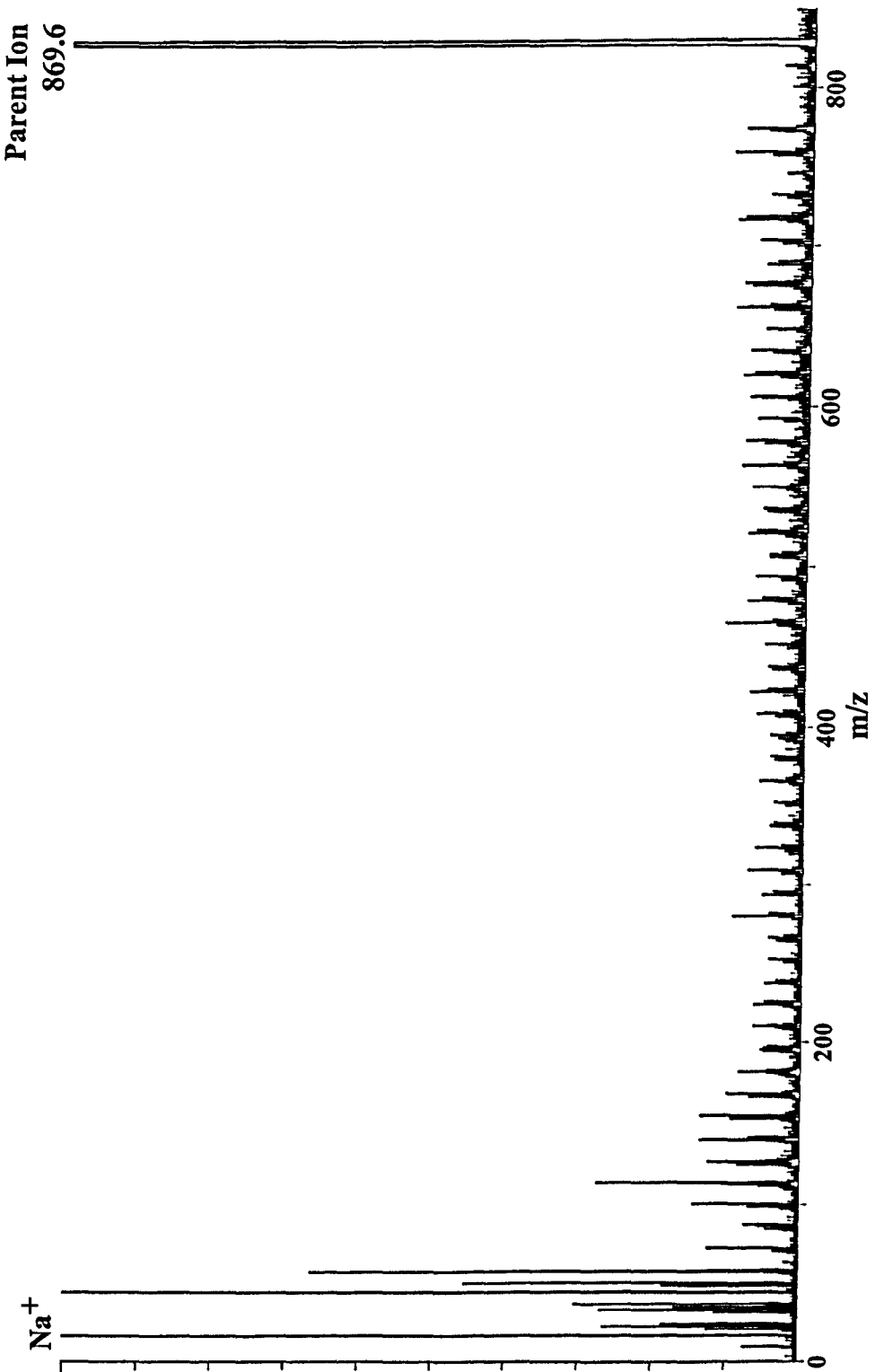

Figure 5.13 - Collision-induced dissociation spectrum of a poly(ethylene glycol)/poly(propylene glycol) random copolymer, $[M+Na]^+$ adduct ion m/z 869.6 (PEG=7 PPG=8) generated by MALDI. Xenon collision gas.

Table 5.4 - m/z vs. intensity list for the collision- induced dissociation spectrum of a poly(ethylene glycol)/poly(propylene glycol) random copolymer, $[M+Na]^+$ adduct ion m/z 869.6 (PEG=7 PPG=8) generated by MALDI, using xenon collision gas.

m/z_{obs}	Intensity	m/z_{obs}	Intensity	m/z_{obs}	Intensity
869.6	100.0	489.3	0.42	200	0.15
853.6	0.3	487.3	0.17	199.1	0.26
839.6	0.2	475.3	0.38	198.1	0.48
811.6	0.6	473.4	0.13	197.1	0.26
809.5	0.3	461.3	0.27	196.1	0.12
795.4	0.4	459.3	0.25	184.1	0.65
793.5	0.2	447.2	0.32	183.1	0.32
781.6	0.2	445.3	0.41	182.1	0.26
767.5	0.3	443.2	0.15	170.2	0.75
765.4	0.2	433.3	0.14	168.2	0.53
753.5	0.5	431.3	0.35	156.1	0.3
751.5	0.5	429.3	0.15	155.1	0.25
737.5	0.4	417.4	0.3	154.1	0.77
735.4	0.3	415.2	0.18	153.2	0.3
723.6	0.2	403.3	0.21	141.1	0.25
721.5	0.3	401.3	0.35	140.1	0.78
709.4	0.5	389.3	0.15	139.1	0.36
707.4	0.4	387.2	0.41	138.1	0.45
695.7	0.2	385.2	0.1	126.1	1.36
693.5	0.5	373.2	0.19	125.1	0.57
691.6	0.3	371.2	0.13	124.1	0.3
679.5	0.3	359.2	0.27	123.1	0.11
663.6	0.3	357.2	0.3	112	0.72
651.4	0.4	345.3	0.17	111	0.24
649.4	0.5	343.3	0.27	110	0.47
647.4	0.2	341.2	0.14	98.1	0.48
635.3	0.5	329.2	0.3	97	0.3
633.3	0.2	327.3	0.15	96.1	0.13
621.4	0.5	315.3	0.27	95	0.18
619.4	0.2	313.3	0.27	82.1	0.58
607.4	0.5	301.3	0.27	81	0.1
605.4	0.4	299.2	0.45	80	0.17
593.5	0.2	287.2	0.13	68.1	0.2
591.4	0.4	285.3	0.27	67.1	3.64
589.5	0.2	283.2	0.16	66.1	0.16
579.3	0.1	271.3	0.23	59	2.41
577.4	0.4	269.2	0.1	57	1.14
575.3	0.2	257.2	0.22	53	7.55
563.3	0.3	255.2	0.22	45	1.65
561.4	0.3	243.1	0.35	43.1	0.88
549.5	0.4	241.2	0.35	42.1	0.3
547.5	0.5	229.2	0.11	41.1	1.52
545.5	0.2	228.2	0.23	39	0.58
535.3	0.2	227.2	0.28	31	1.09
533.3	0.3	226.2	0.15	29.1	1.25

531.4	0.2
519.3	0.3
505.3	0.4
503.4	0.4
491.3	0.21

225.1	0.1
214.2	0.19
213.2	0.27
212.2	0.3
211.1	0.19

28.1	0.2
27.1	0.55
23	56.8
15.1	0.31
14.1	0.11

† Intensity of peak heights. The parent ion intensity corresponds to 100%. The fragment ion intensities are given as percentages of the parent ion intensity. Fragment ions with intensities greater than a threshold value of 0.1% are displayed.

above m/z ~ 200 the most intense peaks observed could all be assigned as **D** and **E** type fragments. It could thus reasonably be assumed that for a poly(ethylene glycol)/poly(propylene glycol) copolymer that **D** and **E** fragments would predominate above m/z ~ 200. A further consideration was the parent ions were unsymmetrical, having a butyl group at one end of the chain. A fragment with charge-retention on the end of the ion containing the alkyl end-group would therefore have a different mass from a fragment with charge retention on the end of the ion without the alkyl end-group (for a dissociation at equivalent positions along the polymer chain). Figures 5.14-5.17 show all the possible combinations of **D** and **E** type fragments with either an alkyl containing end-group or a non-alkyl containing end-group (in total 284 combinations). In each of figures 5.14-5.17 the number of repeat units decreases through each subsequent level of the diagram. Moving downwards and to the left indicates an additional propylene glycol unit is 'lost' during fragmentation, and moving downwards and to the right indicates the 'loss' of an additional ethylene glycol unit. For example, consider a **D**-type fragmentation that takes place at the non-alkyl terminal of the copolymer with charge retention at the alkyl end (corresponding to the first level in figure 5.14). As this was a random copolymer, the terminal repeat unit could be *either* an ethylene glycol *or* a propylene

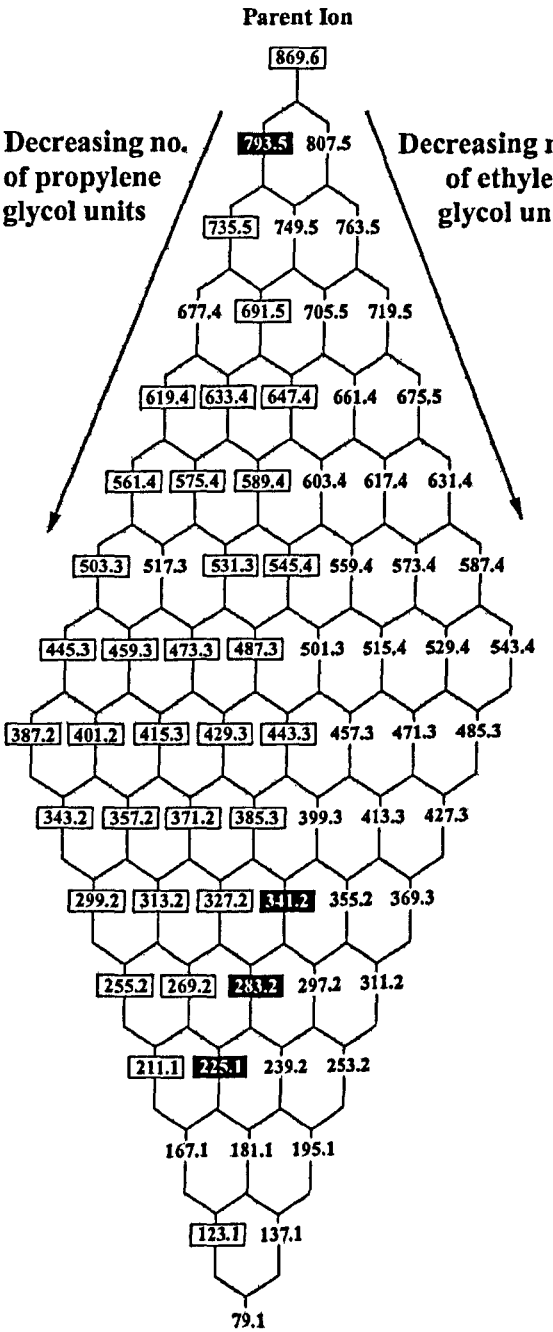

Figure 5.14 - Diagram showing all the possible **D** fragments resulting from fragmentation with charge retention on the alkyl containing end of the ion.
Numbers outlined with a box correspond to peaks actually observed in the CID spectrum.
Numbers within a filled box correspond to peaks observed in the CID spectrum that were not members of other series (figures 5.15-5.17).

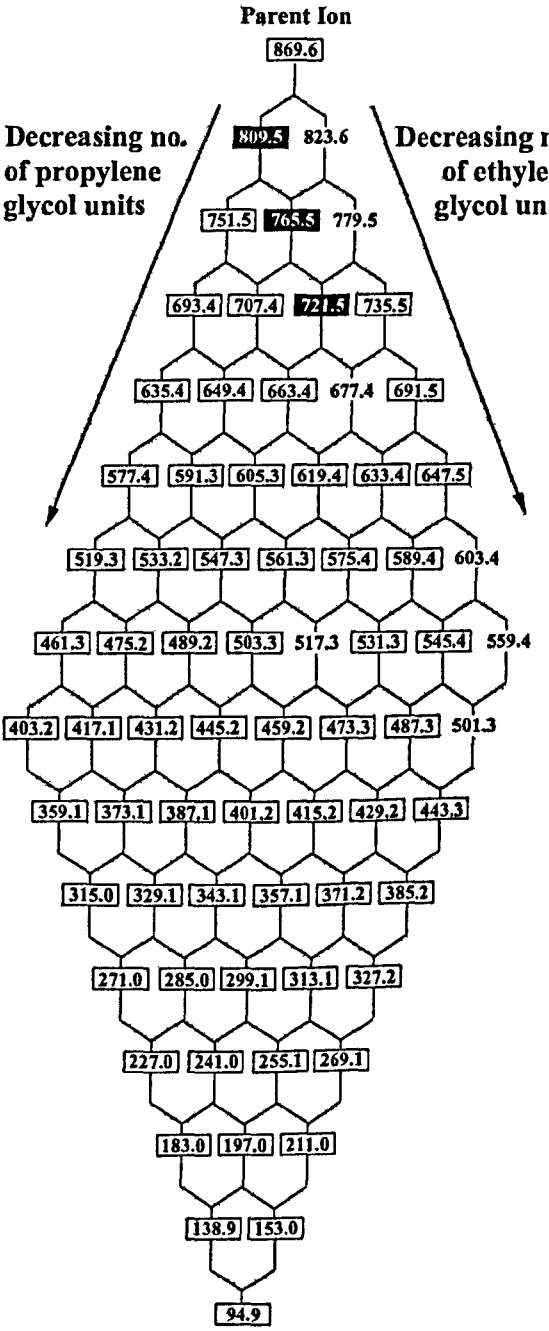

Figure 5.15 - Diagram showing all the possible E fragments resulting from fragmentation with charge retention on the alkyl containing end of the ion.
Numbers outlined with a box correspond to peaks actually observed in the CID spectrum.
Numbers within a filled box correspond to peaks observed in the CID spectrum that were not members of other series (figures 5.14, 5.16 and 5.17).

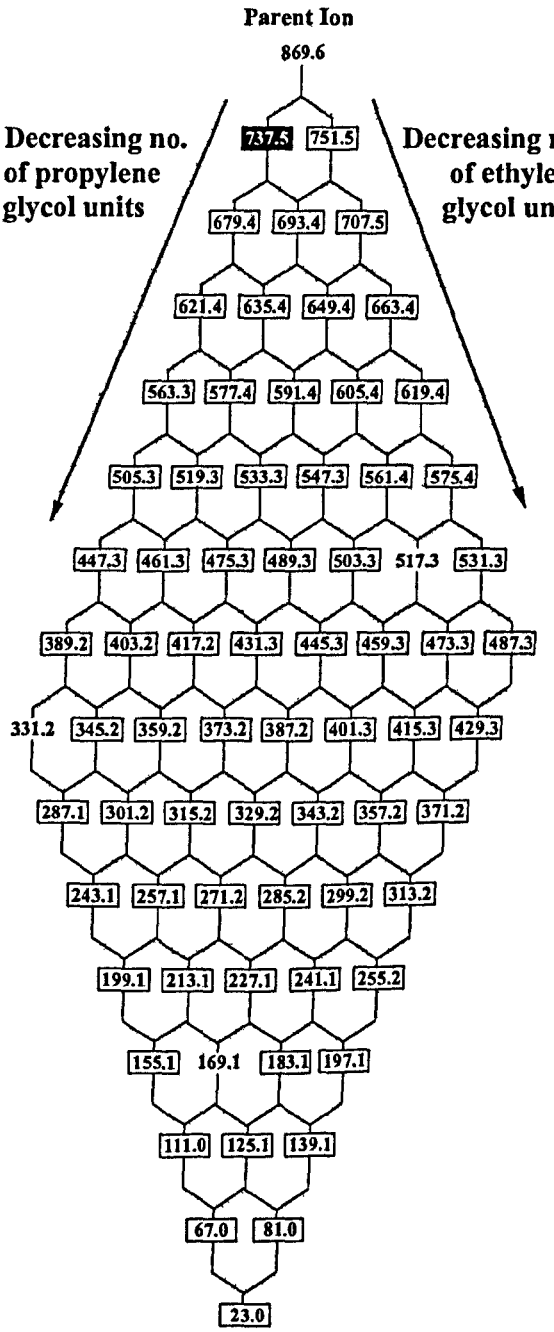

Figure 5.16 - Diagram showing all the possible **D** fragments resulting from fragmentation with charge retention on the non-alkyl containing end of the ion.
Numbers outlined with a box correspond to peaks actually observed in the CID spectrum.
Numbers within a filled box correspond to peaks observed in the CID spectrum that were not members of other series (figures 5.14, 5.15 and 5.17).

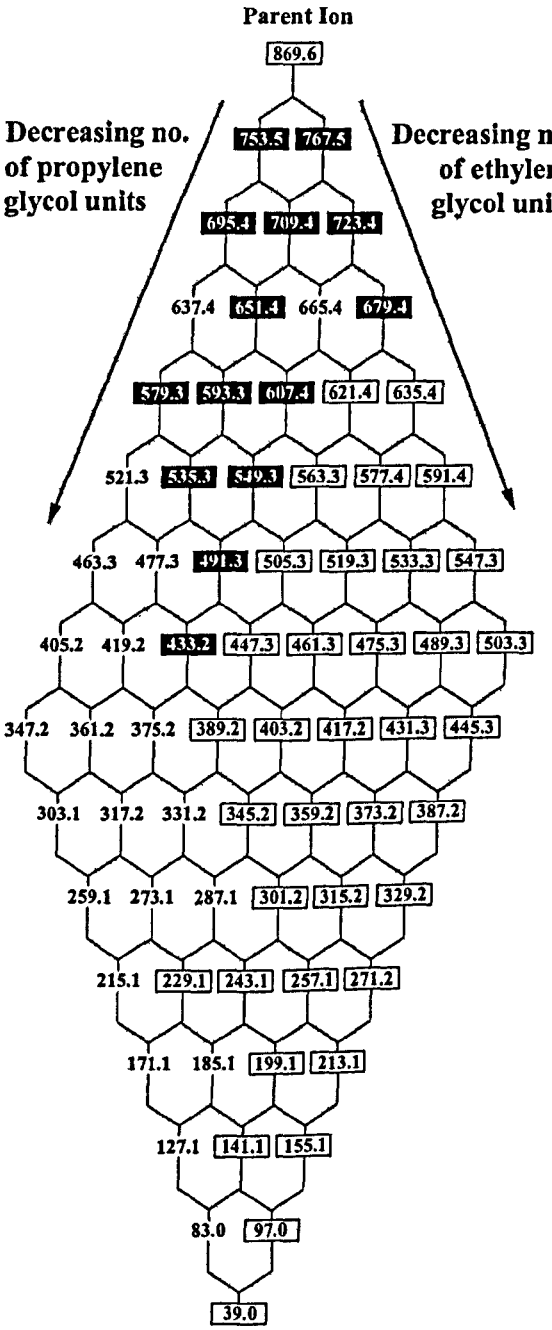

Figure 5.17 - Diagram showing all the possible E fragments resulting from fragmentation with charge retention on the non-alkyl containing end of the ion.
Numbers outlined with a box correspond to peaks actually observed in the CID spectrum.
Numbers within a filled box correspond to peaks observed in the CID spectrum that were not members of other series (figures 5.14- 5.16).

glycol unit. A fragment from this position could thus correspond to the loss of an ethylene glycol unit, 44.03+18.01, giving a fragment m/z of 807.5 or the loss of a propylene glycol unit, 58.04+18.01, giving a fragment m/z of 793.5. The second level of figure 5.14 corresponds to the loss of two repeat units. This could be two propylene glycol units (m/z 735.5), 1 propylene glycol unit and 1 ethylene glycol unit (m/z 749.5), or 2 ethylene glycol units (m/z 807.5).

The combinations of possible fragment ions shown in figures 5.14-5.17 that correspond to peaks listed in table 5.4 are highlighted, and those peaks that can be unambiguously assigned are also highlighted.

It was immediately evident that the majority of peaks could not be unambiguously assigned, as they corresponded to 2 or more members of figures 5.14-5.17. Consider, for example, the peak observed at m/z 503.4. This particular peak could be an alkyl-containing **D** (figure 5.14) or **E** (figure 5.15) fragment or a non-alkyl containing **D** (figure 5.16) or **E** (figure 5.17) fragment, or may even arise from all of these.

Within this context, it was perhaps more meaningful to examine which structural combinations were *not* observed in the collision-induced dissociation spectrum. From figure 5.14 it was apparent that the combinations of possible fragments only correlated with peaks actually observed in the CID spectrum over the left side of the diagram. No correlation was observed on the right side of figure 5.14 There was no observation of the loss of ethylene-glycol-only blocks from the molecule ions e.g. m/z's 807.5, 763.5, 719.5, 675.5 etc. This suggests that there was a tendency for there to be few ethylene glycol units at the end of the ion where this particular fragmentation took place (in this case the non-alkyl end). In fact, no peaks corresponding to an ethylene glycol loss were observed until level 3 of figure 5.14.

From figure 5.17 a correlation between possible and observed peaks could be observed for the centre and right of the diagram. Loss of propylene-glycol-only blocks larger than 4 units (m/z 579.3) could not be observed, suggesting a high probability of ethylene glycol at this end of the ion (the alkyl end). Figures 5.15 and 5.16 do not elucidate much information about the copolymer structure, as the majority of possible fragment ions corresponded with peaks observed from the CID spectrum.

Figures 5.14 and 5.17 thus suggest that though the copolymer was supposedly random, there may be some block-like structure, and especially a tendency for propylene glycol to predominate at the non-alkyl end.

Figure 5.18 shows a comparison between the low m/z region of the collision-induced dissociation spectrum of the copolymer and the low m/z regions of the high-energy xenon CID spectra of poly(ethylene glycol) and poly(propylene glycol). From figure 5.18 it was clear that the most intense peaks in the low m/z region of the CID spectrum of the copolymer corresponded to peaks that were intense in either the CID spectrum of poly(ethylene glycol) or the CID spectrum of poly(propylene glycol). The most intense peak that was only observed in the CID spectrum of the copolymer, highlighted in figure 5.18 as *, was m/z 57. This peak can be assigned as $CH_3CH_2CH_2CH_2^+$, and identifies the butyl end-group of the copolymer.

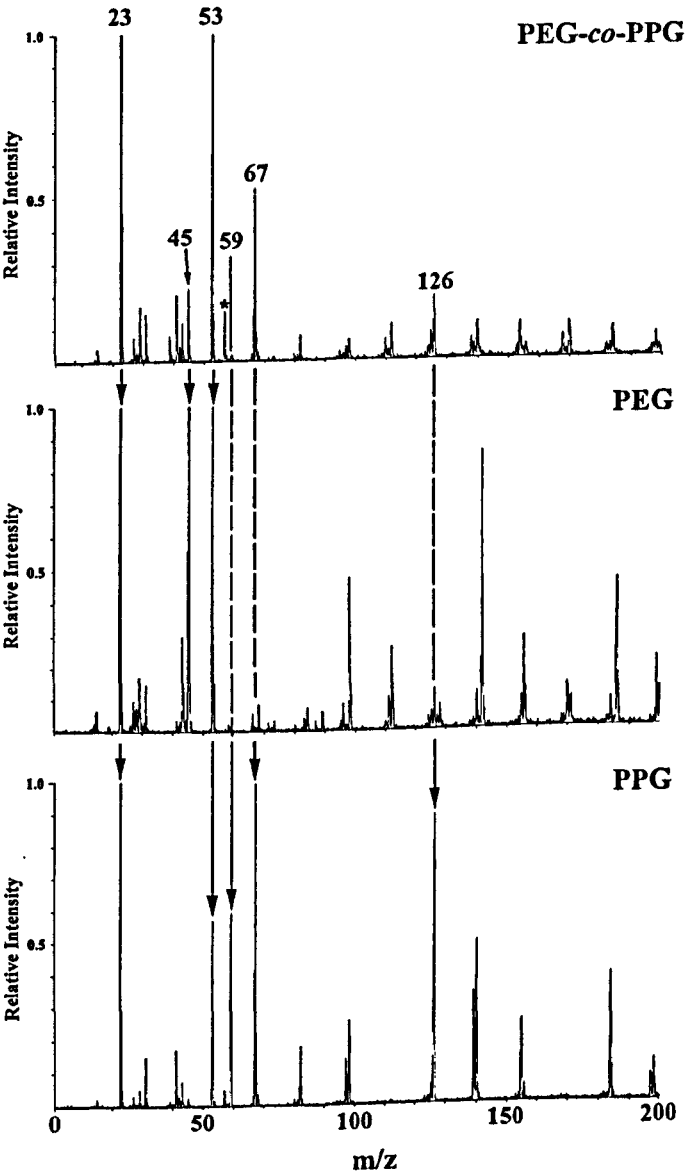

Figure 5.18 - comparison of the low m/z regions of the xenon CID spectra of:
TOP - poly(ethylene glycol)-co-poly(propylene glycol) monobutyl ether m/z 869.6
CENTRE - poly(ethylene glycol) m/z 1097.6
BOTTOM - poly(propylene glycol) m/z 969.7

5.6 Determination of End Groups of Polyglycol Ions Generated by Matrix-Assisted Laser Desorption/Ionisation using High-Energy Collision-Induced Dissociation

$[M+Na]^+$ adduct ions of acetyl-, butanoyl-, benzoyl and palmitoyl end-terminated poly(ethylene glycol) (figure 5.19) were selected in turn by adjusting the magnetic-field strength in MS-1 of the MAG-TOF instrument. Collision-induced dissociation was performed upon the selected ion by introducing an inert gas (helium or xenon were used) into the collision chamber.

Figure 5.20 shows the high-energy collision-induced dissociation spectra of the acetyl end-terminated poly(ethylene glycol) $[M+Na]^+$ adduct ion m/z 1181.7 (n=24) using helium (a) and xenon (b) collision gases. It was apparent from these spectra that there was a slight increase in the relative intensity of the low m/z ions using Xe

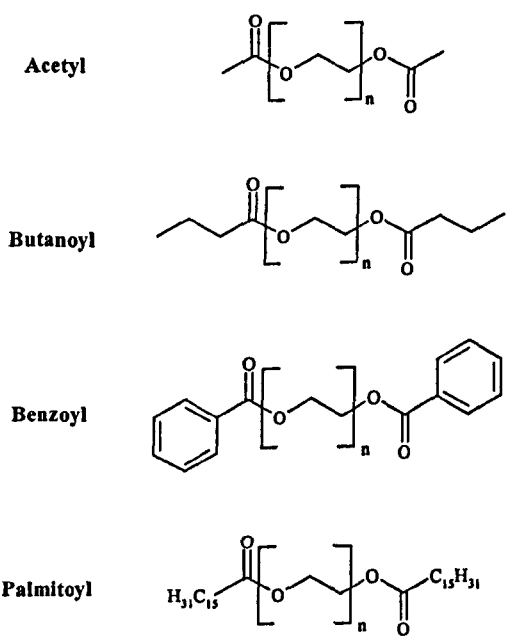

Figure 5.19 - structures of the different poly(ethylene glycol) samples investigated, illustrating the different end-groups.

as the collision gas, as compared with He. An $m/z_{(observed)}$ vs. intensity list for the xenon CID spectrum is given in table 6.5. The majority of fragment ion peaks observed for the CID of acetyl end-terminated poly(ethylene glycol) were found to be analogues of the fragment ion series observed for standard poly(ethylene glycol) (chapter 5.3). Assignments **A-E** in table 5.5 are proposed to arise from the acetyl-analogues of reactions 5.3[A]-5.3[E].

A comparison of the low m/z region of figure 5.20 compared with the low m/z region of the CID spectrum of a poly(ethylene glycol) standard $[M+Na]^+$ adduct ion m/z 1097.6 (n=24) is shown in figures 5.21 (a) and (b). The distinguishing features in the low m/z region of the CID spectrum of acetyl end-terminated poly(ethylene glycol) (figure 5.21 (b)) are the intense m/z 43 and m/z 87 peaks. An m/z 43 peak was observed for the CID of the poly(ethylene glycol) standard, but this weak, and no m/z 87 was observed for the CID of the poly(ethylene glycol) standard. These peaks observed in the low m/z region of figure 5.21 (b) are attributed to $[CH_3CO]^+$ (m/z 43) and $[CH_3CO+C_2H_4O]^+$ (m/z 87).

Xenon was used as the collision gas for the collision-induced dissociation of butanoyl and benzoyl end-terminated poly(ethylene glycol), as the higher centre-of-mass collision energies achieved using xenon were advantageous for promoting the intensities of the low m/z fragment ions. A comparison of the low m/z regions of the xenon CID spectra of the butanoyl end-terminated poly(ethylene glycol) $[M+Na]^+$ adduct ion m/z 1237.7 (n=24), the benzoyl end-terminated poly(ethylene glycol) $[M+Na]^+$ adduct ion m/z 1305.7 (n=24) and the terminated poly(ethylene glycol) $[M+Na]^+$ adduct ion m/z 1097.6 (n=24) is shown in figure 5.22. The distinguishing features of the xenon CID spectrum of butanoyl poly(ethylene

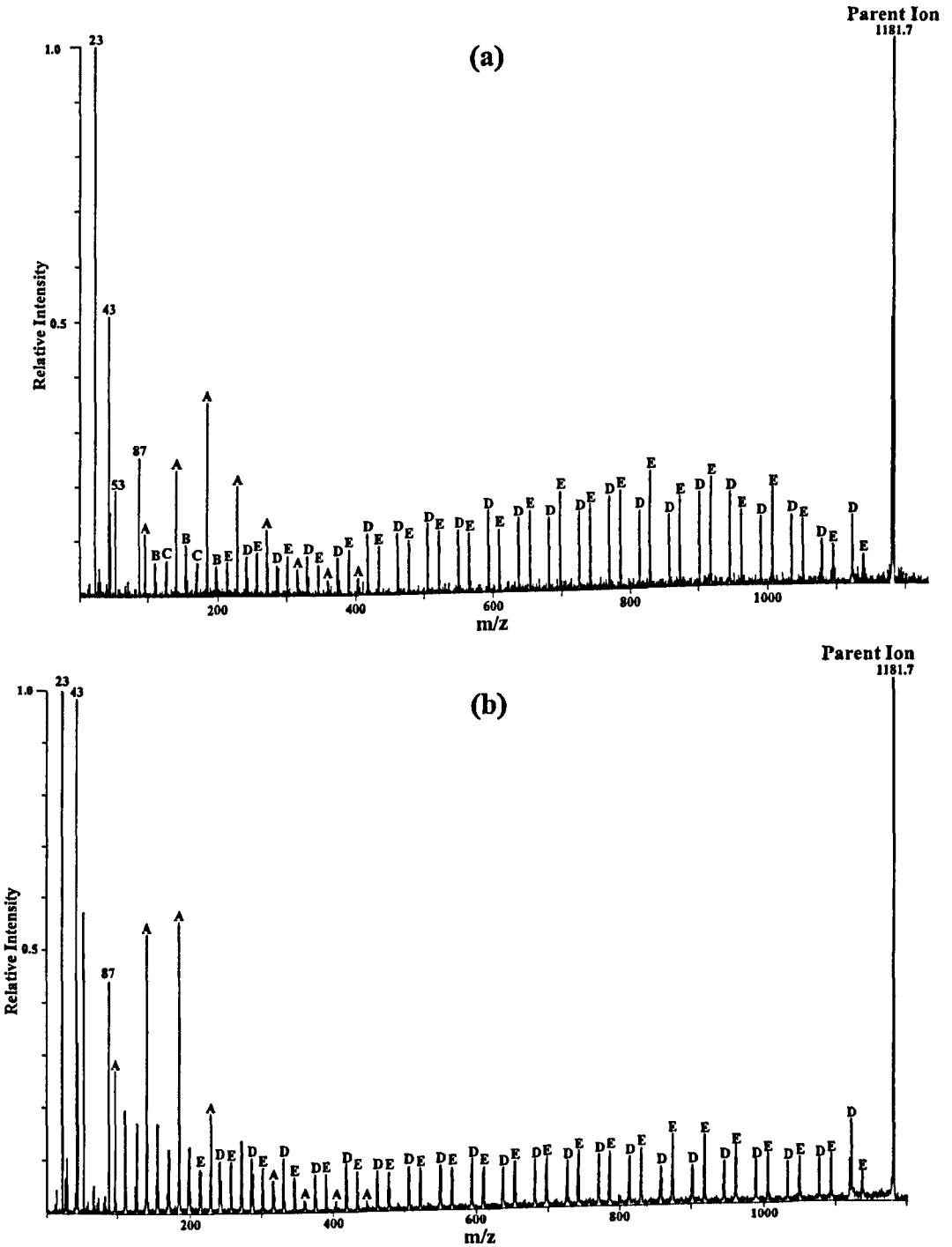

Figure 5.20 - high-energy CID spectra of acetyl end-terminated poly(ethylene glycol) $[M+Na]^+$ m/z 1181.7 (n=24) using helium (a) and xenon (b) collision gas.

Table 5.5 - Analysis of the CID spectrum of acetyl end-terminated poly(ethylene glycol) $[M+Na]^+$ adduct ion m/z 1181.7 (n=24) using xenon collision gas.

m/z_{obs}	Intensity	Assignment	m/z_{calc}	$m/z_{obs} - m/z_{calc}$
1181.7	100.00	Parent	1181.65	0.05
1137.7	0.75	E	1137.71	-0.01
1121.8	1.02	D	1121.72	0.08
1119.5	0.52			
1093.7	0.59	E	1093.68	0.02
1077.7	0.60	D	1077.69	0.01
1049.7	0.61	E	1049.65	0.05
1033.6	0.54	D	1033.66	-0.06
1005.4	0.70	E	1005.62	-0.22
989.5	0.53	D	989.63	-0.13
961.6	0.66	E	961.59	0.01
945.6	0.55	D	945.60	0.00
917.6	0.83	E	917.56	0.04
901.5	0.50	D	901.57	-0.07
873.5	0.87	E	873.53	-0.03
857.5	0.58	D	857.54	-0.04
829.6	0.73	E	829.50	0.10
813.7	0.67	D	813.51	0.19
785.7	0.68	E	785.47	0.23
769.6	0.68	D	769.48	0.12
741.7	0.85	E	741.44	0.26
725.8	0.63	D	725.45	0.35
697.6	0.70	E	697.41	0.19
681.6	0.66	D	681.42	0.18
653.5	0.60	E	653.38	0.12
637.5	0.58	D	637.39	0.11
609.6	0.55	E	609.35	0.25
593.6	0.67	D	593.36	0.24
565.5	0.54	E	565.32	0.18
549.6	0.63	D	549.33	0.27
521.4	0.58	E	521.29	0.11
505.4	0.66	D	505.30	0.10
477.4	0.58	E	477.26	0.14
461.4	0.47	D	461.27	0.13
433.3	0.54	E	433.23	0.07
417.4	0.63	D	417.24	0.16
389.3	0.46	E	389.20	0.10
373.3	0.50	D	373.21	0.09
360.2	0.13	A	360.20	0.00
345.4	0.48	E	345.17	0.23
329.3	0.62	D	329.18	0.12
316.1	0.42	A	316.17	-0.07
301.3	0.61	E	301.14	0.16
287.2	0.47			
285.3	0.66	D	285.15	0.15
272.4	0.83	A	272.14	0.26

271.3	0.93			
257.3	0.75	E	257.11	0.19
241.3	0.67	D	241.12	0.18
228.2	1.34	A	228.11	0.09
214.2	0.61	C	214.09	0.11
213.1	0.62	E	213.08	0.02
198.2	0.83	B	198.09	0.11
197.2	0.45	D	197.09	0.11
184.2	3.67	A	184.08	0.12
170.2	0.85	C	170.06	0.14
169.2	0.58	E	169.05	0.15
168.1	0.26			
156.2	0.26			
155.1	0.33			
154.2	1.13	B	154.06	0.14
153.2	0.40	D	153.06	0.14
140.1	3.63	A	140.05	0.05
126.2	1.12	C	126.03	0.17
125.1	0.33	E	125.02	0.08
124.2	0.37			
112.1	0.25			
111.1	0.55			
110.1	1.34	B	110.03	0.07
96.2	1.76	A	96.02	0.18
95.2	0.40			
87.1	3.07	CH_3-(C=O)-$C_2H_4O^+$		
82.1	0.18			
80.1	0.14			
73.1	0.25	$C_3H_5O_2^+$		
71.1	0.21			
67.1	0.32			
66.0	0.30			
59.1	0.15			
53.0	3.70	$NaCH_2O^+$		
45.1	2.30	$C_2H_5O^+$		
44.1	0.34	$C_2H_4O^+$		
43.0	6.83	CH_3-$C{=}O^+$		
41.1	0.21	C_2HO^+		
31.0	0.38	CH_3O^+		
29.0	0.75	$C_2H_5^+$/CHO^+		
28.0	0.46	$C_2H_4^+$		
27.0	0.42	$C_2H_3^+$		
23.0	24.33	Na^+	22.99	0.01
15.0	0.32	CH_3^+		

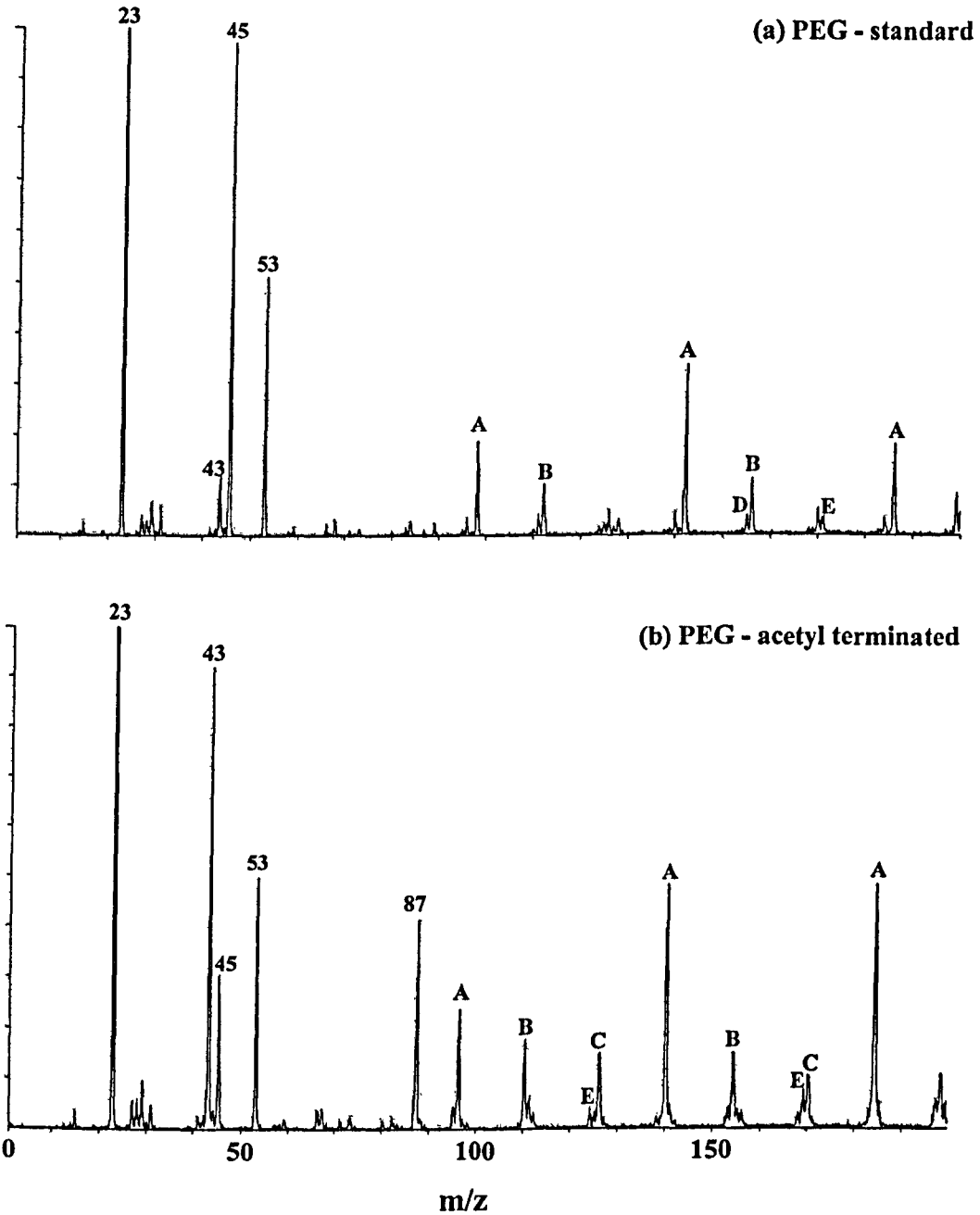

Figure 5.21 - comparison of the low m/z regions of the xenon CID spectra of (a) poly(ethylene glycol) $[M+Na]^+$ adduct ion m/z 1097.6 (n=24) and (b) acetyl end-terminated poly(ethylene glycol) $[M+Na]^+$ adduct ion m/z 1181.7 (n=24).

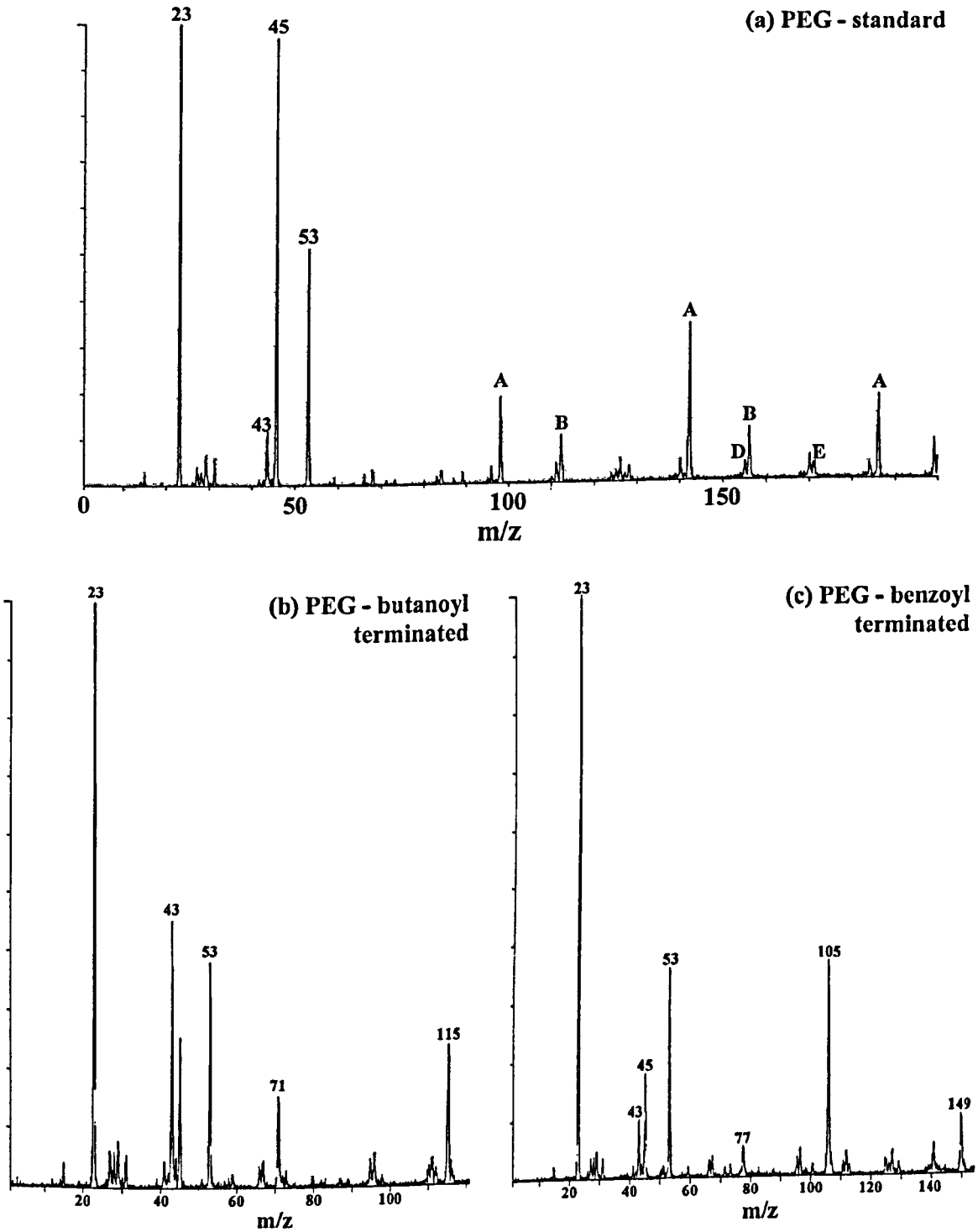

Figure 5.22 - comparison of the low m/z regions of the xenon CID spectra of (a) poly(ethylene glycol) $[M+Na]^+$ adduct ion m/z 1097.6 (n=24), (b) butanoyl end-terminated poly(ethylene glycol) $[M+Na]^+$ adduct ion m/z 1237.7 (n=24) using xenon collision gas and (c) benzoyl end-terminated poly(ethylene glycol) $[M+Na]^+$ adduct ion m/z 1305.7 (n=24).

glycol) (figure 5.22 (b)) were the intense fragment ion peaks at m/z 43, 71 and 115. It is proposed that the intense m/z 43 peak arises from the $[CH_3CH_2CH_2]^+$ fragment. The strong peak at m/z 71 is attributed to $[CH_3CH_2CH_2CO]^+$, and the peak at m/z 115 attributed to $[CH_3CH_2CH_2CO+C_2H_4O]^+$.

The xenon CID spectrum benzoyl end-terminated poly(ethylene glycol) (figure 5.22 (c)) showed intense peaks at m/z 105, attributed to $[C_6H_5CO]^+$, and m/z 149 attributed to $[C_6H_5CO+C_2H_4O]^+$. The peak observed at m/z 77 was attributed to the aryl ion $[C_6H_5]^+$.

The significance of these low m/z peaks observed in the CID spectra of acetyl, butanoyl and benzoyl end-terminated poly(ethylene glycol) was that the end-groups of the polymer were easily identifiable, as were fragments of the end-groups.

The collision-induced dissociation spectrum of the palmitoyl end-terminated poly(ethylene glycol) $[M+Na]^+$ adduct ion m/z 1001.8 (n=11), using helium as the collision gas, is shown in figure 5.23. An analysis of the CID spectrum is given in table 5.6.

The distinguishing feature of the CID spectrum of palmitoyl end-terminated poly(ethylene glycol) is an intense series of fragment ions, that have been labelled C_3 through C_{15}. These correspond to fragment ions resulting from C-C bond dissociations of the palmitoyl end-group at the positions shown in figure 5.24. Similar fragment ion series have been reported for CID spectra of saturated fatty acids.[161] Several mechanisms have been postulated to give rise to the C-C bond dissociations observed for saturated fatty acids, including 1,4-H_2-elimination proposed by Jensen et al.,[162] direct homolytic cleavage of the C-C bond proposed by Wysocki and Ross,[163] and a multistep radical mechanism involving elimination of an $H^{\cdot}$ radical as an initial rate-determining step.[164]

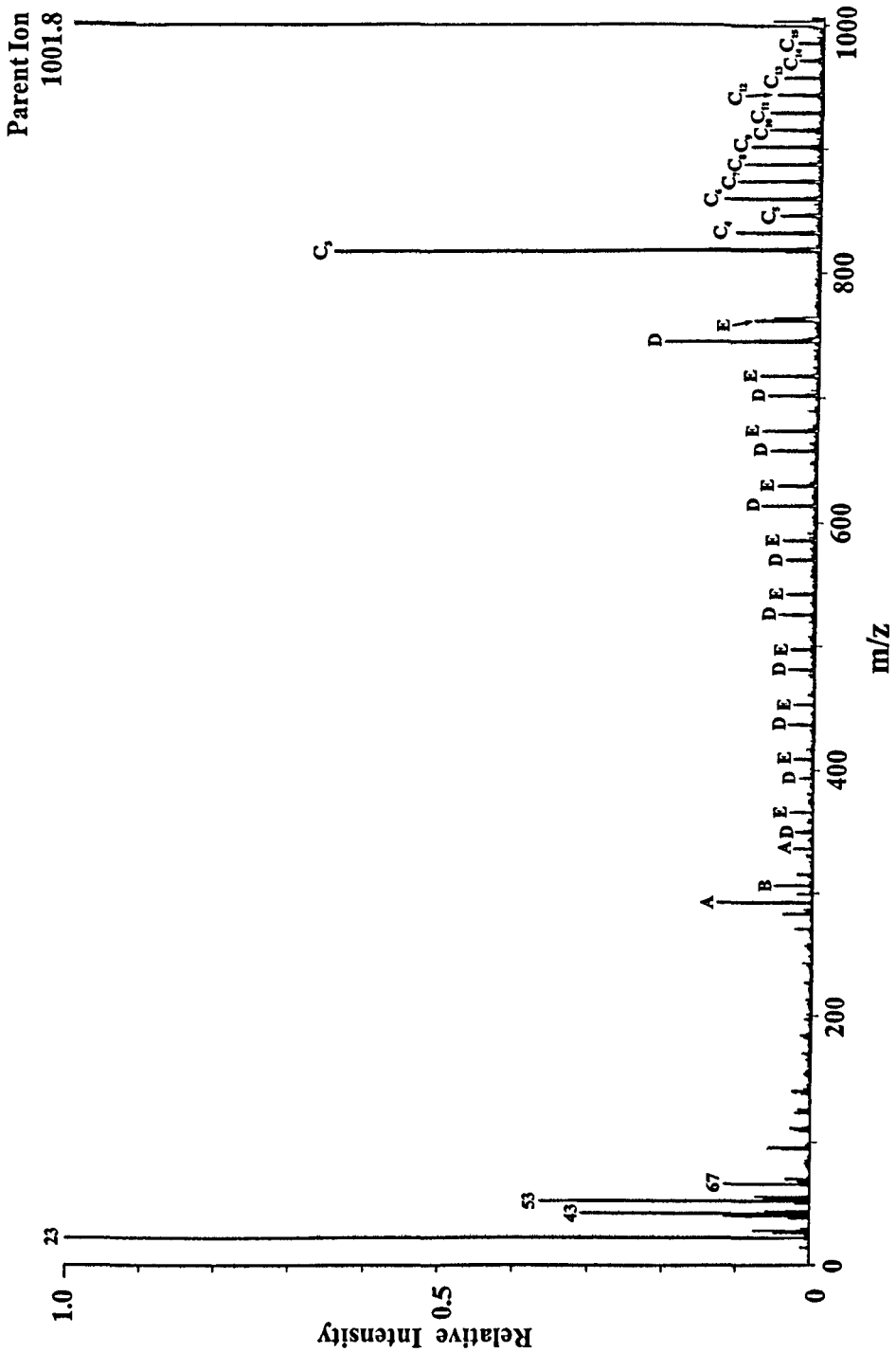

Figure 5.23 - Collision-induced dissociation spectrum of the palmitoyl end-terminated poly(ethylene glycol) $[M+Na]^+$ adduct ion m/z 1001.8 (n=11) using helium collison gas.

Table 5.6 - Analysis of the CID spectrum of palmitoyl end-terminated poly(ethylene glycol) $[M+Na]^+$ adduct ion m/z 1001.8 (n=11) using helium collision gas.

m/z_{obs}	Intensity	Assignment	m/z_{calc}	m/z_{obs} - m/z_{calc}
1001.8	100.00	Parent Ion	1001.8	0.0
985.9	0.38	C_{15}	985.7	0.2
971.9	0.33	C_{14}	971.7	0.3
957.7	0.52	C_{13}	957.6	0.1
943.6	0.62	C_{12}	943.6	0.0
929.6	0.71	C_{11}	929.6	0.0
915.6	0.73	C_{10}	915.6	0.0
901.7	0.96	C_9	901.6	0.2
887.6	1.08	C_8	887.5	0.1
873.5	1.13	C_7	873.5	0.0
859.5	1.32	C_6	859.5	0.0
845.5	0.57	C_5	845.5	0.0
831.6	1.13	C_4	831.5	0.1
817.6	6.46	C_3	817.4	0.2
763.7	0.62			
761.6	0.87	E	761.6	0.1
745.6	2.18	D	745.6	0.1
717.8	0.81	E	717.5	0.3
701.9	0.71	D	701.5	0.4
673.9	0.78	E	673.5	0.4
657.9	0.63	D	657.5	0.4
629.8	0.56	E	629.5	0.3
613.9	0.74	D	613.5	0.4
585.7	0.48	E	585.4	0.3
569.7	0.42	D	569.4	0.3
541.6	0.39	E	541.4	0.2
525.6	0.50	D	525.4	0.2
497.4	0.33	E	497.4	0.0
481.4	0.35	D	481.4	0.0
453.5	0.31	E	453.3	0.2
437.5	0.38	D	437.3	0.2
409.4	0.27	E	409.3	0.1
393.6	0.18	D	393.3	0.3
365.5	0.33	E	365.3	0.2
349.5	0.22	D	349.3	0.2
336.4	0.28	A	336.3	0.1
315.3	0.19			
306.4	0.53	B	306.3	0.1
299.3	0.21			
292.3	1.25	A	292.2	0.1
283.3	0.40			
271.1	0.23			
140.1	0.25	$C_{10}H_{20}^+$		
126.1	0.17	$C_9H_{18}^+$		
123.1	0.19			
111.1	0.27			

110.0	0.21			
109.0	0.16			
96.1	0.58			
95.1	0.39			
71.1	0.34	$CH_3(CH_2)_4^+$		
69.1	0.18			
67.0	1.18			
57.0	0.73	$CH_3(CH_2)_3^+$		
55.0	0.63			
53.0	3.58			
51.0	0.21			
45.0	0.63			
43.0	3.13	$CH_3CH_2CH_2^+$		
41.0	1.21			
39.0	0.33			
29.0	0.77	$CH_3CH_2^+$		
28.0	0.20	C2H4+		
27.0	0.50	C2H3+		
23.0	46.67	Na+	23.0	
15.0	0.15	CH_3^+		

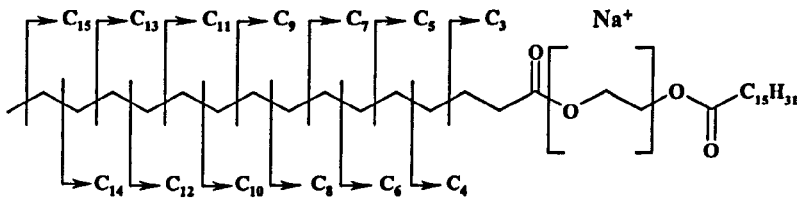

Figure 5.24 - nomenclature for C-C bond dissociation of the palmitoyl end-group.

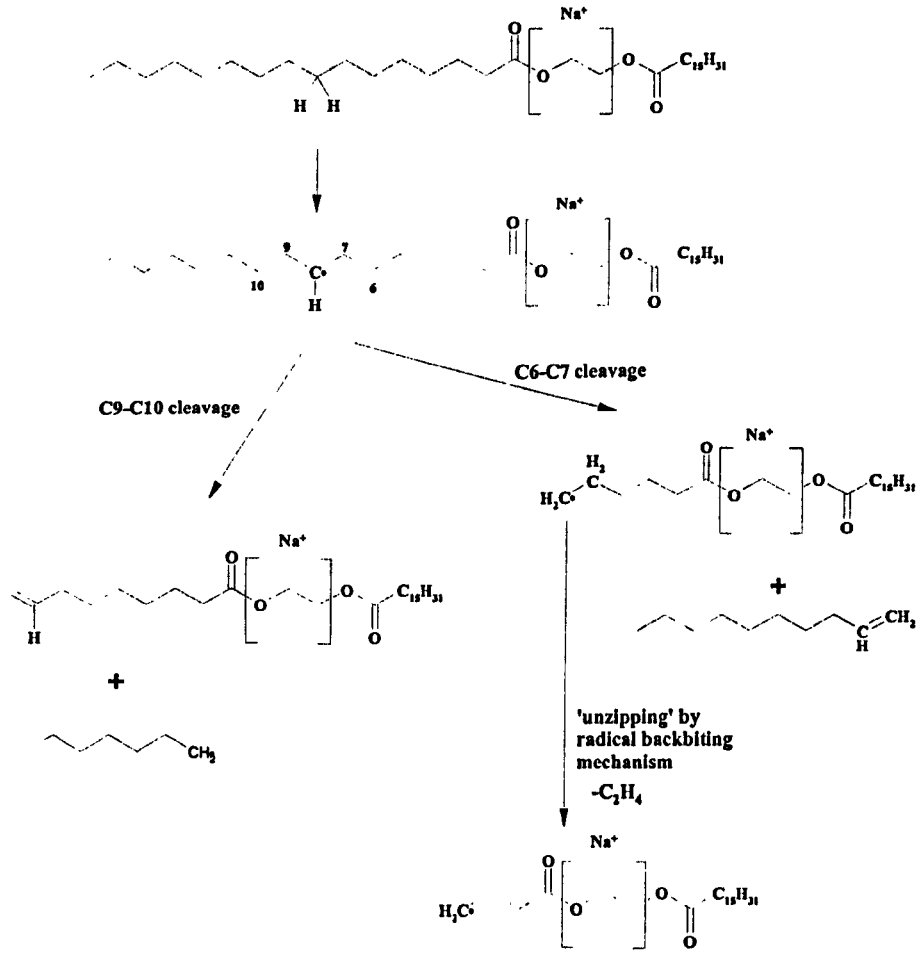

Figure 5.25 - radical mechanism to rationalise C_n ions formed by high-energy collision-induced dissociation of the palmitoyl end-terminated poly(ethylene glycol) $[M+Na]^+$ adduct ion m/z 1001.8 (n=11).

It can be seen from figure 5.23 that the C_3 fragment ion was particularly intense, and that there is a general trend for decreasing intensity with increased m/z for the C_n fragment ion series. This observation could rationalise a radical mechanism as a major fragmentation route in the CID of palmitoyl end-terminated poly(ethylene glycol), as 'unzipping', possible in a radical mechanism, would lead to increased intensity of the smaller members of the C_n series (see figure 5.25). No odd-electron were observed, however, in the CID spectra i.e. $C_n^{\bullet}$ was not observed.

The significance of the C_n series of ions is that the structure of the palmitoyl end-group can be unambiguously determined from the CID spectrum. The C_n series of ions would also make it possible to determine between isomeric alkyl chain end-groups, locate positions of substituent groups or locate double bond positions in the polymer end-groups.

Chapter Six –*Collision-Induced Dissociation of Protonated Polyglycols.*

6.1 Introduction

It was not possible to readily generate $[M+H]^+$ ions of poly(ethylene glycol) and poly(propylene glycol) by matrix-assisted laser desorption/ionisation.. It was thus necessary to utilise a different ionisation technique in order to investigate the CID of $[M+H]^+$ ions of of poly(ethylene glycol) and poly(propylene glycol)poly(propylene glycol). Field desorption was chosen, as it has been widely reported to produce $[M+H]^+$ ions for a range of polyglycol polymers. .[165, 166, 167]

Field desorption ionisation was not available on the MAG-TOF instrument, so all experiments were carried out using another sector/time-of-flight hybrid instrument, the ZabSpec *oa*-TOF.[168, 169] . A schematic diagram of the ZabSpec *oa*-TOF instrument is shown in figure 6.1. Due to the restrictive nature of the orthogonal time-of-flight analyser, the maximum laboratory-frame collision energy that could be used was 800 eV.

$[M+H]^+$ ions of poly(ethylene glycol), poly(propylene glycol), acetyl end-terminated poly(ethylene glycol) and benzoyl end-terminated poly(ethylene glycol), were generated in turn by field desorption, and accelerated by a potential of 8 kV. A

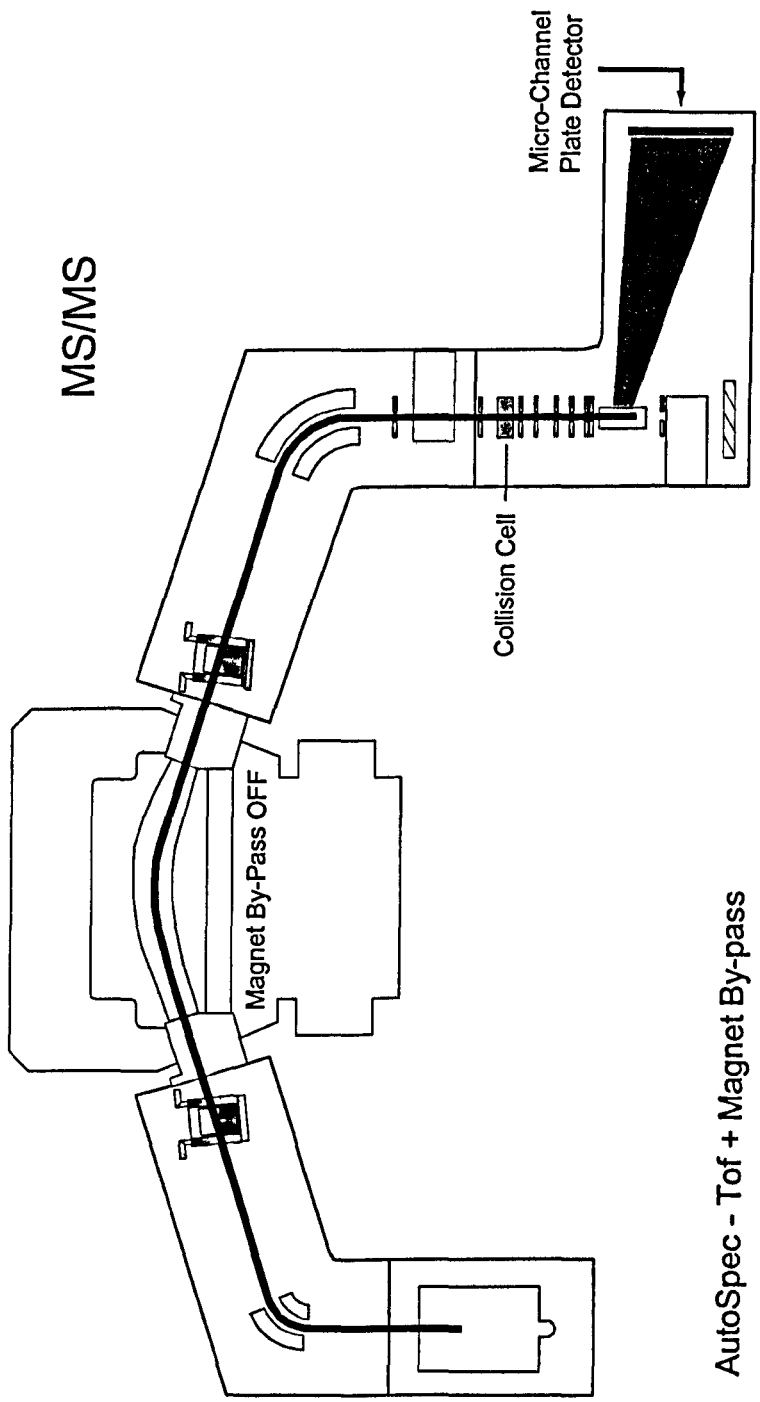

Figure 6.1 – Schematic diagram of a ZabSpec *oa*-TOF instrument.

particular oligomer from the polymer series was selected by adjusting the magnetic field strength in MS-1.The resolution of the double-focusing mass spectrometer was sufficient to ensure that only the monoisotopic (^{12}C only) isotope passed through the exit-slit of MS-1. Prior to collision the ions were decelerated, such that the laboratory-frame collision-energy was 800 eV. Collision-induced dissociation was performed on the selected ion by introducing an inert gas into the collision chamber. The fragments from these collisions were observed using an orthogonal-acceleration time-of-flight analyser.

The low-energy collision-induced dissociation spectra of the $[M+H]^+$ n=32 (where n is the number of repeat units) oligomer of poly(ethylene glycol), m/z = 1427.8, using helium as the collision gas is shown in figure 6.2. The centre-of-mass collision energy was 1.12 eV.

The low-energy collision-induced dissociation spectra of the $[M+H]^+$ n=16 oligomer of poly(propylene glycol), m/z = 947.8, using helium as the collision gas is shown in figure 6.3. The centre-of-mass collision energy was 1.68 eV.

The low-energy collision-induced dissociation spectra of the $[M+H]^+$ n=22 oligomer of acetyl end-terminated poly(ethylene glycol), m/z = 1071.7, using helium as the collision gas is shown in figure 6.4. The centre-of-mass collision energy was 1.49 eV.

The low-energy collision-induced dissociation spectra of the $[M+H]^+$ n=21 oligomer of benzoyl end-terminated poly(ethylene glycol), m/z = 1151.6, using helium as the collision gas is shown in figure 6.5. The centre-of-mass collision energy was 1.39 eV.

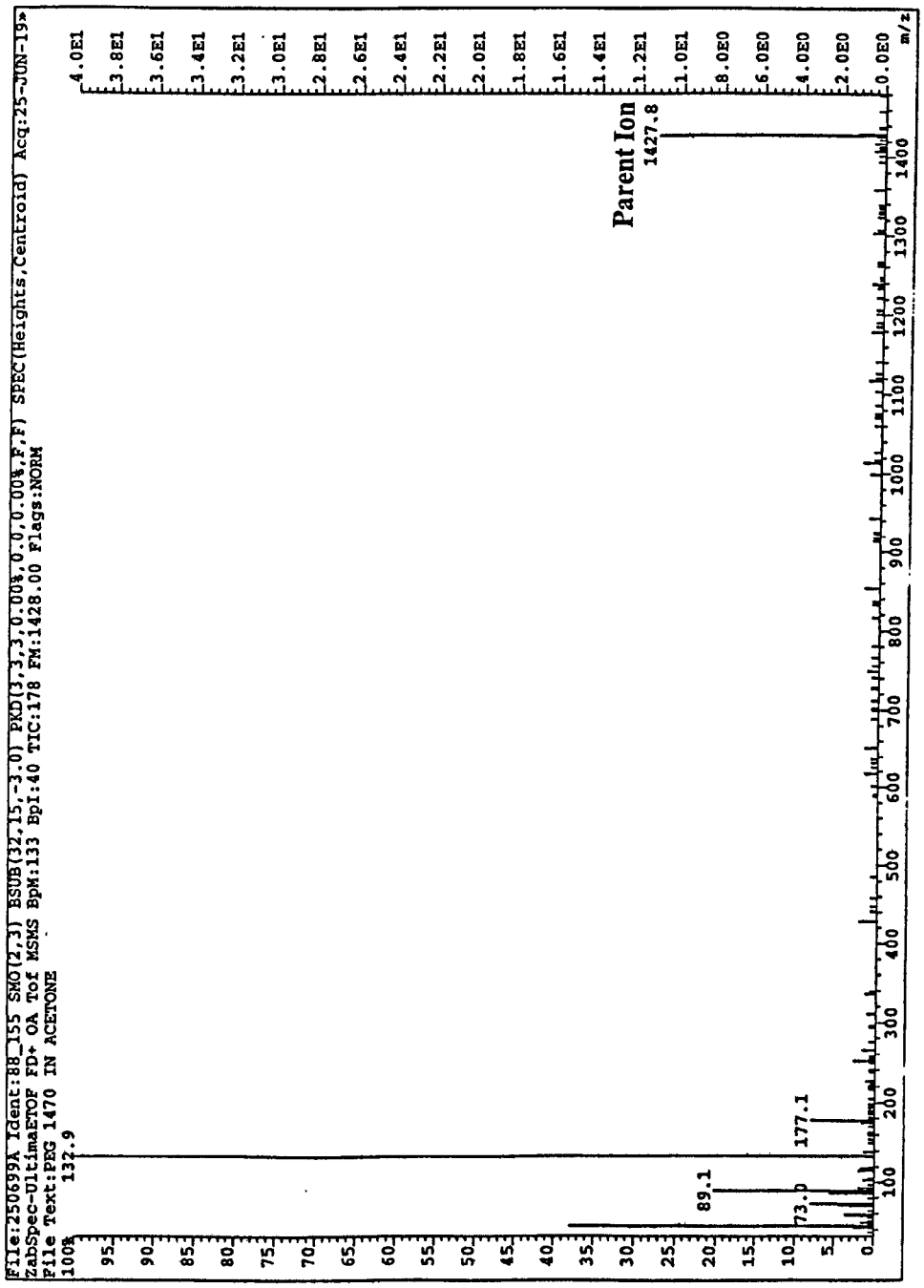

Figure 6.2 – Low-energy collision-induced dissociation of the $[M+H]^+$ n=32 oligomer of poly(ethylene glycol), generated by field desorption and using helium collision gas.

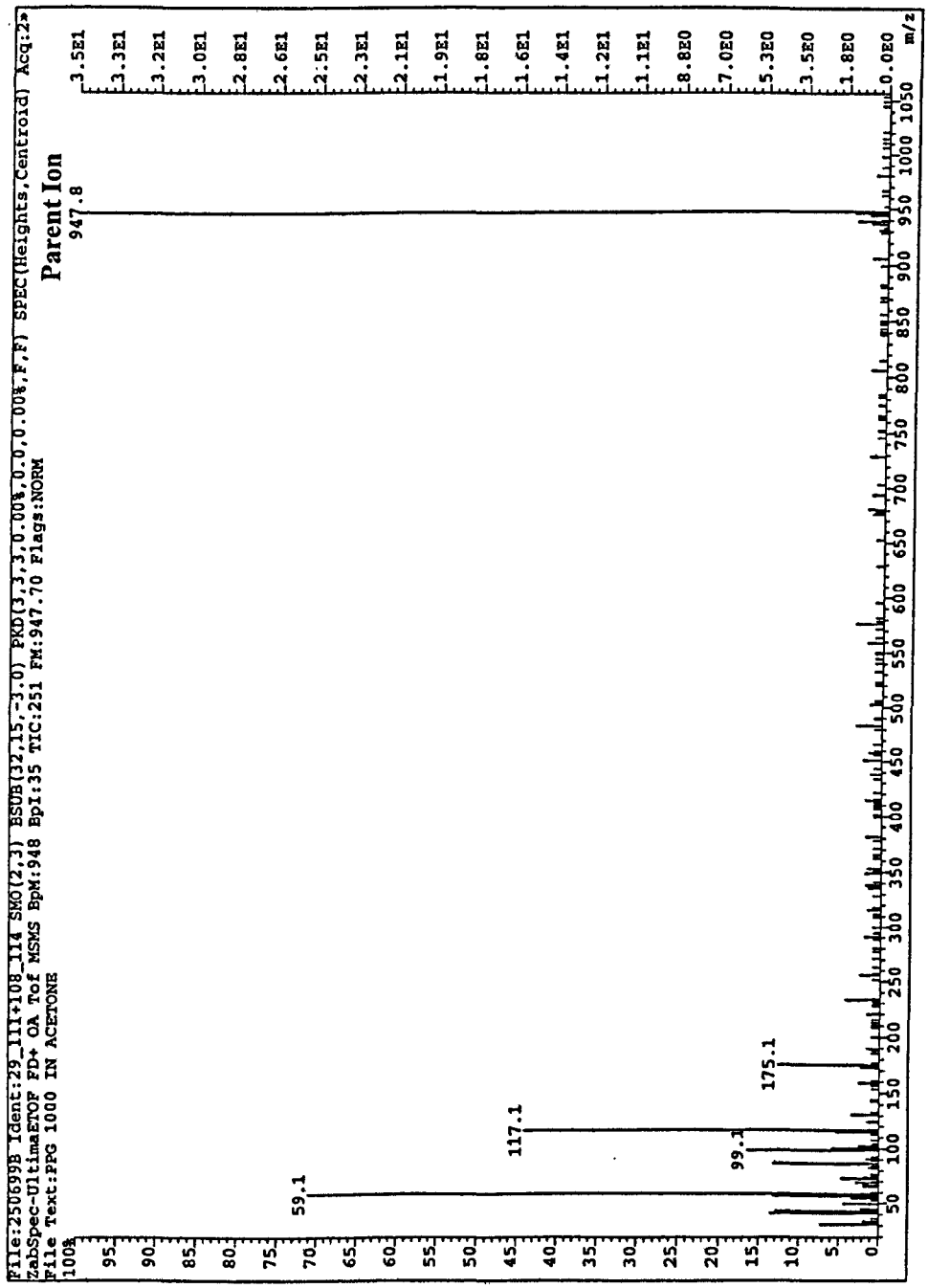

Figure 6.3 – Low-energy collision-induced dissociation of the $[M+H]^+$ n=16 oligomer of poly(propylene glycol), generated by field desorption and using helium collision gas.

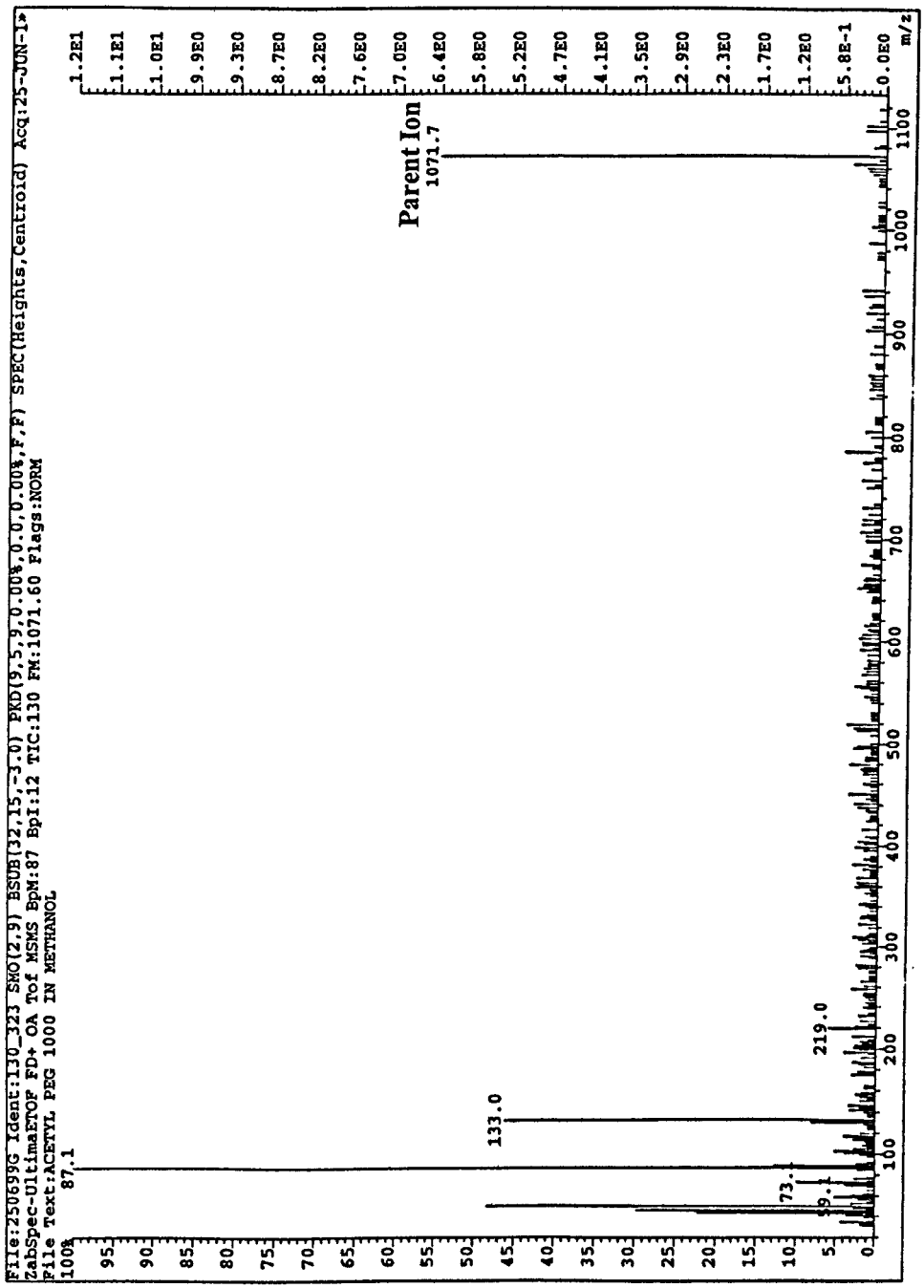

Figure 6.4 – Low-energy collision-induced dissociation of the $[M+H]^+$ n=22 oligomer of acetyl end-terminated poly(ethylene glycol), generated by field desorption and using helium collision gas.

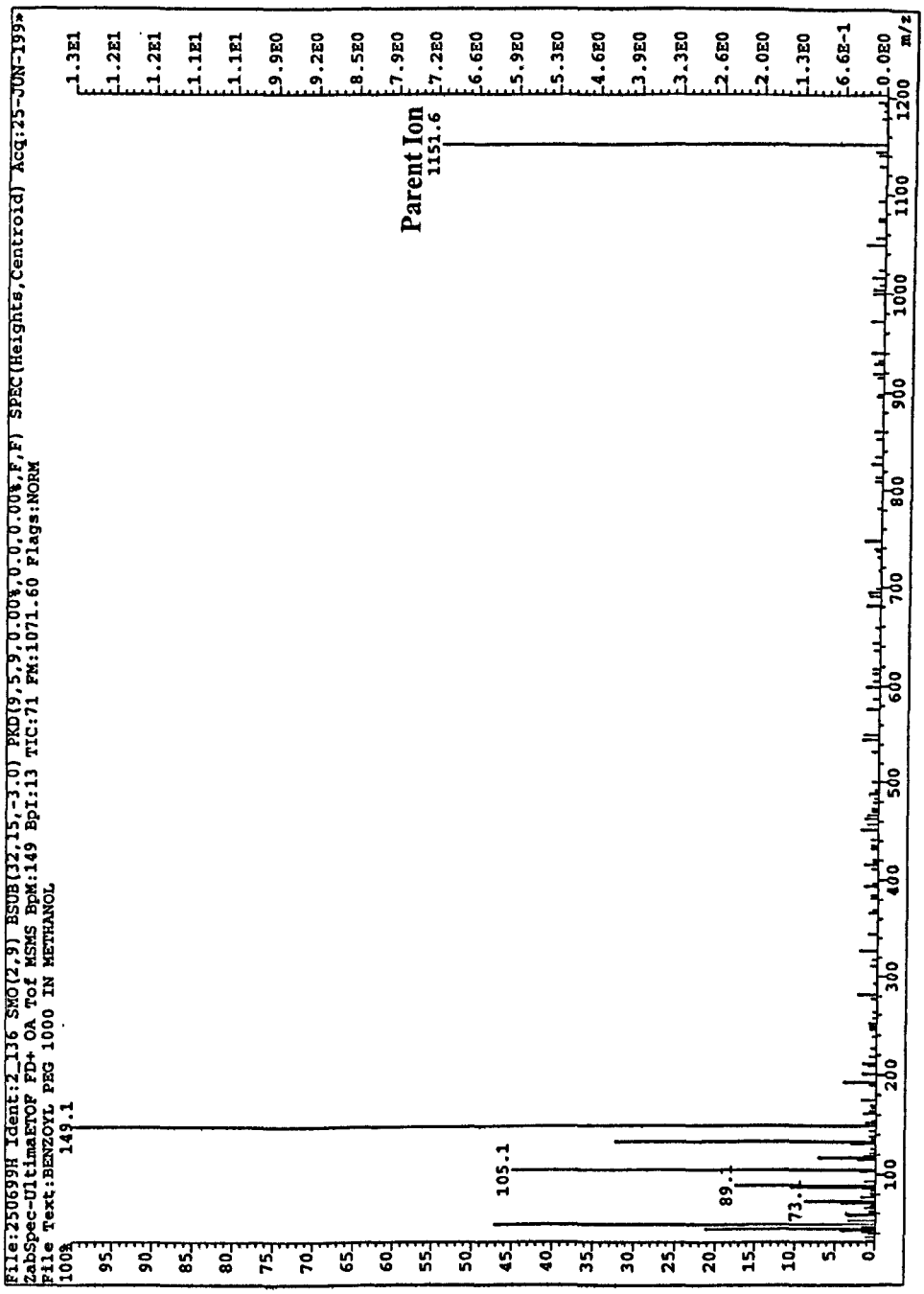

Figure 6.5 – Low-energy collision-induced dissociation of the $[M+H]^+$ n=21 oligomer of poly(ethylene glycol), generated by field desorption and using helium collision gas.

All of the fragments that were observed in figures 6.2-6.5 were low m/z fragments. In particular, figures 6.4 and 6.5 show the low m/z fragments associated with the polymer end-groups that were reported in chapter 5.

The observation of intense low m/z ions is consistent with previous reports of collision-induced dissociation of polyglycol ions generated by field desorption,[146, 147] where the low m/z ions were observed to be the most intense. These previous studies did, however, report fragment-ion series that were observed throughout the m/z range of the CID spectra, and were not observed in figures 6.2-6.5

The main experimental difference of the collision-induced dissociation experiments performed as part of this study was the comparatively low collision energy-regime, necessarily employed due to the orthogonal time-of-flight analyser, of approximately 1.5 eV (compared with >15 eV used by Craig[146] and Agma[147]).

Chapter Seven –*Conclusion*

7.1 The tandem double-focusing/time-of-flight instrument.

Prior to this study, applications of the tandem double-focusing / time-of-flight mass spectrometer (MAG-TOF) had been limited to the collision-induced dissociation of small peptides, such as subtance P and renin substrate tetradecapeptide,[170] due to a lack of sensitivity. Experimental results obtained from the collision-induced dissociation of C_{60}^+ (figure 3.1) and $[M+Na]^+$ adduct ions of poly(ethylene glycol) (figure 3.2) exemplified this lack of sensitivity.

Transmission of ions through the ion source so as to match the acceptance parameters of the double-focusing mass spectrometer was found to be low through the use of SIMION ion trajectory calculations. The first focusing electrode acting on ion-beam was situated at a distance of 53 mm from the sample probe tip. By the time the ion-beam had reached this position, it was shown to be highly divergent and was difficult to correct.

In order to provide adequate focusing and collimation of the ion beam it was necessary to introduce focusing elements closer to the point of ion formation. Practically this meant removing the extraction plate (that provided little collimation of the ion-beam) and introducing a set of electrostatic lens between the accelerating electrode and the source cradle that would provide both extraction and collimation of

the ion-beam.

An accelerating einzel lens of rotational symmetry was modelled using the SIMION ion trajectory software. An accelerating einzel lens was shown to provide sufficient collimation for the ion-beam to match the acceptance parameters of the double-focusing mass spectrometer. The potential required to be applied to the centre electrode of the einzel lens was shown to be approximately −11 kV. The resulting time-aberration from such a lens was 3 ns.

An accelerating einzel lens, based upon the SIMION ion trajectory calculations, was manufactured and installed in the ion-source of the MAG-TOF instrument. An increase in the ion-transmission through the instrument was determined experimentally to be in excess of a factor of 5 (cf. figures 3.2 and 6.1).

7.2 High-energy collision-induced dissociation of fullerenes.

In order to test the capabilities of the new ion-source design of the MAG-TOF instrument, a series of collision-induced dissociation experiments were performed on fullerenes. Additionally, the collision-induced dissociation of fullerenes allowed new protocols to be established for the calibration of the MAG-TOF instrument (see Appendix I).

The collision-induced dissociation of C_{60}^+ and C_{70}^+ had already been reported.[95, 96] In the high m/z region of the CID spectra obtained using the MAG-TOF instrument, all the fragment ion peaks corresponded to C_{2n} loss from the parent. C_n loss was detected in the low m/z region of the CID spectra, where n=31-55 for C_{60}^+ and n=36-67 for C_{70}^+.

The collision-induced dissociation of $^{12}C_{59}{}^{13}C_1{}^+$ using helium as the collision gas showed a similar spectrum to that observed for $C_{60}{}^+$ in that C_{2n} loss was observed in the high m/z region of the spectrum, and that C_n loss was observed for n>30. All the fragment ions observed contained either 1 or 0 ^{13}C atoms:

for each $^{12}C_{59}{}^{13}C_1{}^+$ ion undergoing fragmentation, there was a possibility that the ^{13}C atom could be one of the atoms lost. For each carbon atom lost this was a cumulative 1 in 60 chance i.e. if two carbon atoms are lost there is a 2 in 60 possibility that this will be the ^{13}C atom. $^{12}C_{57}{}^{13}C_1{}^+$ will make up (58/60)*100% of the ion intensity for 58 carbon atoms, the rest (2/60)*100% will be isotopically pure $^{12}C_{58}$.

No helium adducts of $^{12}C_{59}{}^{13}C_1{}^+$ were observed due to a high noise level above the parent ion. Helium adducts were observed, however, for the loss of 2, 4, 6, 8 and 10 carbon atoms. As fullerenes are closed-cage structures, and that fragment adducts were observed for the loss of up to 10 carbon atoms, it is most likely that the adduct is endohedrally bound by the fullerene cage.[171] Assignments were made for, $He@^{12}C_{49}{}^{13}C_1{}^+$, $He@^{12}C_{51}{}^{13}C_1{}^+$, $He@^{12}C_{53}{}^{13}C_1{}^+$, $He@^{12}C_{55}{}^{13}C_1{}^+$ and $He@^{12}C_{57}{}^{13}C_1{}^+$. The laboratory-frame collision energy employed for the formation of these endohedrally bound helium-adducts was of the range 8-12 keV, giving a centre-of-mass collision energy of 44-66 eV. Studies by other workers have shown that the formation of $He@C_{60}$ could be optimised for laboratory-frame collision energies of between 5 and 6 keV, and was most probable for a centre-of-mass collision energy range of 31±3 eV, explaining the very low intensities of the endohedrally bound helium adducts using the much higher collision energy regime.

The structure of a fullerene, C_{130}^+, formed by coalescence under the conditions of laser desorption was probed by high-energy collision-induced dissociation. The observation of C_{2n} loss from C_{130}^+ indicates that the structure of this fullerene was that of a "giant" fullerene, rather than two smaller fullerenes "stuck" together. The absence of intense C_{60}^+ and C_{70}^+, indicated that there was no memory of the pre-coalescence structure, and refutes the idea that the structure consists of two smaller fullerenes "stuck" together.

Hydrogen loss from $C_{60}H_{36}^+$ under laser desorption conditions had been reported previously. High-energy collision-induced dissociation was performed upon three species generated from the laser desorption of $C_{60}H_{36}^+$, namely $C_{60}H_{35}^+$, $C_{60}H_{30}^+$ and $C_{60}H_{25}^+$. Collision-induced dissociation of these species did not result in the C_{2n} loss that was typical for pure carbon fullerenes.

H_m loss was observed, and appeared to show an odd/even effect. The intensity of peaks corresponding to the loss of an even number of hydrogen atoms was more intense than those observed for the loss of an odd number of hydrogen atoms (e.g. $C_{60}H_{58}^+ > C_{60}H_{59}^+$). This effect could not be observed once a carbon atom was lost from the fullerene cage.

In all cases, C_nH_m loss was observed for n=1-57. Fragments corresponding to odd numbers of carbon atoms were observed in the high m/z region of the CID spectra (unlike pure carbon fullerenes). No visible difference was observed between the intensities of fragments containing odd and even numbers of carbon atoms. Since each carbon atom was initially bound to a maximum of one hydrogen, for each carbon atom lost, a number of H_m losses also occurred.

As the number of carbon atoms that were lost increased, the number of hydrogen atoms that were lost increased much more sharply. For example, in the CID spectra of $C_{60}H_{30}^+$, for the loss of 2 carbon atoms $C_{58}H_{19}^+$ was the most intense peak (a loss of 11 H atoms), and for the loss of 3 carbon atoms (5% of total number of C atoms), $C_{57}H_{15}^+$ was the most intense peak, a loss of 15 hydrogen atoms (50% of total number of H atoms). This indicates that the loss of the exohedrally bound hydrogen atoms from the fullerene was facile.

The smaller $C_nH_m^+$ fragments (n=3-18) were only observed for m=1, 2 or 3, with 2 generally being the most intense. The intensity of these peaks showed no relationship with the intensity of the low m/z peaks observed for C_{60}^+ and C_{70}^+, suggesting different structures. It was not possible to gain information regarding the identity of these structures.

7.3 High-energy collision-induced dissociation of alkali-metal cationised poly(ethylene glycol) and poly(propylene glycol).

The high-energy collision-induced dissociation spectra of poly(ethylene glycol) and poly(propylene glycol) were dominated by the intensity of the low m/z fragments. It is suggested that the energy taken up during collision is great enough to allow multiple consecutive fragmentations of the selected ion, thereby accounting for the presence of these low m/z fragment ions.

In addition to the low m/z ions, a number of fragment-ion series were observed throughout the collision-induced dissociation spectra for both poly(ethylene glycol) and poly(propylene glycol).

Reaction mechanisms for the fragment-ion series produced by the high-energy collision-induced dissociation of poly(ethylene glycol) have been explained. It has previously been proposed that direct homolytic cleavage of C-C and C-O bonds in the polymer backbone occurs to produce odd-electron fragment ions and odd-electron neutrals, as shown in reactions 5.1[A]-[C].[146] Fragment-ion series **A, B** and **C** can arise from these mechanisms.

Odd-electron fragment ions were limited to the low m/z region of the collision-induced dissociation spectra of poly(ethylene glycol). The even-electron fragment-ion series, observed throughout the CID spectra, cannot be explained by direct homolytic cleavage of C-C and C-O bonds in the polymer backbone. It is proposed that there is sufficient energy taken up during collision for the scission of a C-H bond (the strongest of the poly(ethylene glycol) bonds). Subsequent rearrangement results in scission of the polymer chain at one of two possible positions β to the site of the initial C-H cleavage. The first of these positions results in an even-electron ion and odd-electron neutral, and it is proposed that fragment-ion series **D** and **E** arise from this mechanism. The second of these positions results in an odd-electron ion and even-electron neutral, and this mechanism is proposed as an alternative (additional) route for the formation of fragment-ion series **A, B** and **C.**

For the high-energy collision-induced dissociation of poly(propylene glycol) seven fragment-ion series were observed. The analysis of these fragment-ion series was complicated as the poly(propylene glycol) molecule is unsymmetrical.

Direct chain-scissions of C-C, C-O and C-H bonds were again proposed for the odd-electron fragment-ion series **A1, B** and **C,** that were analogous to those proposed for poly(ethylene glycol). C-H scission was proposed to give rise to the even-electron

fragment-ion series **D**, **E** and **F1**. For two of the fragment-ion series, **A1** and **F1**, it was possible to assign them unambiguously as fragments with charge-retention on one particular end of the ion. For the five other fragment-ion series it was not possible to assign which end of the parent ion they had originated from as fragments arising from different ends were isomers. Neither was it possible to reject any of the postulated isomeric species by examining their likelihood of formation.

A future method to try and assess whether any of these fragment-ions are formed from one particular end of the ion would be to modify *one* of the end-groups of the polymer, so that fragment from that end are mass shifted.

It is proposed that even-electron fragment-ion series **G** occurs as a result of homolytic cleavage of a C-CH_3 bond. This would explain why a similar series was not observed for poly(ethylene glycol).

7.4 Determination of End Groups of Polyglycol Ions Generated by Matrix-Assisted Laser Desorption/Ionisation using High-Energy Collision-Induced Dissociation

Four poly(ethylene glycol) polymers with differing modified end-groups were investigated. For each, fragment-ion series were observed that were analogous to those observed for unmodified poly(ethylene glycol), but m/z shifted due to the end-groups.

The high-energy collision-induced dissociation of these modified poly(ethylene glycol) polymers were dominated by the intensity of the low m/z ions. These intense low-mass fragment ions fall into two categories of fragments: end-groups and internal fragments. For each polymer, it was found that the end-group fragment-ions present in the low m/z region acted as a fingerprint for determining the structure of the polymer end-groups. The end-group fragments did not contain sodium, indicative of their formation being due to high-energy processes. These sodium-free ions have been reported to be much less significant for experiments utilising lower-energy regimes.[145, 172]

The internal fragment m/z 53 (observed for every poly(ethylene glycol) investigated) corresponds to a sodiated fraction of the repeat unit, the formation of which would again be expected to be a high-energy process. This fragment, m/z 53, is not significant in the collision-induced dissociation spectra of alkali-metal cationised poly(ethylene glycol) performed with lower collision energy.

A second relevant comparison is between the collision-induced dissociation of alkali metal cationised poly(ethylene glycol) ions generated by matrix-assisted laser

desorption/ionisation, and the collision-induced dissociation spectra of of alkali metal cationised poly(ethylene glycol) ions generated by field desorption (using similar energy regimes).[146, 147] These field desorption spectra resemble the low-energy collision-induced dissociation spectra of of alkali-metal cationised poly(ethylene glycol) ions generated by MALDI.

The relative abundances of fragment ions produced by CID of a precursor ion depend upon both the structures of the ions and on their internal energies. When ions are produced by the same ionisation technique and the conditions of collision are carefully controlled, internal energy effects are normally assumed to be small and differences in the spectra ascribed to structural differences. If a particular precursor ion is produced by the use of different ionisation techniques, the average internal energy of the ion will depend on the ionisation technique employed. If it is assumed that the a constant average amount of energy is transferred to the ion on collision (for high-energy collision at the same high energy), the variation in total internal energy content due to the ionisation technique may be expected to be reflected by changes in the relative abundance of ions in the collision-induced dissociation spectra.

The upper limit of internal energy which the precursor ion may possess is the difference between the appearance energy of its lowest energy fragment and the energy required to produce the precursor ion. Internal energy effects will be greatest for precursor ions where this energy difference is large. Furthermore, internal energy effects should be most noticeable for ions containing few atoms where the internal energy is distributed amongst relatively few degrees of freedom.

There have been very few reports of the effects on the collision-induced dissociation spectra by generating the precursor ions from different ionisation techniques with a view to varying their internal energy prior to collision. Bowers et al showed that for

a series of small ions, such as $C_2H_4N^+$ and $CH_3NH_3^+$, the CID spectrum depended strongly on the internal energy of the ion before collision.[173, 174] The internal energy of protonated molecules of valinomycin (MH^+) formed by chemical ionisation (CI), fast atom bombardment (FAB) and electrospray ionisation (ESI) was reported not to significantly affect the fragment ion spectra.[175, 176] It was suggested that the electron ionisation (EI) and field desorption (FD) collision-induced dissociation spectra of the valinomycin molecular ion ($M^{+\bullet}$) differed as a consequence of the different structures of the precursor ion, rather than because of internal energy effects.

The conclusion that can be tentatively drawn from the differences in abundances of the low m/z ions for the collision-induced dissociation of $[M+Na]^+$ adduct ions of poly(ethylene glycol) generated by MALDI and field desorption (using the same collision energy regime) is that the energy driving the fragmentation following CID at a laboratory-frame collision energy of ~8 keV derives to a significant extent from *both* the ionisation process and the collision process. It would then be the combination of global energisation during ionisation and localised energisation during collision that leads to the formation of the especially structurally informative fragment ions, that elucidate both the end-group and repeat unit structures. Experiments using Fourier transform ion cyclotron resonance (FTICR) and sustained off-resonance irradiation (SORI) have confirmed that the low m/z fragment ions are absent from the low-energy tandem mass spectra of alkali metal cationised poly(ethylene glycol) polymers.[177]

For the palmitoyl end-terminated poly(ethylene glycol), a series of intense high m/z peaks were observed. It is proposed that these peaks originate from C-C bond dissociation of the palmitoyl end-group. Similar fragment-ion series have been

reported for collision-induced dissociation of saturated fatty-acids (that contain long alkyl chains),[161] and several mechanisms (all described as being 'charge-remote') have been postulated.[162, 163, 164]

The even-electron fragment-ions observed in this study cannot have arisen from direct homolytic cleavage of a C-C bond in the polymer backbone (as proposed by Wysocki and Ross[163]) as this mechanism results in odd-electron fragment-ions. 1,4-H_2-elimination (as proposed by Jensen et al[162]) involves a concerted mechanism leading to even-electron products. This mechanism seems unlikely from what is generally accepted about concerted mechanisms in organic chemistry.[149, 150, 151, 152] It is proposed that the high m/z fragment-ion series observed in the collision-induced dissociation spectrum of palmitoyl end-terminated poly(ethylene glycol) results from a multistep radical mechanism involving elimination of an $H^{\bullet}$ radical as the initial rate-determining step, followed by subsequent elimination of an odd-electron neutral, in the same manner as has been proposed for saturated fatty acids.[164]

7.5 High-Energy Collision-induced Dissociation of a Random Ethylene Glycol/Propylene Glycol Copolymer

The investigation of the structure of a random ethylene glycol/propylene glycol copolymer using collision-induced dissociation has followed a qualitiative approach. The most intense oligomer of a poly(ethylene glycol)-*co*-(propylene glycol) (monobutyl ether) copolymer, corresponding to 7 ethylene glycol and 8 propylene glycol units, was selected, and a collision-induced dissociation spectrum obtained. Due to the random statistical nature of the copolymer, there are a total of 105 possible combinations of monomer units for this particular oligomer:

$$combinations = \frac{n!}{k!(n-k)!} = 105 \qquad Eq.\ 7.1$$

where n is the number of items (15) and k is the number of items in each combination (2).

More than 150 peaks were observed in the collision-induced dissociation spectrum. The approach used to analyse this CID spectrum was assign all of the possible **D** and **E** fragment-ion series (for both poly(ethylene glycol) and poly(propylene glycol) the **D** and **E** fragment-ion series were the most intense above m/z ~ 200), and rather than analyse which structural combinations were present (as many of the peaks could be assigned as several different structures), analyse which structural combinations were *not* present in the CID spectrum.

This approach has revealed that ethylene glycol blocks (sections of the copolymer containing more than one consecutive ethylene glycol unit) were not present at the non-alkyl end of the ion, i.e. propylene glycol units were present more often at this end of the ion. The implication is that this oligomer (and consequently the polymer) was not actually random (assuming that when ethylene glycol *was* present at the non-alkyl end of the ion, it did not result in discrimination against ionisation).[178, 179]

This approach highlights the challenge of analysing statistical copolymers. It seems unlikely that collision-induced dissociation will be routinely used to produce detailed structural information about random copolymers, as the random initial structure gives a random (seemingly meaningless) set of fragment ions. If the intensities of the fragment ions could be trusted, it would be possible (but time consuming) to obtain a quantitative analysis of the polymer under investigation.

For a polymer that is not completely random then collision-induced dissociation can provide more general information about the copolymer structure (as detailed above). Only if there is a more ordered initial structure (e.g. a well defined block or graft copolymer) will collision-induced dissociation be able to produce detailed information such as copolymer block lengths or the position of side-chains.

7.6 Collision-induced dissociation of protonated polyglycols generated by field desorption.

Matrix-assisted laser desorption/ionisation was found not to readily generate $[M+H]^+$ ions of polyglycols. In order to investigate the collision-induced dissociation of protonated polyglycol polymers, a ZabSpec oa-TOF instrument equipped with a field desorption ion source was employed.

For all of the protonated polyglycol polymers investigated, only low m/z fragments were observed. Previous studies of the CID of protonated polyglycol ions reported the observation of fragment-ion series throughout the mass spectrum (although the low m/z ions were still reported to be the most intense). As the ionisation technique in each case was field desorption, the main experimental difference is the collision energy regime. Centre-of-mass collision energies of ~15 eV have been shown to generate fragment-ion series for ions generated by field desorption. The centre-of-mass collision energies employed in the investigation (using helium as the collision gas) of the collision-induced dissociation of protonated polyglycol ions as part of this study was an order of magnitude lower (~1.5 eV), and appears to be too low to cause fragmentation of the polymer chain.

It was intended to investigate the collision-induced dissociation of the same protonated polyglycol ions using argon as the collision gas. This was not possible due to time constraints of the industrial partners.

Appendix I –*Calibration of the Tandem double-focusing/time-of-flight mass spectrometer.*

The calibration of the tandem double-focusing time-of-flight mass spectrometer (MAG-TOF) for collision-induced dissociation spectra was non-trivial due to the quadratic-field reflectron, ion buncher and associated ion optics.

In order to create a calibration file, the HDT application software[180] that controlled data acquisition allowed the input of up to eight calculated peak m/z's that could be compared against the current peak positions. A first-order polynomial (linear) fit was then used to correct the mass spectrum.

Due to the instrument design, incorporating a quadratic-field reflectron, a first-order polynomial function was not suitable for creating a calibration file that could be applied to different collision-induced dissociation spectra:

for example, consider the CID spectrum of a *particular* parent ion. If several peaks in the CID spectrum were of known m/z, they could be could be calibrated against, and a calibration fitted for that *particular* CID spectrum. On close inspection of any spectrum calibrated by this method, it can be seen that the observed m/z 'drifts' to a slightly higher than expected value as the distance from a calibration point increases. This effect is exemplified for the CID of a sodiated poly(ethylene glycol). Table 5.1 shows a peak list obtained for the xenon CID spectrum of the poly(ethylene glycol) $[M+Na]^+$ adduct ion m/z 1097.6 (n=31). Two of the calibration peaks were m/z's 595.3 and 771.5. Peaks close to the calibrated peaks show very good agreement with

their calculated m/z's (<0.1 Da). At the mid-point between these calibration points the agreement is less good ~ 0.3 Da.

If a calibration file that was generated from fitting the CID spectrum of a particular parent ion was applied to a CID spectrum of a different parent ion, very large discrepancies between the observed and calculated m/z's were seen. For example, if a calibration file that was generated for the poly(ethylene glycol) $[M+Na]^+$ adduct ion m/z 1097.6 (n=24) was applied to a CID spectrum obtained for the n=25 oligomer, the parent ion m/z of the n=25 oligomer was observed at a higher than expected m/z of approximately 1.5 Da. If the same calibration file was applied to a CID spectrum obtained for C_{60}^+, the C_{60}^+ peak was observed at an m/z 150 Da higher than expected.

The approach used to calibrate all of the spectra obtained from the tandem double-focusing/time-of-flight instrument (MAG-TOF) in this study was essentially that described above. It was necessary to generate calibration files for each parent ion selected for collision-induced dissociation. This meant that in each spectrum a number of peaks had to be known (or at least assumed):

1) The CID spectra of C_{60}^+ and C_{70}^+ were already reported in the literature. This meant that calibration was relatively easy, especially as the m/z difference between peaks was always regular (24 Da in the high m/z region, 12 Da in the low m/z region).
2) For the calibration of C_{130}^+ it was evident that the m/z difference between peaks in the high m/z region was 24 Da, making it simple to count down peaks from the

parent ion. The low m/z region showed the same intensity pattern as for C_{60}^+ and C_{70}^+, and peaks could be assigned on the same basis.

3) For the calibration of $C_{60}H_{30}^+$ it was possible to count peaks with a 1 Da m/z difference from the parent ion, making for easy calibration of the high m/z region of the spectrum. By moving down through the spectrum and knowing that the peaks would shift to slightly higher m/z's the further they were from a calibraton point, it was possible to fit by trial-and-error the low m/z region.

4) The calibration of the collision-induced dissociation spectra of poly(ethylene glycol) was more problematic. The approach taken was to initially calibrate just using the two known peaks – the Na^+ and parent ion peaks. The low m/z region of the resulting 'pseudo-calibrated' spectrum was then examined. Knowing that peaks were appearing at slightly higher than expected m/z would allow further re-calibration. For example a peak that occurred at m/z 53.8 could be reassigned as 53.1, and the spectrum re-calibrated using the three (23.0, 53.1 and parent) peaks. Using this trial-and-error process it was quickly possible to identify the low m/z fragments belonging to ion-series **A**, **B**, **C**, **D** and **E**. Due to the repeating nature of the fragment-ion series it was then possible to extend the calibration to all members of these series.

All of the collision-induced dissociation spectra of the alkali-metal cationised polyglycols were finally calibrated using the known positions of the peaks:

a) Na^+

b) m/z 53.1

c) five (evenly spaced) members of fragment-ion series **D**

d) parent ion

References

[1] Beynon, J. H.; Morgan, R. P., *Int. J. Mass Spectrom. Ion Phys.*, **1978**, *27*, 2, ref. to Goldstein, E., Berl. Ber., **1886**, *39*, 691

[2] Thomson, J. J.; Thomson, G. P., "Conduction of Electricity through Gases", CUP, Cambridge, **1933**, *1*, 267

[3] Beynon, J. H.; Morgan, R. P., *Int. J. Mass Spectrom. Ion Phys.*, **1978**, *27*, 2, ref. to Wien, W., Verh. Phys. Gesell., **1898**, 17

[4] Thomson, J. J.; Thomson, G. P., "Conduction of Electricity through Gases", CUP, Cambridge, **1933**, *1*, 265, ref. to Wien, W. Wied. Ann., **1898**, *65*, 440

[5] Thomson, J. J.; Thomson, G. P., "Conduction of Electricity through Gases", CUP, Cambridge, **1933**, *1*, 266, ref. to Wien, W. Wied. Ann. der Phys, **1902**, *8*, 241

[6] Thomson, J. J.; Thomson, G. P., "Conduction of Electricity through Gases", CUP, Cambridge, **1933**, *1*, 246, ref. to Thomson, J. J., Phil. Mag., **1899**, *48*, 547

[7] Beynon, J. H.; Morgan, R. P., *Int. J. Mass Spectrom. Ion Phys.*, **1978**, *27*, 2, ref. to Aston, F. W., Phil. Mag., **1919**, 38, 707

[8] Herzog, R., *Z. Phys.*, **1934**, *89*, 447

[9] Mattauch, J.; Herzog, R., *Z. Phys.*, **1934**, *89*, 786

[10] Johnson, E. G.; Nier, A. O., *Phys. Rev.*, **1953**, *91*, 10

[11] Stephens, W. E., *Phys. Rev.*, **1946**, *69*, 691

[12] Skoog , D. A.; Holler, F. J.; Nieman, T. A., *"Principles of Instrumental Analysis"*, fifth edition, Saunders College Publishing, Orlando, USA, **1992**, 184

[13] Wiley, W. C.; MacLaren, I. H., *Rev. Sci. Instr.*, **1955**, *26*, 1150

[14] Mamyrin, B. A. *USSR Patent No. 198,034*, **1996**

[15] Mamyrin, B. A.; Karataev, V. I.; Shmikk, D. V.; Zagulin, V. A. *Sov. Phys. JETP*, **1973**, *37*, 45

[16] Karataev, V. I.; Mamyrin, B. A.; Shmikk, D. V. *J. Tech. Phys.*, **1971**, *16*, 1498

[17] Gall, L. N.; Golikov, M. L.; Alexsandrov, M. L.; Pechalina, Y. E.; Holin, N. R., *USSR Inventor's Certificate No. 1,247,973*, **1986**

[18] Makarov, A. A., *J. Phys. D; Appl. Phys.*, **1991**, *24*, 533

[19] Derrick, P. J.; Colburn, A. W.; Giannakopulos, A. E.; Raptakis, E. N.; Reynolds, D. J.; Davis, S. C.; Hoffmann, A. D.; Wright, B., *Proceedings of 42nd ASMS Conference on Mass Spectrometry and Allied Topics, Chicago*, **1994**, 1152

[20] Munson, M. S. B.; Field, F. H., *J. Am. Chem. Soc.*, **1966**, *88*, 2621

[21] Munson, M. S. B., *Anal. Chem.*, **1977**, *49*, 722A

[22] Beckey, H. D., *Int. J. Mass Spec. and Ion Phys.*, **1969**, *2*, 500

[23] Bray, R. G.; Hochstrassee, R. M.; Wessel, J. E., *Chem. Phys. Lett.*, **1974**, *27*, 167

[24] Schlag, E. W.; Neusser, H. J., *J. Am. Chem. Soc.*, **1966**, *88*, 2621

[25] Müller, E. W., *Z. Physik*, **1936**, *102*, 734

[26] Müller, E. W., *Naturwissenschaften*, **1953**, *27*, 290

[27] Inghram, M. G.; Gomer, R., *J. Chem. Phys.*, **1954**, *22*, 1279

[28] Derrick, P.J.; Robertson, A. J. B., *Int. J. Mass Spectrom. Ion Proc.*, **1972**, *10*, 315

[29] Beckey, H. D.; Heinsing, H.; Hey, H.; Metzinger, H. G., *Adv. Mass Spectrom.*, **1968**, *4*, 817

[30] Beckey, H. D., *Int. J. Mass Spec. and Ion Phys.*, **1969**, *3*, 161

[31] Dole, M.; Hines, R. L.; Mack, R. C.; Mobley, R. C.; Ferguson, L. D.; Alice, M. B., *J. Chem. Phys.*, **1968**, *49*, 2240

[32] Whitehouse, C. M.; Dreyer, R. N.; Yamashita, M.; Fenn, J. B., *Anal. Chem.*, **1985**, *57*, 675

[33] Fenn, J. B., *J. Am. Soc. Mass Spectrom.*, **1993**, *4*, 524

[34] Dole, M.; Hines, R. L.; Mack, R. C.; Mobley, R. C.; Ferguson, L. D.; Alice, M. B., *J. Chem. Phys.*, **1970**, *52*, 4977

[35] Iribarne, J. V.; Thomson, B. A., *J. Chem. Phys.*, **1976**, *64*, 2294

[36] Iribarne, J. V.; Thomson, B. A., *J. Chem. Phys.*, **1979**, *71*, 4457

[37] Johnston, P. M.; Bergman, M. R.; Zakheim, D., *J. Chem. Phys.*, **1975**, *62*, 2500

[38] Tanaka, K.; Waki, H.; Ido, Y.; Akita, S.; Yoshida, Y.; Yoshida, T., *Rapid Commun. Mass Spectrom.*, **1988**, *2*, 151

[39] Karas, M.; Bachmann, D.; Hillenkamp, F., *Anal. Chem.*, **1985**, *57*, 2935

[40] Karas, M.; Bachmann, D.; Bahr, U.; Hillenkamp, F., *Int. J. Mass Spectrom. Ion Proc.*, **1987**, *78*, 53

[41] Karas, M.; Hillenkamp, F., *Anal. Chem.*, **1988**, *60*, 2299

[42] Hillenkamp, F.; Karas, M., *Methods in Enzymlogy*, **1990**, *193*, 280

[43] Spengler, B., *J. Mass Spectrom.*, **1997**, *32*, 1019

[44] Mo, W.; Takao, T.; Shimonishi, Y., *Rapid Commun. Mass Spectrom.*, **1997**, *11*, 1829

[45] Ross, P. L.; Davis, P. A.; Belgrader, P., *Anal. Chem.*, **1998**, *70*, 2067

[46] Garozzo, D.; Nasello, V.; Spina, E.; Sturiale, L., *Rapid. Commun. Mass Spectrom.*, **1997**, *11*, 1561

[47] Spengler, B.; Kirsch, D.; Lemoine, J.; Kaufmann, R., *J. Mass Spectrom.*, **1995**, *30*, 782

[48] Smith, P. B.; Pasztor Jr., A. J.; McKelvy, M. L.; Meunier, D. M.; Froelicher, S. W.; Wang, F. C.-Y., *Anal. Chem.*, **1997**, *69*, 95R

[49] O'Connor, P. B.; Duursma, M. C.; van Rooij, G. J.; Heeren, R. M. A.; Boon, J. J., *Anal. Chem.*, **1997**, *69*, 2751

[50] Whittal, R. M.; Schriemer, D. C.; Li, L., *Anal. Chem.*, **1997**, *69*, 2734

[51] Zenobi, R.; Knochenmuss, R., *Mass Spectrom. Rev.*, **1998**, *17*, 337-366

[52] Strupat, K.; Karas, M.; Hillenkamp, F., *Int. J. Mass Spectrom. Ion Proc.*, **1991**, *111*, 89

[53] Beavis, R. C.; Chait, B. T., *Rapid Commun. Mass Spectrom.*, **1989**, *3*, 432

[54] Beavis, R. C.; Chaudhary, T.; Chait, B. T., *Org. Mass Spectrom.*, **1992**, *27*, 156

[55] Aston, F. W., *Proc. Cambridge Philos. Soc.*, **1919**, 19

[56] Yost, R. A.; Enke, C. G., *Anal. Chem.*, **1979**, *51*, 1251A

[57] Beynon, J. H.; Cooks, R. G.; Amy, J. W.; Baitinger, W. E.; Ridley, T. Y., *Anal. Chem.*, **1973**, *45*, 1023A

[58] Durup, J., *Recent Developments in Mass Spectrometry*, Ogata, K. and Hagakawa, T. (eds.), University Park Press, Baltimore, 1970.

[59] Neumann, G. M.; Sheil, M. M.; Derrick, P. J., *Z. Natursforsch.*, **1984**, *39a*, 584

[60] Kim, M. S., *Org. Mass Spectom.*, **1991**, *26*, 565

[61] Neumann, G. M.; Derrick, P. J., *Org. Mass Spectrom.*, **1984**, *19*, 165

[62] Uggerud, E.; Derrick, P. J., *J. Phys. Chem.*, **1991**, *95*, 1430

[63] Bradley, C. D.; Curtis, J. M.; Derrick, P. J.; Sheil, M. M., *J. Chem. Soc. Faraday Trans.*, **1994**, *90*, 239

[64] Bradley, C. D.; Derrick, P. J., *Org. Mass Spectrom.*, **1993**, *28*, 390

[65] Jarrold, M. F.; Bower, J. E., *J. Am. Chem. Soc.*, **1992**, *114*, 459

[66] Stults, J. T.; Enke, C. G.; Holland, J. F., *Anal. Chem.*, **1983**, *55*, 1323

[67] Strobel, F. H.; Solouki, T.; White, M. A.; Russel, D. H., *J. Am. Soc. Mass Spectrom.*, **1990**, *2*, 91

[68] Pinkston, J. D.; Rabb, M.; Watson, J. T.; Allison, J., *Rev. Sci. Instrum.*, **1986**, *57*, 583

[69] Jardine, D. R.; Morgan, J.; Alderdice, D. S.; Derrick, P. J., *Org. Mass Spectrom.*, **1992**, *27*, 1077

[70] Cornish, T. J.; Cotter, R. J., *Anal. Chem.*, **1993**, *65*, 1043

[71] Sakurai, T.; Ito, H.; Matsuo, T., *Anal. Chem.*, **1994**, *66*, 2313

[72] Andersen, U. N.; Colburn, A. W.; Makarov, A. A.; Raptakis, E. N.; Reynolds, D. J.; Derrick, P. J.; Davis, S. C.; Hoffman, A. D.; Thomson, S., *Rev. Sci. Instrum.*, **1998**, 69, 1650

[73] Chan, T.-W. D.; Thomas, I.; Colburn, A. W.; Derrick, P. J., *Chem. Phys. Lett.*, **1994**, *222*, 579

[74] Boesl, U.; Weinkauf, C.; Weickhardt, C.; Schlag, E. W., *Int. J. Mass Spectrom. Ion Proc.*, **1994**, *131*, 87

[75] Zavoiskii, E. K.; Fanchenko, S. D., *Sov. Phys.: Doklady*, **1956**, *1*, 285

[76] Kroto, H. W.; Heath, J. R.; O'Brien, S. C.; Curl, R. F.; Smalley, R.E., *Nature*, **1985**, *318*, 162

[77] Kroto, H. W., *Nature*, **1987**, *329*, 529

[78] Hawkins, J. M.; Meyer A.; Lewis, T. A.; Loren, S.; Hollander, F. J., *Science*, **1991**, *252*, 312

[79] Krätschmer, W.; Lamb, L. D.; Fostiropoulos, K.; Huffman, D. R., *Nature*, **1990**, *347*, 354

[80] Olah, G. A.; Bucsi, I.; Lambert, C.; Aniszfeld, R.; Trivedi, N. J.; Sensharma, D. K.; Surya Prakash, G. K., *J. Am. Chem. Soc.*, **1991**, *113*, 9385

[81] Wood, J. M.; Kahr, B.; Hoke, S. H.; Dejarme, L.; Cooks, R. G.; Ben-Amotz, D., *J. Am. Chem. Soc.*, **1991**, *113*, 5907

[82] Callahan, J. H.; McElvany, S. W.; Ross, M. M., *Int. J. Mass Spectrom. Ion Proc.*, **1994**, *138*, 221

[83] Kan, S. Z.; Lee, S. A.; Byun, Y. G.; Freiser, B. S., *J. Mass Spectrom.*, **1995**, *30*, 194

[84] Kan, S. Z.; Byun, Y. G.; Freiser, B. S., *J. Am. Chem. Soc.*, **1995**, *117*, 1177

[85] Bausch, J. W.; Surya Prakash, G. K.; Olah, G. A.; Tse, D. S.; Lorents, D. C.; Bae, Y. K.; Malhotra, R., *J. Am. Chem. Soc.*, **1991**, *113*, 3205

[86] Chen, G.; Cooks, R. G.; Corpuz, E.; Scott, L. T., *J. Am. Soc. Mass Spectrom.*, **1996**, *7*, 618

[87] Heath, J. R.; O'Brien, S. C.; Zhang, Q.; Liu, Y.; Curl, R. F.; Kroto, H. W.; Tittel, F. K.; Smalley, R.E., *J. Am. Chem. Soc.*, **1985**, *107*, 7779

[88] Christian, J. F.; Wan, Z.; Anderson, S. L., *J. Chem. Phys.*, **1993**, *99*, 3468

[89] Saunders, M.; Jiminez-Vaquez, H. A.; Cross, R. J.; Poreda, R. J., *Science*, **1993**, *259*, 1428

[90] Saunders, M.; Jiminez-Vaquez, H. A.; Cross, R. J.; Mroczkowski, S.; Gross, M. L.; Giblin, D. E.; Poreda, R. J., *J. Am. Chem. Soc.*, **1994**, *116*, 2193

[91] Chai, Y.; Guo, T.; Jin, C.; Haufler, R. E.; Chibante, L. P. F.; Fure, J.; Wang, L.; Alford, J. M.; Smalley, R. E., *J. Phys. Chem.*, **1991**, *95*, 7564

[92] Guo, T.; Jin, C.; Smalley, R. E., *J. Phys. Chem.*, **1991**, *95*, 4948

[93] Andreoni, W.; Gygi, F.; Parrinello, M., *Chem. Phys. Letts.*, **1992**, *190*, 159

[94] Lamparth, I.; Nuber, B.; Schick, G.; Skiebe, A.; Grosser, T.; Hirsch, A. *Angew. Chem. Int. Ed. Engl.*, **1995**, *34*, 2257

[95] Ross, M. M.; Callahan, J. H., *J. Phys. Chem.*, **1993**, *95*, 5720

[96] Moseley, J. A., *Ph.D. Thesis*, University of Warwick, **1996**

[97] McHale, K. H.; Polce, M. J.; Wesdemiotis, C., *J. Mass Spectrom.*, **1995**, *30*, 33

[98] Hvelpund, P.; Andersen, L. H.; Haugen, H. K.; Lindhard, J.; Lorents, D. C.; Malhotra, R.; Ruoff, R., *Phys. Rev. Letters*, **1992**, *69*, 1915

[99] Doyle Jnr., R. J.; Ross, M. M., *J. Phys. Chem.*, **1991**, *95*, 4954

[100] Takayama, M., *Org. Mass Spectrom.*, **1993**, *28*, 61

[101] Mosely, J. A.; Cooper, H. J.; Gallagher, R. T.; Derrick, P. J., *Eur. Mass Spectrom.*, **1995**, *1*, 501

[102] Yeretzian, C.; Hansen, K.; Diederich, F.; Whetten, R. L., *Nature*, **1992**, *359*, 44

[103] Beck, R. D.; Weis, P.; Bräuchle, G.; Kappes, M. M., *J. Chem. Phys.*, **1994**, *100*, 262

[104] Liu, Z.-Y.; Wang, C.-R.; Huang, R.-B.; Zheng, L.-S., *Int. J. Mass Spectrom. Ion Proc.*, **1995**, *145*, 1

[105] Shartsburg, A. A.; Hudgins, R. R.; Dugourd, P.; Jarrold, M. F., *J. Phys. Chem.*, **1997**, *101*, 1684

[106] Lebrilla, C. B., *Department of Chemistry, University of Davis, California, USA.*

[107] Drewello, T., *D Department of Chemistry, University of Warwick, Coventry, UK.*

[108] Barrow, M. P., *unpublished data.*

[109] Bahr, U.; Depe A.; Karas, M.; Hillenkamp, F.; Giessmann, U. *Anal. Chem.* **1992**, *64*, 2866

[110] Belu, A. M.; DeSimone, J. M.; Linton, R. W.; Lange, G. W.; Friedman, R. M. *J. Am. Soc. Mass Spectrom.* **1996**, *7*, 11

[111] Lloyd, P. M.; Suddaby, K. G.; Varney, J.V.; Scrivener, E.; Derrick, P.J.; Haddleton, D. M. *Eur. Mass Spectrom.*, **1995**, *1*, 293

[112] Hoberg, A.-M.; Haddleton, D. M.; Derrick, P. J. *Eur. Mass Spectrom.*, **1997**, 3, 471

[113] Creel, H. S. *Trends Pol. Sci.* **1993**, *1*, 336

[114] Jackson, C. A.; Simonsick, W. J. *Curr. Op.. Sol. S. Mat. Sci.* **1997**, *2*, 661

[115] Danis, P. O.; Karr, D. E.; Simonsick, W. J.; Wu, D. T. *Macromolecules* **1995**, *28*, 1229

[116] Danis, P. O.; Karr, D. E.; Xiong, Y.; Owens, K. G. *Rap. Comm. Mass Spectrom.* **1996**, *10*, 862

[117] Suddaby, K. G.; Hunt, K. H.; Haddleton, D. M. *Macromolecules* **1996**, *29*, 8642

[118] Maloney, D. R.; Hunt, K. H.; Lloyd, P. M.; Muir, A. V. G.; Richards, S. N.; Derrick, P. J.; Haddleton, D. M. *J. Chem. Soc. Chem. Comm.* **1995**, 561

[119] Montaudo, G.; Montaudo, M. S.; Puglisi, C.; Samperi, F. *J. Pol. Sci. A Pol. Chem.* **1996**, *34*, 439

[120] Williams, J. B.; Gusev, A. I.; Hercules, D. M. *Macromolecules* **1997**, *30*, 3781

[121] Montaudo, G.; Montaudo, M. S.; Puglisi, C.; Samperi, F.; Sepulchre M. *Macromol. Chem. and Phys.* **1996**, *197*, 2615

[122] Zammit, M. D.; Davis, T. P.; Haddleton, D. M.; Suddaby, K. G. *Macromolecules* **1997**, *30*, 1915

[123] Guttman, C. M.; Blair, W. R.; Danis, P. O. *J. Polym. Sci. Part B, Polym. Physics* **1997**, *35*, 2409

[124] Duncalf, D. J.; Wade, H. J.; Waterson, C.; Derrick, P. J.; Haddleton, D. M.; McCamley, A. *Macromolecules* **1996**, *29*, 6399

[125] Nielen, M. W. F. *Anal. Chem.* **1998**, *70*, 1563

[126] Montaudo, M. S.; Puglisi, C.; Samperi, F.; Montaudo, G. *Rap. Comm. Mass Spectrom.* **1998**, *12*, 519

[127] Jackson, C.; Larsen, B.; McEwen, C. *Anal. Chem.* **1996**, *68*, 1303

[128] Kassis, C. E.; DeSimone, J. M.; Linton, R. W.; Lange, G. W.; Friedman, R. M. *Rap. Commun. Mass Spectrom.* **1997**, *11*, 1134

[129] Webster, O. W. *Science* **1991**, *251*, 887

[130] Davis, T. P.; Haddleton, D. M.; Richards, S. N. *J. Macromol Sc-Rev. Macromol. Chem. Phys.***1994**, *C34*, 243

[131] Haddleton, D. M.; Waterson, C.; Derrick, P. J.; Jasieczek, C.; Shooter, A. J. *Chem. Commun.* **1997**, 683

[132] Matyjaszewski, K. *J. Phys. Org. Chem.* **1995**, *8*, 197

[133] Yeates, S. G.; Richards, S. N. *Surf. Coat. Int.* **1996**, *10*, 437

[134] Matyjaszewski, K.; Wang, J.-L.; Grimaud, T. J.; Shipp, D. A. *Macromolecules* **1998**, *31*, 1527

[135] Perec, V.; Kim, H. J.; Barboiu, B. *Macromolecules* **1997**, *30*, 8526

[136] Bordoli, R. S.; Bateman, R. H., *Int. J. Mass Spectrom. Ion Proc.*, **1992**, *122*, 243

[137] Nizigiyimana, L.; Van den Heuvel, H.; Claeys, M., *J. Mass Spectrom.*, **1997**, *32*, 277

[138] Barber, M.; Bordoli, R. S.; Sedgewick, R. D.; Tyler, A. N. *Nature*, **1981**, 293, 270

[139] Arberth, W.; Straub, K. M.; Burlingame, A. L. *Anal. Chem.* **1982**, 54, 2029

[140] Banoub, J.; Thibault, P.; Goueth, P. Y.; Ronco, G.; Villa, P., *J. Mass Spectrom.*, **1997**, *32*, 109

[141] Solouki, T.; Reinhold, B. B.; Costello, C. E.; O'Malley, M.; Guan, S.; Marshall, A. G., *Anal. Chem.*, **1998**, *70*, 857

[142] Craig, A. G.; Derrick, P. J. *J. Chem. Soc. Chem. Comm.*, **1985**, 891

[143] Craig, A. G.; Derrick, P. J. *Aust. J. Chem.*, **1986**, 39, 1421

[144] Lattimer, R. P.; Munster, H.; Budzikiewicz, H., *Int. J. Mass Spectrom. Ion Proc.*, **1989**, *90*, 119

[145] Jackson, A. T.; Yates, H. T.; Scrivens, J. H.; Critchley, G.; Brown, J.; Green, M. R.; Bateman, R.H. *Rapid Commun. Mass Spectrom.*, **1996**, 10, 1668

[146] Craig, A. G., *Ph.D. Thesis*, University of New South Wales, Australia **(1984)**

[147] Agma, M., *Ph.D. Thesis*, University of New South Wales, Australia **(1988)**

[148] Selby, T. L.; Wesdemiotis, C.; Lattimer, R. P., *J. Am. Soc. Mass Spectrom.*, **1994**, *5*, 1081

[149] Woodward, R. B.; Hoffmann, R., *Angew. Chem. Int. Ed. Engl.*, **1969**, *8*, 781

[150] Dewar, M. J. S., *Angew. Chem. Int. Ed. Engl.*, **1971**, *10*, 761

[151] Dewar, M. J. S.; Kohn, M. C.; Trinajstic, N., *J. Am. Chem. Soc.*, **1971**, *93*, 3437

[152] March, J., "Advanced Organic Chemistry – Reactions, Mechanisms and Structure", J. Wiley and Sons, Fourth Ed., **1992**, Chapter 15, 844-846

[153] Claeys, M.; Van den Heuvel, H., *Biol. Mass Spectrom.*, **1994**, *23*, 20

[154] Claeys, M.; Nizigiyimana, L.; Van den Heuvel, H.; Derrick, P. J., *Rapid. Commun. Mass Spectrom.*, **1996**, *10*, 770

[155] Hoberg, A.-M.; Jackson, A.-T.; Scrivens, J. H.; Haddleton, D. M.; Derrick, P. J., *Eur. Mass Spectrom.*, **1998**, *4*, 435

[156] Deery, M. J.; Jennings, K. R.; Jasieczek, C. B.; Haddleton, D. M.; Jackson, A. T.; Yates, H. T.; Scrivens, J. H., *Rapid Commun. Mass Spectrom.*, **1997**, *11*, 57

[157] Lattimer, R. P., *J. Am. Soc. Mass Spectrom.*, **1992**, *3*, 225

[158] Thomson, B.; Wang, Z.; Paine, A.; Rudin, A.; Lajoie, G., *JAOCS*, **1995**, *72*, 11

[159] Prior, R., *Surfactants in Consumer Products*, Falbe, J., Ed.; Springer-Verlag: Heidelberg, 1987, pp5-22

[160] Ryan, A. J.; Stanford, J. L., *Comprehensive Polymer Science*, Allen, G., Bevington, J. C., Eds.; Pergamon Press: Oxford, UK, 1989; pp 427-455

[161] Adams, J.; Gross, M. L., *Anal. Chem.*, **1987**, *59*, 1576

[162] Jensen, N. J.; Tomer, K. B.; Gross, M. J., *J. Am. Chem. Soc.*, **1985**, *107*, 1863

[163] Wysocki, V. H.; Ross, M. M., *Int. J. Mass Spectrom. Ion Proc.*, **1991**, *104*, 179

[164] Claeys, M.; Nizigiyimana, L.; Van den Heuvel, H.; Derrick, P. J., *Rapid. Commun. Mass Spectrom.*, **1996**, *10*, 770

[165] Lattimer, R. P.; Hansen, G. E., *Macromolecules*, **1981**, *14*, 776

[166] Matsuo, T.; Matsuda, H.; Katakuse, I., *Anal. Chem.*, **1979**, *51*, 1329

[167] Neumann, G. M.; Cullis, P. G.; Derrick, P. J., *Z. Naturforsch.*, **1980**, *35a*, 1090

[168] Manufacturer: *Micromass, Manchester, UK.*

[169] Instrument Location: *Measurement Science Group, Unilever Research Port Sunlight, Bebington, Merseyside.*

[170] Raptakis, E. N., *Ph.D. Thesis*, **1996**, University of Warwick.

[171] Mosely, J. A.; Cooper, H. J.; Gallagher, R. T.; Derrick, P. J., *Eur. Mass Spectrom.*, **1995**, *1*, 501

[172] Jackson, A. T., *Personal communication.*

[173] van Koppen, P. A. M.; Illies, A. J.; Liu, S.; Bowers, M. T., *Org. Mass Spectrom.*, **1982**, *17*, 399

[174] Jarrold, M. F.; Illies, A. J.; Kirchner, N. J.; Bowers, M. T., *Org. Mass Spectrom.*, **1983**, *18*, 388

[175] Curtis, J. M.; Bradley, C. D.; Derrick, P. J.; Sheil, M. M., *Org. Mass Spectrom.*, **1992**, *27*, 502

[176] Sheil, M. M.; Kilby, G. W.; Curtis, J. M.; Bradley, C. D.; Derrick, P. J., *Org. Mass Spectrom.*, **1993**, *28*, 574

[177] Bottrill, A. R.; Lafitte, D.; Feng, X.-D., *unpublished result.*

[178] Amado, F. M. L.; Domingues, P.; Graca Santana-Marques, M.; Ferrer-Correia, A. J.; Tomer, K. B., *Rapid Commun. Mass Spectrom.*, **1997**, *11*, 1347

[179] McEwen, C. N.; Jackson, C.; Larsen, B. S., *Int. J. Mass Spectrom. Ion Proc.*, **1997**, 387

[180] Reynolds, D. J., *Copyright 1996*